Measurements of Two-Particle Correlations with respect to Higher-Order Event Planes in $\sqrt{s_{NN}} = 200$ GeV Au + Au Collisions at RHIC-PHENIX

Takahito TODOROKI

January 2014

Measurements of Two-Particle Correlations with respect to Higher-Order Event Planes in $\sqrt{s_{NN}} = 200$ GeV Au + Au Collisions at RHIC-PHENIX

Takahito TODOROKI
Doctoral Program in Physics

Submitted to the Graduate School of
Pure and Applied Sciences
in Partial Fulfillment of the Requirements
for the Degree of Doctor of Philosophy in
Science

at the
University of Tsukuba

Abstract

Quarks and Gluons are fundamental composition elements of nuclear matters and their behavior is ruled by the strong interaction described by Quantum Chromodynamics (QCD). Quark and gluons are confined in a hadron and QCD predicts they are de-confined from a hadron and they undergo a phase transition to a new state of matter called Quark-Gluon-Plasma (QGP) at an extremely high temperature and energy density. The unique tool to achieve such hot and dense state on the Earth is ultra-relativistic heavy ion collisions with a large accelerator.

In heavy ion collisions, a pair of hard-scattered partons propagate inside a QGP medium losing its energy by interactions with the medium. The consequent two-particle correlations are modified from a simple back-to-back correlations in p+p collisions. Hence, the two-particle correlation measurements are one of useful tools to diagnose the possible behavior of hard-scattered partons in the space-time evolution of medium such as

- path length dependence of parton energy-loss coming from geometry of QGP medium,
- re-distribution of lost parton energy also correlates with path-length by the geometry of medium.

The remarkable observations of two-particle correlation measurements at the Relativistic Heavy Ion Collider (RHIC) are as following, depending on transverse momentum p_T:

- suppression of away-side correlation yield of high p_T hadrons in central collisions,
- away-side double humps in azimuthal correlation, and near-side long-range correlation in rapidity direction of intermediate p_T hadrons.

While numbers of theoretical efforts have been made to describe the observed features in two-particle correlations, recently the existence of higher-order flow harmonics v_n is discovered, which is originating from parton density fluctuations due to participant fluctuations at initial heavy ion collisions. In order to a provide robust experimental constraints to theoretical models, the contribution of v_n must be subtracted from two-particle correlations.

In this thesis, we present the two-particle charged hadron correlation measurements in Au+Au collisions at $\sqrt{s_{NN}} = 200$ GeV with the data obtained by the RHIC-PHENIX Experiment in 2007, considering the backgrounds from $v_n (n = 2, 3, 4)$. The rapidity gap between trigger and associate particles in this measurement is $|\Delta\eta| < 0.7$.

The representing results of the two-particle correlations at high-p_T trigger particles of p_T =4-10 GeV/c are as following:

- suppression of away-side in most-central collisions at 0-10%,
- single-peaked away-side similar to that in p+p collisions at centrality 10-50%.

Those of the two-particle correlations of intermediate-p_T trigger $p_T < 4$ GeV/c are as following:

- suppressed or broadened away-side in most-central collisions at 0-10%,
- double-hump structures of away-side at centrality 10-50%.

The significance of latter feature is observed at most 1σ level in terms of the systematics in v_4 measurements. The double-hump position of experimental data above associate at p_T=1 GeV/c is approximately more than 4 times larger than that of Cherenkov-Gluon-Radiation. The p_T independence seen in the experimental data is also seen in Mach-Cone and Energy-Momentum Loss model, and their opening angle is about 20% larger and smaller than the experimental data, respectively. The opening angle of Hot-Spot Model is almost 50% larger than the experimental results.

The two-particle correlations with a trigger selection with respect to second and third-order event-planes, Ψ_2 and Ψ_3, are also measured for three p_T combinations of p_T: 2-4x1-2, 2-4x2-4, and 4-10x2-4 GeV/c. The representing results of Ψ_2 dependent correlations of p_T 2-4x1-2 GeV/c are as following;

- yield increases close to in-plane direction of Ψ_2 especially for mid-central to peripheral collisions,
- yield increases close to out-of-plane direction of Ψ_2 especially for most-central collisions.

The increase of in-plane yield from central to peripheral collisions, where the average path length decreases, can be taken as the increase of penetration probability due to less parton energy loss. While the increase of out-of-plane yield in central collisions, where the average path length becomes larger, can be regarded as a result of possible increase of re-distribution of the lost energy in the long path-length. Neither of this clear path-length dependence is seen in Ψ_3 dependent correlations.

The azimuthal anisotropy of correlated associate yield v_n^{PTY} with respect to Ψ_2 and Ψ_3 is calculated from the event-plane dependent correlations. We see following features in v_n^{PTY} via correlations in p_T: 2-4x1-2 GeV/c:

- positive near and away-side v_2^{PTY} above centrality 20% and negative near-side one in centrality 0-10%,
- positive near-side v_3^{PTY} but negative away-side v_3^{PTY} above centrality 20%.

The negative v_2^{PTY} cannot be explained by hydrodynamics or the suppression via parton-energy loss because the v_2 values calculated by both effects are positive: we need to consider an effect neither hydrodynamics nor the suppression. The centrality and near-away dependence of v_n^{PTY} is different between Ψ_2 and Ψ_3 dependent correlations, which may suggest parton-medium coupling is different in the second and third-order geometry of a media.

The peak shift of near and away-side correlations is also seen depending on trigger direction. A value A_{LR} to quantify the degree of peak shift is compared between Ψ_2 and Ψ_3 dependent correlations. A_{LR} of Ψ_2 dependent correlations shows the sign change depending on trigger direction on the other hand that of Ψ_3 dependent correlations is always negative. This value also shows different trend between Ψ_2 and Ψ_3 dependent correlations.

We suggest the importance of considering the re-distribution effect of lost parton energy and the different results of jet-medium interplay in the second and third-order geometry of media in future theoretical calculations.

Contents

List of Figures

List of Tables

Acknowledgements

I would like to first appreciate Prof. Y. Miake for giving me an opportunity to have great experiences in the filed of heavy ion physics and incisive but sincere advices to my activity. I also would like to express my cordial gratitude to Prof. S. Esumi. My activity at graduate school has been tremendously supported by his continuous encouragement, detailed advices and fruitful discussions. I learned many things from him, the knowledge on the heavy ion physics, experimental technique, and detail of data analysis. I am very grateful to the staffs in University of Tsukuba, Prof. T. Chujo, Prof. M. Inaba, Prof. H. Masui, Dr. M. Konno, Dr. T. Horaguchi, Mr. S. Kato, and Ms. H. Sakai for their insightfule advices and suggestions, and enormous help in developing a comfortable research environment.

I would like to thank very much the colleagues of graduate school, Dr. M. Shimomura, Dr. K. Miki, Dr. S. Dousatsu, Mr. R. Tanabe, Mr. Y. Ikeda, Mr. K. Watanabe, Mr. M. Sano, Dr. T. Niida, Ms. J. H. Bhom, Mr. H. Yokoyama, Ms. M. Kajigaya(Sato), Mr. E. Hamada, Ms. M. Kimura(Okamoto), Mr. C. Peng, Mr. S. mizuno, Mr. Y. Watanabe, Mr. Y. Kondo, Mr. S. Kubota, Mr. J. Nakazato, Mr. R. Funato, Ms. K. Gunji, Mr. M. Horiuchi, Ms. T. Nakajima, Mr. N. Tanaka, Mr. H. Nakagomi, Mr. D. Watanabe, Mr. T. Kobayashi, Mr. K. Kihara, Mr. K. Oshima, Ms. H. Ozaki, Mr. T. Nonaka, Mr. K. Yodogawa, Mr. H. Watanabe, Mr. W. Sato,Mr. R. Hosokawa, Mr. R. Aoyama, Mr. J. I. I, Ms. I. Sakatani, Mr. T. Shioya, Mr. M. Hirano, and Mr. H. Yamamoto for their friendship and useful discussions.

I also would like to thank the staffs and students of the University of Tokyo and Hiroshima University for their friend ship and sincere advices in my activity.

I am very grateful to Prof. K. Ozawa for having lead PHENIX-J program and financial support to have activity at Brookhaven National Laboratory. I would like to express a deep gratitude to Director. H. En'yo, Dr. Y. Akiba, Dr. T. Hachiya and many other staffs of the Radiation Laboratory of RIKEN Nishina Center for their financial support and the stimulating experiences as a RIKEN-JRA student.

I would like to express my many thanks to the PHENIX Collaboration. I appreciate the Spokespersons, Prof. B. V. Jacak, Prof. J. Nagle, Dr. D. Morrison for their interest and encouragement to my activity at the PHENIX. I would like to thank many collaborators, Prof. J. E. Frantz, Dr. M. P. McCumber, Dr. J. C. H. Chen, Dr. P. W. Stankus, Dr. T. Sakaguchi, Prof. R. Seto, Prof. S. Bathe, Dr. G. David, Prof. R. Lacey, Prof. A. Taranenko, Prof. J. Jia, Prof. M. Rossati, Prof. A. Frawley, Dr. A. Sickles, Mr. Y. Gu for their kind advices and long-term supports in developing my physics analysis.

Finally, I would like to thank my parents, grandparents, and other families. This thesis could not be completed without their understandings and moral supports.

Chapter 1

Introduction

1.1 Quantum Chromodynamics and Quark Gluon Plasma

Quarks and Gluons are elemental blocks of nuclear matters and their strong interactions are described by Quantum Chromodynamics (QCD) based on color charge in analogous to electricity charge in Quantum Electrodynamics (QED). In QCD framework, gluons mediate the strong interaction between (among) color charges. Since gluons are also color-charged, gluons themselves interact with other color charges, on the other hand photons have no electric charge and do not interact with each other.

In QCD, the Lagrangian density is given as

$$\mathcal{L} = \sum_{f}^{N_f} \bar{q}_f (i\gamma^\mu D_\mu - m_f) - \frac{1}{4} F^a_{\mu\nu} F^{\mu\nu}_a, \tag{1.1}$$

where f (=1, 2, 3) is a flavor of quark, q_f is a quark field of flavor f, and m_f is an invariant mass of quark. The gluon field strength tensor $F^a_{\mu\nu}$ is defined as

$$F^a_{\mu\nu} = \partial_\mu A^a_\nu - \partial_\nu A^a_\mu + g f_{abc} A^b_\mu A^c_\nu, \tag{1.2}$$

where A^a_μ is the gluon field (a=1, $\cdots$, 8) and g is the strength of quark-gluon and gluon-gluon interactions defined as $g \equiv \sqrt{4\pi\alpha_s}$, and α_s is the coupling constant of strong interaction. f_{abc} denotes the structure constant in the SU(3) group. The covariant derivative D_μ of QCD is given as

$$D_\mu = \partial_\mu + ig\frac{\lambda_a}{2} A^a_\mu, \tag{1.3}$$

where λ_a denotes the eight Gell-Mann matrices.

The anti-screening effect of the color charge due to the colored-feature of gluons leads to the running coupling constant of the strong force getting small at short distance between color charges. The coupling constant decreases when the typical length decrease or the momentum scale increases vice versa. This property of QCD is called “asymptotic freedom”. The behavior of QCD can be calculated with perturbative calculation method, which is called perturbative QCD (pQCD), only in interactions with a large momentum transfer at a small distance range. Fig. 1.1 is α_s calculated by pQCD[1] compared among previous experimental measurements. The pQCD

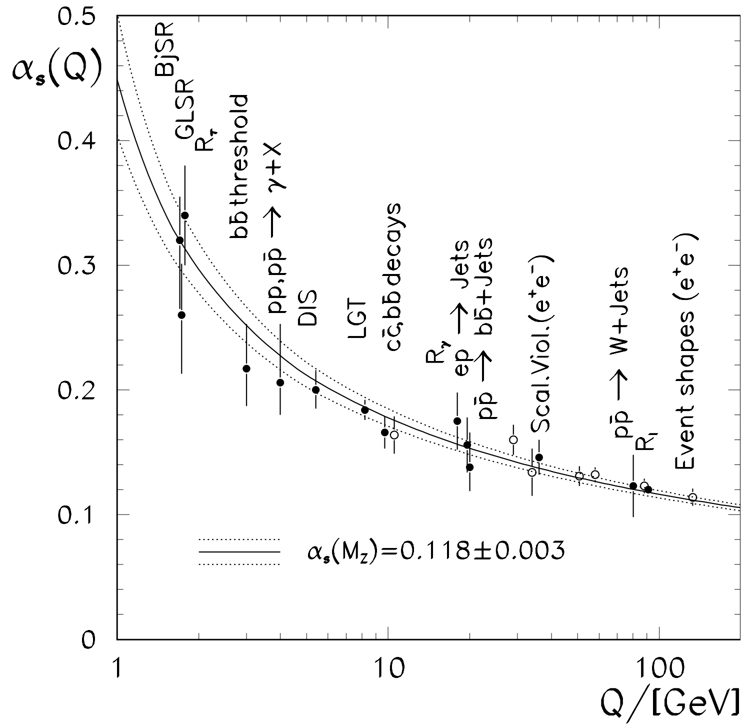

Figure 1.1: The calculation of running strong coupling constants as a function of momentum transfers[1] compared among previous experimental measurements.

calculation is consistent with experimental results up to large momentum transfer region. For interactions with large coupling constants, where pQCD calculation is no longer validated, Lattice QCD calculations are powerful tools to describe behaviors of quarks and gluons. A Lattice QCD calculation of thermodynamic behavior of quarks and gluons at finite temperature and density[2] predicts phase transition phenomena of nuclear matter at a high temperature and energy density, which is a de-confinement of quarks and gluons from hadrons. Fig.1.2 shows energy density ε over biquadrate of temperature T^4 as a function of T/T_c, where T_c is a critical temperature. The rapid evolution of ε/T^4 happens around $T_c \sim 150 - 170$ MeV, which corresponds to critical energy density $\varepsilon_c \sim 1$ GeV/fm^3. Since the ε/T^4 is a quantity corresponding to the degree of freedoms of quark and gluons, the rapid evolution of ε/T^4 indicates the de-confinement of quark and gluons from a hadron, which is a nuclear phase called as "Quark–Gluon–Plasma" (QGP). The arrows in the right side indicate the Stefan-Boltzmann limits of ideal QCD gas. The slight decrease is considered originating from the strong coupling of quarks and gluons in QGP.

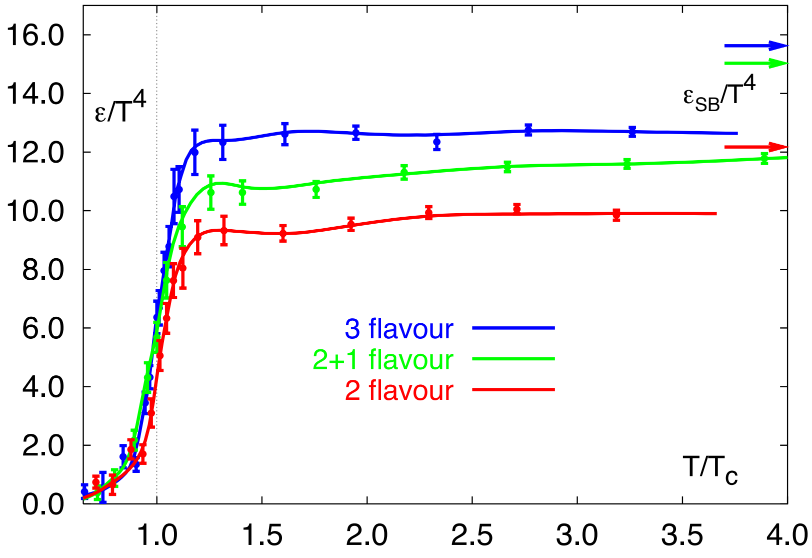

Figure 1.2: The lattice QCD calculations [2] of the energy density over biquadrate of temperature (ε/T^4) as a function of temperature T scaled by critical temperature T_c. The Stefan-Boltzmann limits of ideal gas for two and three flavor QCD calculation are expressed by the arrows in the right side.

1.2 Relativistic Heavy Ion Collisions

A nuclear matter phase, Quark Gluon Plasma (QGP), is predicted by Lattice QCD calculation as mentioned in the last section. Several relativistic heavy ion collision experiments have tried to achieve the sufficient temperature and energy density to form QGP using large accelerator facilities, constructed at Brookhaven National Laboratory (BNL) and European Organization for Nuclear Research (Cern). Currently, the relativistic heavy ion collision experiment is an unique way to form QGP on the Earth. Tab.1.1 is a summary of previous experiments of relativistic heavy ion collisions. The data analyzed in this thesis is obtained by "the Pioneering High Energy Nuclear Interaction eXperiment" (PHENIX), which is one of large experiments at RHIC. Heavy ion collisions have various phases in its space time evolution from initial collision to freeze out. Collision geometry is categorized using a spectator-participant picture.

Table 1.1: Summary of High Energy Heavy Ion Experiments

Accelerator	Laboratory	year	Collision Systems	Collision Energy $\sqrt{s_{NN}}$ [GeV]
AGS	BNL	1986	^{16}O, ^{28}Si	5.4
		1992	^{197}Au	4.8
SPS	CERN	1986	^{16}O, ^{32}S	19.4
		1994	^{208}Pb	17.4
RHIC	BNL	2000	^{197}Au	130
		2001	^{197}Au	200
		2003	d+^{197}Au	200
		2004	^{197}Au	62.4
		2005	^{63}Cu	200
		2007	^{197}Au	200
LHC	CERN	2010	^{208}Pb	2760

1.2.1 Collision Geometry

Due to extent of gold nucleus and the short time scale of relativistic heavy ion collisions compared to Fermi motion of nucleons in a nuclei, the collision geometry can be described by the participant-spectator model. Fig. 1.3 shows a schematic idea of heavy ion collisions of two Lorentz contracted colliding Au nuclei in the view of center of mass frame. Here b is an impact parameter, which is the distance between the centers of the two nuclei. In an interaction of nuclei, spectator nucleons pass away the collision region along beam direction without losing momenta of nucleons. On the other hand, participant nucleons produce particles over a large rapidity range in Au+Au collisions. The degree of overlap of two nuclei "centrality" can be determined measuring the amount of participants *i.e.* multiplicity.

A determined impact parameter provides details of heavy ion collisions, the number of participant nucleons N_{part}, number of nucleon-nucleon collisions N_{coll}, and participant spatial eccentricity ε_n, based on Glauber Model [5]. The Glauber Model assumes that

- Nucleons keep flying straight on initial orbit,

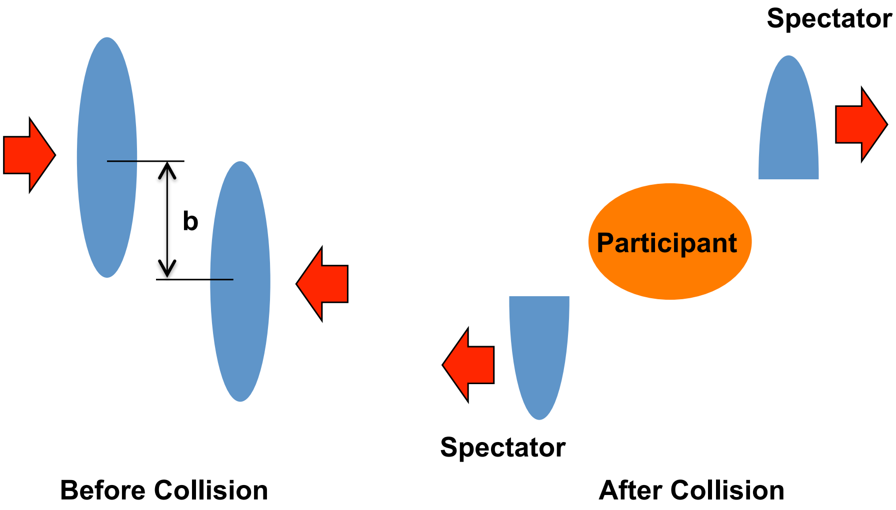

Figure 1.3: A schematic idea of the space-time evolution of relativistic heavy-ion collisions.

- Nucleus collisions are built up from inelastic nucleon interactions,
- Cross-section of inelastic nucleon interaction is independent of number of collisions N_{coll}.

The analytical formulation of the Glauber Model is obtained based on the Wood-Saxon potential of nucleons ρ^A by assuming a nucleus which has a mass number A. ρ^A is characterized by a radius of a nucleus R_A and a diffusion parameter a^A as

$$\rho^A(r) = \frac{\rho_0^A}{1 + e^{(r-R_A)/a^A}}, \tag{1.4}$$

where ρ_0^A is a normalization to satisfy $\int d^3r\rho^A(r) = A$. If we consider Au nuclei of mass number $A = 197$, thus we have R_A=6.38 fm and a^A=0.54 fm. The cross section of an inelastic p+p collision is $\sigma_0 = 42$ mb at $\sqrt{s_{NN}}$ =200 GeV [6]. The nucleon density function is calculated by the integral of $\rho^A(x, y, z)$ in z direction as

$$T_A(x, y) = \int_{-\infty}^{\infty} dz\rho^A(x, y, z). \tag{1.5}$$

The density function of number of participants n_{part} in a nucleus collision is given as

$$\begin{aligned} n_{part}(x, y; b) &= T_A(x + b/2, y)\left\{1 - \left(1 - \frac{\sigma_0 T_B(x - b/2, y)}{B}\right)^B\right\} \quad (1.6) \\ &+ T_B(x + b/2, y)\left\{1 - \left(1 - \frac{\sigma_0 T_A(x + b/2, y)}{A}\right)^A\right\}, \quad (1.7) \end{aligned}$$

where b is an impact parameter, and A and B are mass numbers of two colliding nuclei. The number of participants N_{part} can be given by the integral of n_{part} in x-y direction as

$$N_{part}(b) = \int dxdyn_{part}(x, y; b). \tag{1.8}$$

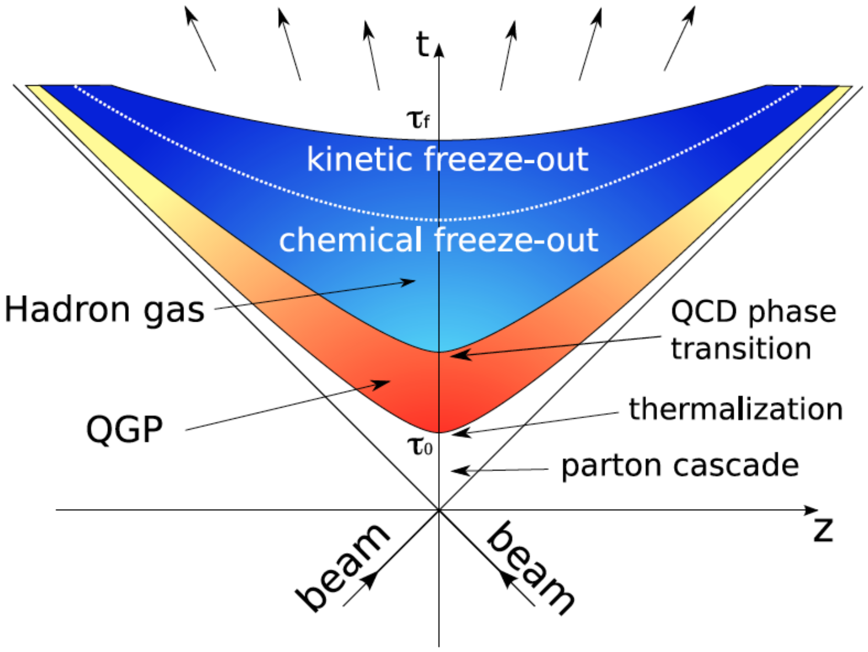

Figure 1.4: A schematic idea of the space-time evolution of relativistic heavy-ion collisions [4].

For number of binary collisions, the density function n_{coll} is given by the product of σ_0, T_A, and T_B as

$$n_{coll}(x, y; b) \quad = \quad \sigma_0 T_A(x + b/2, y) T_B(x + b/2, y). \tag{1.9}$$

The number of binary collisions N_{coll} is expressed as an integral of n_{coll}

$$N_{coll}(b) = \int dx dy n_{coll}(x, y; b). \tag{1.10}$$

1.2.2 Space-Time Evolution

Space-time evolution of relativistic heavy ion collisions, assuming it creates QGP, undergoes multiple phases as shown in Fig.1.4. This section introduces the phases of relativistic heavy ion collisions elapsed since the initial collisions.

$0 < \tau < \tau_0$, Parton Cascade and Thermalization

The mechanics of initial nucleon collisions *i.e.* parton cascades are described by several models such as color-string models[7], a color glass condensate[8], and a perturbative QCD model[9]. The real mechanics of initial parton cascade have not become clear so far, which is one of main topics in heavy ion physics. The entropy increases in parton cascade and QCD matter reaches local thermalization at proper time τ_0, which is the initial condition of hydrodynamic evolution of QGP. Typical τ_0 at RHIC energy is less than 1 fm/c in hydrodynamical models assuming QGP is perfect fluid [10].

$\tau_0 < \tau < \tau_f$, QGP and QCD Phase Transition

QGP expands in transverse and longitudinal directions based on relativistic hydrodynamics after thermalization. In relativistic hydrodynamics, energy-momentum tensor $T^{\mu\nu}$ and baryon number current j^μ are conserved as

$$\partial_\mu T^{\mu\nu} = 0, \tag{1.11}$$

$$\partial_\mu j^\mu_B = 0. \tag{1.12}$$

With a definition of the fluid four-velocity $u^\mu = \gamma(1, v_x, v_y, v_z)$, the energy-momentum tensor becomes

$$T^{\mu\nu} = (\epsilon + P)u^\mu u^\nu - g^{\mu\nu} P, \tag{1.13}$$

which is

$$T^{\mu\nu}(x) = \begin{bmatrix} \varepsilon(x) & 0 & 0 & 0 \\ 0 & P(x) & 0 & 0 \\ 0 & 0 & P(x) & 0 \\ 0 & 0 & 0 & P(x) \end{bmatrix}, \tag{1.14}$$

where ε denotes the energy density and P denotes the pressure. baryon number current is defined as

$$j^\mu_B = n_B u^\mu, \tag{1.15}$$

where n_B is Baryon number. The expansion of QGP lasts until the temperature of QGP reduces to critical temperature T_C, then QGP becomes hadron gas phase.

$\tau_f < \tau$, Freeze-Out

The expansion of hadron gas also reduces the temperature of fluid and hadronization lasts until a certain temperature, then number of hadrons and hadron species no longer changes. This is **chemical freeze-out**. The expansion of hadron gas finally reaches an energy density and temperature where the interaction among hadrons cannot happen any more. This is **kinetic freeze-out**.

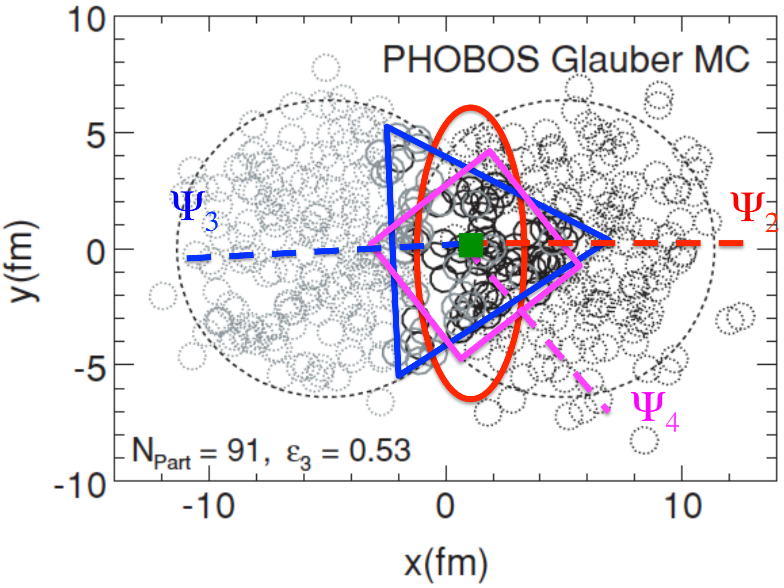

Figure 1.5: The PHOBOS Glauber Monte Carlo in Au+Au collisions [11]. Dashed lines are the schematic idea of higher-order harmonic event-planes defined in terms of participants.

1.3 Higher-Order Flow Harmonics

In the past understanding of the space time evolution in relativistic heavy ion collisions, the smooth initial distribution of participants *i.e.* smooth parton density distribution has been assumed in the initial stage of the collisions. With this assumption, the Fourier coefficients in the azimuthal distribution of emitted particles (flow) with respect to only the second-order event-plane have been take into account.

However, recent studies have revealed the existence of fluctuations of parton energy density in the initial collisions stage and the consequent higher-order flow harmonics in the azimuthal distribution of emitted particles. This section introduces the concept of the parton density fluctuation at initial stage to the flow harmonics of the freeze-out particles.

1.3.1 Higher-Order Event-Plane and Participant Eccentricity

The fluctuation of participants at initial stage of heavy ion collisions is studied via Glauber Monte Carlo Simulations. The definition of a participant eccentricity ε_n and event-plane Ψ_n^{part} is presented by [11, 12] as

$$\varepsilon_n = \sqrt{< r^2 \cos n\phi_{part} >^2 + < r^2 \sin n\phi_{part} >^2} / < r^2 >, \tag{1.16}$$

$$\Psi_n^{part} = atan2(< r^2 \cos n\phi_{part} >^2 + < r^2 \sin n\phi_{part} >^2)/n, \tag{1.17}$$

where ϕ_{part} is a participant azimuthal angle and n is an order of harmonics.

Fig.1.5 shows the schematic picture of the participant distribution, its higher-order eccentricities, and event-planes at $n =$ 2,3,4. The second-order eccentricity of participant is driven by mainly an almond like shape of two overlapping nuclei and participant fluctuation, on the other hand the third-order eccentricity is purely generated by the fluctuation.

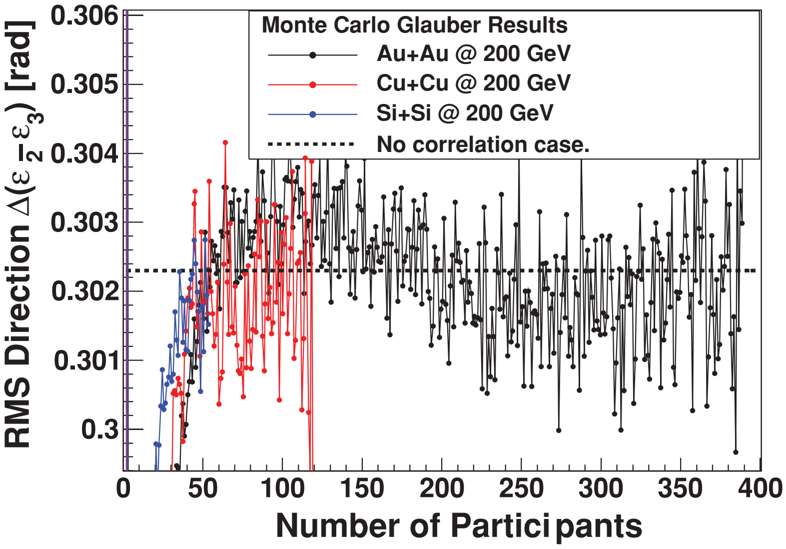

Figure 1.6: The root mean square (rms) of the angular difference between the second and third-order participant event-planes $\sigma(\varepsilon_2 - \varepsilon_3)$ as a function of N_{part} in (Black) Au+Au, (Red) Cu+Cu, and (Blue) Si+Si collisions at $\sqrt{s_{NN}}$=200 GeV [12].

The root mean square (rms) of the angular difference between the second and third-order participant event-planes (*i.e.* a direction of participant eccentricities) $\sigma(\varepsilon_2 - \varepsilon_3)$ as a function of N_{part} is presented in Fig.1.6. The dashed line around 0.302 indicate the expected value of the rms in case of no correlation between ε_2 and ε_3 directions. The rms values in Au+Au, Cu+Cu are consistent with the no correlation case above $N_{part} > 50$ within the statistical fluctuations. In Au+Au collisions, those two orders are uncorrelated at the participant level in the framework of the the Glauber Monte Carlo simulation.

In $N_{part} < 50$, which is corresponding to very peripheral collisions, $\sigma(\varepsilon_2 - \varepsilon_3)$ seems to have a correlation, however this centrality range is not used in the analysis of this thesis.

The same study is performed but between ε_2 and ε_4, and the results are shown in Fig. 1.7. The ε_2 and ε_4 is clearly correlated for all collisions systems at $N_{part} < 250$. The possible explanation of this correlation is that ε_4 can be considered to be formed by combination of pure fluctuation of participants and the initial almond shape. Since the cycle of second-order axes is equivalent to the half cycle of fourth-order axes, the second-order axes can give a contribution to the two of all the four axes of fourth-order axes.

In the real heavy ion collision experiment, the direction of an event-plane is determined by emitted particles after freeze out, which is not the same quantity as ψ_n^{part}. The strength of two-event-plane correlations between different-order and same-order event-planes $\left\langle \cos\left(j[\Phi_n^{Det.1} - \phi_m^{Det.2}]\right)\right\rangle$ in the real heavy ion collisions are assessed using several event-plane detectors as presented in Fig.1.8. The figure shows (c) the correlated Φ_2 and Φ_4, and (d) uncorrelated Φ_2 and Φ_3. Where Φ_n denotes the event-planes defined in [22]. Those observations among Φ_n are qualitatively consistent with the trends seen in participant eccentricity and event-planes in the Glauber MC simulation.

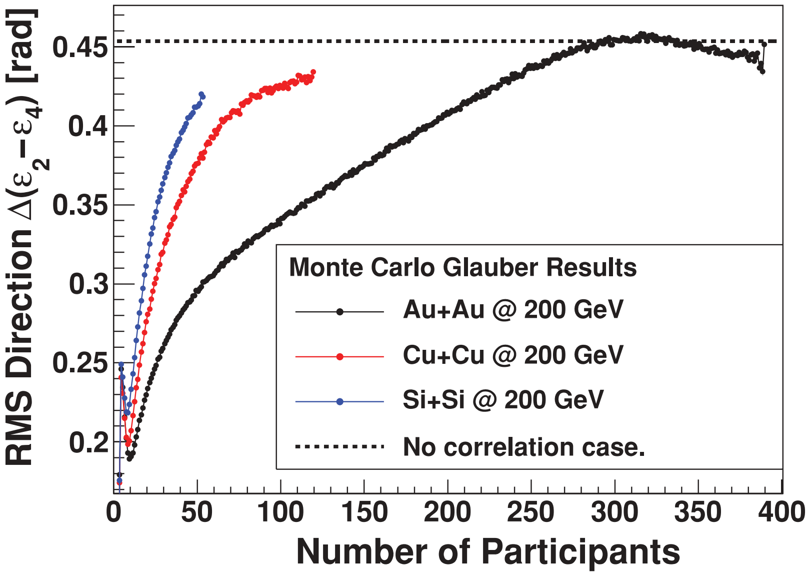

Figure 1.7: The root mean square (rms) of $\Delta(\varepsilon_2 - \varepsilon_4)$ as a function of N_{part} in Au+Au, Cu+Cu, and Si+Si $\sqrt{s_{NN}}$=200 GeV collisions [12].

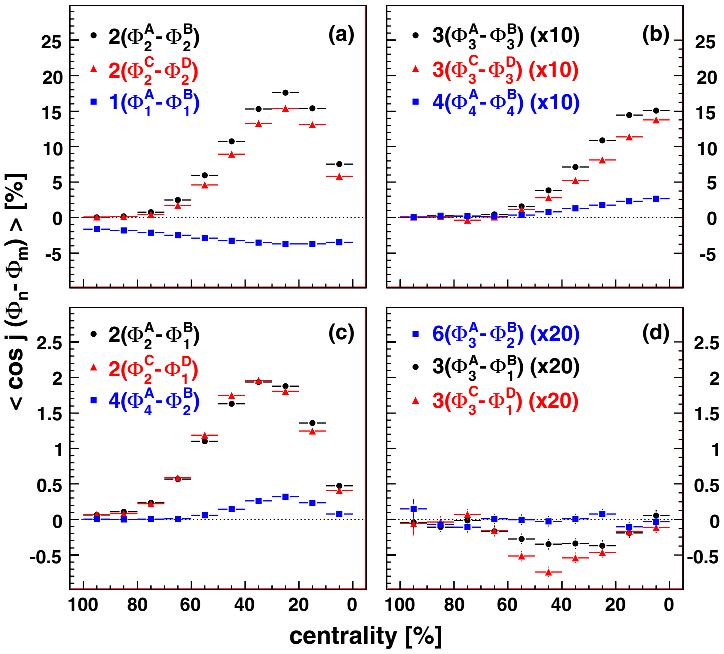

Figure 1.8: Correlations strength $\left\langle \cos\left(j[\Phi_n^{Det.1} - \phi_m^{Det.2}]\right)\right\rangle$ as a function of centrality, where Φ_n^{A-B} is a higher-order event-plane [22]. The two sub-event correlations for $m = n$ are shown in (a) and (b), and for $m \neq n$ are shown in (c) and (d). The detector index indicates A: Reaction-Plane in the North arm, B: Beam-Beam-Counter in the South arm, C: Muon-Piston-Chamber in the North arm, and D: Muon-Piston-Chamber in the South arm of the PHENIX detector. The detail of those detectors are given in the Analysis section.

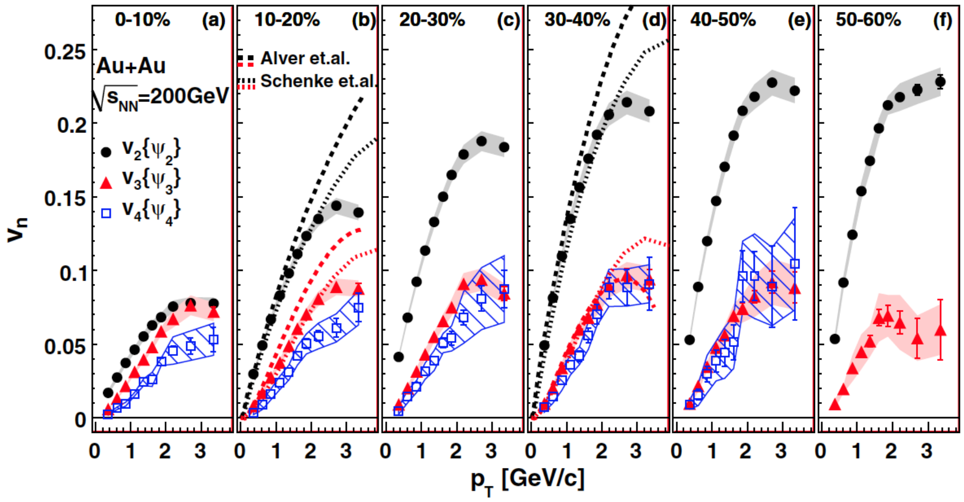

Figure 1.9: Flow harmonics v_n as a functions of p_T in centrality 10 % interval measured at Au+Au $\sqrt{s_{NN}}$=200 GeV collisions by the PHENIX Experiment[22].

1.3.2 Higher-Order Flow Harmonics at RHIC and LHC

The azimuthal distribution in heavy ion collisions can be characterized by Fourier Series with respect to Ψ_n as

$$\frac{dN}{d\phi} = \{1 + 2\sum v_n \cos n(\phi - \Psi_n)\}, \tag{1.18}$$

$$v_n =< \cos n(\phi - \Psi_n) >, \tag{1.19}$$

where Ψ_n is an event-plane determined by the experimental data, ϕ is an azimuthal angle of a particle, and v_n is a higher-order azimuthal anisotropy (flow harmonics).

Fig. 1.9 shows the higher-order flow harmonics v_n as a function of transverse momentum p_T for $n = 2, 3, 4$ in Au+Au $\sqrt{s_{NN}}$=200 GeV collisions by the PHENIX Experiment at RHIC [22] via event-plane method. The amplitudes of v_n are comparable at centrality 0-10% beyond harmonics, and the order of those amplitudes is $v_2 > v_3 > v_4$. While the amplitude of v_2 rises with increase of centrality, amplitude of v_3 is almost independent of centrality. v_4 also increases with increase of centrality, v_4 catches v_3 up at centrality 30% within systematic uncertainties.

Fig. 1.10 shows higher-order flow harmonics v_n of charged hadrons as a function of p_T for $n = 2, 3, 4, 5, 6$ in Pb+Pb $\sqrt{s_{NN}}$=2.76 TeV collisions by the ATLAS Experiment [35] via event-plane method. The amplitudes of flow harmonics are $v_2 > v_3 > v_4 > v_5 > v_6$ at centrality 5-10%. On the other hand in most central collisions, v_2 is less than v_3 around p_T=3 GeV/c. v_2 also increases with increase of centrality at LHC collision energy, which is similar to that of RHIC energy. v_3 is always larger than v_4.

Four model calculations of v_2 and v_3 in p_T=0.75–1.0 GeV/c and 1.75–2.0 GeV/c as a function of N_{part} are compared with the PHENIX data in Fig. 1.11. Initial conditions and shear viscosity over entropy density η/s in hydrodynamics calculation are combined in each theoretical model, “MC-KLN+$4\pi\eta/s$=2”, “Glauber+$4\pi\eta/s$=1(1)” [23], “Glauber+$4\pi\eta/s$=1(2)” [24], and “UrQMD” [25]. While all these combinations of the initial condition and the viscosity succeeded

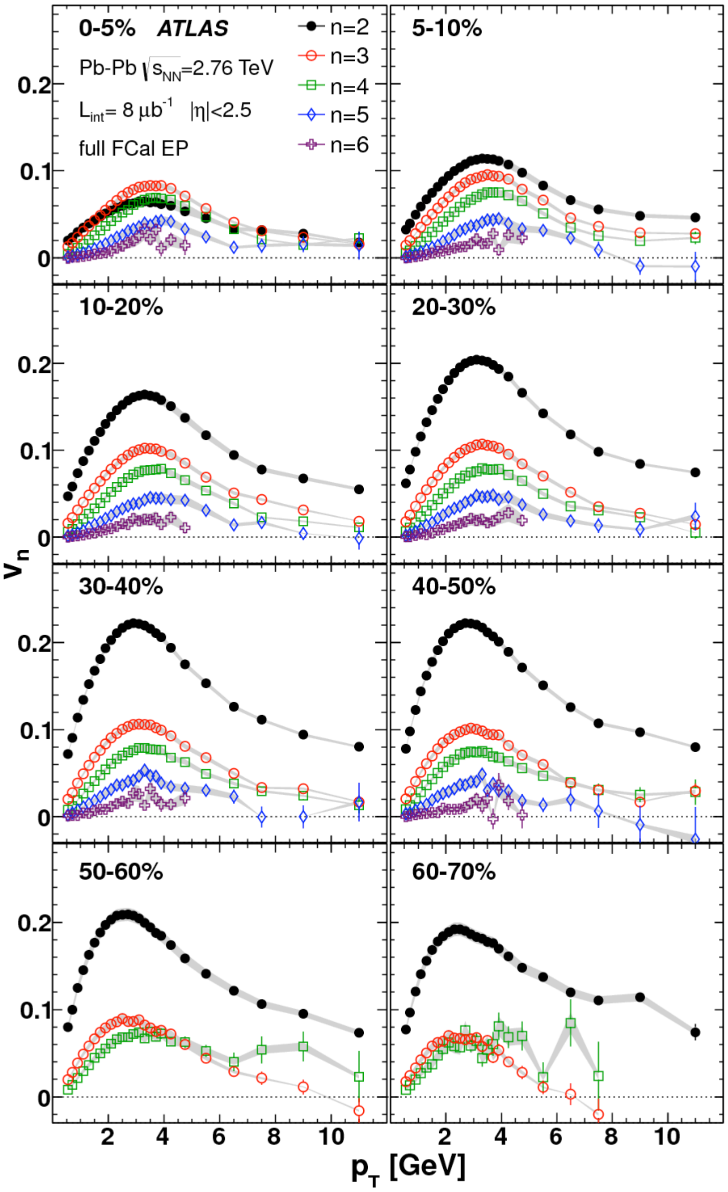

Figure 1.10: Flow harmonics v_n as a function of p_T measured by the ATLAS Experiment in Pb+Pb $\sqrt{s_{NN}}$=2.76 TeV collisions[35].

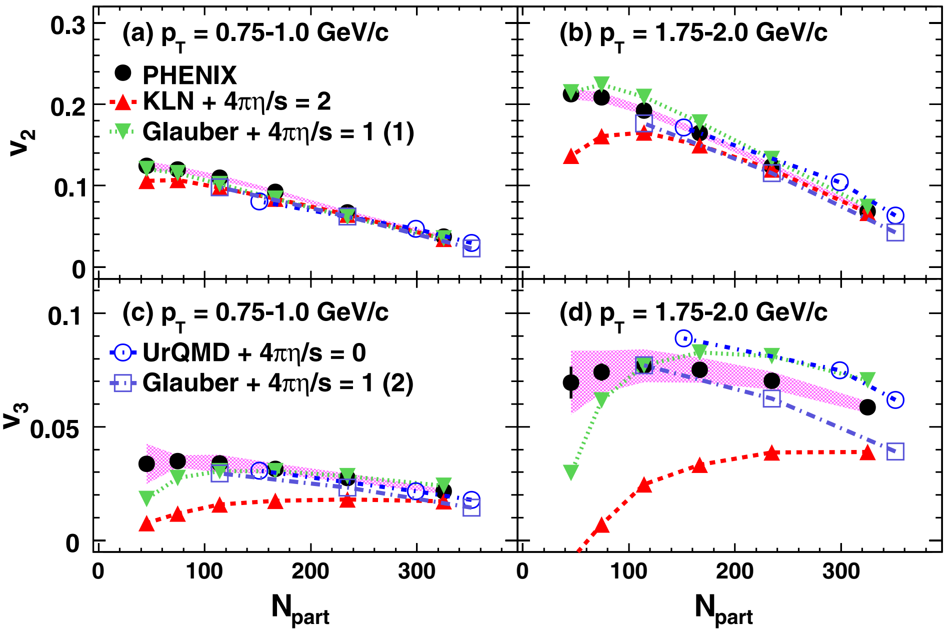

Figure 1.11: Flow Harmonics (a,b) $v_2\{\Psi_2\}$ and (b,c) $v_3\{\Psi_3\}$ as a function of N_{part} [22], compared with theoretical calculations: "MC-KLN+$4\pi\eta/s$=2" and "Glauber+$4\pi\eta/s$=1(1)" [23], "Glauber+$4\pi\eta/s$=1(2)" [24], and "UrQMD" [25].

to describe v_2, the degeneracy among models is disentangled at v_3. The measured v_3 indicates that Glauber+ $4\pi\eta/s$=1 is more favorable than KLN(CGC) + $4\pi\eta/s$=2. However, this comparison does not necessarily mean CGC frame work is disfavored. The comparison only suggests more like perfect fluid than viscous fluid. It is expected that higher-order flow harmonics at $n \geq 4$ provides more discriminating power to the theoretical hydrodynamic calculations and play a important role in an accurate determination of the initial condition and shear viscosity.

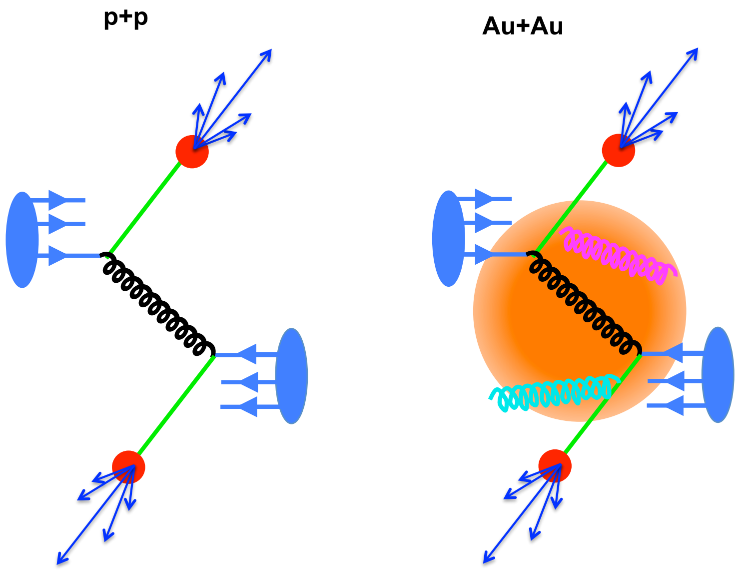

Figure 1.12: Schematic picture of parton hard scattering and back-to-back jet by parton fragmentation.

1.4 Jet-Quenching

In high energy nucleus collisions, partons inside participants are scattered with large momentum transfer, which is called hard-scattering, with a certain probability. The hard scattered partons fly back-to-back direction due to momentum conservation. The scattered partons fragment to two bunches of particles partitioning its energy and result in back-to-back jets. In p+p collisions, scattered partons are not considered to have interaction with other soft particles, since QGP is not considered to be formed in such small collision systems. In Au+Au collisions, QGP medium is formed up to mid-central collisions, which interacts with the hard-scattered partons. Thus the hard-scattered parton loses its energy inside QGP medium and the deposited energy is redistributed to the medium. Fig.1.12 is a schematic idea of a hard collision of a parton pair in p+p and Au+Au collisions. Surveying the modification of experimental observables in Au+Au collisions from those in p+p collisions helps to diagnose the energy loss mechanism in QGP medium.

1.4.1 Nuclear Modification Factor R_{AA}

Nuclear modification factor R_{AA} is one of probes to confirm the sign of parton energy loss in QGP medium. R_{AA} is defined by the ratio of invariant yield of particles in Au+Au collisions over those in p+p collisions, with scaled factor on the size of collision systems as

$$R_{AA} = \frac{d^2N^{AA}/dp_T d\eta}{N_{coll} d^2 N^{pp}/dp_T d\eta}, \tag{1.20}$$

where N^{AA} is a number of emitted particles in Au+Au collisions, N^{pp} is a number of emitted particles in p+p collisions, and N_{coll} is a number of binary collisions. The PHENIX Experiment has measured R_{AA} of various particle species.

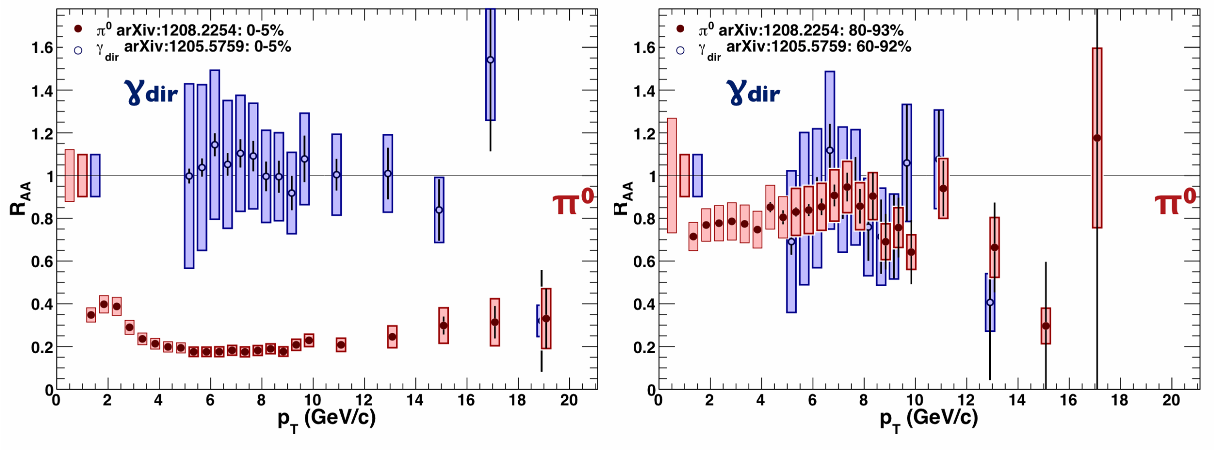

Figure 1.13: Nuclear modification factor R_{AA} for π^0[13] and direct photon[14] as a function of transverse momentum p_T (Left) in most central collisions and (Right) in peripheral collisions.

The R_{AA} of π^0[13] and direct photon [14] in most central and most peripheral collisions are shown in Fig.1.13. In most central collisions, where the QGP medium is thick *i.e.* parton path length is long, π^0 R_{AA} is around 0.2 in $p_T > 5$ GeV/c, which means the invariant yield in Au+Au collisions is factor 5 suppressed compared to p+p collisions.

In most peripheral collisions *i.e.* parton path length is short, π^0 R_{AA} is consistent with 1 above $p_T > 7$ GeV/c, which means invariant yield in Au+Au collisions are not suppressed compared to that in p+p collisions. The centrality dependence of invariant yield suppression is consistent with the scenario of parton energy loss in QGP medium, since it can be easily considered that partons propagate the longer path in QGP lose the more energy.

On the other hand direct photon R_{AA} is always consistent with 1 within statistical and systematic uncertainties. The transparence of QGP to direct photons is due to small cross section of photons in QGP medium since photons can not have strong interaction. The trend of direct photon also complements the observation of hadron suppression, since none suppression of direct photon indicates that the method of R_{AA} does not produce an artificial bias.

1.4.2 Two-Particle Correlations

The R_{AA} gives information on the hadron suppression in QGP medium, however the directions of leading and sub-leading jets are not considered in the measurements. Additionally, measurements of two-particle correlations help to figure out the energy loss mechanism, with a consideration of spatial information of back-to-back jets. The spatial coordinate in two-particle correlation measurements is defined by the azimuthal angle ϕ and pseudo-rapidity $\eta = -\ln[\tan(\theta/2)]$, where θ is a polar angle from the beam axis. Different physics can be dealt with by the two-particle correlations depending on p_T selections of trigger and associate particles. At high p_T pairs, correlations are corresponding to back-to-back jets itself. On the other hand at intermediate p_T, correlations would treat deposited energy from hard-scattered partons to QGP medium in addition to the back-to-back jets.

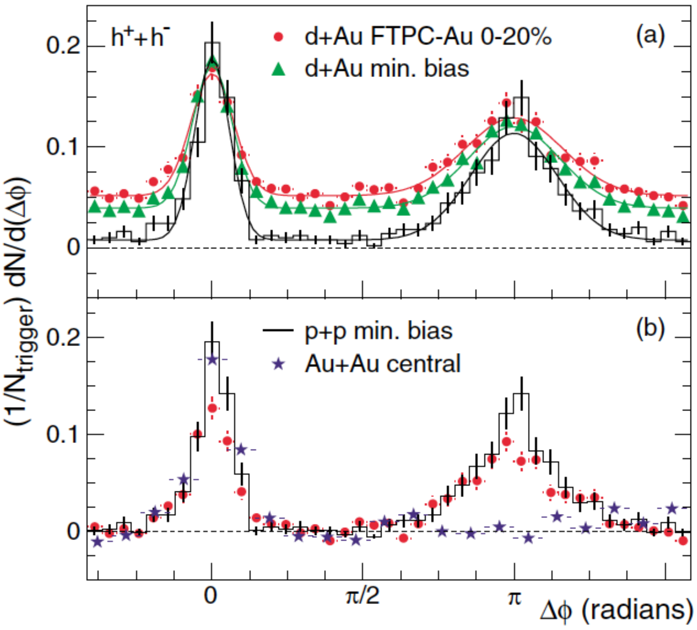

Figure 1.14: Two particle correlations measured by the STAR Experiment[15, 16] in (a) d+Au collisions, and (b) Minimum Bias p+p and central Au+Au collisions. Momentum ranges are $4 < p_T^{trig.} < 6$ GeV/c for trigger particles and $2 < p_T^{asso} < p_T^{trig}$ GeV/c for associate particles.

High p_T pair correlations

Fig.1.14 shows high p_T two-particle correlations in p+p, d+Au, and Au+Au collisions at $\sqrt{s_{NN}}$ =200 GeV by the STAR Experiment[15, 16] in Minimum Bias centrality. The representing pedestals have been subtracted in the correlations in p+p and d+Au collisions, and a background from v_2 is subtracted from the correlations in Au+Au collisions. In panel (a), correlations in p+p and d+Au collisions have clear back-to-back peaks, while in panel (b) correlations in Au+Au collisions show the disappearance of away side yield. Since near side yield of correlations in Au+Au collisions are still comparable to that in p+p collisions, the suppression of invariant yield can be regarded due to the suppression of a sub-leading jet in a QGP medium.

There is a study scanning the path length dependence of high p_T two-particle correlations. The path length is controlled by selecting trigger particles with respect to the second-order event-plane $\phi_s = \phi^t - \Psi_2$. The path length becomes longer/shorter with the selection of trigger particles in out-of-plane/in-plane direction. Fig.1.15 presents I_{AA}, ratio of correlation yield in Au+Au collisions over that in p+p collisions, as a function of ϕ_s, the ratio of π^0-charged hadron correlations with high p_T pairs in Au+Au collisions over that in p+p collisions, measured by the PHENIX Experiment [19]. Contributions from v_2 and $v_4\{\Psi_2\}$ have been subtracted. While near-side yields are consistent with the yields in p+p collisions within statistical and systematic uncertainties independent of Ψ_2, away-side yields show the monotonic suppression with increase of ϕ_s *i.e.* parton path length. This observation is consistent with the trend seen in Fig.1.14.

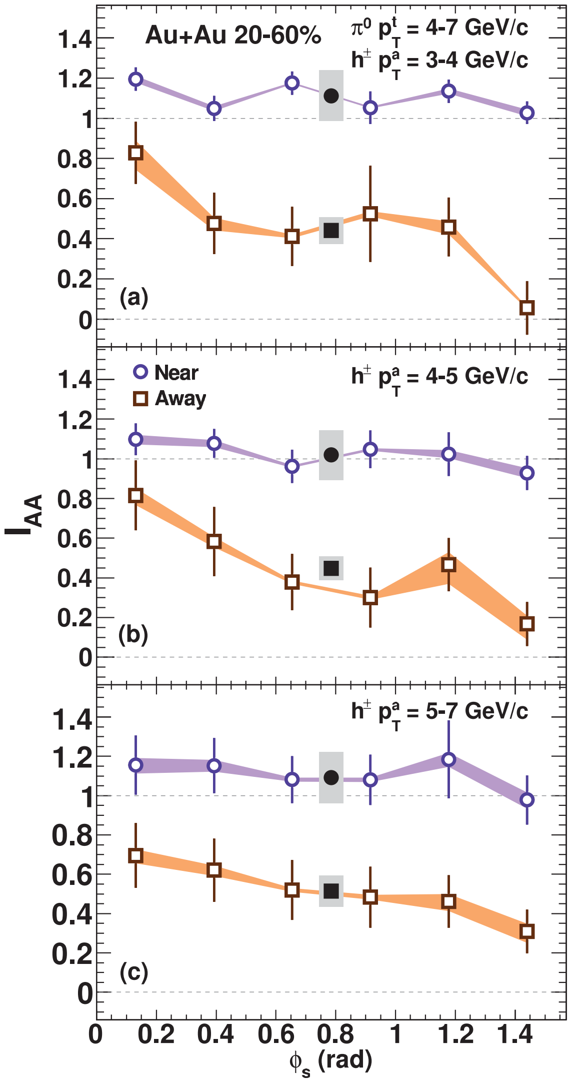

Figure 1.15: Nuclear jet suppression factor I_{AA} of π^0-hadron correlations as a function of trigger angle with respect to the reaction plane ϕ_s for three p_T combinations [19].

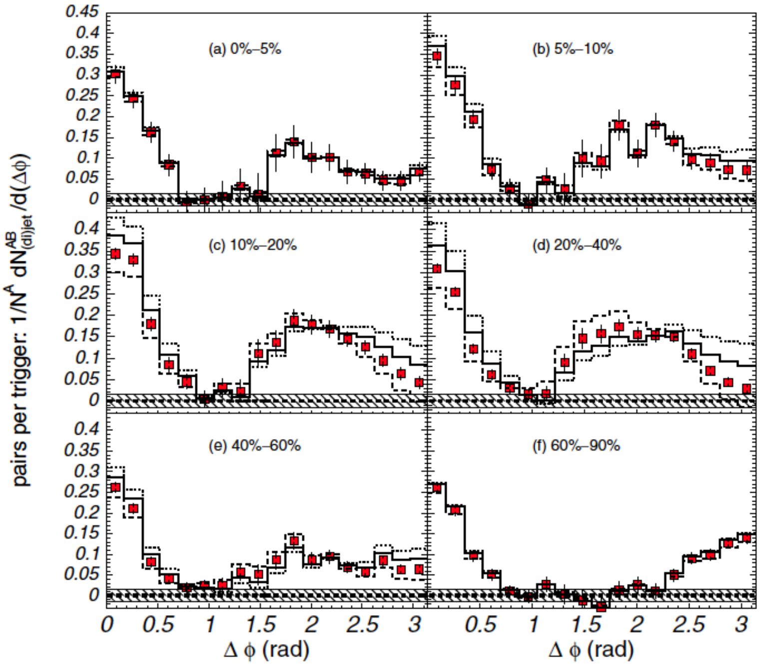

Figure 1.16: Pair yield per a trigger of charged hadrons for six centrality selections [17]. The p_T is 2.5<p_T<4.0 GeV/c for trigger particles and 1.0<p_T<2.5 GeV/c for associate particles.

Intermediate p_T pair correlations

The away-side yield of high p_T pair correlations is suppressed compared to that in p+p collisions, however the away-side of intermediate p_T correlations are rather modified than simply suppressed. Fig.1.16 shows the two particle correlations at 2.5<p_T^t<4.0 GeV/c for trigger particles and 1.0<p_T^a<2.5 GeV/c for associate particles in Au+Au collisions at $\sqrt{s_{NN}}$=200 GeV. The contributions from v_2 is subtracted based on the "Zero Yield At Minimum" (ZYAM) assumption. The ZYAM assumption requires that the minimum value of flow subtracted correlations becomes zero.

The away-side correlations have double hump structure from centrality 0% to 60%. The double hump can be considered due to the parton-medium coupling, since away-side correlation again show the back-to-back peaks seen in p+p and d+Au collisions and the double-humps disappear above 60%, where the thickness of QGP medium is thin. The similar trends are also seen in Cu+Cu collisions at RHIC[20].

Intermediate p_T correlations also show a characteristic structure at near side, which is called "ridge". The ridge structure is a prominence of near-side correlations in pseudo-rapidity direction lasting at least up to $|\Delta\eta| \geq$1.5 at RHIC energy. Fig.1.17 shows the ridge structure observed in Au+Au collisions at $\sqrt{s_{NN}}$= 200 GeV by the STAR Experiment[21]. This thesis doesn't treat ridge measurements, because the acceptance of the PHENIX experiment in pseudo-rapidity η : ±0.35 is inadequate for ridge measurements.

Fig. 1.18 shows three-particle correlations in p+p, d+Au, and Au+Au collisions at $\sqrt{s_{NN}}$= 200 GeV in various centrality selections at trigger particle of 3 < p_T < 4 GeV/c and two associated particles of 1 < p_T < 2 GeV/c [26]. The backgrounds of v_2 and $v_4\{\Psi_2\}$ are subtracted.

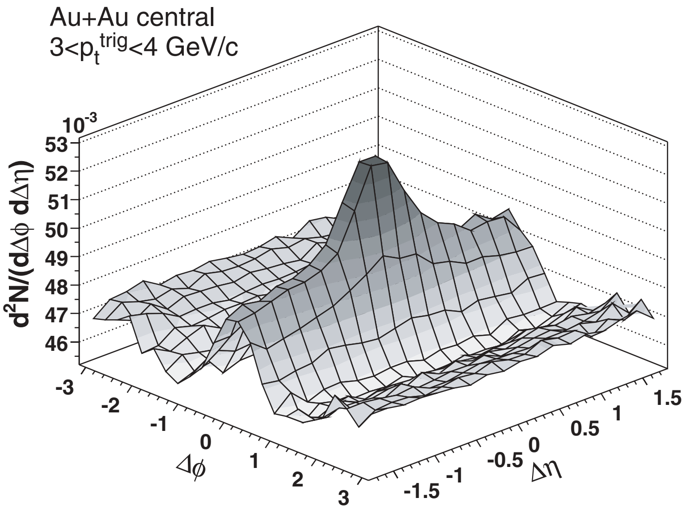

Figure 1.17: Two particle $\Delta\phi$-$\Delta\eta$ correlations of charged hadrons in Au+Au $\sqrt{s_{NN}}$=200 GeV collisions [21]. The momentum range is $3 < p_T^{trig} < 4$ GeV/c for trigger particles and $2 < p_T^{asso} < p_T^{trig}$ GeV/c for associate particles.

Fig. 1.19 shows the projections of away-side three particle correlations onto diagonal and off-diagonal directions in d+Au and centrality 12% Au+Au collisions. The remarkable point of panel (b) of Fig. 1.19 is that both (off-)diagonal correlations have excesses around $\Sigma, \Delta = \pm 1.2$. The structure of correlations seen in both (off-)diagonal directions means that, if a particle exists at either peak of double-humps, in parallel other particles exist at another peak of double humps. That is, the shape of away-side correlations is a conical shape.

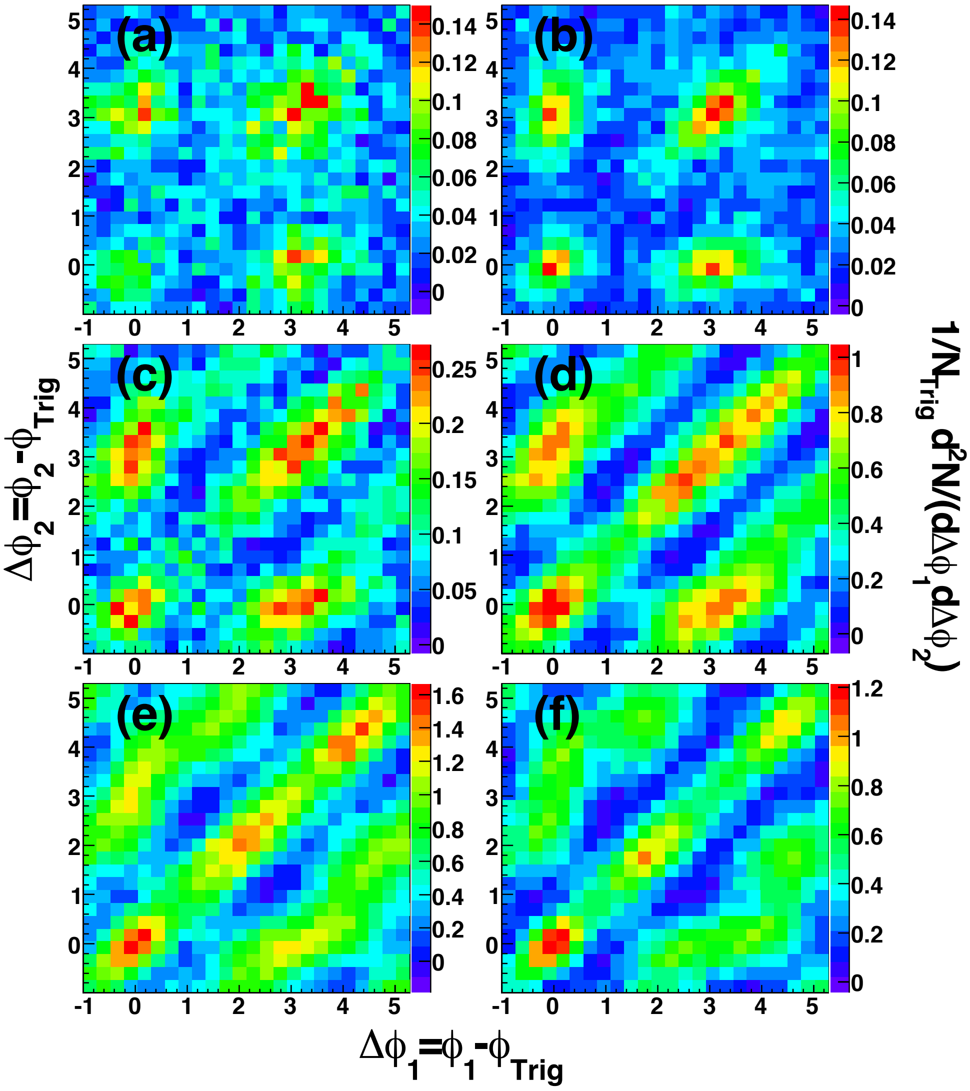

Figure 1.18: Per trigger associate yield in (a) pp, (b) d+Au, (c) 80-50% Au+Au, (d) 50-30% Au+Au, (e) 30-10% Au+Au, and (f) 12% central Au+Au collisions [26]. Statistical errors of data are around ±0.012 in (a) and ±0.006 in (b) at ($\Delta\phi_1$, $\Delta\phi_2$)=(π, π), and are around ±0.022 (c), ±0.049 (d), ±0.099 (e) and ±0.077 (f). Those values are similar for all ($\Delta\phi_1$, $\Delta\phi_2$) bins for panel (c) - (f).

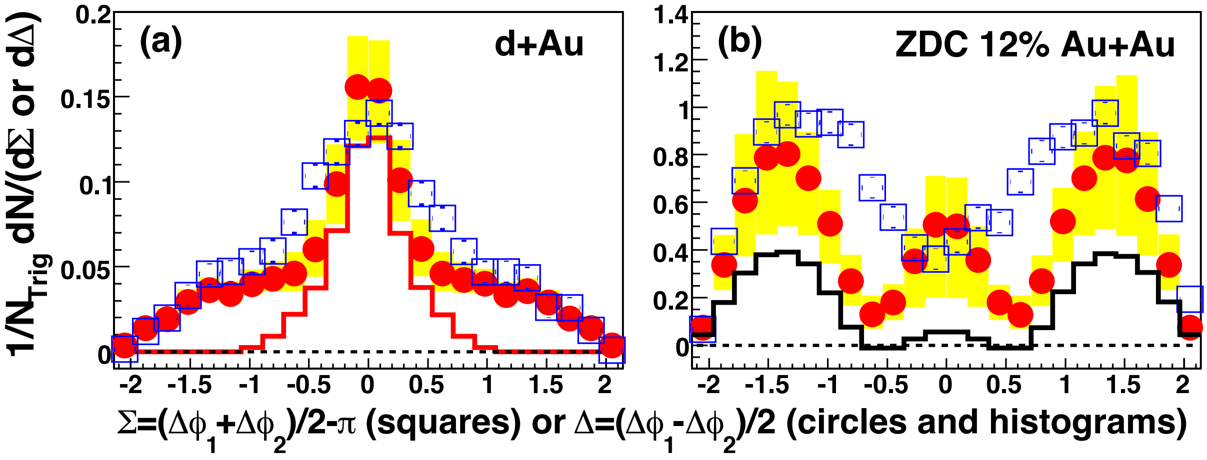

Figure 1.19: Away-side three-particle correlations projected onto the off-diagonal Σ (circles) and the diagonal Δ (squares) directions with slice widths $|\Sigma|< 0.35$ and $0<\Delta<0.35$ in (a) d+Au and (b) 12% central Au+Au collisions.

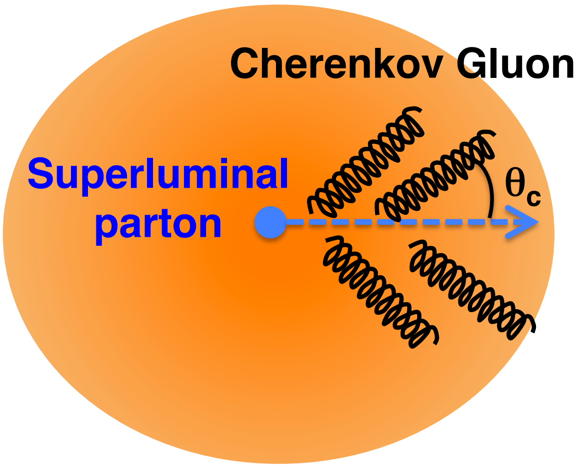

Figure 1.20: Schematic idea of Cherenkov Gluon Radiation by a superluminal parton inside a QGP medium.

1.5 Models for Away-Side Double-Hump Structure

Number of theoretical models and possible explanations from experiments for away-side double-hump structure have been developed in past years. In this section, we briefly introduce four theoretical predictions, Cherenkov Gluon Radiation, Mach-Cone Shock Wave, Energy-Momentum Loss, and Hot-Spot Models and recent experimental explanation of double-humps by higher-order flow harmonics.

1.5.1 Cherenkov Gluon Radiation

Theoretical calculation predicts that if a speed of parton is faster than the speed of light in a QGP at $T >> T_c$, gluons are radiated from the superluminal parton in the medium in analogous to Cherenkov photon radiation in a matter as shown in Fig.1.20. A possible behavior of Cherenkov

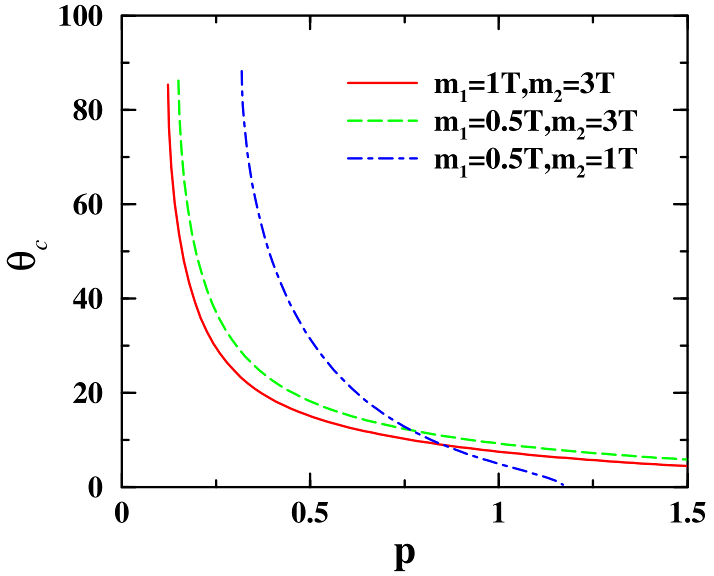

Figure 1.21: Opening angle [rad] of Cherenkov Gluon Radiation from a superluminal parton inside a medium as a function of radiated gluon momentum [27].

Gluon Radiation is constructed based on a calculation of the dispersion relation of a gluon, which interacts with two different massive resonance states in [27]. The parton reduces its energy due to the radiation of a gluon with a radiation angle θ_c determined as

$$\cos\theta_c \quad = \quad \frac{c}{n(p)v_{parton}} \approx \frac{1}{n(p)}, \tag{1.21}$$

where c is the speed of light, v_{parton} is a speed of a parton, and the $n(p)$ is the index of refraction. Since the value of c and v_{parton} is similar in GeV energy scale, $\cos\theta_c$ is effectively a function of $n(p)$. The radiation angle θ_c as a function of a radiated gluon momentum is plotted in Fig.1.21. The value of θ_c becomes larger at lower p_T, which means a wide distance in the angle is seen between two away-side double humps, if two-particle correlations are really constructed by gluon radiation.

1.5.2 Mach-Cone Shock Wave

Here, we introduce a theoretical prediction of behaviors of supersonic partons in a QGP medium. As we already know that a shock-wave is induced by a supersonic object in a fluid, it is also expected a supersonic object in a QGP medium also induces a shock-wave as shown in a schematic idea of Fig.1.22. A cone angle of a shock wave θ_{Mach} can be characterized using the speed of sound c_s in a QGP and the speed of supersonic parton v_{part} as performed in [28]

$$\cos\theta_{Mach} = c_s/v_{part}. \tag{1.22}$$

v_{part} is almost independent of p_T at ultra-relativistic limit, hence the Mach-Cone angle is dominated by the speed of sound in QGP. The speed of sound can be estimated by the dispersion relation $E = c_s p$ and a general expression of speed of sound $c_s^2 = \partial p(T)/\partial\varepsilon(T)$, where E is the

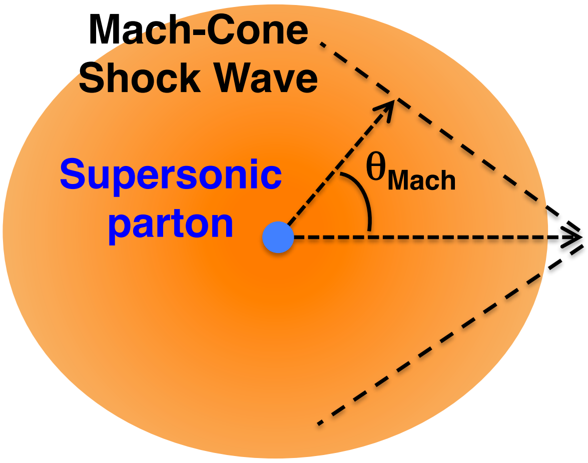

Figure 1.22: Schematic idea of Mach Cone Shock-Wave by a supersonic parton inside a QGP medium.

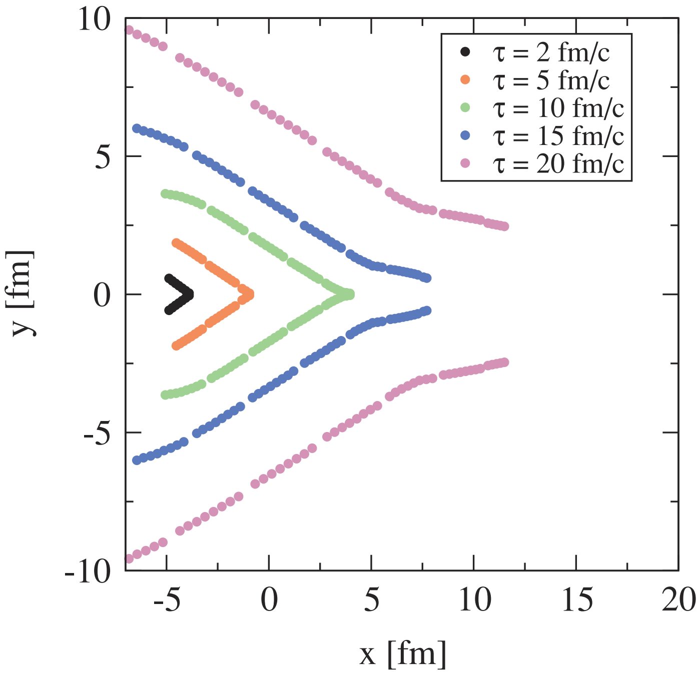

Figure 1.23: Mach cones induced by a jet propagating from $(x, y) = (5, 0)$ fm towards the positive x direction [28].

medium energy, $p(T)$ is the pressure, and $\varepsilon(T)$ is the energy density if we set speed of light c=1. These quantities depend on temperature T, therefore θ_{Mach} is determined by temperature alone. Fig.1.23 shows a propagation of shock-wave surface in medium varying a time scale τ obtained by the calculation in [28]. Mach cones induced by a jet propagating from $(x, y) = (5, 0)$ [fm] towards the positive x direction, where $(x, y) = (0, 0)$ is the center of QGP medium.

Fig.1.24 shows the temperature dependence of c_s presented in [29] using Polyakov-Nambu-Jona-Lasinio (PNJL) model varying chemical potential μ_0 with a fixed isospin potential $\mu_i = 0$.

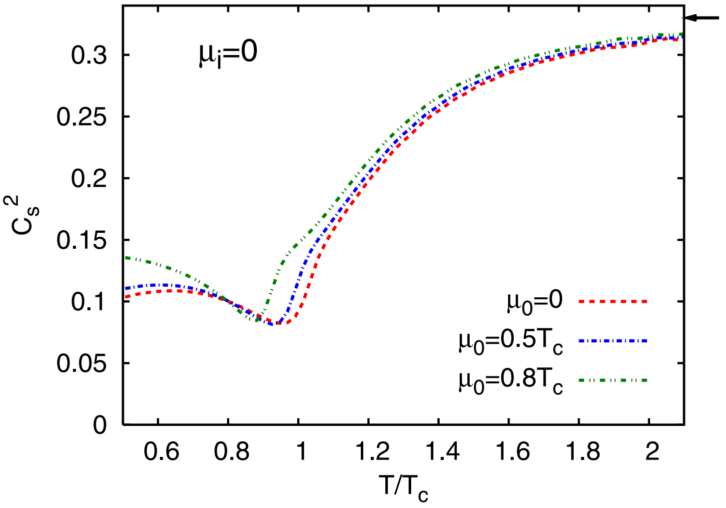

Figure 1.24: Squared speed of sound c_s^2 as a function of relative temperature T/T_c at $\mu_0 = 0$, $\mu_0 = 0.5T_c$, and $\mu_0 = 0.5T_c$ [29].

The speed of sound rapidly increases above $T/T_c > 1$ and it saturates around $T = 2T_c$.

1.5.3 Energy-Momentum Loss Model

The Cherenkov Gluon Radiation and Mach-Cone Models are the scenario where the direction of jet propagation is unchanged and radiated gluon or shock wave creates away-side double hump. Here we can also consider a model in which a jet itself is deflected inside a QGP medium due to energy and(or) momentum loss and interaction with flowing medium. A schematic idea is presented in Fig.1.25.

A theoretical calculation of jet deflection is presented in [30] based on ideal (3+1) hydrodynamics calculation using additional term S^ν in the conservation equations of the energy-momentum tensor as

$$\partial_\mu T^{\mu\nu} = S^\nu, \tag{1.23}$$

where S^ν denotes the tensor of the energy and momentum loss by a jet. The function form is given as

$$S^\nu(t,\vec{x}) = \frac{1}{(\sqrt{2\pi}\sigma)^3} \exp\left[-\frac{[\vec{x}-\vec{x}_{jet}(t)]^2}{2\sigma^2}\right] \left(\frac{dE}{dt}, \frac{dM}{dt}, 0, 0\right) \left[\frac{T(t,\vec{x})}{T_{max}}\right]^3, \tag{1.24}$$

where Gaussian term indicate the path of a jet traversing, the vector indicates the energy-momentum loss rate as a function of time, and the last term indicates the temperature dependence. $T_{max} = 200$ MeV is assumed in Au+Au collisions. This equation is validated as long as $T > T_{cut}$ ($T_{cut} = 130$ MeV), since jet deflection can not occur outside the medium where temperature is less than 130 MeV. The fluid is converted to particles using Cooper-Frye freeze-out and two-particle correlations are constructed using obtained particles. Fig.1.26 shows the two-particle correlations of trigger p_T=3.5 GeV/c and associate p_T at (Left) $p_T = 2$ GeV/c and (Right) $p_T = 3$ GeV/c. We can find the momentum loss of a parton to medium is a key mechanics to reconstruct the away-side double humps.

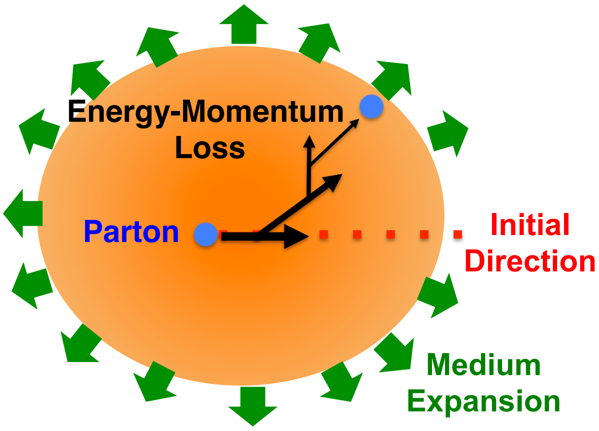

Figure 1.25: Schematic idea of jet deflection by energy momentum loss and push by flowing medium.

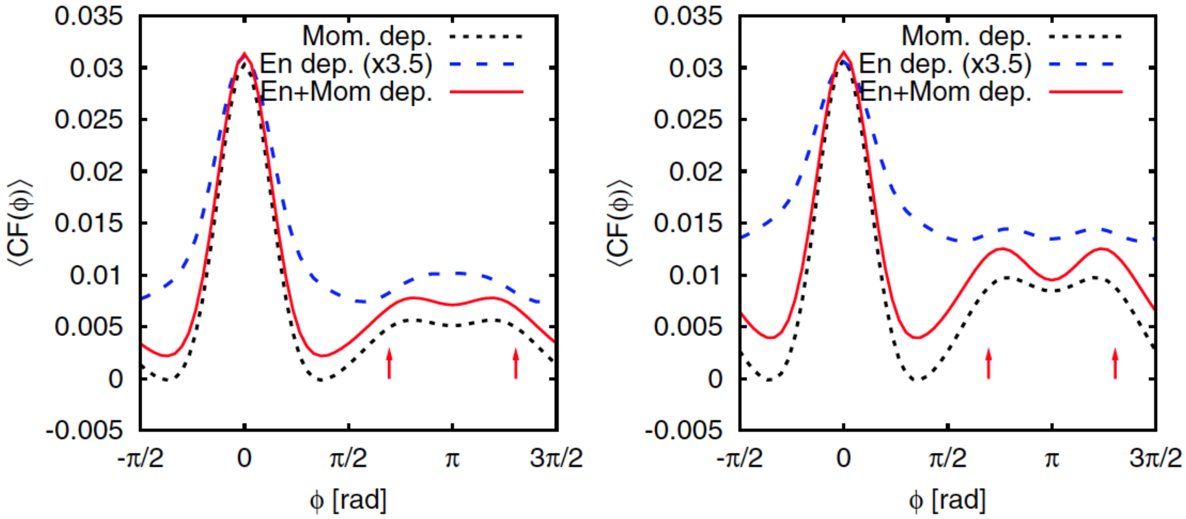

Figure 1.26: The two-particle correlation obtained by (solid red line): Energy-Momentum loss, (short-dashed black line): Pure momentum loss, and (long-dashed blue line): Pure energy loss (scaled by a factor 3.5) for trigger p_T=3.5 GeV/c and associate p_T (Left) p_T = 2 GeV/c and (Right) p_T = 3 GeV/c. Arrows indicate the emission angle by Mach cone calculation [30].

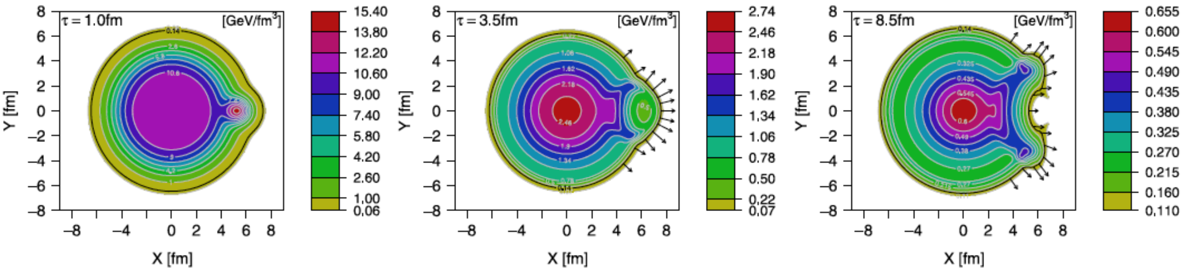

Figure 1.27: The space-time evolution of medium in NexSPheRIO+hot-spot model at τ = 1.0,3.5, and 8.5[fm] [31].

1.5.4 Hot Spot

The above models consider the situation where a hard-scattered parton exists and propagates inside a QGP medium, on the other hand the Hot-Spot model suggests a possible forming mechanism of double-hump structure without a hard-scattered partons. The Hot-Spot model considers the hydrodynamical evolution of a domain inside a medium which has larger parton density compared to other region, due to participant fluctuation at initial collision.

In the original calculation of [32], the NeXSPheRIO package is used, which takes the initial condition from Nexus[33] and the hydrodynamical expansion using SPHERIO[34]. Fig.1.27 shows the space-time evolution of a medium with a simplified smooth parton density and a hot-spot generated by the Nexus model, at times $\tau = 1.0$, 3.5, and 8.5 fm [31]. The split of hot-spot into two directions can be seen. Two-particle correlations calculated by particles obtained by this model is presented in Fig.1.28, where the representing pedestal is subtracted. One can see that the splitting between double humps depends on the radius of hot-spot tube.

1.5.5 Contribution of Higher-Order Flow Harmonics

Recent study of ATLAS Experiment at LHC [35] using Pb+Pb collisions at $\sqrt{s_{NN}} = 2.76$ TeV revealed that higher-order flow harmonics v_n can reconstruct $\Delta\phi$ correlations in terms of rapidity gap between trigger and associate particles. Fig.1.29 shows $\Delta\phi$ correlations with rapidity gap $2 < |\Delta\eta| < 5$ plotted with pure flow contributions composed of v_2 to v_6, where v_1 component and pedestal level is determined by fitting to measured correlations. The measured correlations are well described by the pure flow contributions.

However, this reconstruction of correlations by the flow harmonics is no wonder. Since flow harmonics is determined with the event-plane determined at forward rapidity using mid-rapidity particles. This rapidity gap is equivalent to the rapidity gap between trigger and associate particles in the two-particle correlations. Moreover since the rapidity gap in correlation measurements excludes contributions from non-flow, the correlations are more like collective bulk than jet. In order to diagnose possible parton-medium coupling, it is important to measure correlations without rapidity gap between trigger and associate particles with subtraction of contributions of v_n.

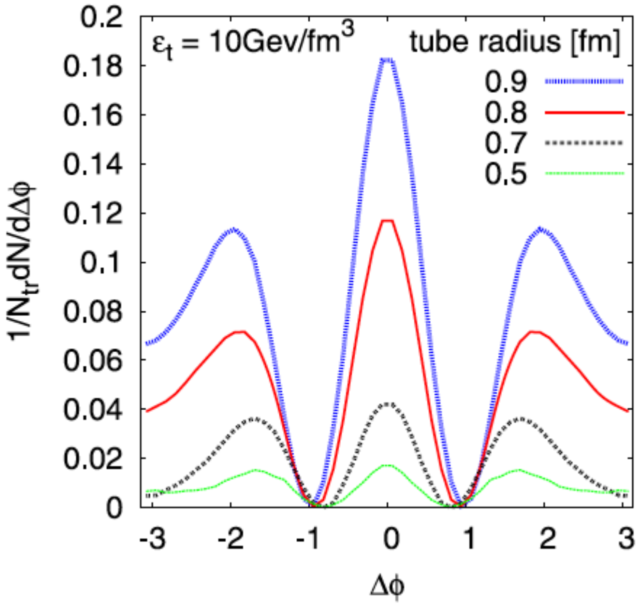

Figure 1.28: Two-particle correlation calculated using particles obtained by NexSPheRIO+hot-spot model varying the radius of hot-spot tube [31].

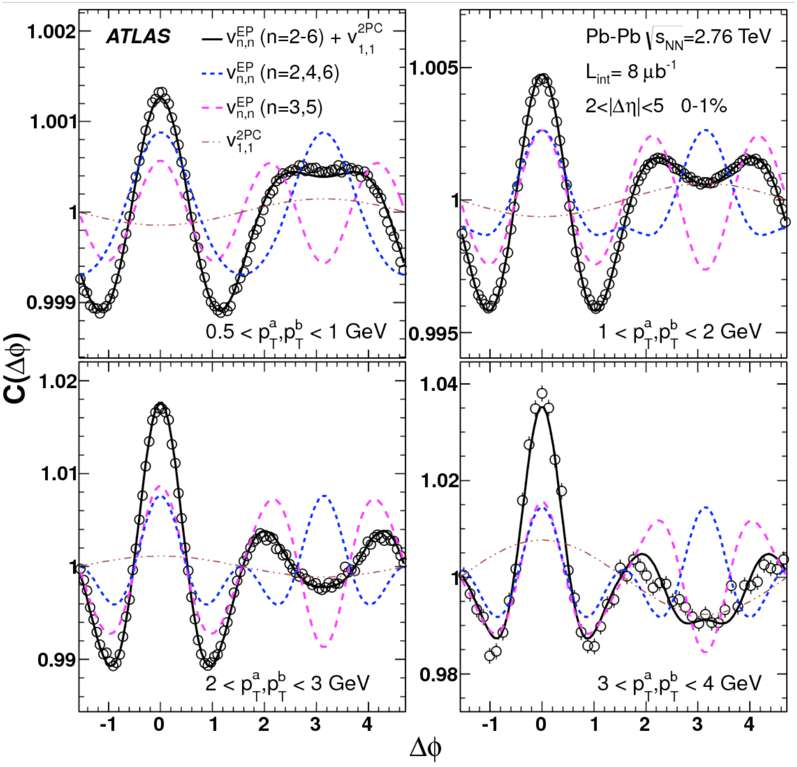

Figure 1.29: Two particle correlations with rapidity gap between two particles($2<|\Delta\eta|<5$) measured by the ATLAS Experiment (Open Circles) in Pb+Pb $\sqrt{s_{NN}}$=2.76 TeV collisions [35], compared with pure flow correlations composed of v_n shown in Fig.1.10.

1.6 Motivation of Thesis

The several correlation measurements have revealed the away-side suppression of high p_T correlations, double-hump and ridge structures of intermediate p_T correlations. The suppression of high p_T correlations can be qualitatively understood as a consequence of parton energy-loss by the results of Ψ_2 dependence of the high p_T correlations, in which the path length of parton propagations in a medium is controlled.

However, the double-hump structure in intermediate p_T correlations have not reached a definitive conclusion of the mechanics, despite of several theoretical efforts trying to explain this phenomena. Moreover, recent progress in the measurements of higher-order flow harmonics suggests the existence of flow background residuals in the previous measured correlations. Hence, the comparison of the previous experimental data with theoretical models is no longer useful to discuss physics of the double-hump structures.

This thesis performs measurements of two-particle correlations at RHIC-PHENIX with $v_n(n = 2, 3, 4)$ contribution subtracted in low p_T to high p_T charged hadrons, that provide new experimental data to be compared with theoretical models.

The measurements of two-particle correlations with a trigger selection with respect to the second Ψ_2 and third-order event-planes Ψ_3 are also presented in this thesis. The motivation for Ψ_2 dependent correlations is to see a path-length dependence after $v_n(n = 2, 3, 4)$ contributions subtracted. That of Ψ_3 dependent correlations is as following. Due to triangular shape of third-order geometry of media, the partons in near-side and in away-side can sense different path length, so that possible different results of jet-medium interplays in the second and third-order geometry of media can be reflected in the event-plane dependent correlations. We expect the measurements of event-plane dependent correlations provide more detailed references to model calculations.

Chapter 2

Experimental Apparatus

2.1 Relativistic Heavy Ion Collider (RHIC)

The Relativistic Heavy Ion Collider (RHIC) [36, 37] is a high energy heavy ion collider constructed at the Brookhaven National Laboratory. The rich capability of RHIC leads to colliding various nucleus from A=1 to 197 at various collision energy $\sqrt{s_{(NN)}}$ =7.7 to 510 GeV, even including asymmetric collision systems such as d+Au collisions. The summary of RHIC operations is given in Tab.2.1.

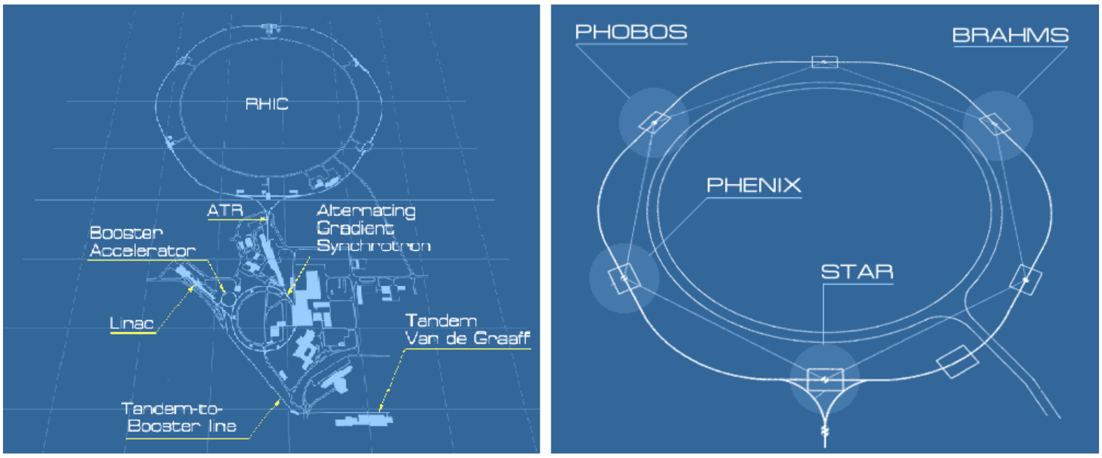

Figure 2.1: Overview of (Left) RHIC Complex and (Right) Experiments in RHIC [36, 37].

The RHIC consists of two circular-like accelerators sharing a common horizontal plane. The accelerators also work as a storage of accelerated ions. The lengths of two rings are approximately 3.8 km. The accelerator drives beam to the clockwise direction is called "Blue Ring", and the other one to the counter-clockwise direction is called "Yellow Ring". Existing accelerators used for previous experiments, such as the Tandem Van de Graff, the Booster, and the Alternating Gradient Synchrotron (AGS), are components of the RHIC complex: a chain of pre-accelerator and injector to the RHIC main rings. Fig.2.1 shows the configurations of the RHIC complex and experimental detectors.

Table 2.1: RHIC run summary as of Run7

Run	year	Collision Systems	$\sqrt{s_{NN}}$ GeV	$\int Ldt$	N_{event}
Run1	2000	Au+Au	130	1 μb^{-1}	10M
Run2	2001-2002	Au+Au	200	24 μb^{-1}	170M
		p+p	200	0.15 pb^{-1}	3.7G
Run3	2002-2003	d+Au	200	2.74 nb^{-1}	5.5G
		p+p	200	0.35 pb^{-1}	6.6G
Run4	2003-2004	Au+Au	200	241 μb^{-1}	1.5G
		Au+Au	62.4	9 μb^{-1}	58M
		p+p	200	0.35 pb^{-1}	6.6G
Run5	2004-2005	Cu+Cu	200	3 nb^{-1}	8.6G
		Cu+Cu	62.4	0.19 nb^{-1}	0.4G
		Cu+Cu	22.5	2.7 μb^{-1}	9M
		p+p	200	3.8 pb^{-1}	85G
Run6	2005-2006	p+p	200	10.7 pb^{-1}	230G
		p+p	62.4	0.1 pb^{-1}	28G
Run7	2006-2007	Au+Au	200	813 μb^{-1}	50.1G

2.2 Overview of the PHENIX Detector

The PHENIX detector, one of large experiments at RHIC, consists of four instrumented spectrometers (arms) and four global detectors [38, 40]. Each arm contains several subsystems. Fig. 2.2 shows the schematic view of the subsystem configurations. Table 2.2 show the summary of the pseudo-rapidity and azimuthal acceptance, and features of each subsystems employed in this thesis.

2.3 Central Magnet System

A magnetic field is applied by the central magnet (CM) around the beam interaction vertex points parallel to the beam direction, for the purpose of determining particle momenta in the PHENIX central-arm ($|\eta|$ <0.35, $|\Delta\phi|$<360°) by bending particle orbits. The CM system [38] consists of three spectrometer magnets (shown in Fig.2.2) with warm iron yokes and water-cooled copper coils. Two pairs of concentric coils: inner and outer coils, excite CM. The acceptance of CM is shown in Table 2.2.

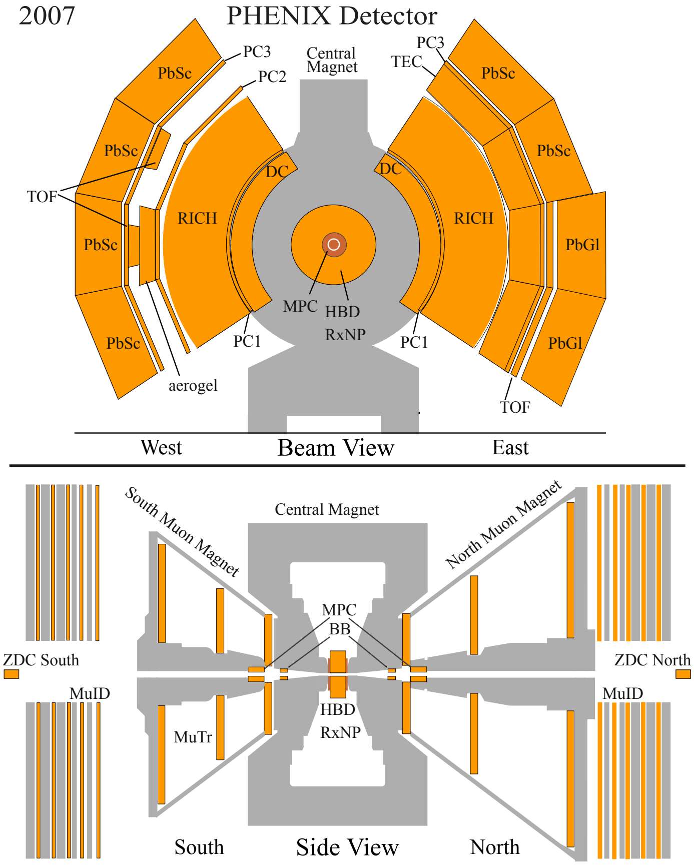

Figure 2.2: The configuration of the PHENIX subsystems in Run7(2006-2007) viewed (Top) along the beam axis and (Bottom) from the perpendicular direction to the beam axis.

Table 2.2: Summary of the PHENIX detector subsystems used in this thesis.

Component	$\Delta\eta$	$\Delta\phi$	Purpose and Special Feature
Magnet: central (CM)	$\|\eta\| <0.35$	360°	Up to 1.15 T·m
BBC	$3.0 < \|\eta\| < 3.9$	360°	Start timing, fast vertex
ZDC	±2 mrad	360°	Minimum bias trigger
DC	$\|\eta\| < 0.35$	90°×2	Good momentum and mass resolution $\Delta m/m$=0.4% at m=1.0 GeV
PC	$\|\eta\| < 0.35$	90°×2	Pattern recognition, tracking for nonbend direction
RICH	$\|\eta\| < 0.35$	90°×2	Electron identification
PbSc EMCal	$\|\eta\| <0.35$	90°+45°	Photon and electron detection
PbGl EMCal	$\|\eta\| <0.35$	45°	Good $e^{\pm}/\pi^{\pm}$ separation $p > 2.0$ GeV/c by EM shower and $p < 0.35$ GeV by TOF $K^{\pm}/\pi^{\pm}$ separation up to 1 GeV/c by TOF
RXN	$1.0 < \|\eta\| < 2.8$	360°	Good resolution for reaction plane

2.4 Global Detectors

There are several global properties in heavy ion collisions: centrality, event-plane direction, interaction vertex position and timing, and trigger information. These quantities are measured by the "Global detectors" such as Zero Degree Calorimeter (ZDC), Beam Beam Counter (BBC), and Reaction Plane detector(RXN) installed since Run-7 (2006-2007) experimental period.

2.4.1 ZDC

Fig.2.3 A) shows the overhead schematic view of the PHENIX interaction region near beam pipe. The ZDC detectors[44] are installed in the both North and South side of beam interaction region behind the DX magnets. The locations of ZDCs are approximately 18m away from beam collision points, which corresponds to $|\eta|>6$.

The DX magnets provide the rejection power of charged particles from ZDC hits. Fig.2.3 B) shows the degree of bending of neutrons, Au ions, and protons from beam pipe by the application of DX magnet field. The minimum bias trigger is given by the combination of ZDC neutron hits and BBC hits.

Fig. 2.4 shows the engineering drawing of the ZDC module. One ZDC module is the sampling layer composed of Tungsten plates and optical fiber ribbons. The Cherenkov lights from neutrons are transferred to a PMT via those optical fibers.

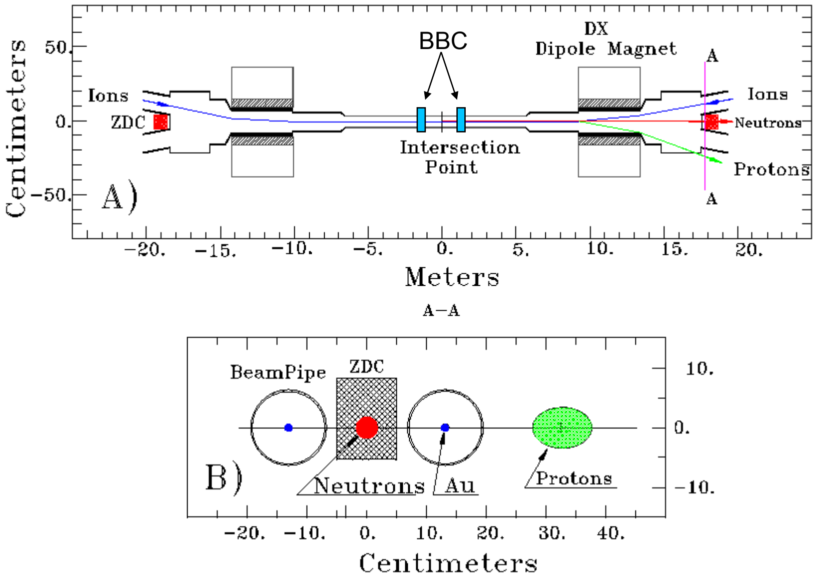

Figure 2.3: (A) The installation location of north and south ZDC in a view along the beam axis. The distance from beam collision point to both ZDC is approximately 18 meters. (B) The schematic indication of the degree of deflections for neutrons, protons, and Au ions by DX magnet [44].

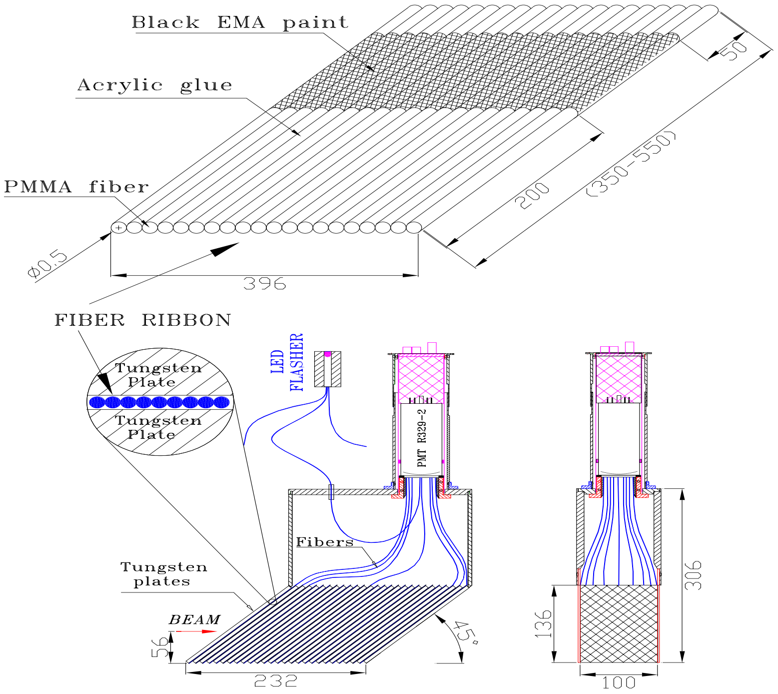

Figure 2.4: Engineering drawing of a ZDC module. The units of numbers in figure are millimeters [44].

2.4.2 BBC

The Beam-Beam Counter (BBC) [39] consists of two modules installed in the north and south side along beam axis. The coverage of north and south BBCs is pseudo-rapidity $3<|\eta|<3.9$, which is 144 cm away from the center of interaction point, with full azimuthal acceptance surrounding the beam pipe.

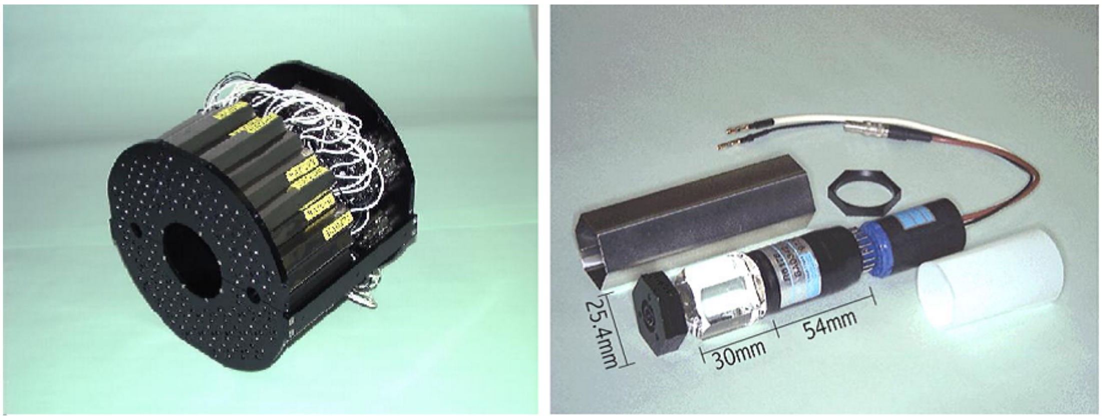

Figure 2.5: (Left) One BBC module consists of 64 sub channels. (Right) Single constituent BBC counter built up of one-inch mesh dynode photomultiplier tubes equipped with a 3 cm quartz radiator.

The intent of BBC is to provide following information in physics experimental operations as

- hit information for the Local Level-1 trigger in PHENIX (Sec.3.1),
- collision time and the vertex point of beams in beam axis coordinate,
- centrality determination (Sec.3.2) and the event-plane azimuthal angle (Sec.3.3, also by RXN in this thesis).

For the physics purpose above, BBC satisfies the following requirements;

- being capable of working over 1 to 30 MIP regions corresponding to p+p to most-central Au + Au collisions,
- being durable for very high-level radiation due to the location of BBC near the collision point surrounding the beam pipe,
- being able to work under high magnetic field (∼3 kG) due to the central magnet installed near BBC.

Each BBC module contains 64 one-inch diameter mesh-dynode photomultiplier tubes (Hamamatsu R6178). Each PMT has 3 cm thick quarts on the head of the PMT as a Cherenkov radiator.

Fig.2.5 shows (Left) a BBC module composed of 64 BBC elements and (Right) a single BBC counter. The estimated number of charged particles per BBC element is approximately 15 particles for a central Au+Au collisions at $\sqrt{s_{NN}}$=200 GeV. Laser signals are used for calibrations of individual BBC elements and the signals are also used for Time-of-Flight and Electromagnetic Calorimeter calibrations.

The collision time T_0 and vertex position in beam axis coordinate z_{vtx} are reconstructed from the arrival time of leading charged particles for BBCN and BBCS. The systematic shifts caused by the time walk of the discriminator and time offset are adjusted for each individual BBC element.

Writing the corrected average timing of each BBC T_{BBCN} and T_{BBCS} and the speed of light c, then we can obtain T_0 and z_{vertex} given as

$$T_0 = (T_{BBCN} + T_{BBCS})/2, \tag{2.1}$$

$$z_{vtx} = c \cdot (T_{BBCN} - T_{BBCS})/2. \tag{2.2}$$

The typical resolution of BBC is 40 ps for timing, and is 0.6 cm for vertex position.

2.4.3 RXN

The measurements of azimuthal anisotropy v_2 of various particle species at RHIC provided great information of properties of QCD hot and dense medium. For the measurements of more rare particles such as high p_T particles, heavy flavor electrons, and heavy hadrons, excellent event-plane resolutions are crucial for accurate measurements. The Reaction Plane Detector (RXN) had been installed since Run7 to Run10 experimental period. The BBC was used for event-plane determination before Run7 in PHENIX, and its resolution $< \cos 2(\Psi_2^{obs} - \Psi_2^{real}) >$ is approximately 0.4 in minimum bias Au+Au collisions at $\sqrt{s_{NN}}$= 200 GeV. The event-plane resolution of RXN is approximately 0.7, which corresponds to the improvement of the effective statistics in v_2 measurements about a factor of $(0.7/0.4)^2 \sim 3.5$.

The RXN has two sectors in north and south side of interaction region along beam pipe. Each RXN consisted of 24 plastic scintillators and a PMT for each scintillator. The thickness of a scintillator is 2 cm and it is located at $38 < |z| < 40$ cm from center of the beam interaction region. The coverage of RXN is full azimuthal angle and pseudo-rapidity of $1.5 < |\eta| < 2.8$ for outer rings and $1.0 < |\eta| < 1.5$ for inner rings. Fig. 2.6 shows the front view of the RXN detector and precise size of its elements.

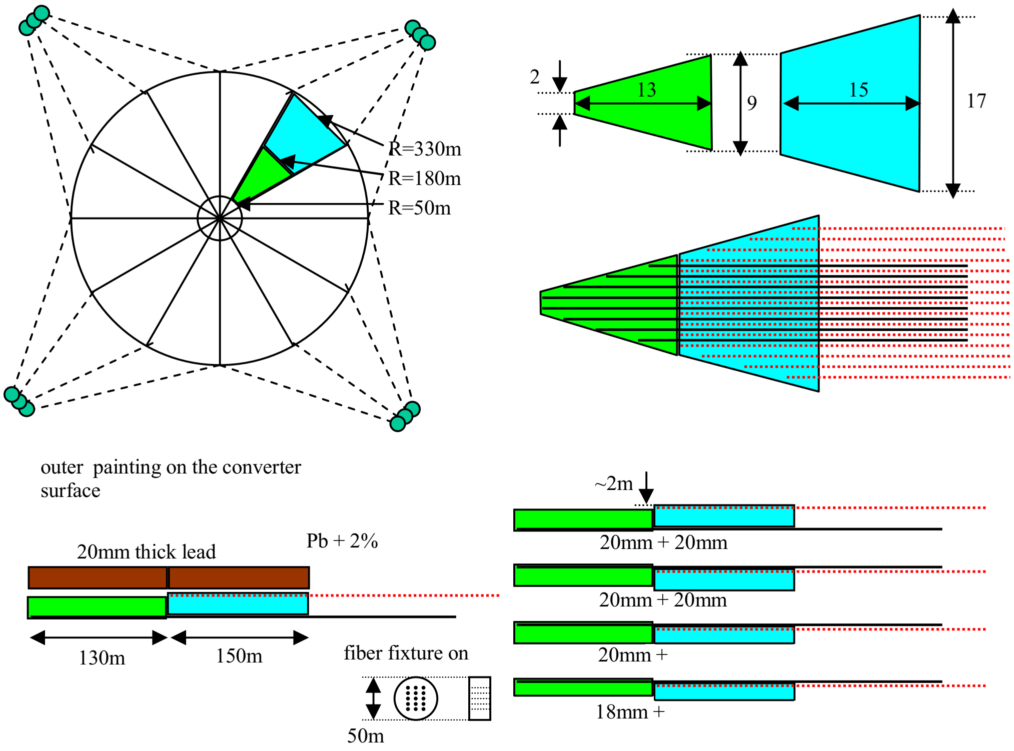

Figure 2.6: (Top figures) Front view of the RXN detector and its inner and outer segments and (Bottom figures) Overhead view of the inner and outer segments [40].

2.5 Central Arm Detectors

The PHENIX detector has a tracking and particle identification system at mid-rapidity $|\eta|<0.35$ called "central arm" or "CNT". The central arm is divided into east and west arms. The coverage of each arm is $\pi/2$ in azimuthal angle and pseudo-rapidity $|\eta|<0.35$ as shown in the Fig.2.2.

Mainly, Drift Chamber (DC) and Pad Chambers (PC) are used for charged particle tracking in order to determine particle momenta and spatial informations. Secondarily, Electromagnetic Calorimeter designed for photon measurements and particle identification is also used as an additional tracking detector. Time Expansion Chamber has not been used for any data analysis since the installation. The schematic configuration of these detectors can be seen in Fig.2.7 (a) and (b).

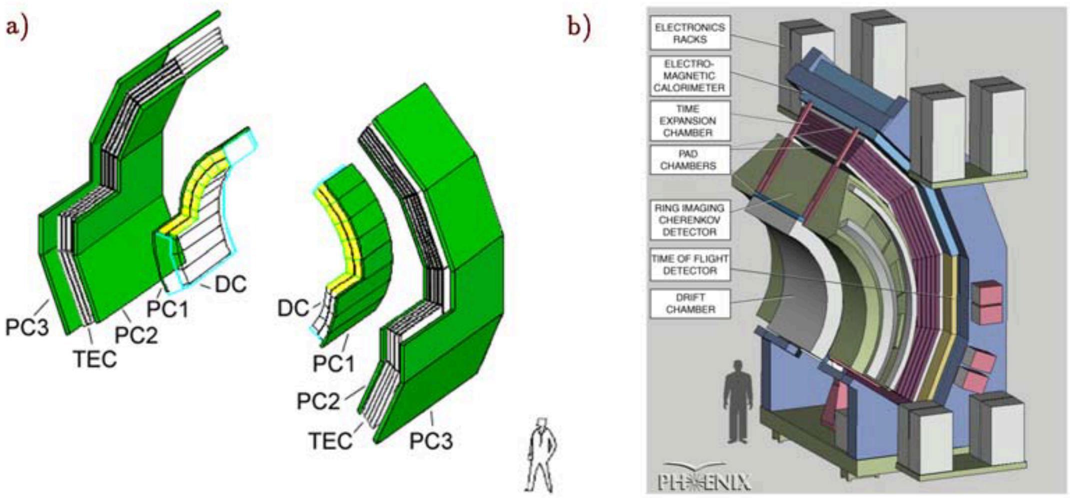

Figure 2.7: (a) The installation overview of the pad chamber, drift chamber, and time expansion chamber, and (b) the configurations of all detectors in east arm [41].

The DC provides transverse momenta p_T with a high resolution $\Delta p_T/p_T \sim 0.5\%$ and information of most inner hit for track matching in the outer subsystems.

Two PC layers PC1 and PC3 are used for providing three dimensional positions of charged particle track hits which have straight trajectories outside the CM field. PC1 is also used to determine the three-dimensional momentum vector by giving polar angle θ of charged particle tracks at the exit of the DC.

The power of particle identification is given by Ring Imaging Cherenkov counter (RICH), Time-Of-Flight (TOF), Aerogel Cherenkov Counter (ACC or AGEL), Lead Scintillator Electromagnetic Calorimeter (PbSc), and Lead Glass Electromagnetic Calorimeter (PbGl). An excellent separation of electrons from hadrons is provided by RICH over a wide momentum range $0.2<p<$ 5.0 GeV/c or higher momentum. The π, K, and p separation is provided by TOF detectors up to 3.0 GeV/c for π/K separation and up to 4.0 GeV/c for K/p in the east arm, those separation can be extended up to around 6 GeV/c using the information of number of Cherenkov photons counted in ACC in the west arm. The both PbSc and PbGl provide information of energy and spatial position of photon and electron clusters, and positions of charged particle hits as a secondary tracking detector. The schematic configuration of these detectors can be again seen in Fig.2.7 (b).

In the following sections, we introduce details of the PHENIX central arm spectrometers focusing on the subsystems that are used in this analysis: DC, PC, PbSc, and PbGl. More details of the PHENIX detector have been reported in [44, 45, 46].

2.5.1 Drift Chamber(DC)

The DC module is installed in a titanium frame at the most inner layer of the both east and west arms of the central arm: 2.02 to 2.46 m away from beam vertex in the radius direction, $\pi/2$ in the azimuthal direction, and 180 cm along the beam axis. The strength of residual magnetic filed is at most 0.6 kG in DC.

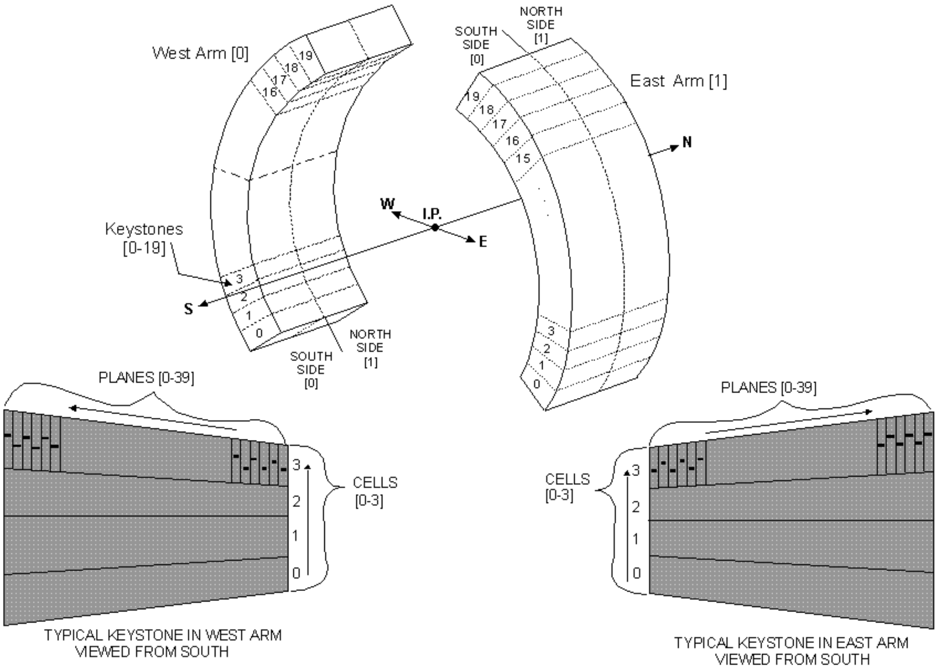

Figure 2.8: A sketch of DC frame configurations.

The configurations of DC frame with other subsystems in the central arm is shown in Fig.2.7. The sketch of the detailed DC frame and the stacking way of the sectors are shown in Fig.2.8. The shape of DC module is cylindrical and mirror-like symmetric between East and West side.

The DC is composed of 20 sectors in each arms. Every sector contains six types of modules labeled X1, U1, V1, X2, U2, and V2, and each module contains four anode and four cathode wire nets. An anode net consists of anode wires and different types of those: two channel + one guard + one field as well as four termination wires, while cathode nets consist of only cathode wires.

There are 12 anode wires in an anode net of X-module and 4 anode wires in an anode net of U and V-modules. Wires in X-modules run in the parallel direction to the beam axis, wires in U and V-modules run inclining ±5° from the beam axis to reconstruct full three-dimensional track information. Fig. 2.9 shows the mutual configurations of the X and U, V wire nets.

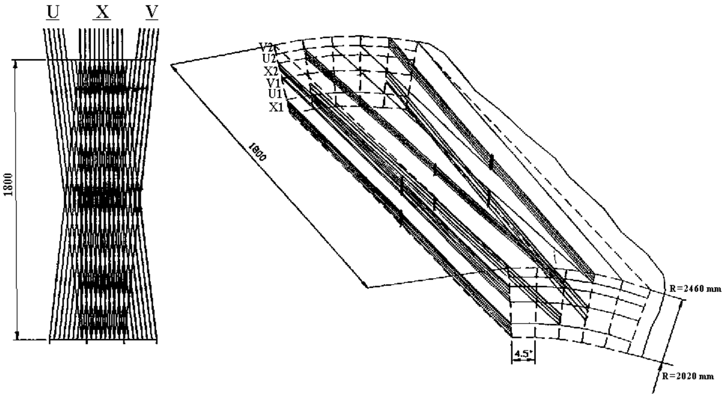

Figure 2.9: A sketch of the stereo wire orientations from (Left) overhead view and (Right) diagonal view.

2.5.2 Pad Chamber(PC)

The PC [42] is a multi-wire proportional chamber composed of three layers. The three layers of PC are termed as PC1, PC2, and PC3 from most inner to outer. The distance from the beam interaction point to each layer is 2.5 m for PC1, 4.2 m for PC2, and 4.9 m for PC3. The role of PC complex is to determine hit points of tracks along straight-orbit trajectories, since magnetic filed of central magnet is enough attenuated at (R<2.4m). The z position of tracks at the exit of DC determined by PC1 is crucial for determining 3-dimensional momentum vector of a particle.

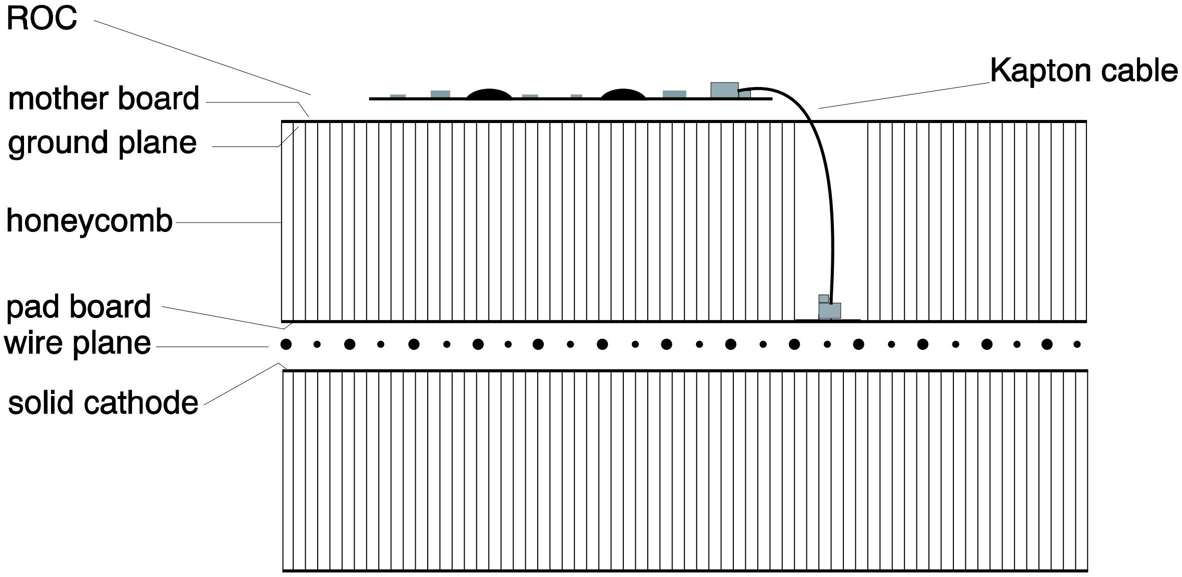

Figure 2.10: Vertical cut of a pad chamber.

Each Pad Chamber is composed of wires in a single plane bounded by two cathodes inside a gas vessel as shown in Fig. 2.10.

Cathode in a gas vessels is divided into a fine array of pixels. A charged particle going thorough a chamber makes electron avalanches on an anode wire, and the induced charges are read out by the readout electronics.

The pixels are engineered to achieve enough resolution in the z-coordinate and a small occupancy for good tracking qualities in high multiplicity events. The required position resolution was 4 mm and the computed space of an anode to achieve the requirements is 8 mm. Finally, the anode space of 8.4 mm was adopted since a square cell geometry was favored.

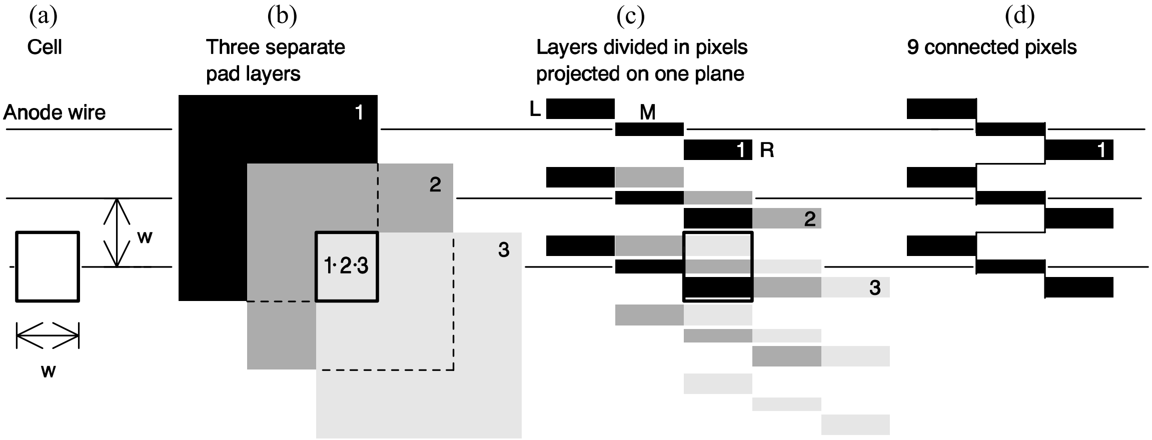

Figure 2.11: The layer and pixel layouts of the PHENIX pad chamber [42].

We require the electron avalanches are sensed by three pad layers in order to have a robust particle hits and exclude the electric and other noise sources. For this purpose, a cell contains three layers inside is introduced. Figure 2.11 gives a schematic idea of the cell definition. The square shown in (a) indicates the required size of a cell and three layers must exists inside a cell as shown in (b). By dividing each layers to pixels and distributing them as shown in (c), we can have three pixels inside a cell and an avalanche can be now caught by three neighboring and independent pixels.

Since this pixel configuration needs a large amount of electronic readouts, we have connected 9 pixels together into a single preamplifier and discriminator as shown in (d) in order to reduce construction costs. This technique does not reduce the position resolution, because the cell is still unique triplets of pixels from different connected pad layers, so that the spatial information of charged tracks are conserved. The performance of PC are summarized in the Table 2.4 [42].

Table 2.3: Summary of PC performance

Chamber	Wire distance (mm)	z resolution (mm)	perp. resolution (mm)	radiation thickness
PC1	8.4	1.7	2.5	1.2 %
PC2	13.6	3.1	3.9	2.4 %
PC3	16.0	3.6	4.6	2.4 %

2.5.3 Lead-Scintillator Calorimeter (PbSc)

The Lead-Scintillator Calorimeter (PbSc) is installed for measurement of photon and electron clusters, however in this thesis PbSc and Lead-Glass Calorimeter (PbGL) are used as the most outer tracking detectors to ensure the quality of charged particle tracking.

The PbSc is a shashlik type sampling calorimeter consisting of 15552 individual towers in total. Single tower comprises 66 sampling cells assembled by alternating tiles of lead and scintillators. These cells are connected by 36 optical fibers to transfer lights to phototubes behind the towers. Four mechanical-bonded towers form a module. Fig. 2.12 shows a decomposed view of a PbSc module. A PbSc super-module is composed of 36 modules bonded together and covered by welded stainless steel skins, and a sector is built up from 18 super-modules. Details of the design and construction methods of PbSc modules have been reported in [48]. The nominal energy resolution is $8.1\%/\sqrt{E}(\mathrm{GeV}) \pm 2.1\%$.

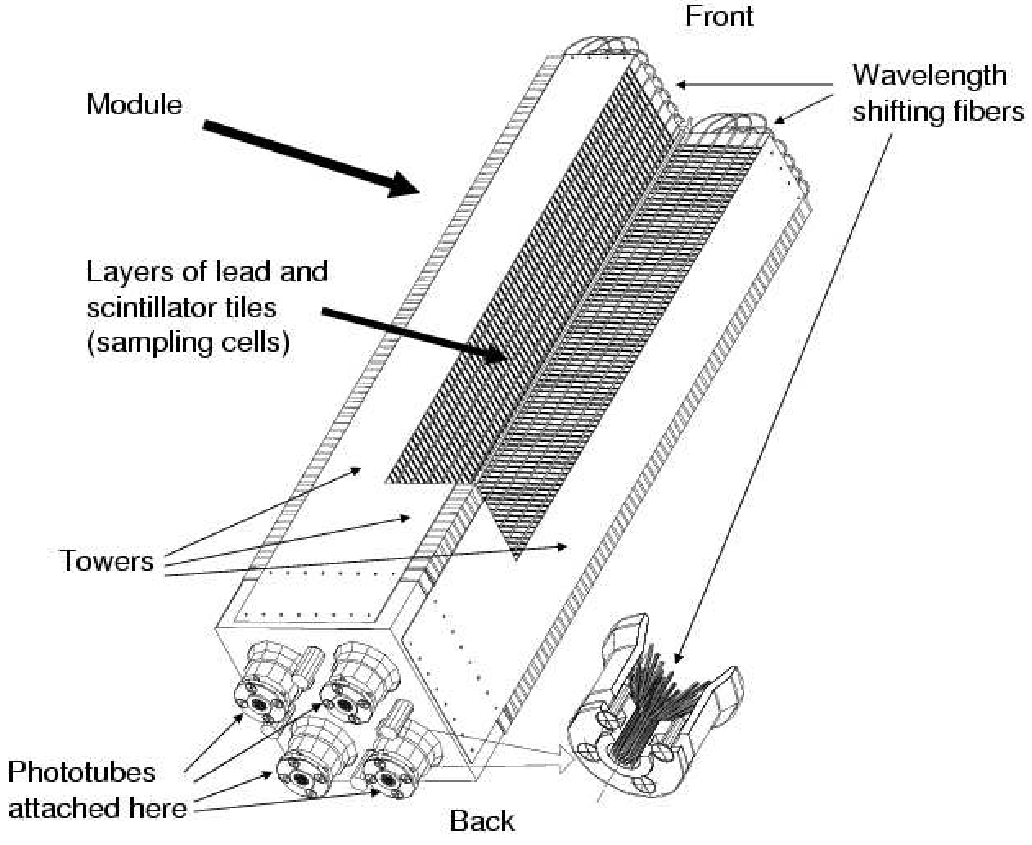

Figure 2.12: Interior structure of a Lead-Scintillator calorimeter module. A tower contains alternating tiles of scintillator and lead plates. Wavelength shifting fiber readout and leaky fiber are inserted into towers through the holes [47].

2.5.4 Lead-Glass Calorimeter (PbGl)

The PbGl is also used as a supporting tracking detector in this thesis. The PbGl consists of 9216 modules based on a technique previously used by the WA98 experiment [49] at CERN. Each

PbGl sector is composed of 192 super-modules and each super-module consists of 24 modules. A decomposed schematic drawing of PbGl super-module is shown in Figure 2.13. Each super-module is equipped with a gain monitoring system using a set of 3 LEDs which can be sensed by all 24 modules of a PbGl super-module. A photo diode with a preamp is attached to all the super-modules of PbGl to monitor the absolute yield of lights from the LEDs.

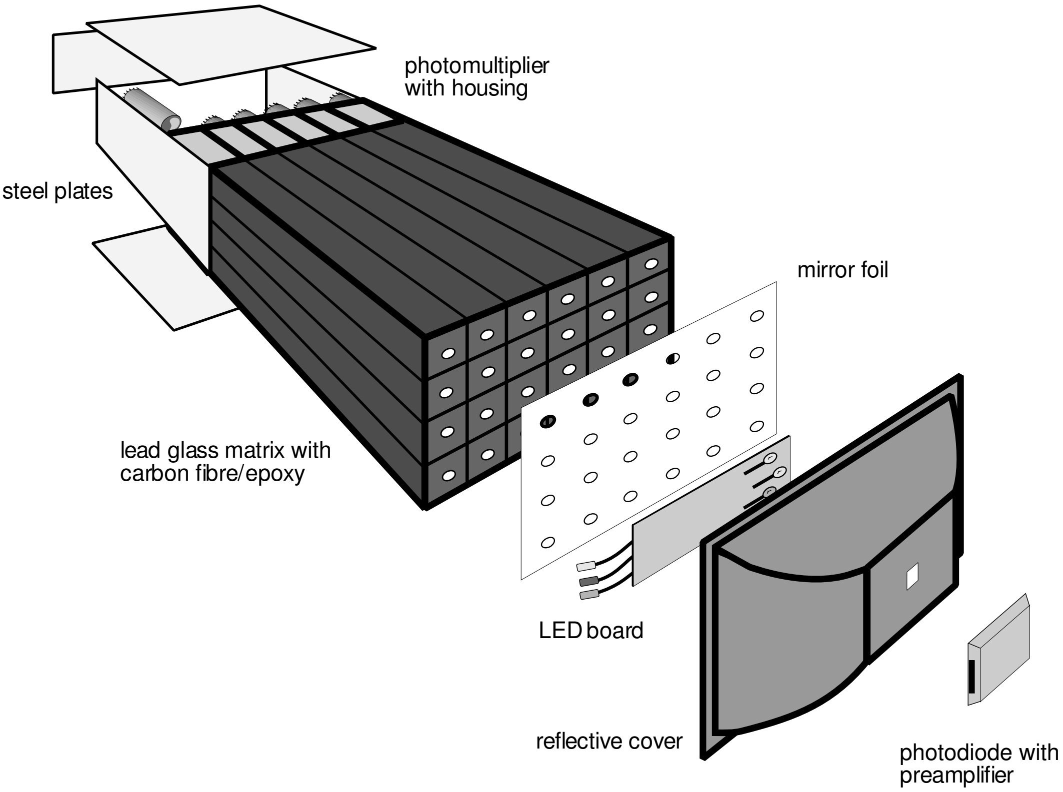

Figure 2.13: Decomposed view of a Lead-Glass calorimeter super-module. Single module is a read out using FEU-84 photomultiplier.

Chapter 3

Data Analysis

This chapter details three large parts of this analysis, (i) Determination of global variables as primary vertex, centrality and event-planes and the reconstruction of charged particles, (ii) Measurements of higher-order flow harmonics, and (iii) Measurements of two-particle correlations.

3.1 Event Selections

In this thesis, we analyzed approximately 4.4 billion "Minimum Bias Trigger" events in Au+Au collisions at $\sqrt{s_{NN}}$ = 200 GeV obtained by the RHIC-PHENIX Experiment in 2007. The Minimum Bias Trigger, the criteria of data acquisition, requires at least two coincident hits in both BBC South and North, at least one coincident forward neutron hit in both ZDC South and North, and a primary vertex position along with beam axis $|z^{vertex}|$<38 cm in the BBC Local level-1. The trigger condition is summarized in Tab.3.1.

Table 3.1: Requirements of Minimum Bias Trigger

BBC	**ZDC**	**BBCLL1**
South≥2∩North≥2	South≥1∩North≥1	|z-vertex|<38 cm

The data reduction z^{vertex}<30 cm is also required in addition to Minimum Bias Trigger in offline analyses to reduce potential backgrounds. The condition is determined by considering the bunch length of beam and the detector acceptances. The efficiency of Minimum Bias Trigger for Au+Au collisions has been evaluated employing HIJING event generator system[51] in the BBCLL1 logic, and its value is 92.3% ±0.4%(stat.) ±1.6%(syst.) [52] when z^{vertex}<30 cm is taken into account.

3.2 Centrality

The centrality is the degree of overlap of two colliding nuclei in heavy ion collisions. This value is determined by means of total charge sum of BBC. The number of events vs total charge sum of BBC is divided into each centrality percentile to contain same number of events as shown in Fig.3.1. In the PHENIX experiment, centrality can be determined from 0 to 93%. The small/large centrality indicates most central/peripheral collisions.

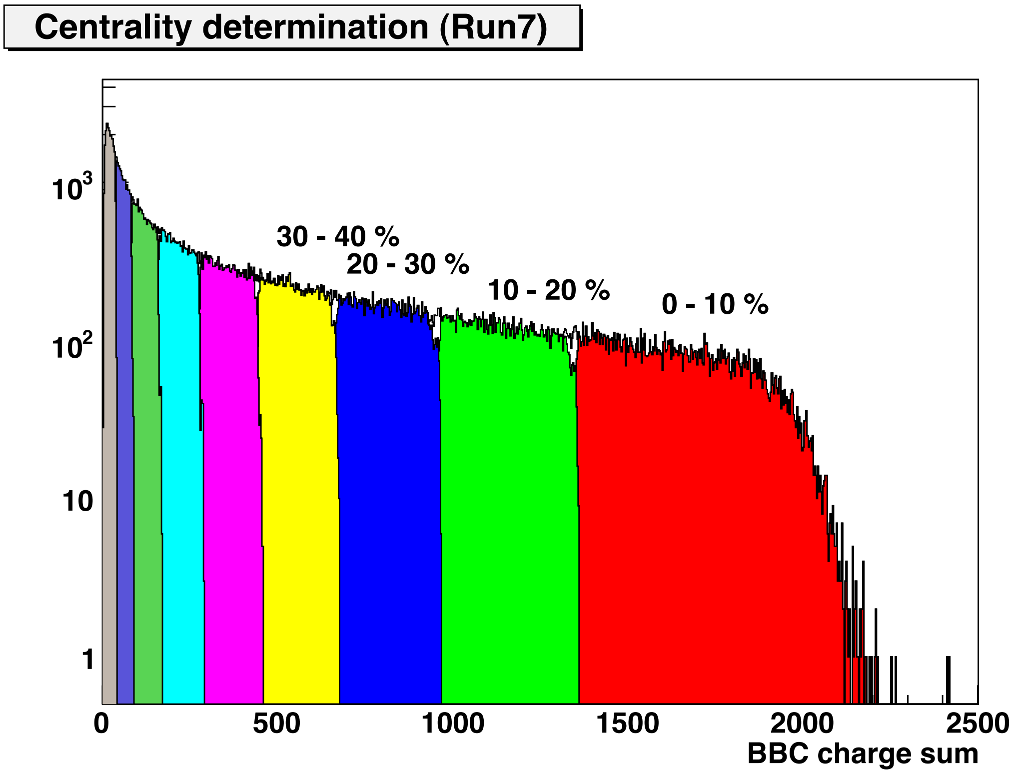

Figure 3.1: The number of events vs BBC charge sum and centrality division of the PHENIX Run7 experimental period.

3.3 Higher-Order Event Planes and Flow Harmonics

In this section, the ideas of higher-order event-planes originating from the fluctuations of initial participant density *i.e.* parton density and the Fourier expansion of azimuthal particle distribution with respect to each harmonic event-plane is introduced. Methods of determination of event-planes and its resolution as well as higher-order flow measurements are also introduced in this section.

Due to the periodic boundary condition, azimuthal distributions of emitted particles $dN/d\phi$ can be naturally described by Fourier number series to meet 2π period as

$$\begin{aligned} \frac{dN}{d\phi} &= \frac{x_0}{2\pi} + \frac{1}{\pi}\sum_{n=1} \{x_n \cos(n\phi) + y_n \sin(n\phi)\} \qquad (3.1) \\ &= \frac{x_0}{2\pi}\left\{1 + 2\sum_{n=1}\left\{\frac{x_n}{x_0}\cos(n\phi) + \frac{y_n}{x_0}\sin(n\phi)\right\}\right\}. \end{aligned}$$

The Fourier coefficient x_n and y_n can be determined by integrating $\frac{dN}{d\phi}\cos(n\phi)$ and $\frac{dN}{d\phi}\sin(n\phi)$ for each order due to the orthonormality of the sin/cos functions. These integrations can be substituted by the simple summations of all particles detected in the events as

$$x_n = \int_0^{2\pi} d\phi \frac{dN}{d\phi}\cos(n\phi) = \sum_i^M w_i \cos(n\phi_i) \equiv Q_x, \qquad (3.2)$$

$$y_n = \int_0^{2\pi} d\phi \frac{dN}{d\phi}\sin(n\phi) = \sum_i^M w_i \sin(n\phi_i) \equiv Q_y, \qquad (3.3)$$

where i denotes the index for all the particles up to the multiplicity M of the event, ϕ_i is the azimuthal angle of i-th particle and w_i is the weight to that (p_T, multiplicity, etc.). The w_i is necessary in order to minimize the dispersion in determining the event-plane, i.e. to maximize event-plane resolutions. A vector, $\mathbf{Q}$=(Q_x, Q_y) called “Q(flow) vector”, is used for event-plane determination in experimental analyses. The detail will be given in later section.

If we define the azimuthal angle ϕ with respect to event-planes, $dN/d\phi$ can be rewritten only with even functions as

$$\begin{aligned} \frac{dN}{d\phi} &= \frac{x_0}{2\pi}\left\{1 + 2\sum_{n=1}\left\{\frac{x_n}{x_0}\cos(n\phi) + \frac{y_n}{x_0}\sin(n\phi)\right\}\right\} \qquad (3.4) \\ &= \frac{x_0}{2\pi}\left\{1 + 2\sum_{n=1}\{v_n \cos(n[\phi - \Psi_n])\}\right\}, \qquad (3.5) \end{aligned}$$

where Ψ_n^{real} is the real n-th order event-plane and v_n is the amplitude of azimuthal anisotropy in each harmonics. These two quantities are defined as

$$\begin{aligned} \Psi_n &= \frac{1}{n}\tan^{-1}(y_n/x_n), \quad 0 \le \Psi_n \le 2\pi/n \qquad (3.6) \\ v_n &= \frac{\sqrt{x_n^2 + y_n^2}}{x_0}, \quad x_0 = M\langle w\rangle. \qquad (3.7) \end{aligned}$$

If we again follow this discussion in the experimental situations, the measured azimuthal distribution of particles $r^m(\phi)$ can be written as

$$\begin{aligned} r^m(\phi) &= \frac{x_0}{2\pi}\left\{1+2\sum_{n=1}\left\{\frac{x_n}{x_0}\cos(n\phi)+\frac{y_n}{x_0}\sin(n\phi)\right\}\right\} && (3.8)\\ &= \frac{x_0}{2\pi}\left\{1+2\sum_{n=1}\left\{v_n^{obs}\cos(n\phi)+v_n^{obs}\sin(n\phi)\right\}\right\} && (3.9)\\ &= \frac{x_0}{2\pi}\left\{1+2\sum_{n=1}\left\{v_n^{obs}\cos(n[\phi-\Psi_n^{obs})\right\}\right\}. && (3.10)\end{aligned}$$

The azimuthal angle of event-planes Ψ_n^{obs} is experimentally determined using Q-vector in an event-by-event basis. Since the azimuthal angle of the experimental event-plane Ψ_n^{obs} has different value from that of real plane Ψ_n^{real}, Ψ_n^{obs} can be expressed as a sum of the real plane Ψ_n^{real} and the difference from real plane $\Delta\Psi_n$ as Ψ_n^{obs}=Ψ_n^{real}+$\Delta\Psi_n$. By accumulating enough number of events, the relation between the measured azimuthal anisotropy v_n^{obs} and real azimuthal anisotropy v_n can be given as

$$\begin{aligned} v_n^{obs} &= \left\langle\cos(n[\phi-\Psi_n^{obs}])\right\rangle && (3.11)\\ &= \left\langle\cos(n[\phi-\Psi_n]-n[\Psi_n^{obs}-\Psi_n])\right\rangle && (3.12)\\ &= \langle\cos(n[\phi-\Psi_n])\cdot\cos(n\Delta\Psi_n)\rangle+\langle\sin(n[\phi-\Psi_n])\cdot\sin(n\Delta\Psi_n)\rangle && (3.13)\\ &= \langle\cos(n[\phi-\Psi_n])\rangle\langle\cos(n\Delta\Psi_n)\rangle && (3.14)\\ &= v_n\langle\cos(n\Delta\Psi_n)\rangle && (3.15)\\ v_n &= \frac{v_n^{obs}}{\langle\cos(n\Delta\Psi_n)\rangle}, && (3.16)\end{aligned}$$

with assumptions that $\phi-\Psi_n$ and $\Delta\Psi_n$ are independent and sin terms vanish due to a symmetric geometry with respect to Ψ_n in heavy ion collisions. These assumptions can be applied to a collision system which has enough multiplicity. The denominator of Eq.(3.16) $\langle\cos(n\Delta\Psi_n)\rangle$ means the experimental resolution of event-plane determination.

3.3.1 Event-Plane Determination

Since the direction of impact parameter between two colliding nuclei in heavy ion collisions cannot be controlled by tuning the beam, the azimuthal distributions of event-planes should be flat. The direction of event-planes have to be reconstructed in an event-by-event basis. For this purpose, we used the BBC and RXN detectors in this analysis. The BBC sits on $3.0<|\eta|<3.9$ and has 64 PMTs in each side of North and South arms. The charge deposited in each PMT is used as a weight of event-plane determination. The RXN is located at $1.0<|\eta|<2.8$ and has 24 PMTs in each side. The weight of RXN is adc value of each PMT. The event-planes are reconstructed by measuring the Q-vector, which is introduced in previous section, as

$$Q_x^{obs} = \sum_i w_i \cos(n\phi_i^{PMT}), \tag{3.17}$$

$$Q_y^{obs} = \sum_i w_i \sin(n\phi_i^{PMT}), \tag{3.18}$$

$$\Psi_n^{obs} = \frac{1}{n} \tan^{-1}\left(\frac{Q_y^{obs}}{Q_x^{obs}}\right). \tag{3.19}$$

where, i is an index running over the number of PMTs in each detectors, ϕ_i^{PMT} is the azimuthal angle of i-th PMT of the detector and w_i is the weight of it. This calculation is done in a segment-by-segment basis of detectors.

In usual case, the azimuthal distribution of reconstructed event-plane is not flat due to the beam condition, imperfect acceptance and some dead channels. The non-flatness of the event-plane is shown by the black data points in Fig.(3.2). A two-step calibration is applied for the purpose of correcting the azimuthal distribution of event-planes; the detail will be given in the next sections.

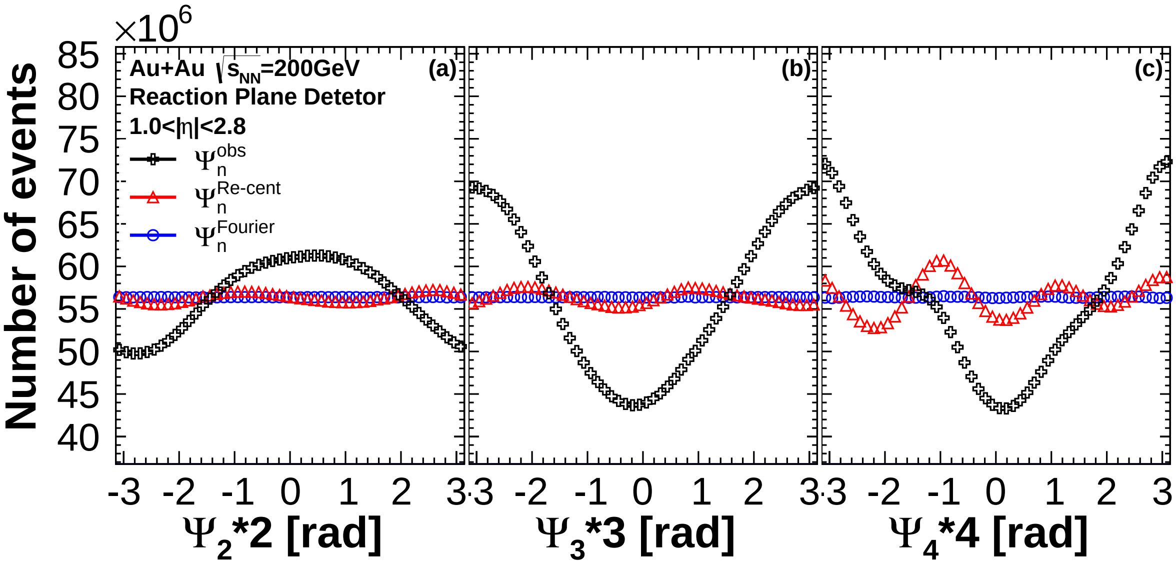

Figure 3.2: (Black) Raw higher-order event-planes, (Red) Higher-order event-planes after re-centering of Q-vector, and (Blue) Higher-order event-planes after re-centering of Q-vector and Fourier flattening (see text).

Re-centering Calibration

The definition of first step “Re-centering calibration” is given as

$$\begin{aligned} Q_x^{rec} &= \frac{Q_x^{obs} - \left\langle Q_x^{obs} \right\rangle}{\sigma_x}, && (3.20) \\ Q_y^{rec} &= \frac{Q_y^{obs} - \left\langle Q_y^{obs} \right\rangle}{\sigma_y}, && (3.21) \\ \Psi_n^{rec} &= \frac{1}{n} \tan^{-1} \left(\frac{Q_y^{Rec}}{Q_x^{Rec}} \right). && (3.22) \end{aligned}$$

where $\left\langle Q_{x,y}^{obs} \right\rangle$ are the mean of Q_x^{obs} and Q_y^{obs}, $\sigma_{x,y}$ are the width of them. Since the $Q_{x,y}^{obs}$ is the projection of event-plane to each axis, the width of those should be basically same between x and y axes, also the mean should be 0. The correction of these component in this procedure largely recovers the flatness of event-plane azimuthal angle as shown by the red data points in Fig(3.2). The small residual from perfect flatness is corrected in the second calibration step.

Flattening Calibration

If we define the small residual from perfect flatness $\Delta\Psi_n$, the flat event-plane $\Psi_n^{Fourier}$ can be written as

$$n\Psi_n^{Fourier} \equiv n\Psi_n^{rec} + n\Delta\Psi_n. \qquad (3.23)$$

$n\Delta\Psi_n$ can be generalized by Fourier number series as

$$n\Delta\Psi_n \equiv \sum_{k=1} [A_k \cos kn\Psi_n^{rec} + B_k \sin kn\Psi_n^{rec}]. \qquad (3.24)$$

The coefficients in Fourier series A_k and B_k can be determined by tuning the average of cos/sin term of $n\Psi_n^{Fourier}$ in k-th order becomes 0, *i.e.* the isotropic distribution of azimuthal angle of the event-plane. If $\Delta\Psi_n$ is enough small, coefficients of cos term can be determined as

$$\begin{aligned} \left\langle \cos kn\Psi_n^{Fourier} \right\rangle &= \langle \cos(kn\Psi_n^{rec} + kn\Delta\Psi_n) \rangle && (3.25) \\ &= \langle \cos kn\Psi_n^{rec} \cos kn\Delta\Psi_n \rangle - \langle \sin(kn\Psi_n^{rec}) \sin(kn\Delta\Psi_n) \rangle \\ &\simeq \langle \cos kn\Psi_n^{rec} \rangle - \langle \sin kn\Psi_n^{rec} \cdot (kn\Delta\Psi_n) \rangle && (3.26) \\ &= \langle \cos kn\Psi_n^{rec} \rangle - kB_k \left\langle \sin^2(kn\Psi_n^{rec}) \right\rangle && (3.27) \\ &= \langle \cos kn\Psi_n^{rec} \rangle - kB_k/2 \quad \left(\left\langle \sin^2(kn\Psi_n^{rec}) \right\rangle = 1/2 \right) && (3.28) \\ &= 0 && (3.29) \\ B_k &= \frac{2}{k} \langle \cos kn\Psi_n^{rec} \rangle . && (3.30) \end{aligned}$$

For sin terms, by following a similar calculation we obtain

$$\begin{aligned}
\left\langle \sin kn\Psi_n^{Fourier} \right\rangle &= \langle \sin\left(kn\Psi_n^{rec} + kn\Delta\Psi_n\right)\rangle && (3.31)\\
&= \langle \sin kn\Psi_n^{rec} \cos kn\Delta\Psi_n\rangle - \langle \cos\left(kn\Psi_n^{rec}\right)\sin\left(kn\Delta\Psi_n\right)\rangle && (3.32)\\
&\simeq \langle \sin kn\Psi_n^{rec}\rangle + \langle \cos kn\Psi_n^{rec} \cdot (kn\Delta\Psi_n)\rangle && (3.33)\\
&= \langle \sin kn\Psi_n^{rec}\rangle + kA_k \left\langle \cos^2\left(kn\Psi_n^{rec}\right)\right\rangle && (3.34)\\
&= \langle \sin kn\Psi_n^{rec}\rangle + kA_k/2 \quad \left(\left\langle \cos^2\left(kn\Psi_n^{rec}\right)\right\rangle = 1/2\right) && (3.35)\\
&= 0 && (3.36)\\
A_k &= -\frac{2}{k}\langle \sin kn\Psi_n^{rec}\rangle . && (3.37)
\end{aligned}$$

The fully corrected event-plane distributions $\Psi_n^{Fourier}$ are shown by the blue data points in Fig(3.2).

3.3.2 Event-Plane Resolutions

The event-plane measured by the experimental method is fluctuating with respect to the real event-plane due to the emission of finite number of particles in heavy ion collisions. We estimate the event-plane resolutions under the following assumptions with simplifying the situation of heavy ion collisions.

- Particles emitted in different rapidity range are uncorrelated each other.
- The number of particles in the experimental acceptance is large enough (N$\gg$1).
- The amplitude of flow does not fluctuate event by event in each centrality.

With these assumptions, the analytical formula of the distributions of measured event-planes (with the corrections, simply denoted Ψ_n^{obs} from here) with respect to real event-planes in each order is given by [53] as

$$\frac{dN^{eve}}{d[kn(\Psi_n^{obs} - \Psi_n^{real})]} = \frac{1}{\pi} e^{-\chi_n^2/2}\left[1 + z\sqrt{\pi}[1 + \mathrm{erf}(z)]e^{z^2}\right], \quad (3.38)$$

where $z = \chi_n \cos kn(\Psi_n^{obs} - \Psi_n^{real})$ and $\mathrm{erf}(z)$ denotes the error function. The resolution of event-planes in each order is also formulated in [54] as

$$\left\langle \cos\left[kn(\Psi_n^{obs} - \Psi_n^{real})\right]\right\rangle = \frac{\sqrt{\pi}}{2\sqrt{2}}\chi_n e^{-\chi_n^2/4}\left[I_{(k-1)/2}\left(\frac{\chi_n^2}{4}\right) + I_{(k+1)/2}\left(\frac{\chi_n^2}{4}\right)\right]. \quad (3.39)$$

The BBC and RXN detectors have the North and South hodoscopes in the both arms of positive and negative pseudo-rapidity ranges. The both hodoscopes are located at the same rapidity region in each arm, that results in an equal multiplicity in both arms. Therefore, the event-plane resolution using each arm can be obtained via measuring the relative azimuthal angle of event-planes between North-South arms as

$$\begin{aligned}
\sqrt{\langle \cos\left[kn(\Psi_n^N - \Psi_n^S)\right]\rangle} &= \sqrt{\langle \cos\left[kn(\Psi_n^N - \Psi_n^{real})\right]\rangle \langle \cos\left[kn(\Psi_n^S - \Psi_n^{real})\right]\rangle} && (3.40)\\
&= \left\langle \cos\left[kn(\Psi_n^{N,S} - \Psi_n^{real})\right]\right\rangle . && (3.41)
\end{aligned}$$

The $\chi_n^{s,n}$ of the south and north arms can be determined by substituting $\left\langle \cos\left[kn(\Psi_n^{N,S} - \Psi_n^{real})\right]\right\rangle$ to Eq.(3.39). Thus, the event-plane resolution combining the both south and north hodoscopes can be obtained by re-input the $\chi_n^{S+N} = \sqrt{2}\chi_n^{s,n}$ to Eq.(3.39), which is determined by the relation of multiplicity in each arm *i.e.* N^{s+n}=$2N^{s,n}$.

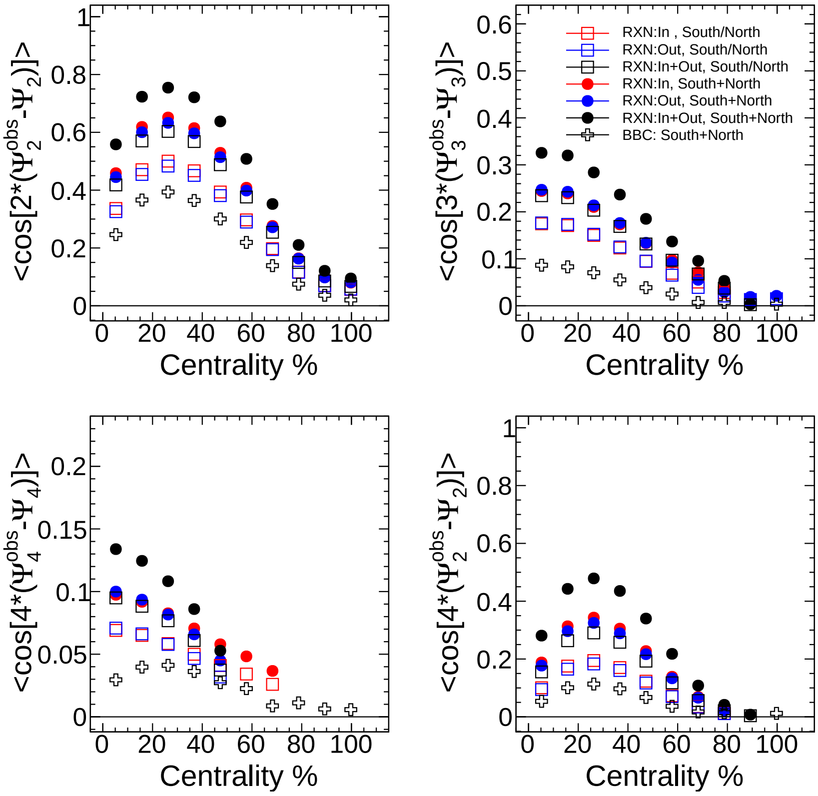

Figure 3.3: Resolutions in second to fourth order event-planes, measured with various RXN module combinations and north and south BBC.

Figure 3.3 shows the event-plane resolution as a function of centrality with different combinations of RXN inner ($1.0 < |\eta| < 1.5$) and outer($1.5 < |\eta| < 2.8$) ring for different combination of south north arms, and the resolution of BBC using all PMTs in both south and north arms.

It is worth pointing out that while second and forth order resolution of Ψ_2 is prominent around centrality 20-40 %, the $\Psi_{3,4}$ resolutions monotonically reduce except BBC in Ψ_4 resolution. This could be driven from a property of initial collision geometry differing in Ψ_2 and higher event-planes, detailed measurements of event-plane correlation even among different orders would help better understanding on these aspects of heavy ion collisions.

3.4 Track Selections

Before the selection of tracks with various cuts in order to be qualified as a charged particle in physics analysis, in first, all tracks are required to meet the following conditions, that are numbered “31” or “63” of DC track quality:

- hits on X1 and X2 wire of DC,
- unique hit on UV wire of PC1,
- (unique) hit in PC1.

In addition to this track selection on DC and PC1, the intersection point of track in z-coordinate $|zed| < 75$ cm is also applied. Tracks reconstructed on DC and PC1, passed the cut conditions on DC, are further projected to outer direction *i.e.* PC3 and EMC detectors. The $\phi - z$ and $\phi - r$ (r:radius) surfaces of the detectors around the intersection point of the projected tracks are scanned to list candidates of the charged particle hits. The closest hit to the intersection point of the projected track is selected as the his associated with the track. The distribution of distance between track intersection and the associated hit in the both ϕ and z directions can be approximated by Gaussian. The tracks within a 2σ window of Gaussian distribution on PC3 and EMC are adopted for the analysis. Tracks, that have one or more photons detected in RICH detector, are not treated as charged hadrons and thrown away. Since those photons are obtained by electrons radiating Cherenkov photons inside the RICH. The cut conditions of charged particles tracked in the central arm are summarized in Tab. 3.2.

Table 3.2: Cut parameters of central arm charged hadron tracks in Au+Au 200GeV.

Track Selection	
DC Track Quality	31 or 63
DC zed	75 cm
p_T cut	p_T >0.2GeV/c
PC3 Matching Cut	$\sqrt{\sigma_\phi^2 + \sigma_z^2}$<2.0
EMC Matching Cut	$\sqrt{\sigma_\phi^2 + \sigma_z^2}$<2.0
RICH number of photons	n_0<1

3.5 Two Particle Correlations

The property of jet-like correlations and jet-medium coupling could be diagnosed by two-particle spatial correlations defined by the ratio of a two-particle probability distribution over the product of single particle probability distributions as

$$C(\Delta\phi, \Delta\eta) = \frac{P(\phi^t, \phi^a, \eta^t, \eta^a)}{P(\phi^t, \eta^t)P(\phi^a, \eta^a)}, \tag{3.42}$$

where $\phi^{t,a}$ and $\eta^{t,a}$ are the azimuthal angles and pseudo-rapidities of trigger and associate particles, $\Delta\phi$=ϕ^a−ϕ^t and $\Delta\eta$=η^a−η^t are the relative position between trigger and associate particles.

In real experimental situations, the correlation function is measured as the ratio of pair distributions, normalized by total number of pairs selected in real and mixed events as

$$C(\Delta\phi, \Delta\eta) = \frac{\frac{1}{\int d\Delta\phi d\Delta\eta \ d^2N_{real}/d\Delta\phi d\eta} d^2N_{real}/d\Delta\phi d\Delta\eta}{\frac{1}{\int d\Delta\phi d\Delta\eta \ d^2N_{mixed}/d\Delta\phi d\eta} d^2N_{mixed}/d\Delta\phi d\Delta\eta}. \tag{3.43}$$

Table 3.3: The event classification for event mixing technique in measurements of two-particle correlations.

Event class binning	
Centrality	10 bins in 100%
z^{vertex}	10 bins in $\lvert z^{vertex}\rvert$<30 cm

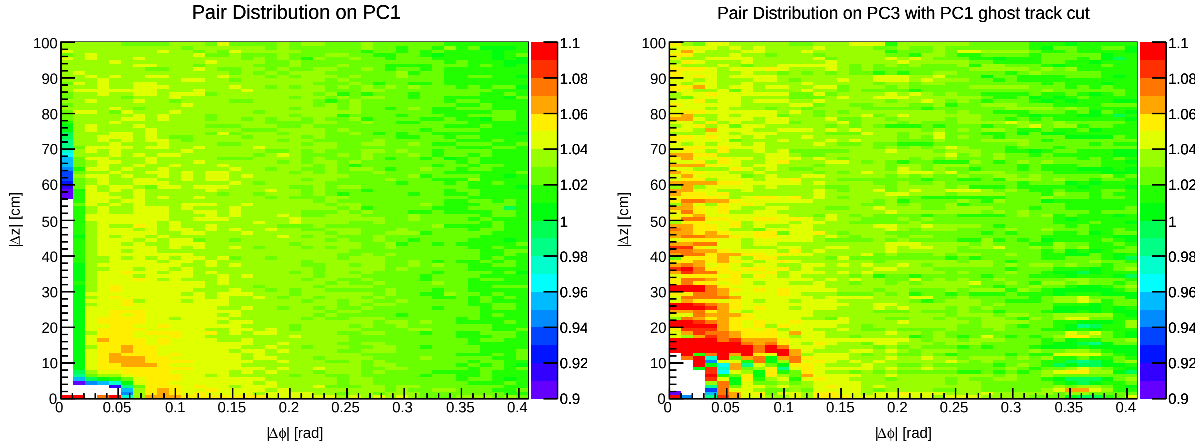

Figure 3.4: $\Delta\phi$-Δz correlations in (Left) PC1 and (Right) PC3 after pair selection in PC1.

The pair distributions in real (same) events correspond to two-particle probability distribution, since those pairs in real event preserve physical correlations. The pair distributions selected from mixed (different) events correspond to the products of single probability distributions, since contrastively those pairs in mixed events have no physical correlations.

This kind of event mixing also corrects the effect of limited acceptance of the PHENIX detector, because the pairs in the both real and mixed events are affected by the limited acceptance, when the events that have similar event properties such as centrality, vertex positions and so on. Table3.3 shows the event class of the event-mixing technique employed in this analysis.

Correlation functions are still biased by the limited tracking resolution of detectors. Particles having hit points close to each other in a detector can be accidentally counted as one particle, or in contrast a particle can be accidentally counted as multiple particles. Fig.3.4 shows the $\Delta\phi$-Δz correlations on PC1 and PC3 measured in a same method analogous to Eq.(3.43) using the event mixing method, where Δz is a relative position in z direction [cm] and $\Delta\phi$ is a relative azimuth [rad] between two-particles on PC1 and PC3. Thus, values of correlations should stay around 1 if we assume an ideal detector.

The vacant areas around $\Delta\phi = 0$ and $\Delta z = 0$ in both left and right panels in Fig.3.4 are inefficient or over-efficient regions of detectors in counting particles. Those areas are excluded

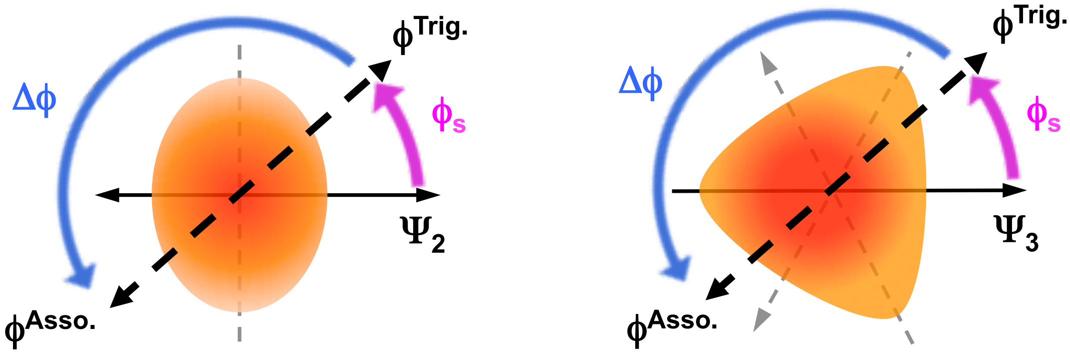

Figure 3.5: Schematic concept of trigger particle selection with respect to the second and third order event-planes. ϕ^{Trig} is an azimuthal angle of trigger particle, ϕ^{Asso} is an azimuth angle of associate particle. $\Delta\phi{=}\phi^{Trig}{-}\phi^{Asso}$ is a relative angle between particles and $\phi_s{=}\phi^{Trig}{-}\Psi_n$ is a relative angle from the event-planes.

by the following ellipsoidal shape cut:

$$\sqrt{(\Delta\phi_{PC1}/0.04)^2 + (\Delta z_{PC1}/90)^2} < 1, \tag{3.44}$$

$$\sqrt{(\Delta\phi_{PC1}/0.08)^2 + (\Delta z_{PC1}/8.0)^2} < 1, \tag{3.45}$$

$$\sqrt{(\Delta\phi_{PC3}/0.07)^2 + (\Delta z_{PC3}/25)^2} < 1. \tag{3.46}$$

The cuts on PC1 have been applied before the correlation in the right figure of Fig.3.4 is calculated.

3.5.1 Trigger and Associate Selections in Two-Particle Correlations

Two-particle correlations reflect various aspects of space-time evolution of heavy ion collisions by selecting p_T range of trigger and associate particles with a subtraction of flow backgrounds. While correlations of high p_T particles give us information of energy loss mechanism of hard-scattered partons inside a QGP[55], correlations of low to intermediate p_T particles provide information to discuss a possible behavior of deposited energy as a consequence of a coupling between hot-dense medium and hard-scattered partons.

Correlation measurements of inclusive trigger particles, *i.e.* without trigger selection with respect to event-planes, give us information of averaged parton behavior inside a medium. In addition, correlation measurements with a trigger selection with respect to the second-order event-plane can control the parton path length inside a medium due to its ellipsoidal shape as shown in Fig. 3.5, which leads to a discussion of path length dependence of a parton behavior. It is also interesting to select trigger particles with respect to the third-order event-plane, because the partons in near-side and in away-side can sense different path length due to triangular shape of third-order geometry of media. We expect possible different results of jet-medium interplay in the second and third-order geometry of media can be reflected in the event-plane dependent correlations.

Table 3.4: p_T selections of inclusive trigger two-particle correlations.

Trigger p_T [GeV/c]	Associate p_T [GeV/c]
4.0 - 10.0	4.0 - 10.0
4.0 - 10.0	2.0 - 4.0
4.0 - 10.0	1.0 - 2.0
4.0 - 10.0	0.5 - 1.0
2.0 - 4.0	2.0 - 4.0
2.0 - 4.0	1.0 - 2.0
2.0 - 4.0	0.5 - 1.0
1.0 - 2.0	1.0 - 2.0
1.0 - 2.0	0.5 - 1.0

Table 3.5: Selection of trigger azimuthal angle relative to second-order and third-order event planes.

Order	ϕ-Ψ_n[rad]	Number of bins
n=2	$[-\pi/2, \pi/2]$	8 bins
n=3	$[-\pi/3, \pi/3]$	8 bins

Selected p_T ranges of correlations with inclusive triggers are tabulated in Tab. 3.4.

The p_T selections of the Ψ_2 and Ψ_3 dependent correlations are p_T: 2-4x1-2, 2-4x2-4, and 4-10x2-4 GeV/c. The trigger direction with respect to Ψ_2 and Ψ_3 is divided into 8 bins as tabulated in Tab.3.5.

3.5.2 Flow Backgrounds in Correlations

In two-particle correlation measurements using real experimental data, it is quite difficult to distinguish an origin of detected particles. Consequently, measured correlations contain particles originating from hard scattering and collective bulk expansions, therefore contributions from bulk expansion in correlations have to be estimated to see possible effects from jets. This section presents the (i) Analytical formula of flow background in the inclusive trigger correlations and (ii) Monte Carlo simulations of flow backgrounds in the correlations with a trigger selection with respect to event-planes. The estimations of background levels are also detailed in this section.

Analytical Formula

With an assumption that space-time evolution of hot and dense medium contains only soft-collective expansion, the distribution of relative angle between trigger and associate particles $\frac{dN^{ta}}{d\Delta\phi}$ can be described by an integral using a product of single particle azimuthal distributions

(Eq.(3.10)) for trigger and associate particles as

$$\frac{dN^{ta}}{d\Delta\phi} = \int_0^{2\pi} d\phi^t \frac{dN^t}{d\phi^t}\frac{dN^a}{d\phi^a} \tag{3.47}$$

$$\propto \int d\phi^t \left\{1 + 2\sum_{k=1} v_k^t \cos k(\phi^t - \Psi_k)\right\}\left\{1 + 2\sum_{l=1} v_l^a \cos l(\phi^a - \Psi_l)\right\}, \tag{3.48}$$

where N^{ta} is the number of pairs, N^t and N^a are the numbers of trigger and associate particles, ϕ^t and ϕ^a are the azimuthal angles of trigger and associate particles, and $\Delta\phi = \phi^a - \phi^t$. Substituing $\phi^a = \phi^t + \Delta\phi$ in the integral, we can write the integral as follows

$$\frac{dN^{ta}}{d\Delta\phi} \propto \int d\phi^t \left\{1 + 2\sum_{k=1} v_k^t \cos k(\phi^t - \Psi_k)\right\}\left\{1 + 2\sum_{l=1} v_l^a \cos l(\phi^t + \Delta\phi - \Psi_l)\right\} \tag{3.49}$$

$$= \int d\phi^t \left\{1 + 2\sum_{k=1} v_k^t \cos k(\phi^t - \Psi_k) + 2\sum_{l=1} v_l^a \cos l(\phi^t + \Delta\phi - \Psi_l)\right. \tag{3.50}$$

$$\left. + \quad 4\sum_{k=1}\sum_{l=1} v_k^t v_l^a \cos k(\phi^t - \Psi_k)\cos l(\phi^t + \Delta\phi - \Psi_l)\right\} \tag{3.51}$$

$$\begin{aligned} = & \int d\phi^t \left\{1 + 2\sum_{k=1} v_k^t \cos k(\phi^t - \Psi_k) + 2\sum_{l=1} v_l^a \cos l(\phi^t + \Delta\phi - \Psi_l)\right. \\ + & \; 2\sum_{k=1}\sum_{l=1} v_l^k v_l^a \cos\left\{(k+l)\phi^t - k\Psi_k - l\Psi_l + l\Delta\phi\right\} \\ + & \; 2\sum_{k=1}\sum_{l=1} v_l^k v_l^a \cos\left\{(k-l)\phi^t - k\Psi_k + l\Psi_l - l\Delta\phi\right\}\left.\right\}, \end{aligned} \tag{3.52}$$

here the formula of trigonometric functions $\cos\alpha\cos\beta = \{\cos(\alpha+\beta) + \cos(\alpha-\beta)\}/2$ is used for simplifying the equation. Considering the relation in the integral of cosine function $\int d\phi \cos n\phi = 0$, the second, third, and forth terms in the right side disappear. The fifth term in the right side survives at $k = l$. Thus the analytical formula becomes

$$\frac{dN^{ta}}{d\Delta\phi} \propto \int d\phi^t \left\{1 + 2\sum_{k=1} v_k^t v_k^a \cos k\Delta\phi\right\} \tag{3.53}$$

$$= b_0 \left\{1 + 2\sum_{k=1} v_k^t v_k^a \cos k\Delta\phi\right\}, \tag{3.54}$$

where b_0 is the total background level of this pure flow background, which is determined by the ZYAM assumption detailed in the later section.

Monte Carlo Simulations

While pure flow backgrounds of the inclusive trigger selections relative to event-plane have a simple analytical formula, those with a trigger selection relative to second-order event-plane are presented in a very tangled shape [56]. Currently, the analytical formula is not a trivial problem to solve in more complicated situations *e.g.* if the left and right sides of trigger direction

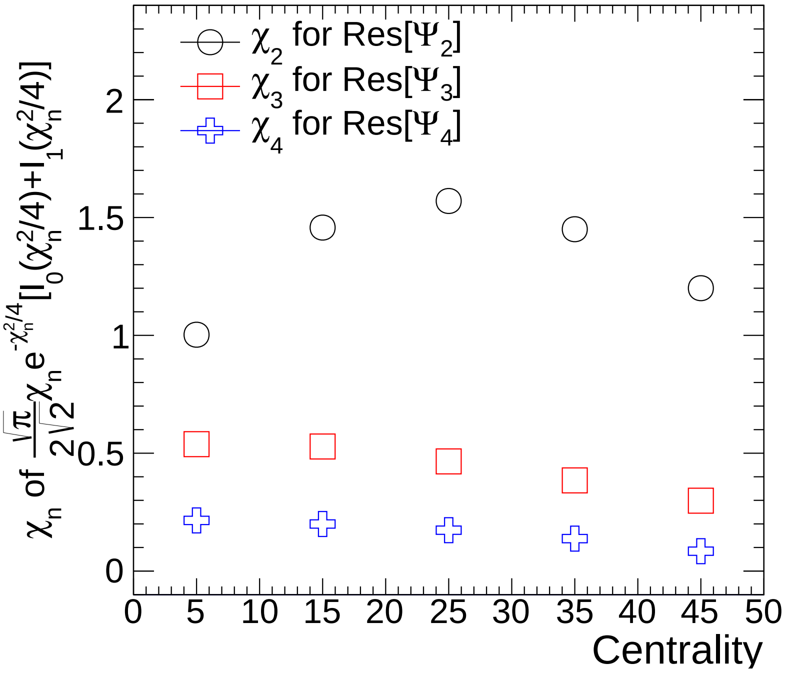

Figure 3.6: χ parameters tuned to reconstruct event-plane resolutions.

relative to the second-order plane are distinguished. Moreover if trigger is selected with respect to the third-order event-plane, all the relations among different order event-planes have to be considered.

Assuming measured v_n with event-plane method to be from purely collective flow, we can estimate the pure flow backgrounds by running a Monte Carlo simulation with the experimental resolution of event-planes, and the strength of $\Psi_2 - \Psi_4$ correlation. The single hadron azimuthal distribution by pure collective flow can be described by a superposition of $v_n(n = 2, 3, 4)$ as

$$\frac{dN}{d\phi} = 1 + 2v_2 \cos 2(\phi - \Psi_2) + 2v_3 \cos 3(\phi - \Psi_3) + 2v_4 \cos 4(\phi - \Psi_4), \tag{3.55}$$

where ϕ denotes the azimuthal direction of an emitted hadrons, Ψ_n is a true n th-order event-plane $[-\pi/n, \pi/n]$.

For Ψ_2 and Ψ_3, they are generated randomly in this simulation with an assumption that Ψ_2 and Ψ_3 are uncorrelated. The experimental event-plane is obtained by adding a dispersion term $\Delta\Psi_n$ to Ψ_n^{real} as $\Psi_n^{obs} = \Psi_n^{real} + \Delta\Psi_n$ in this simulations. The parameter χ of Eq.(3.39) as a function of centrality, tuned to reproduce the event-plane resolutions, is shown in Fig.3.6. Then the tuned χ parameter is put into Eq.(3.38) to determine the distribution of relative angle $\Delta\Psi_n$ between Ψ_n^{obs} and Ψ_n^{real} as shown in Fig.3.7 for Ψ_2 dependent case varying χ as explanatory. In this event-plane oriented correlation measurements, we used the event-planes and its resolution determined by all the segments of RXN detector.

The direction of Ψ_4 is generated with a consideration of the correlation between Ψ_2 and Ψ_4

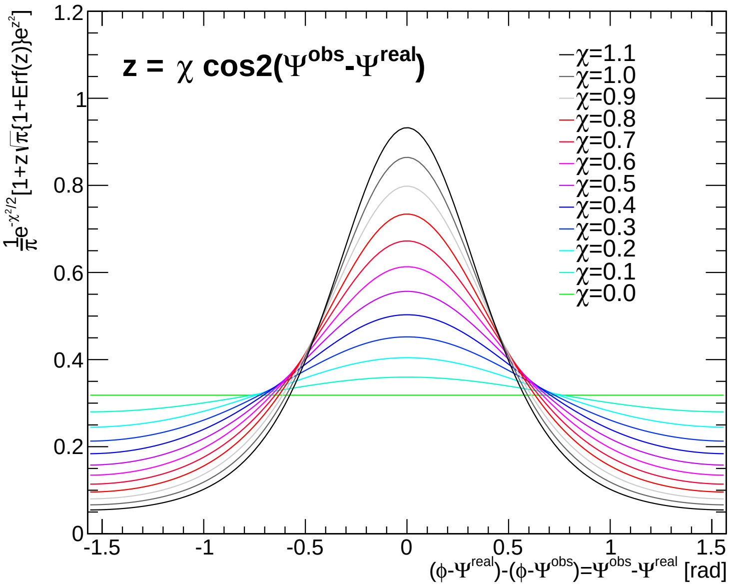

Figure 3.7: Probability distribution vs $\Psi_n^{obs} - \Psi_n^{real}$ at $n = 2$ varying the value of χ.

defined by $< \cos 4(\Psi_4 - \Psi_2) >$, which is determined by the ratio of $v_4\{\Psi_2\}$ and $v_4\{\Psi_4\}$ as

$$\begin{aligned} v_4\{\Psi_2\} &= \langle \cos 4\left[(\phi - \Psi_4) + (\Psi_4 - \Psi_2)\right] \rangle \\ &= \langle \cos 4(\phi - \Psi_4) \rangle \langle \cos 4(\Psi_4 - \Psi_2) \rangle \\ &= v_4\{\Psi_4\} \langle \cos 4(\Psi_4 - \Psi_2) \rangle , \end{aligned}$$

then we have

$$\langle \cos 4(\Psi_4 - \Psi_2) \rangle = v_4\{\Psi_2\}/v_4\{\Psi_4\}. \tag{3.56}$$

The strength of correlation $< \cos 4(\Psi_4 - \Psi_2) >$ is again converted into the χ_{42} parameter with a modified formula based on Eq.(3.39) as

$$\left\langle \cos\left[4(\Psi_4^{real} - \Psi_2^{real})\right] \right\rangle = \frac{\sqrt{\pi}}{2\sqrt{2}} \chi_{42} e^{-\chi_{42}^2/4} \left[I_0\left(\frac{\chi_{42}^2}{4}\right) + I_1\left(\frac{\chi_{42}^2}{4}\right) \right]. \tag{3.57}$$

The χ_{42} as a function of centrality is shown in Fig.3.8, that are tuned to reproduce a ratio by Eq.(3.56) at p_T 2-4, 1-2 GeV/c. The average of the χ_{42} at two different p_T is also plotted in Fig.3.8. Black dashed curves indicate the systematic uncertainties from $v_4\{\Psi_4\}$ and $v_4\{\Psi_2\}$, and grey band indicates the systematics only from $v_4\{\Psi_2\}$. We only consider the systematic uncertainties of $v_4\{\Psi_2\}$ on that of χ_{42}. Because that of $v_4\{\Psi_4\}$ will be taken into account as systematics of input v_n amplitudes. We use the averaged χ_{42} value between p_T:2-4 and 1-2 GeV/c for event-plane dependent correlations of p_T:2-4x1-2, 2-4x2-4, and 4-10x2-4 GeV/c, because v_n *i.e.* $\langle \cos 4(\Psi_4 - \Psi_2) \rangle = v_4\{\Psi_2\}/v_4\{\Psi_4\}$ would contain the auto-correlation by jets at high p_T.

We introduced a dispersion term $\Delta\Psi_{42}$ between Ψ_2 and Ψ_4, as done in Ψ_n case, using an analytical formula defined by Eq.(3.38) at $n = 4$. The direction Ψ_4^{true} is reconstructed as $\Psi_4^{true} =$

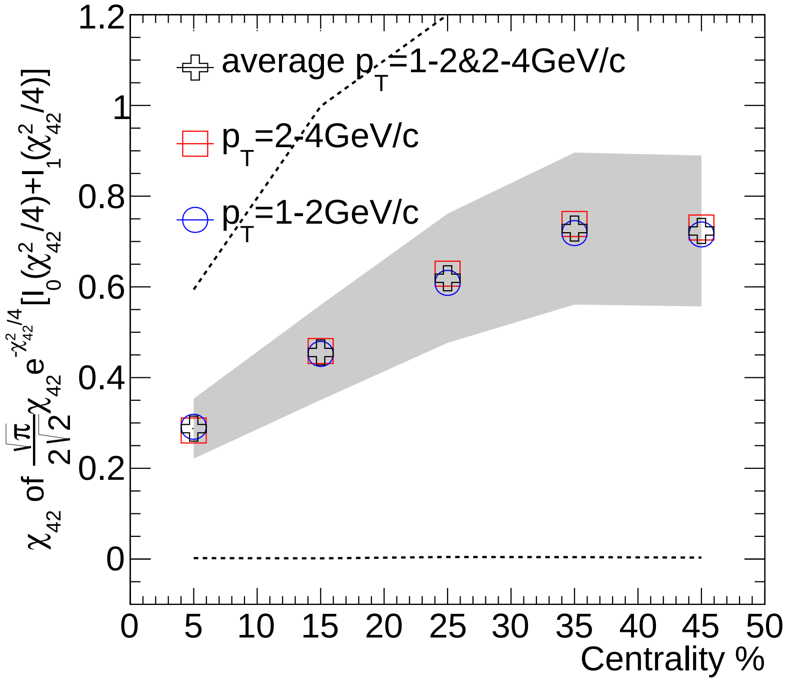

Figure 3.8: χ_{42} parameters tuned to reconstruct $\langle\cos 4(\Psi_4 - \Psi_2)\rangle = v_4\{\Psi_2\}/v_4\{\Psi_4\}$ at p_T (Blue) 1-2 GeV/c, (Red) 2-4 GeV/c, and (Black) its average.

Table 3.6: Summary of Pure Flow Simulations.

Variables	Simulation inputs
v_n	measured higher-order flow harmonics
Ψ_n resolution	Resolution Fig.3.3 reconstructed by Eq.(3.38)
$\langle\cos 4(\Psi_4 - \Psi_2)\rangle$	$v_4\{\Psi_2\}/v_4\{\Psi_4\}$ reconstructed by Eq.(3.38)
$\langle\cos 6(\Psi_3 - \Psi_2)\rangle$	$\langle\cos 6(\Psi_3 - \Psi_2)\rangle = 0$
$\phi^t - \Psi_n$	[-π/n,π/n] 8 bins

$\Psi_2^{true} + \Delta\Psi_{42}$, and the direction Ψ_4^{obs} is reconstructed as $\Psi_4^{obs} = \Psi_2^{true} + \Delta\Psi_{42} + \Delta\Psi_4$. The quantities taken into account in this simulations is summarized in Tab3.6.

The results of experimental correlations and pure flow simulation are presented in Fig.3.9 and 3.10, where pure flow distributions are scaled by the ZYAM method introduced in the following section. Since experimental data includes the contributions from back-to-back jets they have enhance at $\Delta\phi = 0$ and π compared to pure flow distribution, however pure flow distributions succeeded to reconstruct the experimental correlations shape except such region.

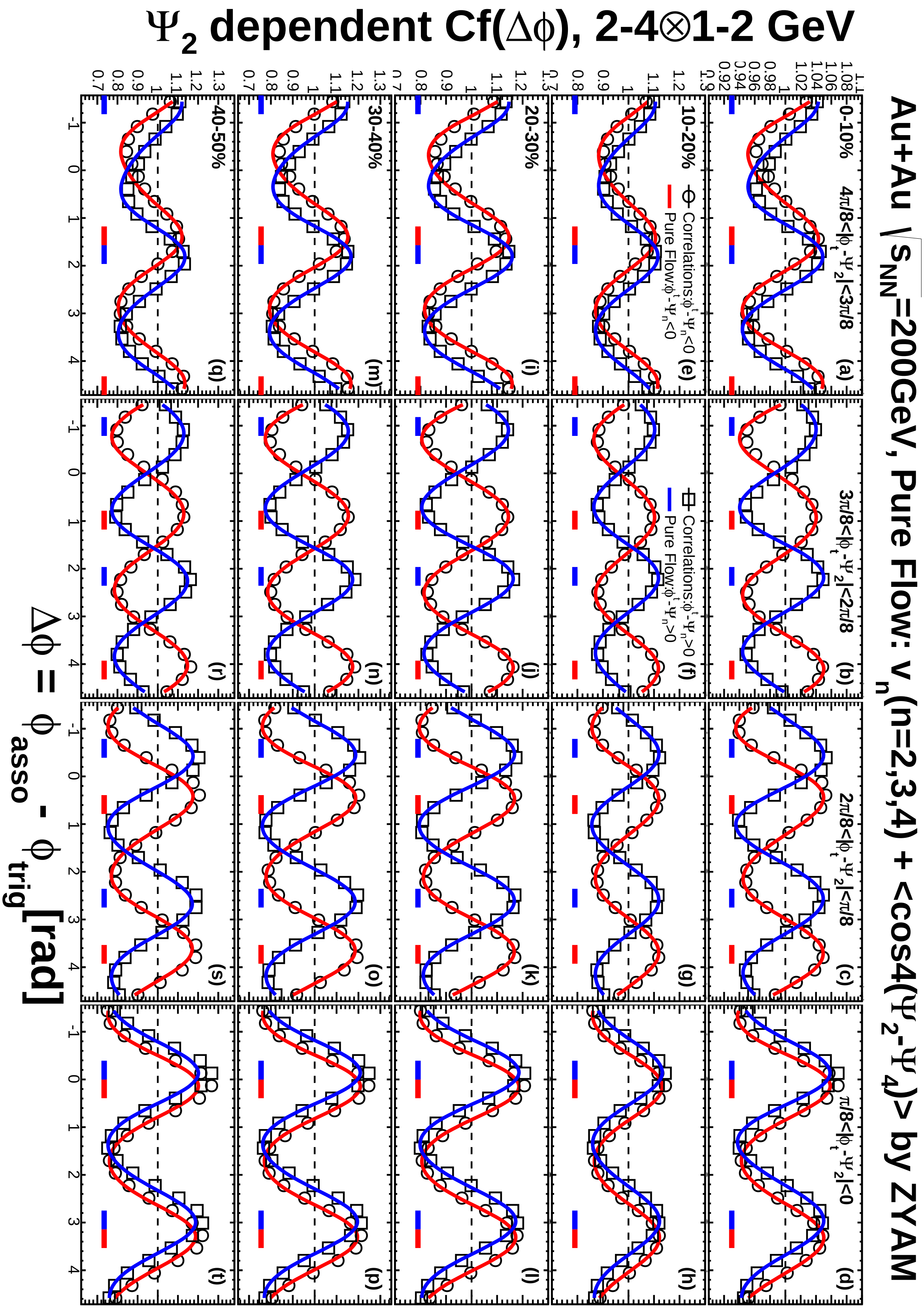

Figure 3.9: Experimental two-particle correlations and pure flow distributions by the Monte Carlo Simulation with respect to Ψ_2 in various centrality selections.

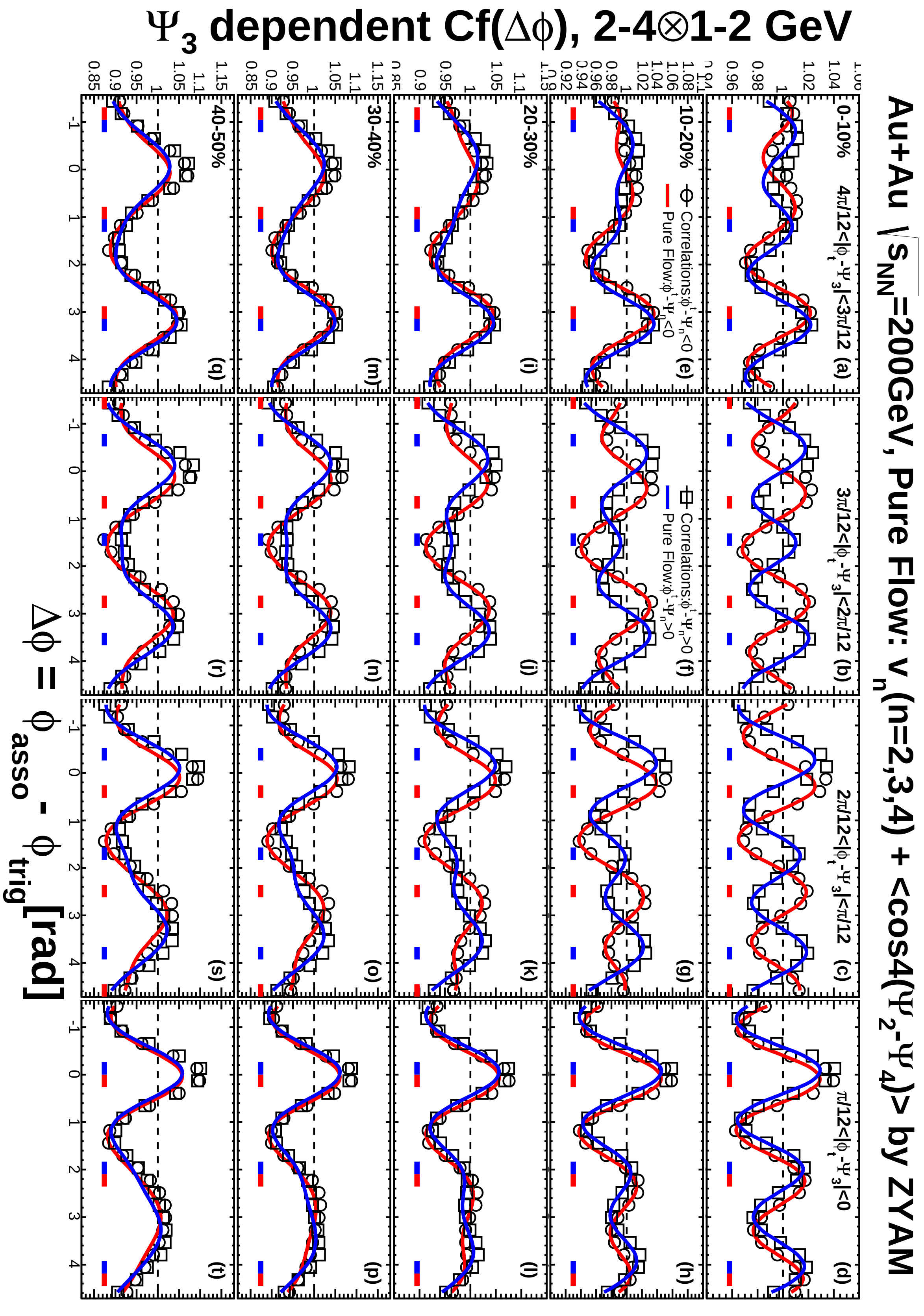

Figure 3.10: Experimental two-particle correlations and pure flow distributions by the Monte Carlo Simulation with respect to Ψ_3 in various centrality selections.

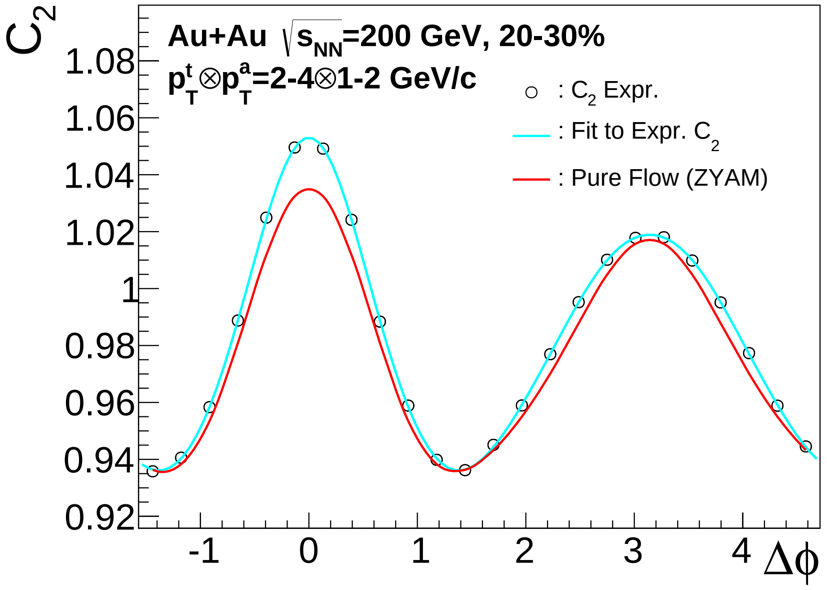

Figure 3.11: Experimental two-particle correlations C_2, fitting to experimental data, and pure flow distribution scaled by the ZYAM assumption at centrality 20-30% at $p_T^t \otimes p_T^a = 2-4 \otimes 1-2$ GeV/c.

3.5.3 Flow Contribution Subtractions

The ZYAM assumption is employed in the determination of background levels b_0 in the background subtractions as formulated in

$$j(\Delta\phi) = C(\Delta\phi) - b_0 \left[1 + \sum_{n=2}^{4} 2 v_n^t v_n^a \cos(n\Delta\phi) \right], \tag{3.58}$$

where $j(\Delta\phi)$ is a flow subtracted two-particle correlations. The ZYAN assumption requires that the minimum value in a correlations to be 0 after the flow background subtractions. To prevent the statistical fluctuation of measured correlations affecting the determination of ZYAM levels, we applied a Fourier fitting to measured experimental data, then the background levels are determined by the fitting results and pure flow distributions as Fig.3.11 shows the example in Au+Au 20-30% at p_T: 2-4x1-2 GeV/c. Usually, the b_0 value depends on centrality, p_T ranges of trigger and associate particles. For event-plane dependent correlations, we also used a single background level determined by the inclusive trigger correlations.

3.5.4 Pair Yield per Trigger Particle

The flow subtracted two-particle correlations are normalized into pair yield per trigger particle (PTY) defined as

$$\frac{1}{N^t} \frac{dN^{ta}}{d\Delta\phi} = \frac{1}{2\pi\varepsilon} \frac{N^{ta}}{N^t} j(\Delta\phi), \tag{3.59}$$

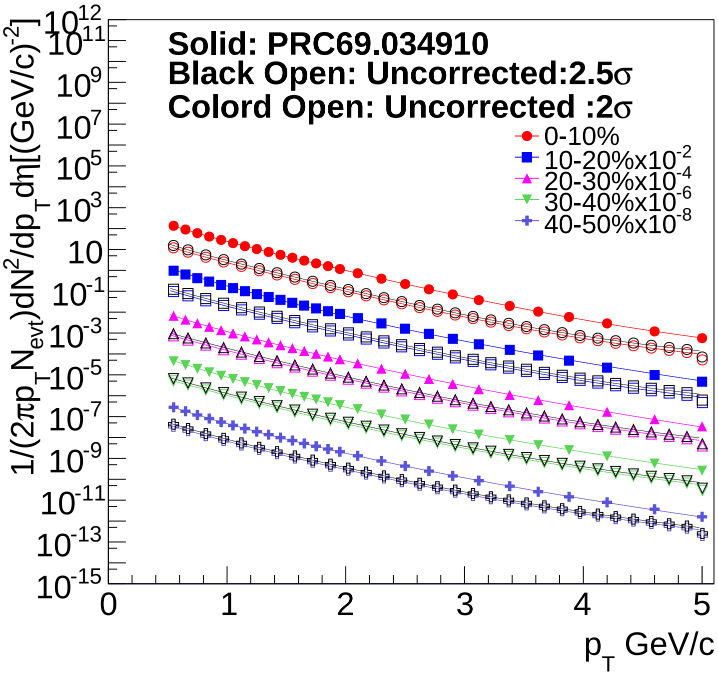

Figure 3.12: Invariant yield of charged hadrons (Solid) with full acceptance and tracking efficiency correction [50] and (Open) without corrections measured in this analysis.

where N^t is a number of trigger particles, N^{ta} is a number of pairs, and $j(\Delta\phi)$ is a flow subtracted two-particle correlations introduced in Eq.(3.58), and ε is a tracking efficiency of particle at an associate p_T range. The tracking efficiency of trigger particles are canceled out by the ratio of N^{ta}/N^t, thus only the efficiency of associate particle has to be corrected.

The tracking efficiency as functions of centrality and p_T is determined by taking ratio of the invariant cross sections $\sigma^{corr.}$ with effects by acceptance and detector fully corrected[50], over those $\sigma^{uncor.}$ in this analysis where such kind of effects are not corrected. The invariant yields are fitted by this formula as a function of p_T in each centrality bins at p_T:0.5-5.0 GeV/c

$$F(p_T) = c_0 * \left(\frac{c_1}{c_1 + p_T}\right)^{c_2}, \tag{3.60}$$

where c_0, c_1, and c_2 are free parameters. The p_T range covers the average p_T of particles at 4-10 GeV/c. The ratios of those invariant yields are calculated via the ratio of fitting functions at the mean of each p_T ranges. The results are tabulated in Tab.3.7.

3.5.5 Unfolding of Trigger Smearing Effect by Iteration Method

Pair yield per trigger with respect to event-plane is smeared by neighboring trigger bins due to limited experimental resolution of event-planes. The smearing effect has to be unfolded to discuss the real event-plane dependence of correlations.

We unfold this effect using the raw per trigger yield and estimated trigger smearing effects in an iterative calculation. The detail is given below.

Table 3.7: Tracking Efficiency of Charged Hadrons

Efficiency Summary								
	p_T [GeV/c]							
	2.0σ matching				2.5σ matching			
Centrality	0.5 - 1.0	1.0 - 2.0	2.0 - 4.0	4.0 - 10	0.5 - 1.0	1.0 - 2.0	2.0 - 4.0	4.0 - 10
0-10%	0.0909	0.0982	0.1038	0.1465	0.1174	0.1262	0.1324	0.1991
10-20%	0.0958	0.1185	0.1328	0.1453	0.1224	0.1507	0.1678	0.1896
20-30%	0.1162	0.1305	0.1420	0.1870	0.1480	0.1664	0.1766	0.2374
30-40%	0.1171	0.1469	0.1616	0.1712	0.1473	0.1828	0.2032	0.2163
40-50%	0.1320	0.1523	0.1672	0.2110	0.1661	0.1909	0.2088	0.2650

Writing per trigger yield as a function of trigger direction $\phi^s = \phi^t - \Psi_n$ and azimuthal angle $\Delta\phi = \phi^a - \phi^t$ as $Y(\phi_s, \Delta\phi)$, we introduce a constant offset $O = 1$ to the per trigger yield as $A(\phi_s, \Delta\phi) = Y(\phi_s, \Delta\phi) + O$ to prevent treating small value around 0 to avoid divergence of calculations in the unfolding. Such a care is necessary, because Y is the value where flow contribution is subtracted in ZYAM assumption. The ϕ_s is divided into 8 bins, those width are $\pi/8$ [rad] in Ψ_2 dependent correlations and $\pi/12$ [rad] in Ψ_3 dependent correlations. The $\Delta\phi$ is divided into 24 bins. Since in this procedure we use matrix calculations, we re-write ϕ_s as $i = 0, -, 7$ and $\Delta\phi$ as $k = 0, -, 23$ as indexes of ϕ_s and $\Delta\phi$ for simplicity. We summarize $A(i, k)$ into a vector $\mathbf{A}(k)$ at a given k as

$$\mathbf{A}(k) = \begin{pmatrix} A(0,k) \\ A(1,k) \\ A(2,k) \\ A(3,k) \\ A(4,k) \\ A(5,k) \\ A(6,k) \\ A(7,k) \end{pmatrix}, \tag{3.61}$$

The event-plane resolution is converted to a parameter χ and the distribution of the difference between real event-plane Ψ_n^{real} and measured event-plane Ψ_n^{obs} can be estimated by Eq.(3.38) using the calculated χ as done in the pure flow Monte Carlo simulation. The angle between Ψ_n^{real} and Ψ_n^{obs} can be easily translated into the difference between real and observed trigger angle from event-plane as $\Psi_n^{real} - \Psi_n^{obs} = (\phi^t - \Psi_n^{real}) - (\phi^t - \Psi_n^{obs})$. Fig.3.13 again shows the probability distribution vs $\Psi_n^{real} - \Psi_n^{obs} = (\phi^t - \Psi_n^{real}) - (\phi^t - \Psi_n^{obs})$. As one can see, the distribution has a peak with finite width depending on χ.

The degree of the contamination by neighboring trigger bin can be estimated by the probability distribution and the width of a trigger bin ϕ_s. Then we can introduce a smearing matrix

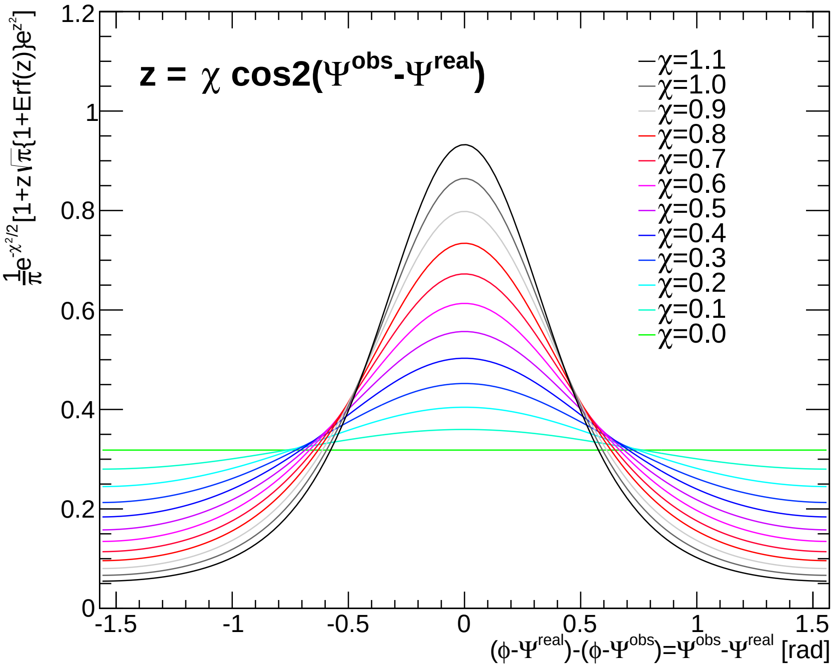

Figure 3.13: $\Delta\phi$-Δz correlations in (Left) PC1 and (Right) PC3 after pair selection in PC1.

$\mathbf{S}(\mathbf{k})$ as

$$S = \begin{pmatrix} s_0 & s_1 & s_2 & s_3 & s_4 & s_3 & s_2 & s_1 \\ s_1 & s_0 & s_1 & s_2 & s_3 & s_4 & s_3 & s_2 \\ s_2 & s_1 & s_0 & s_1 & s_2 & s_3 & s_4 & s_3 \\ s_3 & s_2 & s_1 & s_0 & s_1 & s_2 & s_3 & s_4 \\ s_4 & s_3 & s_2 & s_1 & s_0 & s_1 & s_2 & s_3 \\ s_3 & s_4 & s_3 & s_2 & s_1 & s_0 & s_1 & s_2 \\ s_2 & s_3 & s_4 & s_3 & s_2 & s_1 & s_0 & s_1 \\ s_1 & s_2 & s_3 & s_4 & s_3 & s_2 & s_1 & s_0 \end{pmatrix}, \tag{3.62}$$

where s_n is a contamination from the n trigger bins away from a certain bin, thus $\sum s_n = 1$. s_0 means the fraction of the true signal in a selected trigger bin. Due to the cyclic boundary condition in azimuthal direction, we have $s_5 = s_3$, $s_6 = s_2$, and $s_7 = s_1$.

The vector of smeared correlations $\mathbf{B}(k)$ can be written as the product of $\mathbf{S}(k)$ and $\mathbf{A}(k)$ as

$$\mathbf{B}(k) \quad = \mathbf{S}(k)\mathbf{A}(k). \tag{3.63}$$

We introduce an effective correction matrix $\mathbf{C}(k)$, and its diagonal elements c_{ii} is defined by the ratio of vector elements of original and smeared correlations as

$$c_{ii} \quad = A(i,k)/B(i,k). \tag{3.64}$$

The off-diagonal elements are defined as $c_{ij}(i \neq j) = 0$ since the trigger smearing effect is considered only by the smearing matrix in this study.

Then, we can obtain corrected correlation vector $\mathbf{A^{cor}}(k)$ as

$$\mathbf{A^{cor}}(k) = \mathbf{C}(k)\mathbf{A}(k). \tag{3.65}$$

However in this method, the start point $\mathbf{A}(k)$ are not the real correlation but the experimental results which have been already smeared once by the experimental resolution. We iterate this procedure until the correction factor converges.

In the iteration loop, we re-write $\mathbf{A}$, $\mathbf{B}$, $\mathbf{S}$, and $\mathbf{C}$ as $\mathbf{A^{(1)}}$, $\mathbf{B^{(1)}}$, $\mathbf{S^{(1)}}$, and $\mathbf{C^{(1)}}$ in the first loop. Then we define those vectors and matrixes in the n th loop as following

$$\mathbf{A^{(n)}}(k) = \mathbf{C^{(n-1)}}(k)\mathbf{A^{(1)}}(k), \tag{3.66}$$

$$\mathbf{B^{(n)}}(k) = \mathbf{S}(k)\mathbf{A^{(n)}}(k), \tag{3.67}$$

and the elements of $\mathbf{C^{(n)}}$ become

$$c_{ii}^{(n)} \;=\; A^{(n)}(i,j)/B^{(n)}(i,j), \tag{3.68}$$

$$c_{ij(i\neq j)}^{(n)} \;=\; 0. \tag{3.69}$$

The correction matrix $\mathbf{C^{(n)}}(k)$ needs a smoothing among neighboring k indexes *i.e.* $\Delta\phi$ bins before an iteration moves to next loop, because the correction matrix $\mathbf{C^{(n)}}(k)$ directly reflects the statistical fluctuation of per trigger yields. Repeating iteration without smoothing results in the divergence of fluctuations among $\Delta\phi$ bins. We introduce following smoothing procedure using neighboring correction factors in the k direction, with smoothing factor $r < 0.5$ as

$$c_{ii}^{(n)}(k) = (1-2r)c_{ii}^{(n)}(k) + rc_{ii}^{(n)}(k-1) + rc_{ii}^{(n)}(k+1). \tag{3.70}$$

The next loop starts by getting $\mathbf{A^{(n+1)}}(k) = \mathbf{C^{(n)}}(k)\mathbf{A^{(1)}}(k)$ using smoothed correction factor. The iteration is repeated up to $n = 300$ and $A^{(300)} - O$ is treated as unfolded per trigger yield in this analysis modulo convergence of each values. The summary of this method is given in Fig.3.14 and the explanatory example is presented in Fig.3.15.

3.5.6 Unfolding of Trigger Smearing Effect by Fitting Method

Assuming the per trigger yield of associate particles are distributed with respect to event-plane, we can correct the effect of trigger smearing effect due to limited event-plane resolution in analogous to the resolution correction in the flow measurements of single particles. The azimuthal angle of per trigger yields with respect to Ψ_2 at a given $\Delta\phi$ can be written as

$$\begin{aligned}\frac{dN^{1+PTY}}{d(\phi^a-\Psi_2)} &= 1+Y(\phi_s,\Delta\phi)\\ &= 1+2v_2^Y\cos 2(\phi_s+\Delta\phi)+2v_4^Y\cos 4(\phi_s+\Delta\phi),\end{aligned} \tag{3.71}$$

and similarly with respect to Ψ_3 as

$$\begin{aligned}\frac{dN^{1+PTY}}{d(\phi^a-\Psi_3)} &= 1+Y(\phi_s,\Delta\phi)\\ &= 1+2v_3^Y\cos 3(\phi_s+\Delta\phi).\end{aligned} \tag{3.72}$$

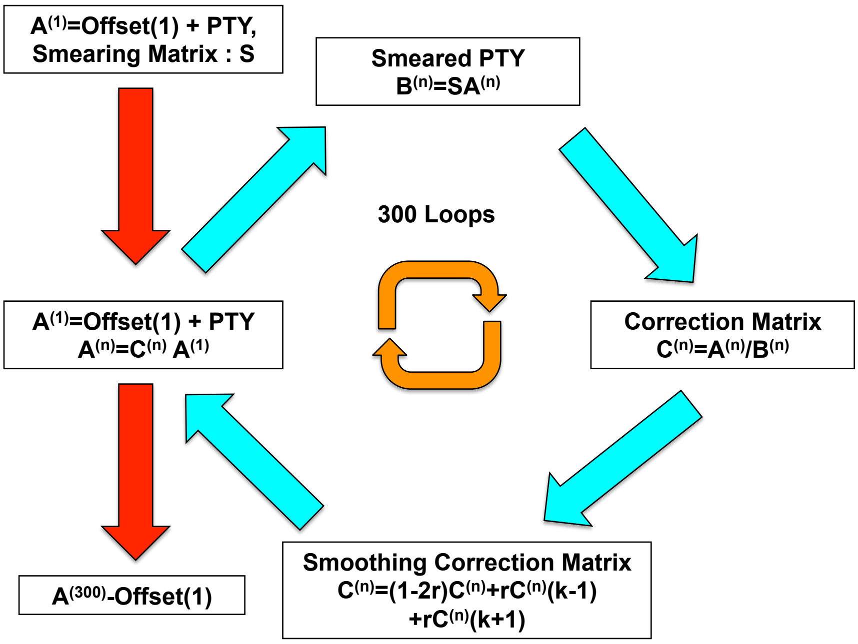

Figure 3.14: Flow chart of the Iteration Method of Unfolding.

where $Y(\phi_s, \Delta\phi)$ is the per trigger yield before unfolding, $\phi_s = \phi^t - \Psi_{2,3}$, $\Delta\phi = \phi^a - \phi^t$ and $v^Y_{2,3,4}$ is a azimuthal anisotropy of per trigger yield. In these distributions, the associate angle from event-plane is characterized by the sum of ϕ_s and $\Delta\phi$ as $\phi_s + \Delta\phi = \phi^a - \Psi_{2,3}$.

Applying a Fourier fitting to $1 + Y(\phi_s, \Delta\phi)$ as a function of ϕ_s with a phase shift $\Delta\phi$, we can determine the anisotropy parameter $v^Y_{2,3,4}$ and can correct the azimuthal distributions using the v^Y_n corrected by the event-plane resolution as

$$\frac{dN^{1+PTY}_{cor}}{d(\phi^a - \Psi_2)} = 1 + 2v^Y_2/\sigma_2 \cos 2(\phi_s + \Delta\phi) + 2v^Y_4/\sigma_{42} \cos 4(\phi_s + \Delta\phi), \tag{3.73}$$

and

$$\frac{dN^{1+PTY}}{d(\phi^a - \Psi_3)} = 1 + 2v^Y_3/\sigma_3 \cos 3(\phi_s + \Delta\phi). \tag{3.74}$$

The ratio of the uncorrected and corrected azimuthal distributions of per trigger yields can be used as a correction coefficient of the per trigger yield with respect to Ψ_2 as

$$\begin{aligned} 1 + Y^{cor}(\phi_s, \Delta\phi) &= \frac{1 + 2v^Y_2 \cos 2(\phi_s + \Delta\phi)/\sigma_2 + 2v^Y_4 \cos 4(\phi_s + \Delta\phi)/\sigma_{42}}{1 + 2v^Y_2 \cos 2(\phi_s + \Delta\phi) + 2v^Y_4 \cos 4(\phi_s + \Delta\phi)} \\ &\times \ (1 + Y^{raw}(\phi_s, \Delta\phi)), \end{aligned} \tag{3.75}$$

$$\begin{aligned} Y^{cor}(\phi_s, \Delta\phi) &= \frac{1 + 2v^Y_2 \cos 2(\phi_s + \Delta\phi)/\sigma_2 + 2v^Y_4 \cos 4(\phi_s + \Delta\phi)/\sigma_{42}}{1 + 2v^Y_2 \cos 2(\phi_s + \Delta\phi) + 2v^Y_4 \cos 4(\phi_s + \Delta\phi)} \\ &\times \ (1 + Y^{raw}(\phi_s, \Delta\phi)) - 1, \end{aligned} \tag{3.76}$$

and similarly with respect to Ψ_3 as

$$1 + Y^{cor}(\phi_s, \Delta\phi) = \frac{1 + 2v^Y_3/\sigma_3 \cos 3(\phi + \Delta\phi)}{1 + 2v^Y_3 \cos 3(\phi + \Delta\phi)}(1 + Y^{raw}(\phi_s, \Delta\phi)), \tag{3.77}$$

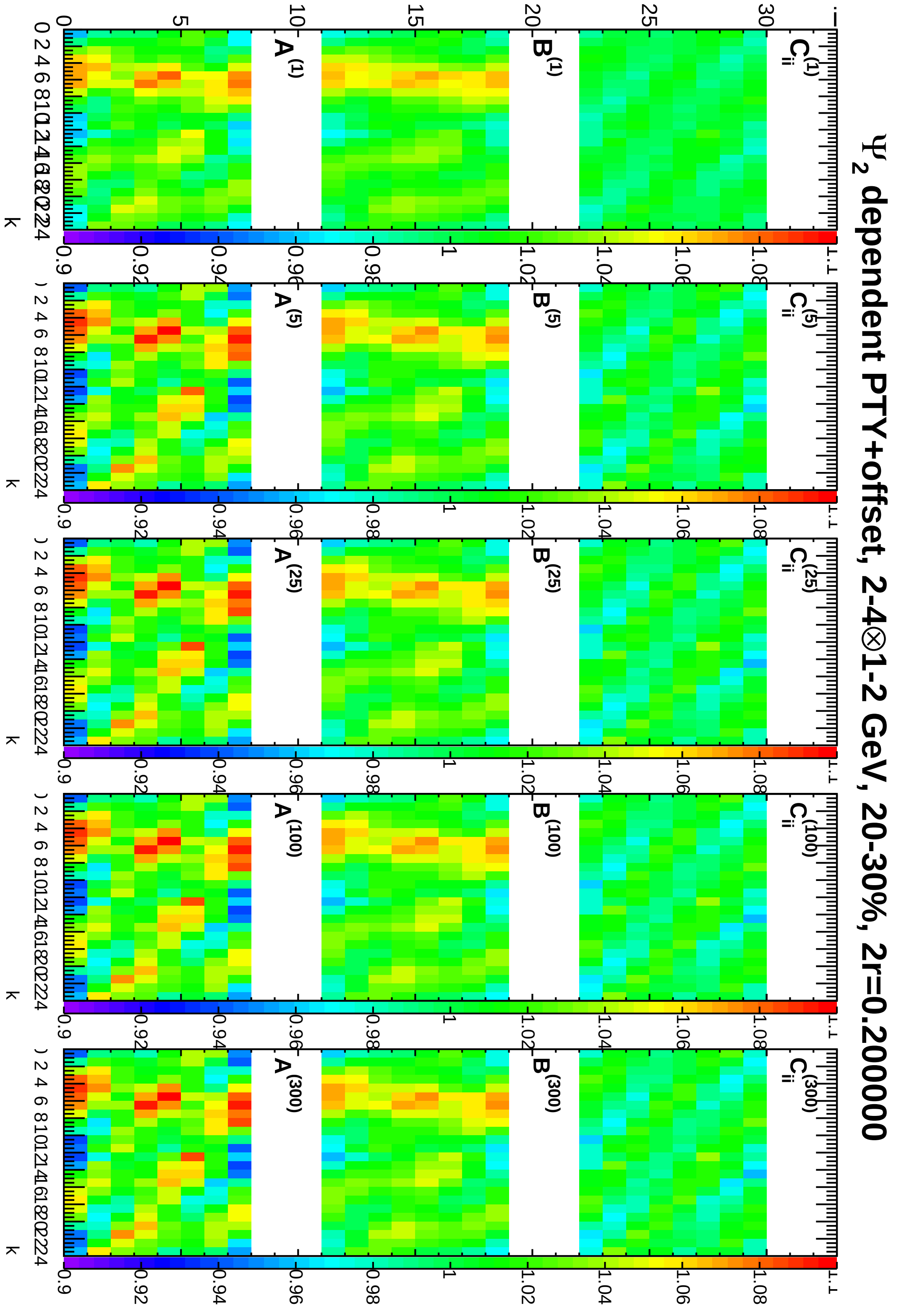

Figure 3.15: **A**, **B**, and the diagonal elements of correction matrix **C** in two-particle correlations with respect to Ψ_2 at centrality 20-30%.

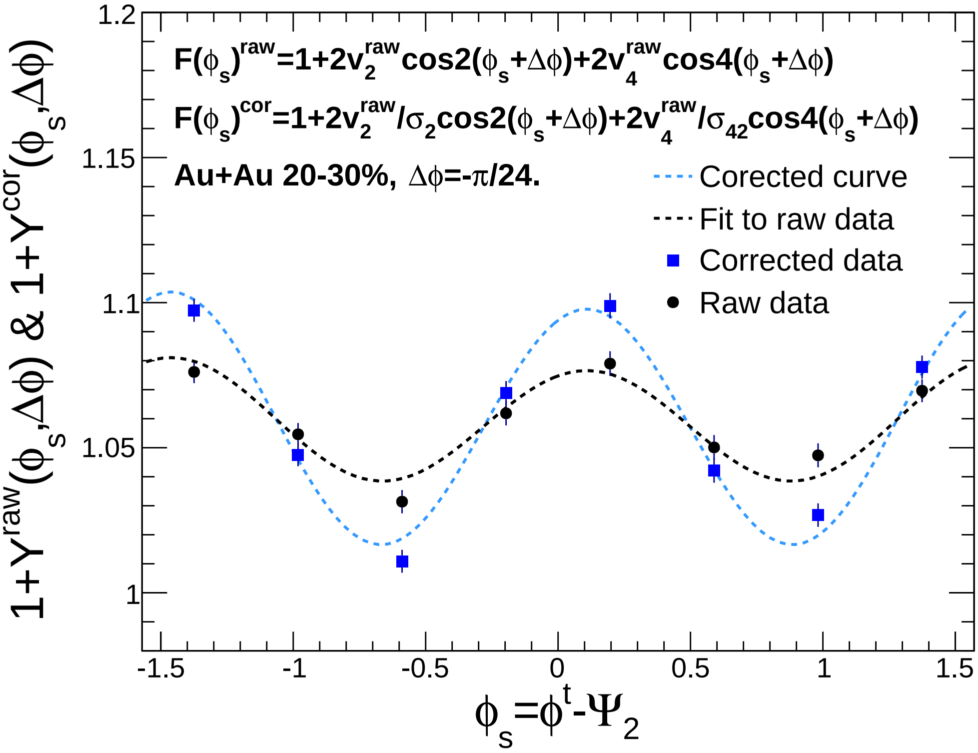

Figure 3.16: Measured per trigger yield as a function of $\phi_s = \phi^t - \Psi_2$ in centrality 20-30% at $\Delta\phi = -\pi/24$. (Black) raw data points. (Blue) Corrected data points. (Black dashed curve) fitting to raw data. (Blue dashed curve) Corrected curve.

$$Y^{cor}(\phi_s, \Delta\phi) = \frac{1 + 2v_3^Y/\sigma_3 \cos 3(\phi + \Delta\phi)}{1 + 2v_3^Y \cos 3(\phi + \Delta\phi)}(1 + Y^{raw}(\phi_s, \Delta\phi)) - 1. \qquad (3.78)$$

Fig.3.16 shows the unfolding procedure by fitting. The raw $1+Y(\phi_s, \Delta\phi)$ is fitted by Fourier series and the resolution corrected curve is calculated. The corrected data points are determined using the ratio of corrected and uncorrected curves, then unfolded per trigger yields are obtained by subtracting 1 from the corrected per trigger yield.

3.6 Systematic Uncertainties in Flow Harmonics

The sources of systematic uncertainties of v_n measurements considered in this analysis are itemized as following,

- Systematic difference of v_n depending on RXN segments,
- Effect of matching cut width of central arm track,
- Effect of rapidity dependence, the difference of v_n between RXN and BBC event-planes.

Fig. 3.17 shows the higher-order flow harmonics v_n measured by the nine different combinations of RXN segments, that are South-Inner, South-Outer, South-all, North-Inner, North-Outer, North-all, S+N-Inner, S+N-Outer, and S+N-all. The averaged v_n values of these 9 combinations of RXN segments are used as main data point. The systematic uncertainties in RXN detector σ_{RXN} is defined by the standard deviation of v_n as

$$\sigma_{RXN} = \sqrt{\sum_{i}^{9}(v_{n,i} - v_n^{avg})^2/9}. \tag{3.79}$$

Fig. 3.18 shows the v_n measured with tracks having matching cut 2σ and 2.5σ. The v_n with 2σ matching cut is used as main data point. The systematic uncertainties on matching cut σ_{Mat} is defined by the absolute value of the difference between these two v_n as

$$\sigma_{Mat} = \left|v_n^{2\sigma} - v_n^{2.5\sigma}\right|. \tag{3.80}$$

Fig. 3.19 shows the v_n measured with event planes determined by RXN and BBC. The v_n with RXN event plane is used as main data point. The systematic uncertainties on rapidity gap between particle and event-plane σ_{Rap} is defined by the absolute value of the difference between these two v_n as

$$\sigma_{Rap} = \left|v_n^{RXN} - v_n^{BBC}\right|. \tag{3.81}$$

The total systematic uncertainties are the quadrature sum of these individual systematics as

$$\sigma^{all} = \sqrt{\sigma_{RXN}^2 + \sigma_{Mat}^2 + \sigma_{Rap}^2}, \tag{3.82}$$

the results are shown in Fig.3.20. The percentile ratio of total systematic uncertainties over flow harmonics σ^{all}/v_n is presented in Tab.3.8 for four p_T selections.

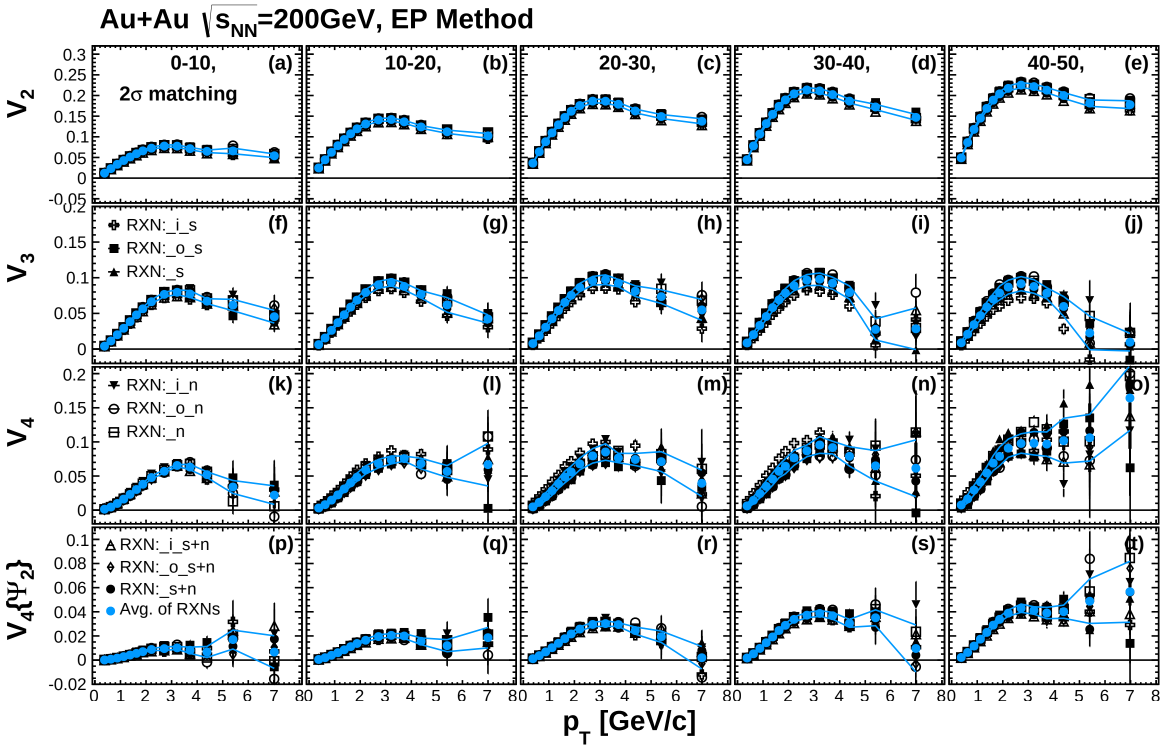

Figure 3.17: Higher-order flow harmonics v_n as a function of p_T measured by (Black) various RXN module combinations, and (Blue) the average of results, and (Blue line) systematics defined by the standard deviation of the 9 results.

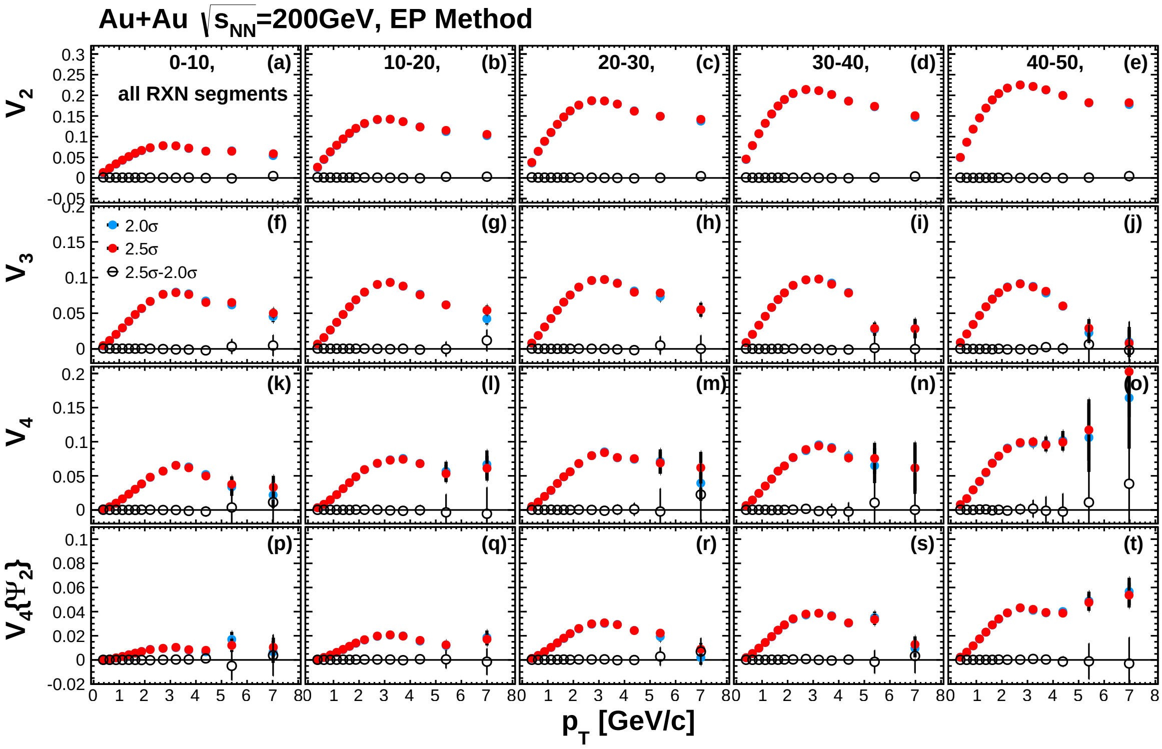

Figure 3.18: Higher-order flow harmonics v_n as a function of p_T measured with all RXN modules in (Blue) 2σ matching width, (Red) 2.5σ matching width, and (Black) difference between 2σ and 2.5σ results.

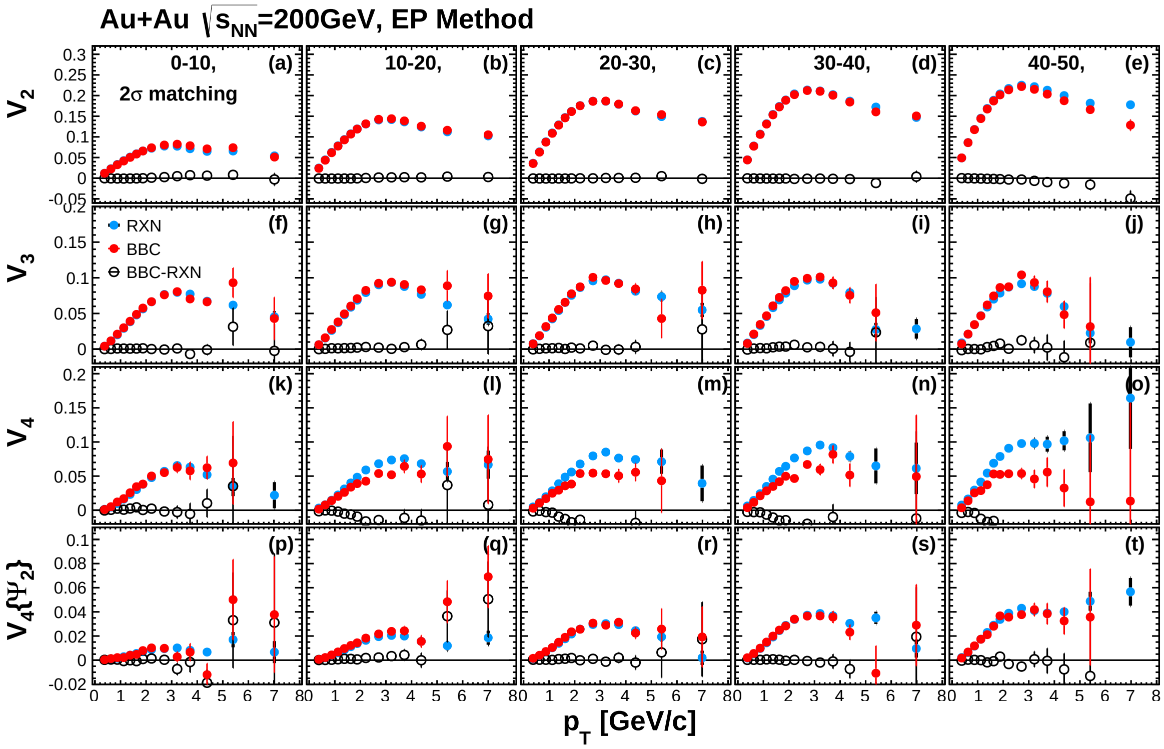

Figure 3.19: Higher-order flow harmonics v_n as a function of p_T measured with in (Blue) RXN, (Red) BBC, and (Black) difference between RXN and BBC results.

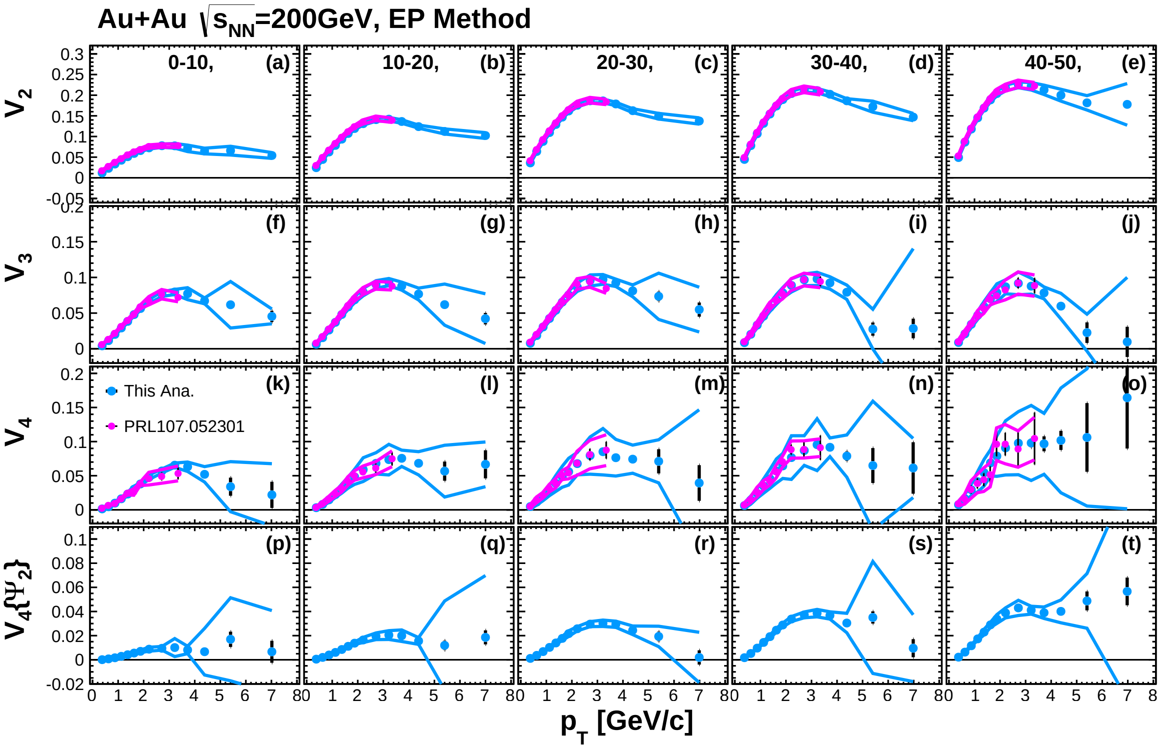

Figure 3.20: Higher-order flow harmonics v_n as a function of p_T measured (Blue) in this analysis with systematics defined by the quadrature sum of systematics in matching cut RXN-BBC difference, and rms of results using RXNs. (Purple) v_n measured by the PHENIX [22].

Table 3.8: Summary of percentile ratio of v_n systematic uncertainties

Centrality %	p_T GeV/c	v_2 sys. %	v_3 sys. %	v_4 sys. %	$v_4\{\Psi_2\}$ sys. %
0-10	0.5-1.0	5.449	6.387	24.87	48
	1.0-2.0	4.32	4.911	10.1	14.66
	2.0-4.0	4.536	4.131	4.412	11.39
	4.0-10.0	10.43	6.184	21.67	191.3
10-20	0.5-1.0	3.658	7.992	28.53	12.17
	1.0-2.0	2.891	6.431	20.16	12.27
	2.0-4.0	2.69	6.163	27.64	13.72
	4.0-10.0	3.124	13.62	19.09	32.09
20-30	0.5-1.0	2.811	9.469	35.48	9.633
	1.0-2.0	2.485	7.818	28.85	8.422
	2.0-4.0	2.391	6.822	28.03	6.577
	4.0-10.0	2.98	9.503	32.24	12.21
30-40	0.5-1.0	2.506	12.42	35.81	7.385
	1.0-2.0	2.462	9.695	29.88	6.509
	2.0-4.0	2.556	9.673	36.75	5.913
	4.0-10.0	2.934	14.18	44.32	31.73
40-50	0.5-1.0	2.575	13.8	32.96	6.338
	1.0-2.0	2.688	12.06	34.44	6.479
	2.0-4.0	3.224	11.7	45.4	10.71
	4.0-10.0	7.877	33.53	77.07	29.33

3.7 Systematic Uncertainties in Two-Particle Correlations

The systematic uncertainties on matching cut and the propagated from v_n systematics are considered in this section for inclusive and event-plane dependent correlations. For study of the effect of matching cut width, we compare correlations with 2σ tracks and those with 2.5σ tracks. In addition to these source of systematic uncertainties, for triggered correlations, systematic uncertainties of strength of Ψ_2–Ψ_4 correlations is also taken into account before the unfolding of the trigger smearing effect due to the limited event-plane resolution.

The systematics from v_n systematics σ_{v_n} after flow subtraction is defined by the RMS of per trigger yield using $v_n \pm 1.0\sigma (n = 2, 3, 4)$ with respect to centroid as

$$\sigma_{v_n} = \sqrt{\sum_k \{|Y^{v_k+}(\Delta\phi) - Y(\Delta\phi)|^2/6 + |Y^{v_k-}(\Delta\phi) - Y(\Delta\phi)|^2/6\}}, \tag{3.83}$$

where $Y^{v_n+}(\Delta\phi)$ is pair yield with flow subtraction using $v_n + 1\sigma$, $Y^{v_n-}(\Delta\phi)$ is that using $v_n - 1\sigma$, and $Y^{v_n}(\Delta\phi)$ is that using the centroid of v_n.

The systematics from matching cut width σ_{mat} after flow subtraction is defined as

$$\sigma_{mat} = |Y^{\sigma=2.5}(\Delta\phi) - Y^{\sigma=2.0}(\Delta\phi)|. \tag{3.84}$$

The total systematics σ_{all} in the inclusive trigger is defined as

$$\sigma_{all} = \sqrt{\sigma_{v_n}^2 + \sigma_{mat}}. \tag{3.85}$$

The additional systematics of the amplitude of χ_{42} in the event-plane dependent correlation is defined as

$$\sigma_{\chi_{42}} = \sqrt{|Y^{\chi_{42}+}(\Delta\phi) - Y(\Delta\phi)|^2/2 + |Y^{\chi_{42}-}(\Delta\phi) - Y(\Delta\phi)|^2/2}. \tag{3.86}$$

The total systematics of the event-plane dependent correlation is defined as

$$\sigma_{all} = \sqrt{\sigma_{v_n}^2 + \sigma_{mat}^2 + \sigma_{\chi_{42}}^2}. \tag{3.87}$$

For event plane dependent correlations, we tested two unfolding method as mentioned in the analysis part, i) Iteration method and ii) Fitting method. In each unfolding method, systematic uncertainties before unfolding are propagated by calculating the unfolded value of upper and lower boundary of systematics. After unfolding we add the difference between fitting and iteration $\sigma_{Met} = |Y^{Itr.} - Y^{Fit}|$ method and the difference between the smoothing factor 20% and 30% $\sigma_{Smo} = |Y^{2r=0.3} - Y^{2r=0.2}|$ of iteration method into total systematics in addition to original systematic uncertainties propagated by unfolding as a quadrature sum as

$$\sigma_{tot} = \sqrt{\left\{\sqrt{{\sigma_{vn}}^2 + {\sigma_{mat}}^2 + {\sigma_{\chi_{42}}}^2}\right\}^2_{unfolded} + {\sigma_{Met}}^2 + {\sigma_{Smo}}^2}. \tag{3.88}$$

The results with 20% smoothing factor is adopted as a main data point.

In this section, only representing explanatory plots are shown in Fig.3.21-3.27. Tab.3.9 summarizes all the items for the estimation of systematic uncertainties in the inclusive and event-plane dependent correlations in the “Appendix A”.

Table 3.9: Summary of plots on systematic uncertainties

Figure	Trigger	Source of Systematic Uncertainty
A.1–A.5	Inclusive	Matching cut width :2σ-2.5σ
A.6–A.10	Inclusive	Upper and Lower Boundary of v_n
A.11–A.16	$\Psi_{2,3}$ dependent	Matching cut width :2σ-2.5σ
A.17–A.46	$\Psi_{2,3}$ dependent	Upper and Lower Boundary of v_n
A.47–A.52	$\Psi_{2,3}$ dependent	Amplitude of χ_{42} from $v_4\{\Psi_2\}$
A.53–A.58	$\Psi_{2,3}$ dependent	Smoothing factor in iterative unfolding
A.59–A.64	$\Psi_{2,3}$ dependent	Difference between in fitting & iterative method

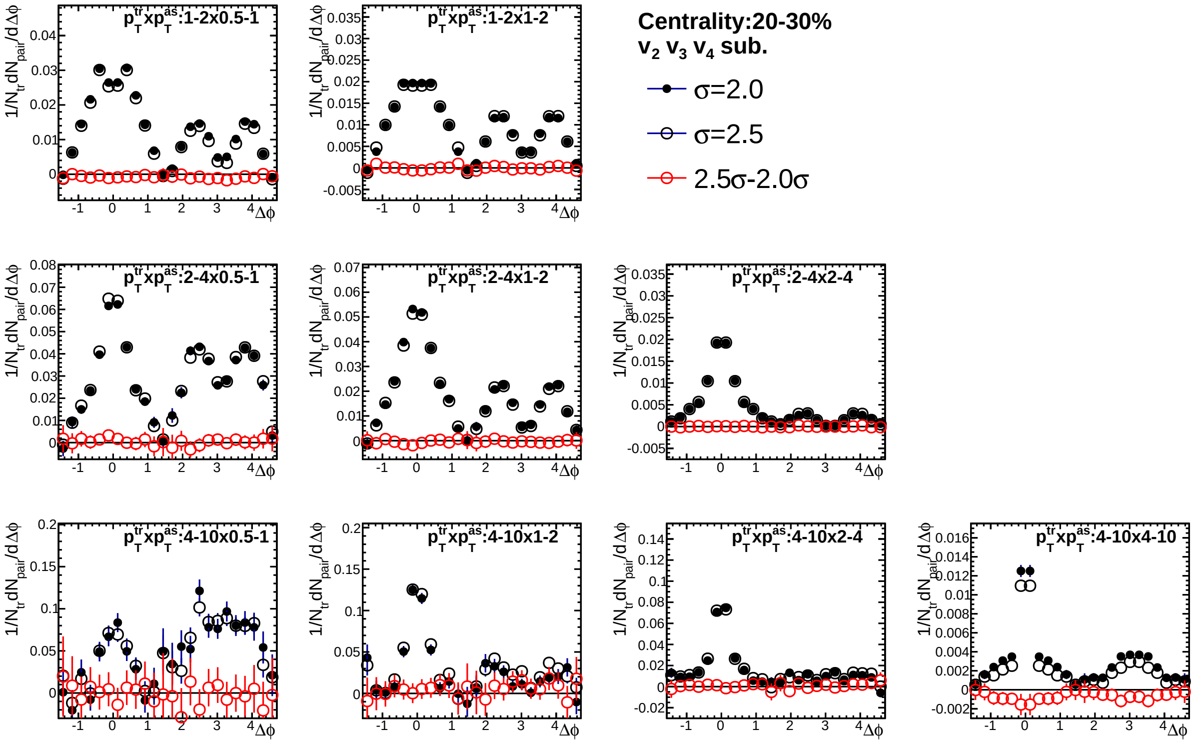

Figure 3.21: Correlations where contributions of v_2, v_3 and v_4 is subtracted in centrality 20-30% with (Solid-Black) 2σ matching cut, (Opened-Black) 2.5σ matching, and (Red) difference of those.

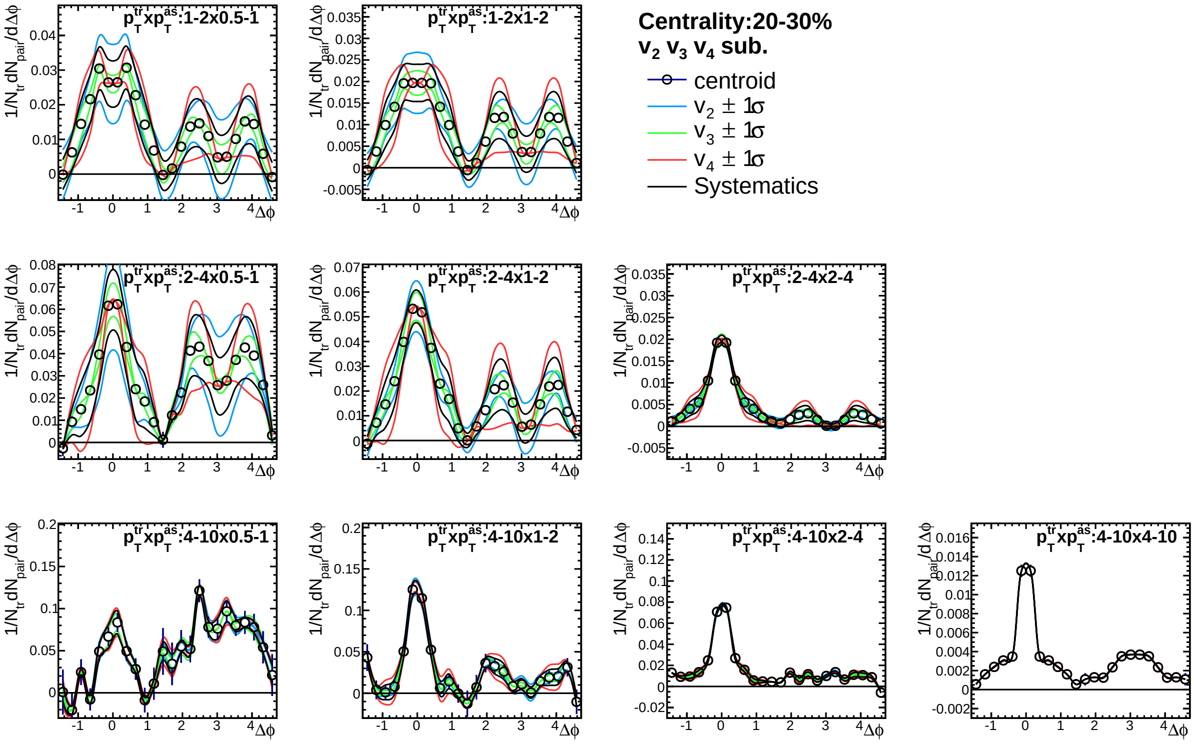

Figure 3.22: Per trigger pair yield where contributions of v_2, v_3, and v_4 is subtracted in centrality 20-30%. v_n value is varied (blue-line) $v_2 \pm 1\sigma$ (green-line) $v_3 \pm 1\sigma$, and (red-line) $v_4 \pm 1\sigma$, other harmonics being fixed. Systematics are expressed by black lines.

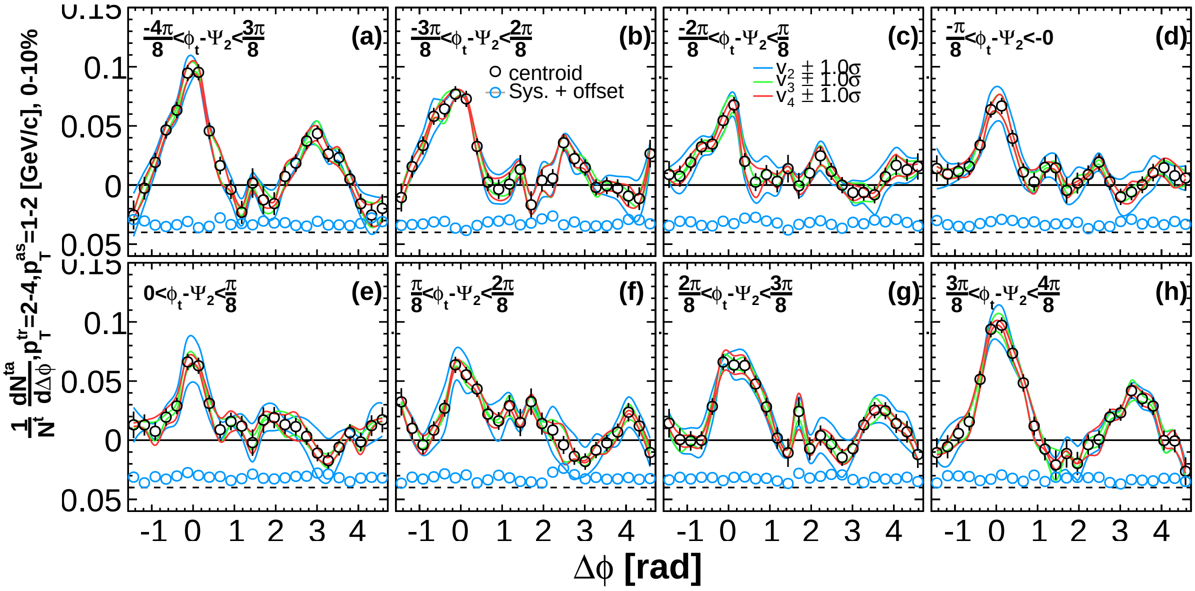

Figure 3.23: Ψ_2 dependent correlations at 2-4⊗1-2 GeV/c before resolution correction where contributions of v_2, v_3, and v_4 is subtracted. v_n value is varied (blue-line) $v_2 \pm 1\sigma$ (green-line) $v_3 \pm 1\sigma$, and (red-line) $v_4 \pm 1\sigma$, other harmonics being fixed. Systematics are expressed by blue open circle with an offset.

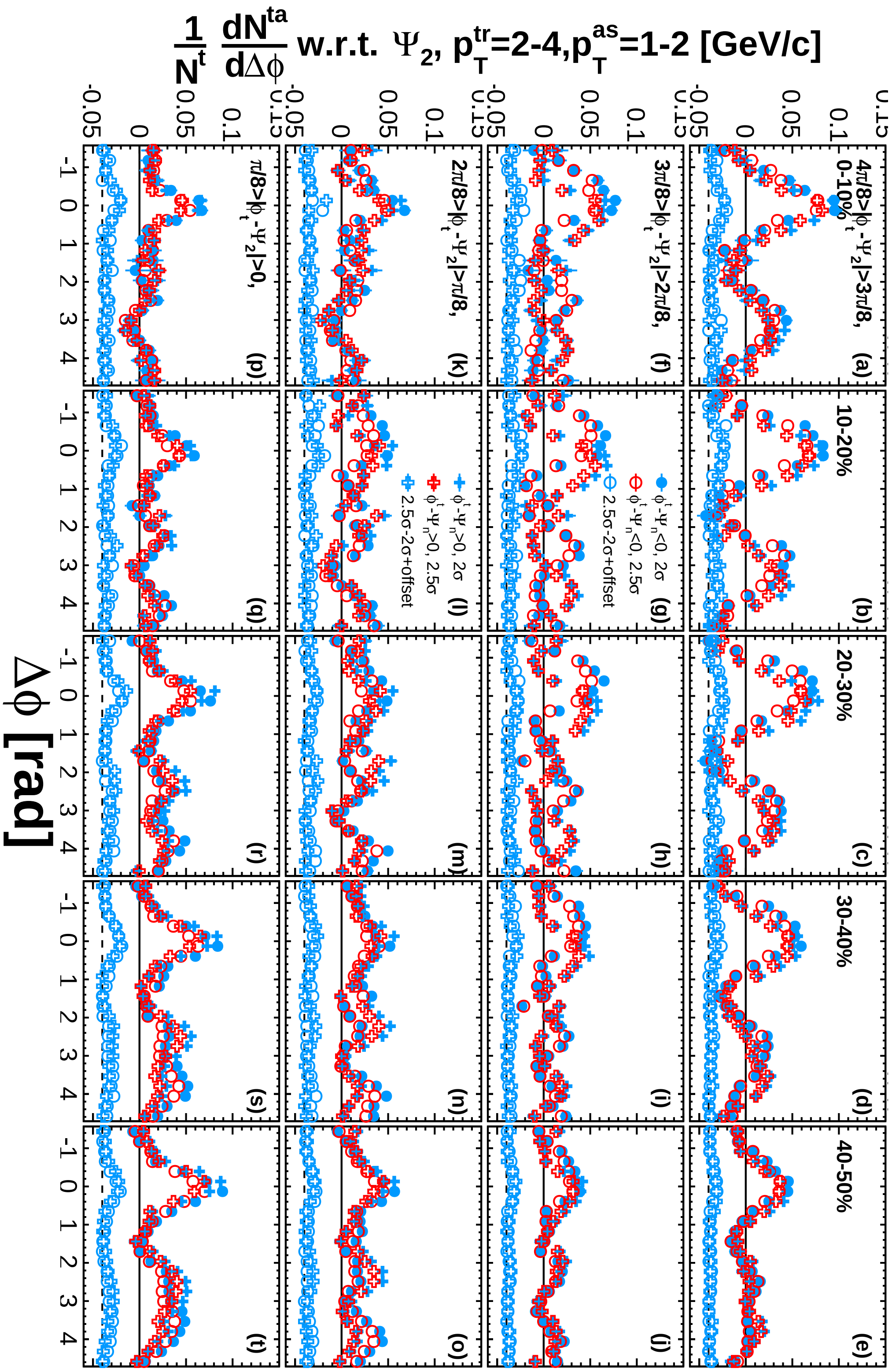

Figure 3.24: Ψ_2 dependent correlations at 2-4⊗1-2 GeV/c before resolution correction where contributions of v_2, v_3, and v_4 is subtracted using (Black) 2σ matching cut, (Red) 2.5σ matching, and (Blue) difference of those.

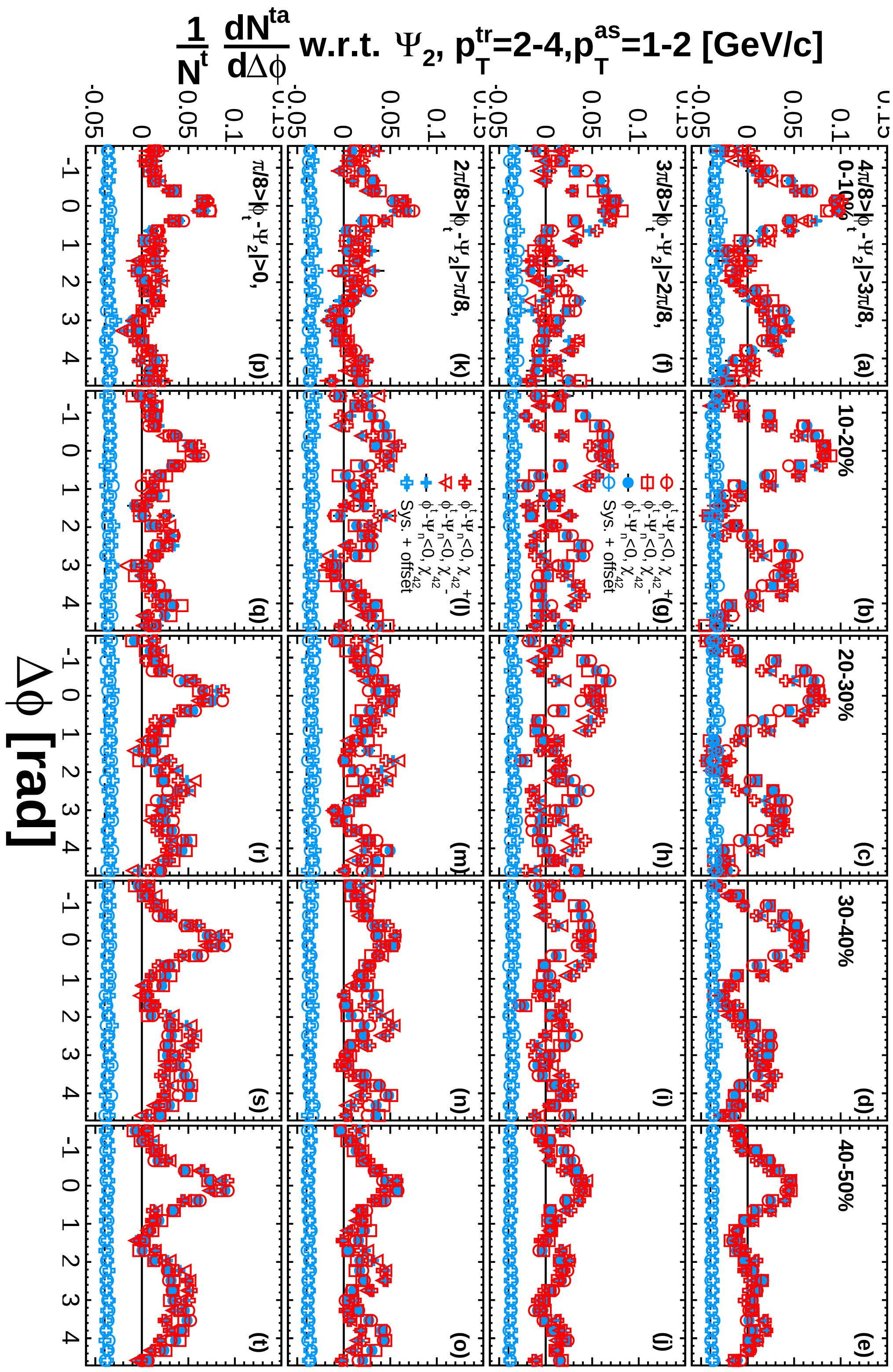

Figure 3.25: Ψ_2 dependent correlations at 2-4⊗1-2 GeV/c before resolution correction where contributions of v_2, v_3, and v_4 is subtracted using (Blue) centroid χ_{42} and (Red) ± 1σ χ_{42}. The systematics are plotted with an offset.

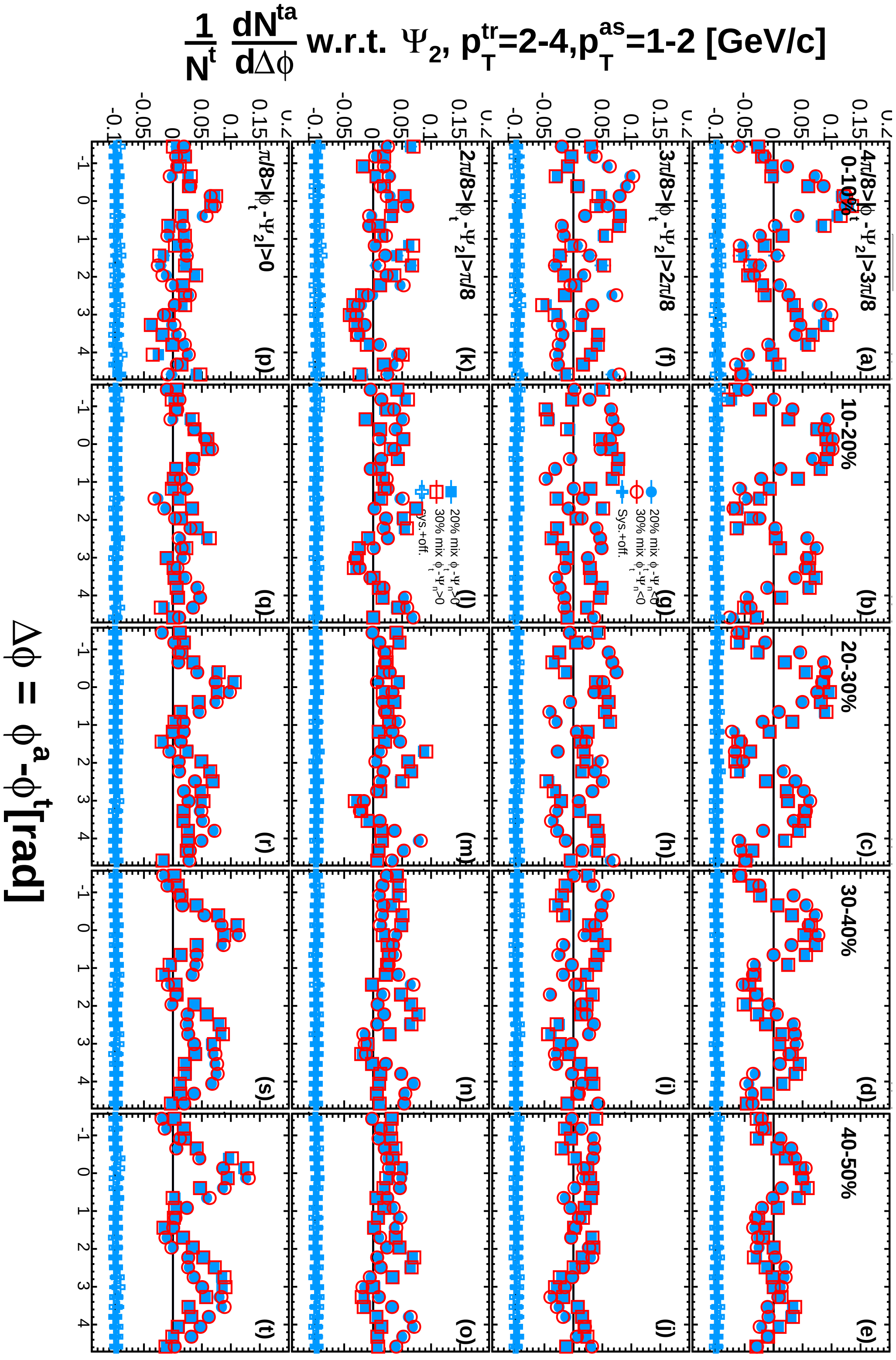

Figure 3.26: Ψ_2 dependent correlations at 2-4$\otimes$1-2 GeV/c where contributions of v_2, v_3, and v_4 is subtracted. Data points show the results of (Blue) 30% and (Red) 20% smoothing factors and their difference with an offset.

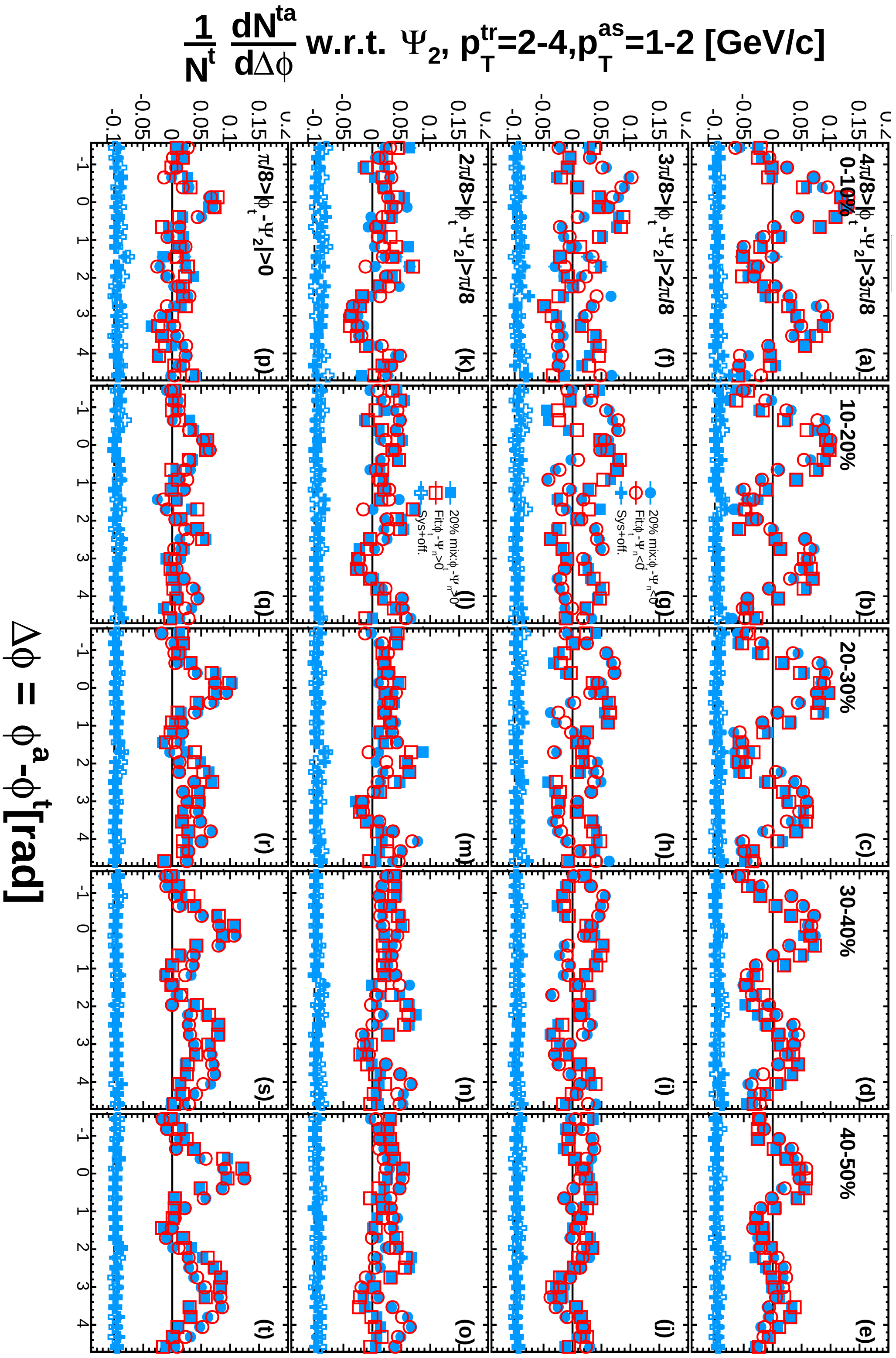

Figure 3.27: Ψ_2 dependent correlations at 2-4⊗1-2 GeV/c where contributions of v_2, v_3, and v_4 is subtracted. Data points show the results of (Blue) iteration and (Red) fitting method and their difference with an offset.

Chapter 4

Results

This chapter presents the results of higher-order flow harmonics used for flow background subtractions in the two-particle correlation analysis and the subtracted results of the two-particle correlations. The higher-order flow harmonics are compared with the PHENIX measurements [22]. The two-particle correlations taking into account only v_2 background are compared with a previous PHENIX measurement[18] for the purpose of consistency check. Then, we show the results of inclusive and event-plane dependent correlations.

4.1 Higher-Order Flow Harmonics

Fig.4.1 shows the results of higher-order flow harmonics measured via event-plane method compared with [22]. As this flow measurement in this analysis uses approximately 100 times larger statistics than that of [22], the statistical uncertainties in Fig.4.1 became much smaller than that in the previous measurements. However, systematics of $v_4\{\Psi_4\}$ in this analysis is larger than the previous one, since this analysis includes the systematics on the rapidity gap between

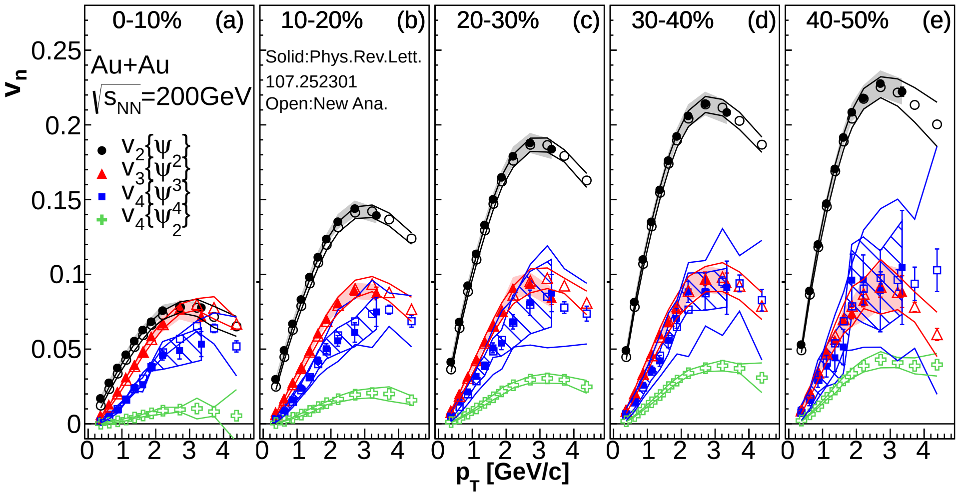

Figure 4.1: Higher-order flow harmonics v_n measured by PHENIX [22] and those in this analysis used as inputs for two-particle correlations.

mid-rapidity particles and the event-planes, estimated from the difference of v_n obtained using RXN and BBC event-planes.

4.2 Consistency with previous analysis

Two-particle correlation results are compared with the previous PHENIX analysis[18] by applying the same analysis method of this thesis for the same p_T and centrality selections. Since the previous PHENIX results are only subtracted v_2 background (published before v_n measurements), the distributions in this comparison are only the background of v_2 subtracted. This comparison is performed for the purpose of confirming the validity of the new analysis presented in this thesis. Fig.4.2, 4.3 and 4.4 show the results of the comparisons for different p_T selections. All the results are consistent within the systematic uncertainties.

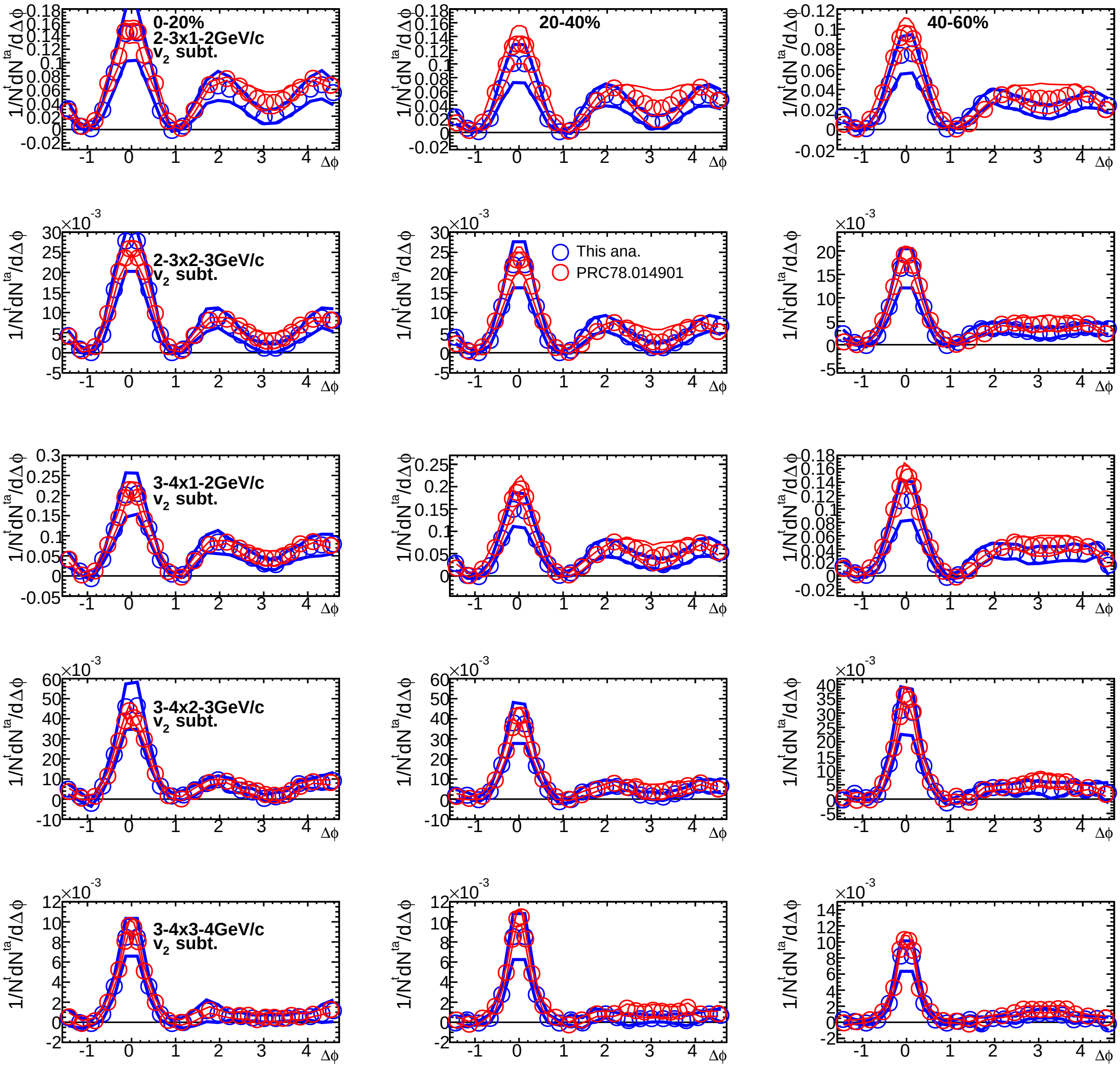

Figure 4.2: Two-particle correlated yield per trigger with v_2 subtracted for low trigger and associate p_T combinations (the ranges are shown as trigger p_T x associate p_T in GeV/c) in centrality 0-20, 20-40 and 40-60%. The blue points show the result of this thesis and red points represent the previous PHENIX analysis [18].

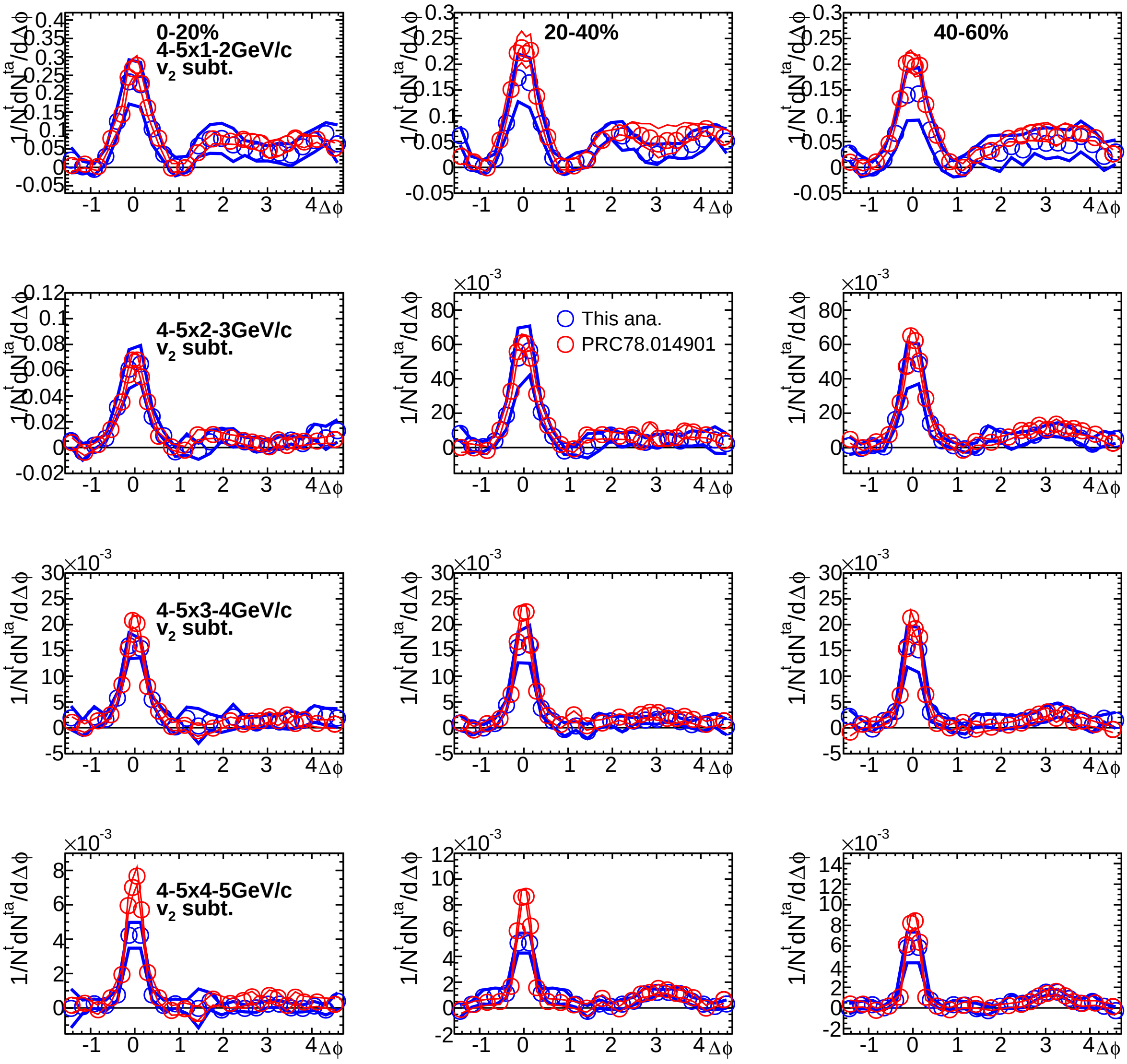

Figure 4.3: Two-particle correlated yield per trigger with v_2 subtracted for intermediate trigger and associate p_T combinations (the ranges are shown as trigger p_T x associate p_T in GeV/c) in centrality 0-20, 20-40 and 40-60%. The blue points show the result of this thesis and red points represent the previous PHENIX analysis [18].

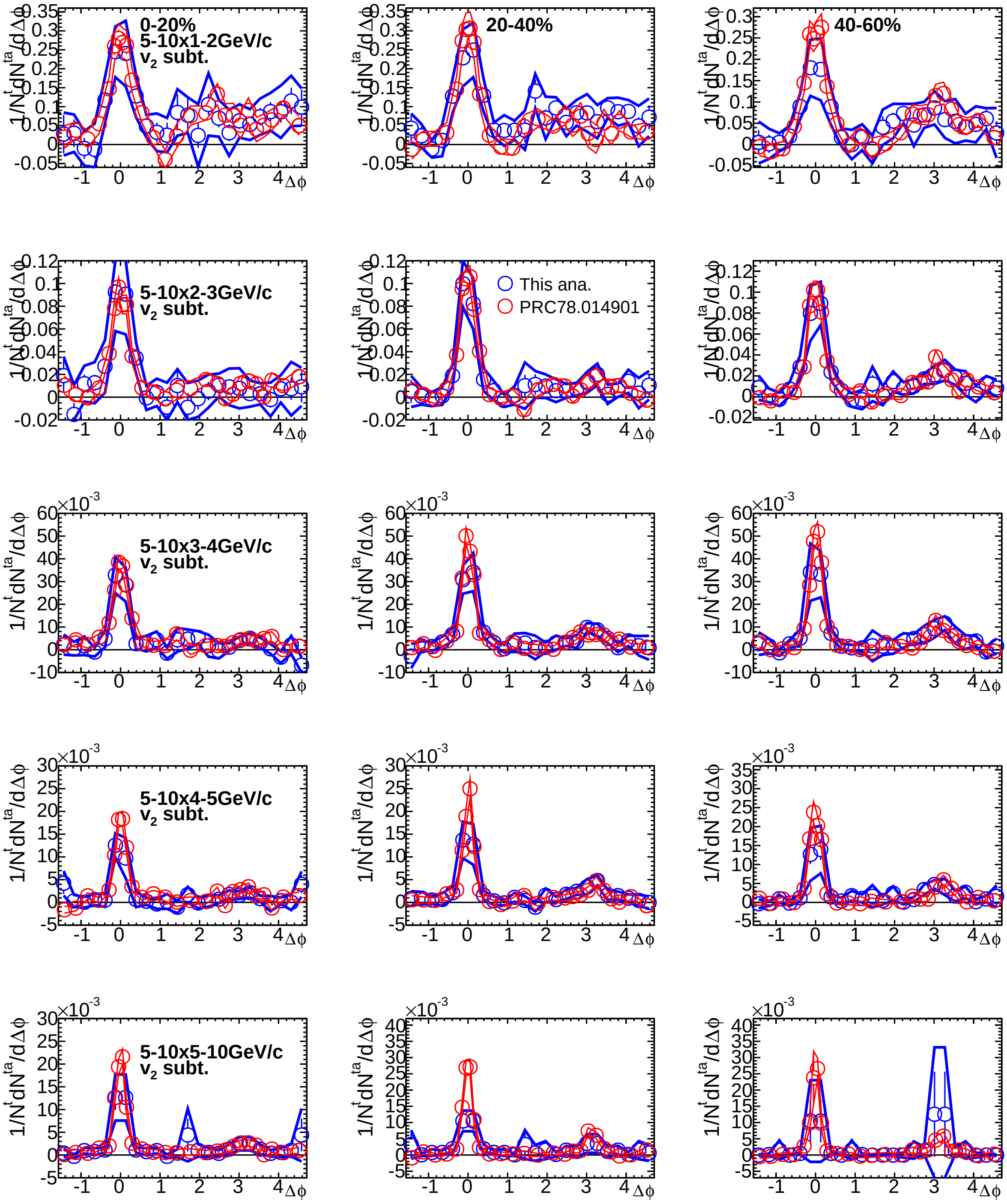

Figure 4.4: Two-particle correlated yield per trigger with v_2 subtracted for high trigger and associate p_T combinations (the ranges are shown as trigger p_T x associate p_T in GeV/c) in centrality 0-20, 20-40 and 40-60%. The blue points show the result of this thesis and red points represent the previous PHENIX analysis [18].

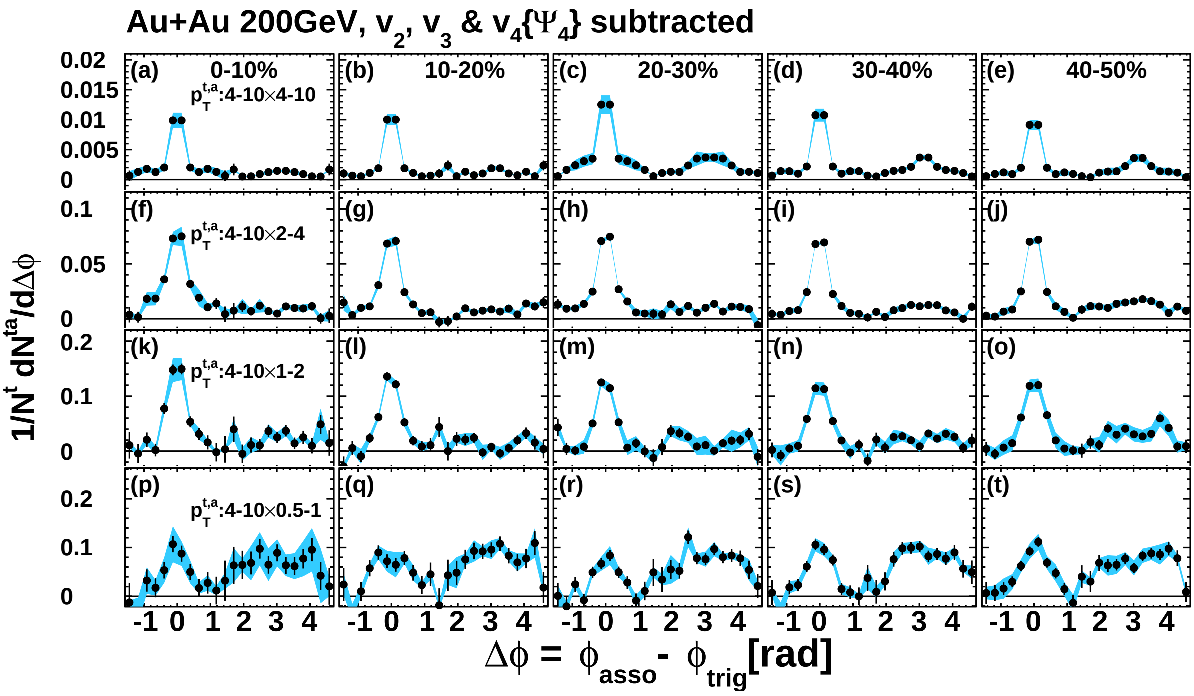

Figure 4.5: Two-particle correlated yield per trigger with $v_n(n = 2, 3, 4)$ subtracted in (a)-(e) $p_T^t \otimes p_T^a =$ 4-10 $\otimes$ 4-10 GeV/c, (f)-(j) $p_T^t \otimes p_T^a =$ 4-10 $\otimes$ 2-4 GeV/c, (k)-(o) $p_T^t \otimes p_T^a =$ 4-10 $\otimes$ 1-2 GeV/c, and (p)-(t) $p_T^t \otimes p_T^a =$ 4-10 $\otimes$ 0.5-1 GeV/c, and in five centrality selections.

4.3 Inclusive Trigger Correlations

The inclusive trigger correlations are measured for trigger p_T ranges: 1-2, 2-4, and 4-10 GeV/c, and associate p_T ranges: 0.5-1.0, 1.0-2.0, and 2.0-4.0 GeV/c. The step of centrality selection is 10 %. In the distributions, $v_n(n = 2, 3, 4)$ backgrounds are subtracted. The results are presented in Fig.4.5 for trigger p_T: 4-10 GeV/c and in Fig.4.6 for trigger p_T<4 GeV/c.

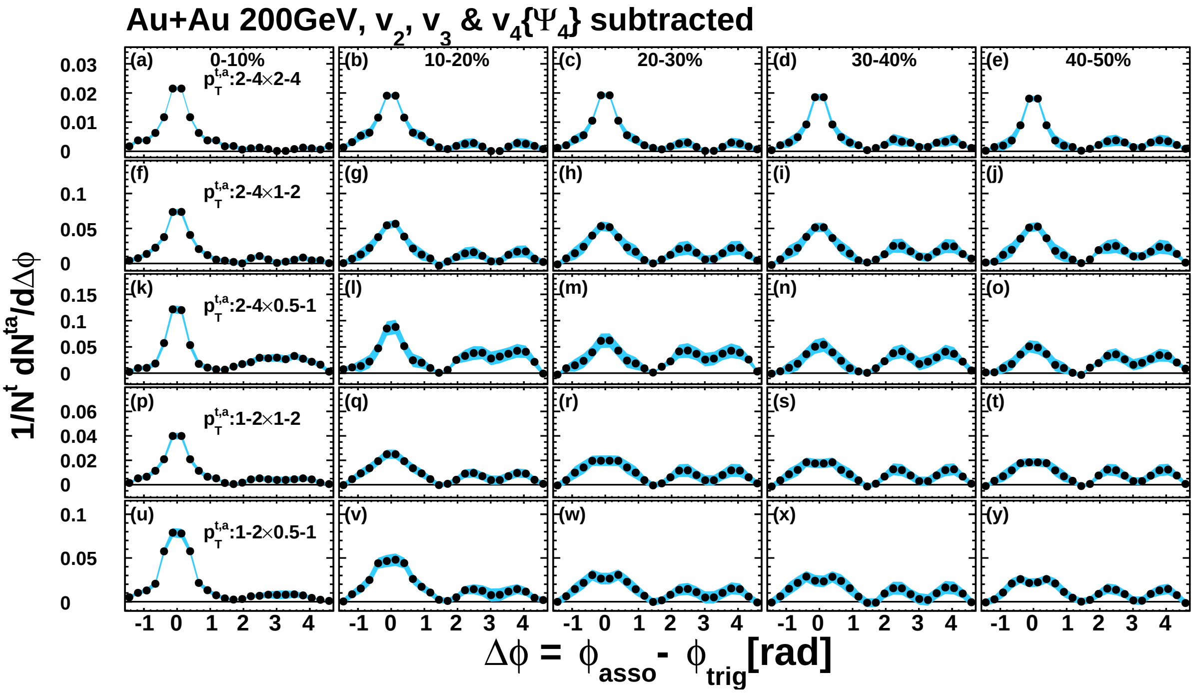

Figure 4.6: Two-particle correlated yield per trigger with $v_n (n = 2, 3, 4)$ subtracted in (a)-(e) $p_T^t \otimes p_T^a$ = 2-4 $\otimes$ 2-4 GeV/c, (f)-(j) $p_T^t \otimes p_T^a$ = 2-4 $\otimes$ 1-2 GeV/c, (k)-(o) $p_T^t \otimes p_T^a$ = 2-4 $\otimes$ 0.5-1 GeV/c, (p)-(t) $p_T^t \otimes p_T^a$ = 1-2 $\otimes$ 1-2 GeV/c, and (u)-(y) $p_T^t \otimes p_T^a$ = 1-2 $\otimes$ 0.5-1 GeV/c, and in five centrality selections.

4.4 Event-Plane Dependent Correlations

The event-plane dependent correlations of three p_T selections: 2-4x1-2, 2-4x2-4, and 4-10x2-4 GeV/c are measured with the $v_n (n = 2, 3, 4)$ subtracted in the 10% step selections of centrality.

Fig.4.7 and 4.8 present the Ψ_2 and Ψ_3 dependent correlations of p_T: 2-4x1-2 GeV/c. Fig.4.9 and 4.10 present those of p_T: 2-4x2-4 GeV/c. Fig.4.11 and 4.12 present those of p_T: 4-10x2-4 GeV/c.

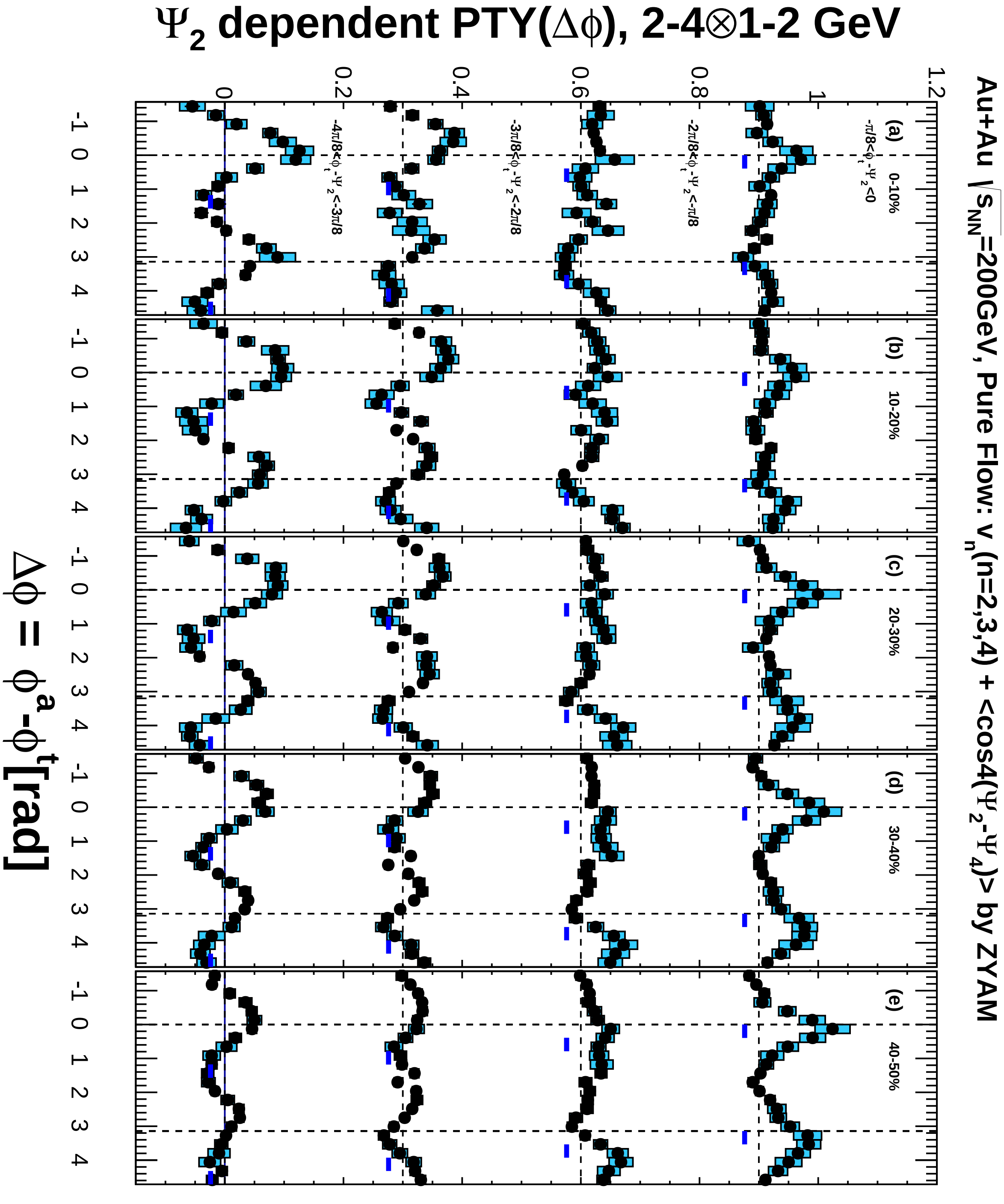

Figure 4.7: Ψ_2 dependent per trigger pair yield in p_T:2-4x1-2 GeV/c for five different centralities, where contributions of $v_n (n = 2, 3, 4)$ are subtracted. Resolution correction was applied using an iteration method.

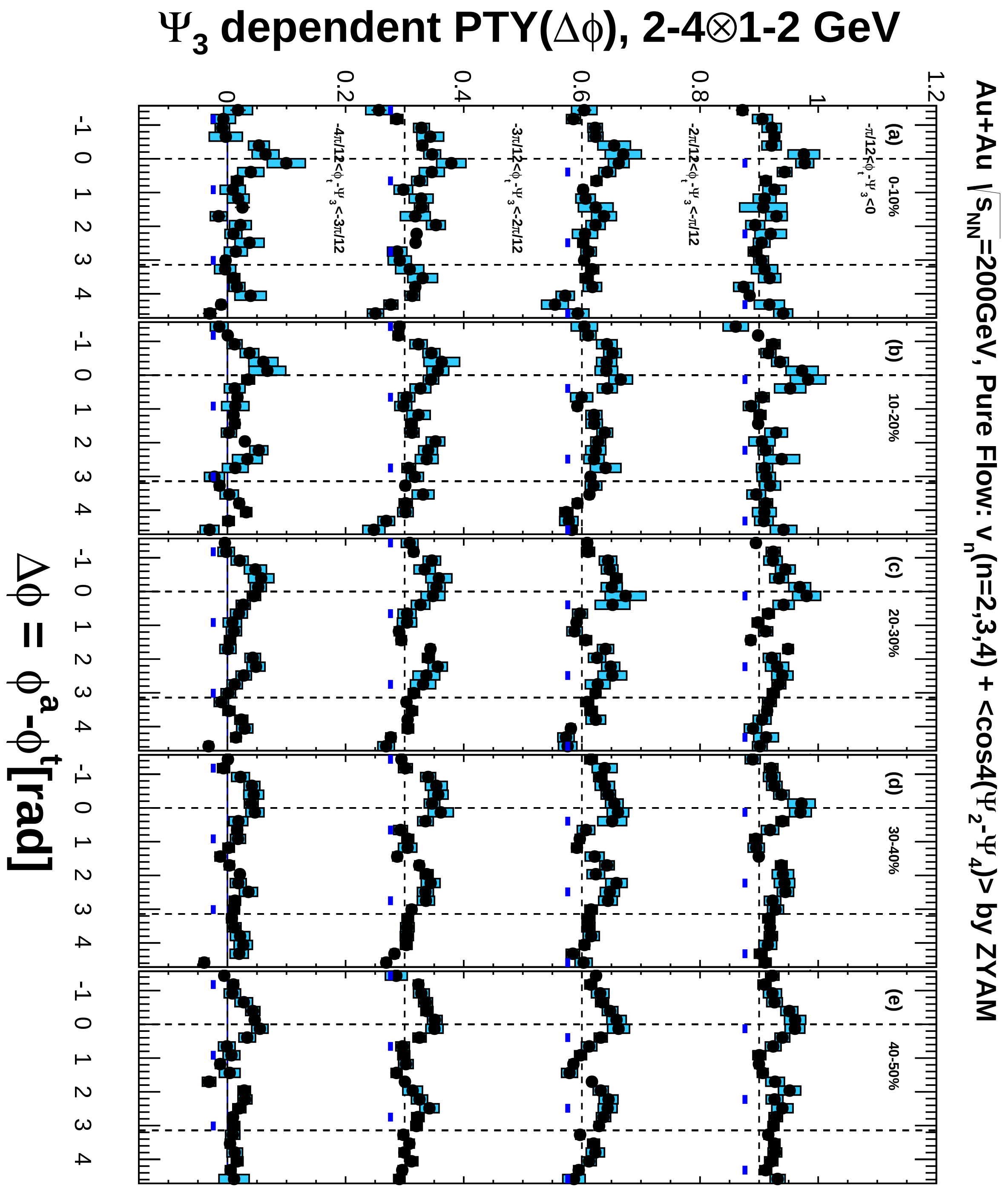

Figure 4.8: Ψ_3 dependent per trigger pair yield in p_T:2-4x1-2 GeV/c for five different centralities, where contributions of $v_n(n = 2, 3, 4)$ are subtracted. Resolution correction was applied using an iteration method.

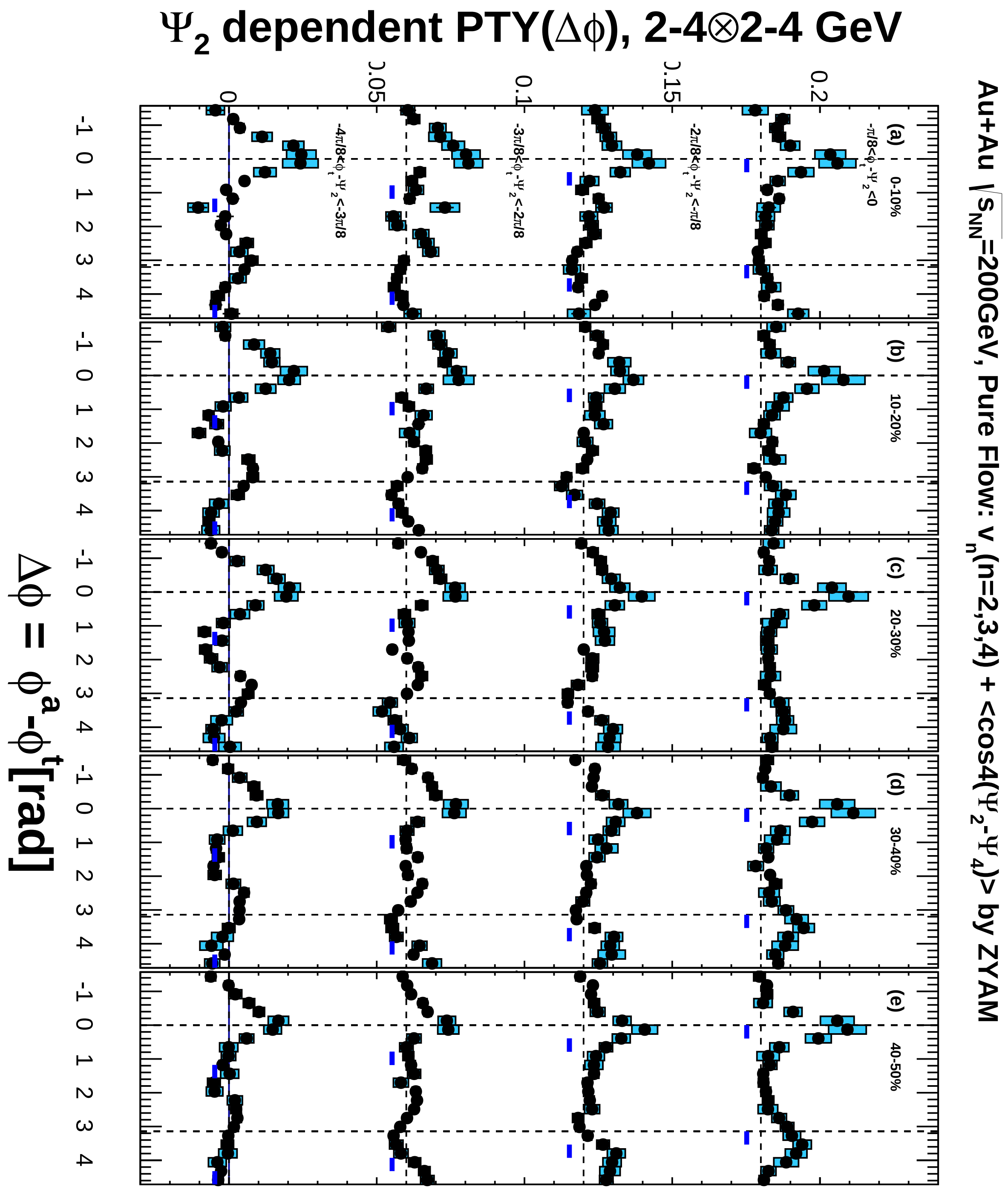

Figure 4.9: Ψ_2 dependent per trigger pair yield in p_T:2-4x2-4 GeV/c for five different centralities, where contributions of $v_n (n = 2, 3, 4)$ are subtracted. Resolution correction was applied using an iteration method.

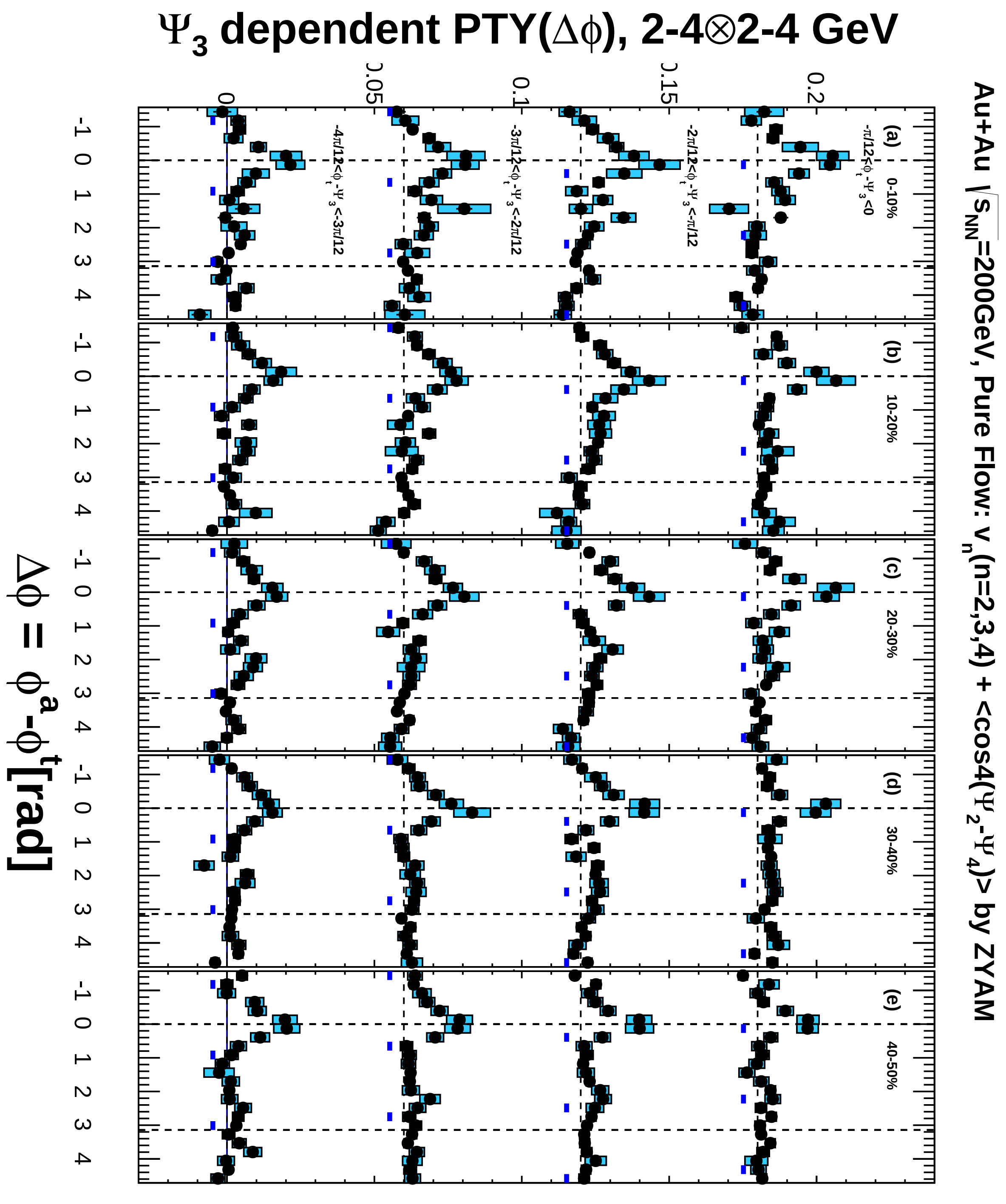

Figure 4.10: Ψ_3 dependent per trigger pair yield in p_T:2-4x2-4 GeV/c for five different centralities, where contributions of $v_n(n = 2, 3, 4)$ are subtracted. Resolution correction was applied using an iteration method.

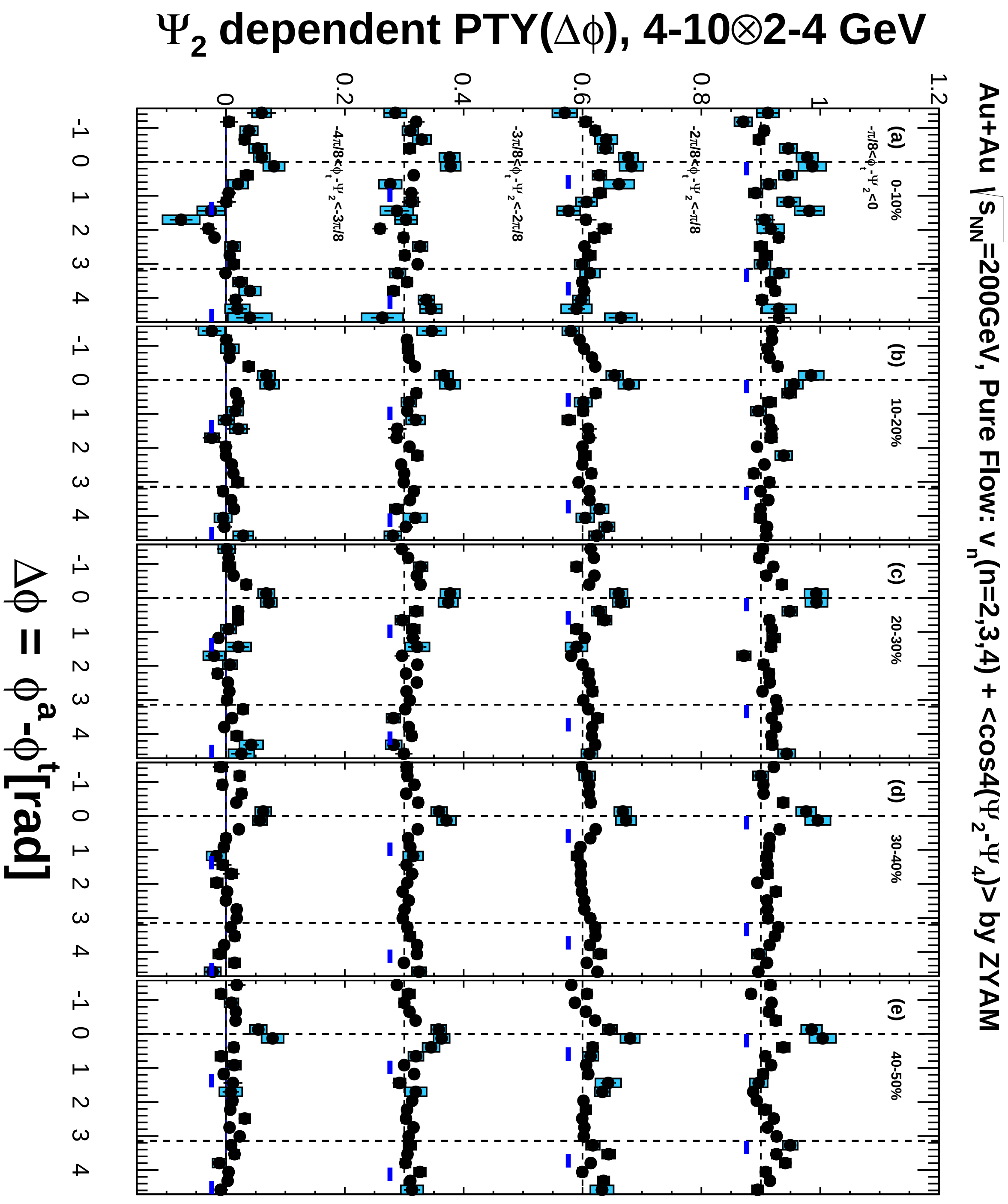

Figure 4.11: Ψ_2 dependent per trigger pair yield in p_T:4-10x2-4 GeV/c for five different centralities, where contributions of $v_n(n = 2, 3, 4)$ are subtracted. Resolution correction was applied using an iteration method.

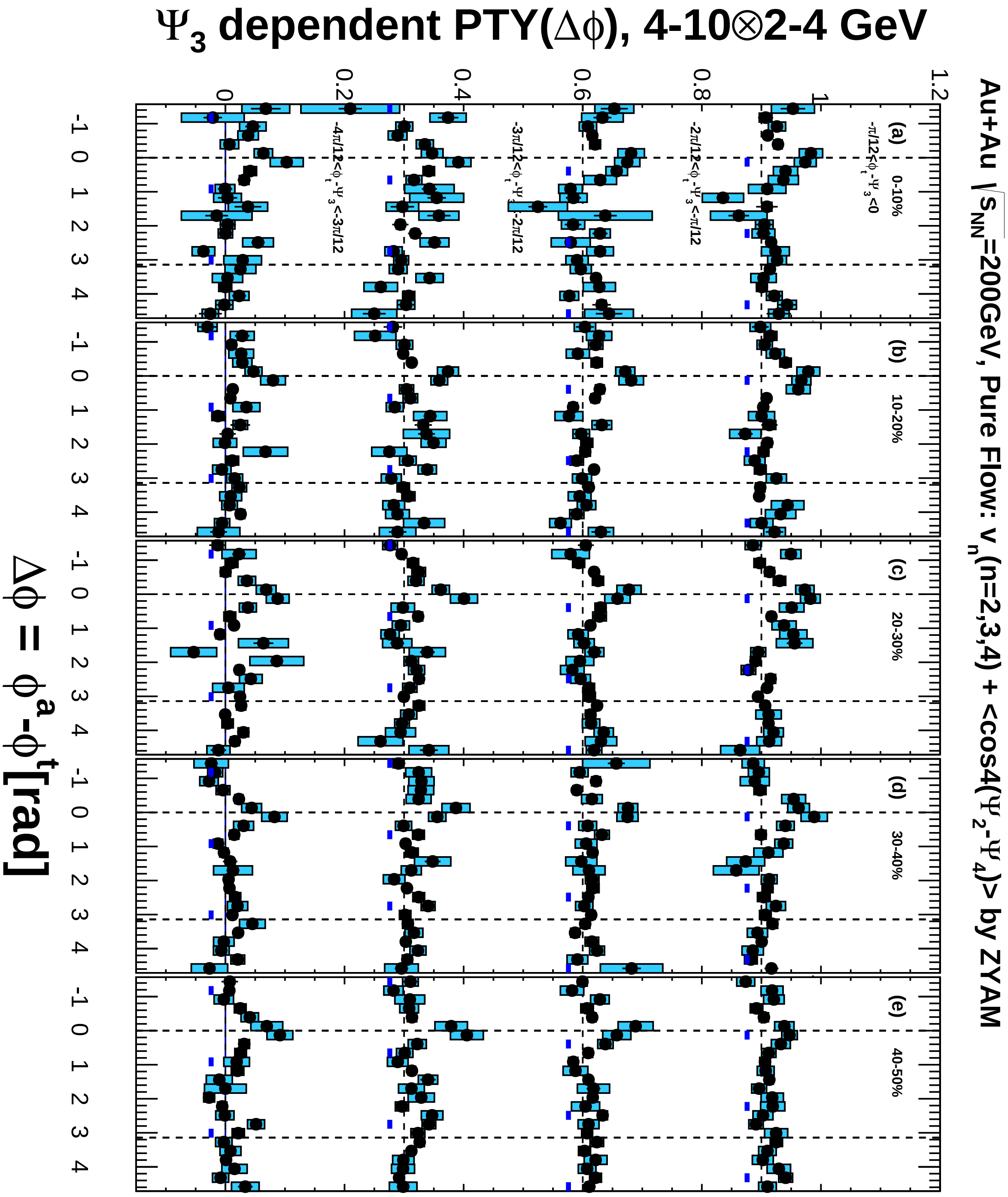

Figure 4.12: Ψ_3 dependent per trigger pair yield in p_T:4-10x2-4 GeV/c for five different centralities, where contributions of $v_n(n = 2, 3, 4)$ are subtracted. Resolution correction was applied using an iteration method.

Chapter 5

Discussions

In this chapter, we discuss interpretations of the inclusive trigger and event-plane dependent two-particle correlations with $v_n (n = 2, 3, 4)$ contributions subtracted. First, the centrality and p_T dependences of inclusive two-particle correlations are discussed, then the experimental results are compared with some theoretical calculations. Finally, we will give a discussion on the path length dependence of the correlated yield and shape of event-plane dependent correlations.

5.1 Inclusive Correlations

Fig.5.1 shows the selected results of two-particle correlations in most-central and mid-central collisions with $v_n (n = 2, 3, 4)$ contributions subtracted, for different trigger and associate p_T combinations. In most-central collisions, the correlation yield at away-side ($|\Delta\phi - \pi| < \pi/2$) is almost suppressed independent of the combinations of trigger and associate p_T ranges. In mid-central collisions, the correlations in trigger p_T: 4-10 GeV/c show single peaks at away-side, that become more distinctive approaching to correlations in p+p collisions with increase of associate particle p_T ranges. The overall trend of two-particle correlations with high trigger p_T is still similar to the previous PHENIX measurements [18], where only the contribution of v_2 is taken into account, because the amplitudes of v_n background are small due to large ratios of jet-signal to flow-background in this p_T range.

The correlations of trigger p_T less than 4 GeV/c have double-peaks at away-side even after $v_n (n = 2, 3, 4)$ subtractions in centrality above 10%. The position of the away-side double-humps seem to be independent of centrality and p_T combinations. The positions of double-humps are characterized in the next section.

5.1.1 Double-hump position of Inclusive Correlations

We quantify the position of double-hump structures by applying a fitting to the away-side of the correlations with the following symmetric two Gaussian function as

$$F(\Delta\phi) = A\mathrm{e}^{-\frac{(\Delta\phi-\pi-D)^2}{\sigma^2}} + A\mathrm{e}^{-\frac{(\Delta\phi-\pi+D)^2}{\sigma^2}}, \tag{5.1}$$

where A is a common height of two Gaussians, D is a common shift of Gaussians from $\Delta\phi = \pi$ but in opposite sign, and σ is a common width of the Gaussians. The fitting to the away-side correlations ($\pi/2<\Delta\phi<3\pi/2$) in p_T:1-2x1-2 GeV/c is performed as in Fig.5.2.

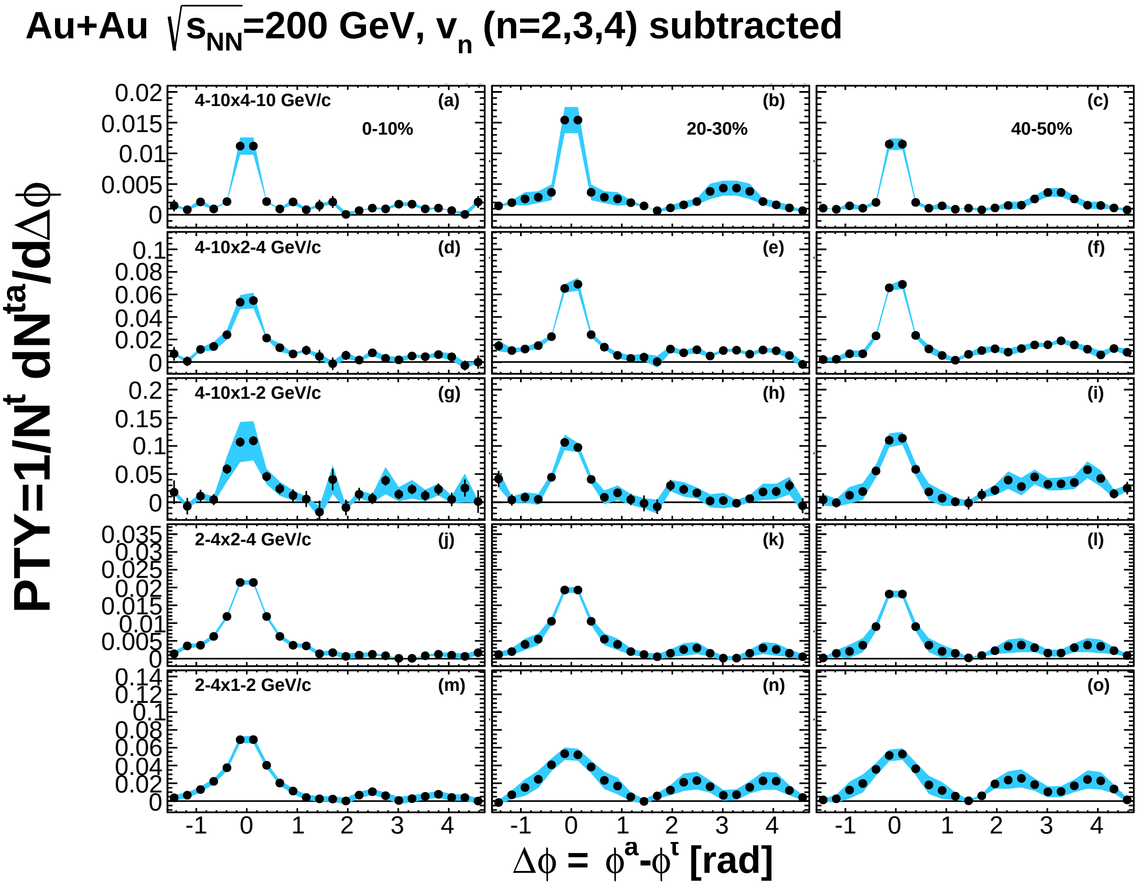

Figure 5.1: Two-particle correlated yield per trigger with $v_n(n = 2, 3, 4)$ subtracted for (a)-(c) p_T: 4-10x4-10 GeV/c, (d)-(f) p_T: 4-10x2-4 GeV/c, (g)-(i) p_T: 4-10x1-2 GeV/c, (j)-(l) p_T: 2-4x2-4 GeV/c, and (m)-(o) p_T: 2-4x1-2 GeV/c and for most-central and two mid-central centrality selections.

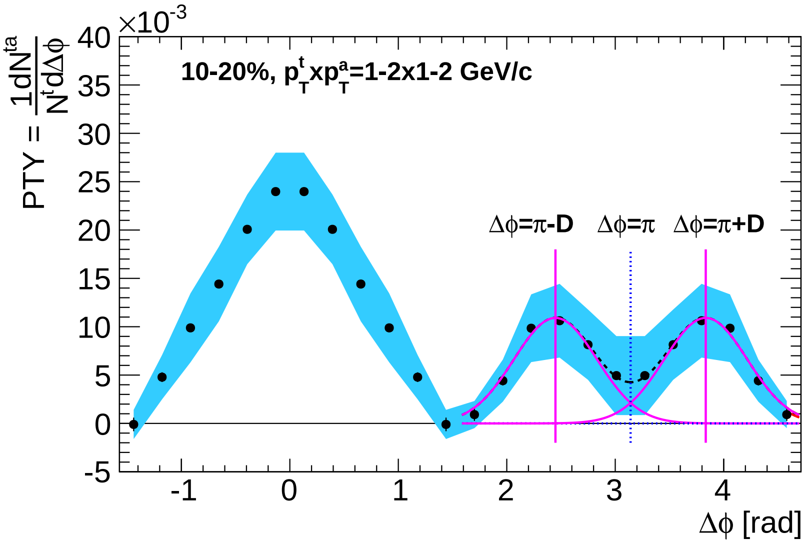

Figure 5.2: The extraction of double-hump position shift D [rad] using a two-Gaussian function fitted to the per trigger yield in centrality 10-20% and in trigger and associate p_t:1-2x1-2 GeV/c. The dashed blue line indicates $\Delta\phi = \pi$ [rad], and two magenta vertical lines indicate the positions of the double-humps.

The extracted D parameter as a function of associate p_T is presented in Fig.5.3 in centrality above 10%, where double-hump is seen in the two-particle correlations. The double-hump position is independent of both trigger and associate p_T and centrality, if the systematic uncertainties are taken into account. The double-hump positions of experimental data appear to be $D = \pi/4$, which is the phase $\cos 4\Delta\phi$ shows a local maximum.

The double-hump position of the experimental data at centrality 10-20% is compared with four theoretical calculations in Fig.5.4, such as (1) Gluon Cherenkov Radiation, (2) Energy Momentum Loss and hydrodynamics, (3) Mach-Cone Shock-Wave, and (4) Hot Spot and Hydrodynamics. Cherenkov Gluon Radiation model shows opening angle distributions of radiation rapidly decrease with p_T reaching less than 0.2 rad at 1 GeV/c, which is approximately 25% of experimental data. Energy Momentum Loss and Mach-Cone Models show a p_T independence of double-hump position as the experimental data, but the values are about 20% smaller or larger than the experimental data. The results of Hot Spot model is about 50% larger than the experimental data. Since results of model calculations easily change depending on parameters in each calculation, we do not give any conclusion to them. This data should be an experimental reference to future theoretical models.

In order to quantify the difference of correlations in between most-central (no double-hump seen) and mid-central collisions (double-hump seen), the correlations are decomposed with a Fourier series function over $-\pi/2 < \Delta\phi < 3\pi/2$ up to seventh-order as

$$J(\Delta\phi) = \sum_{n}^{7} J_n \cos n\Delta\phi. \tag{5.2}$$

Fig.5.5 shows J_n as a function of harmonics-order in the two-particle correlations of p_T: 2-4x1-2 GeV/c as an example of intermediate p_T correlations. J_0 is corresponding to the average of

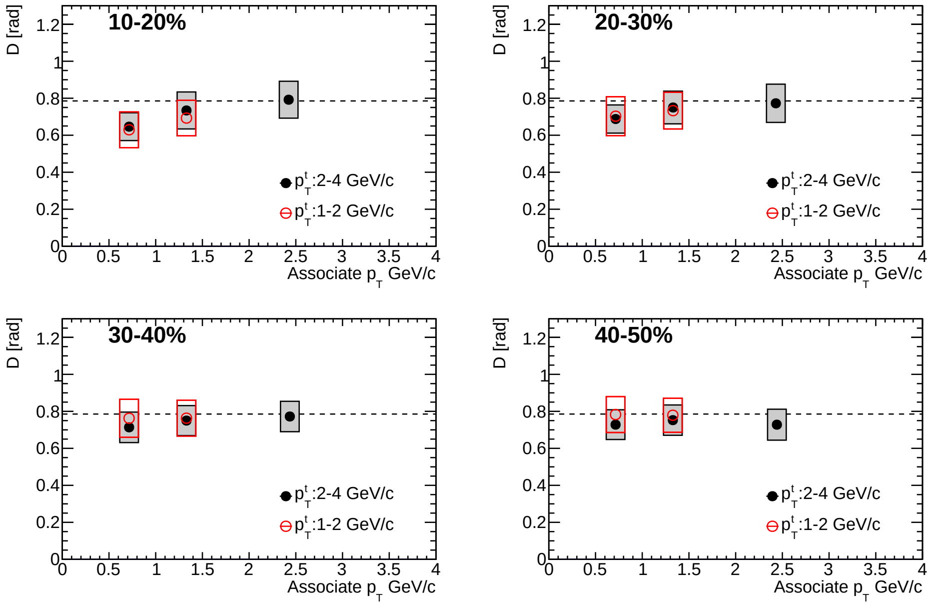

Figure 5.3: Opening angle of away-side double humps D [rad] from $\Delta\phi = \pi$ as a function of associate p_T extracted by two Gaussian fit, for trigger p_T (Black) 2-4 and (Red) 1-2 GeV/c. The dashed line indicates $\pi/4$ [rad].

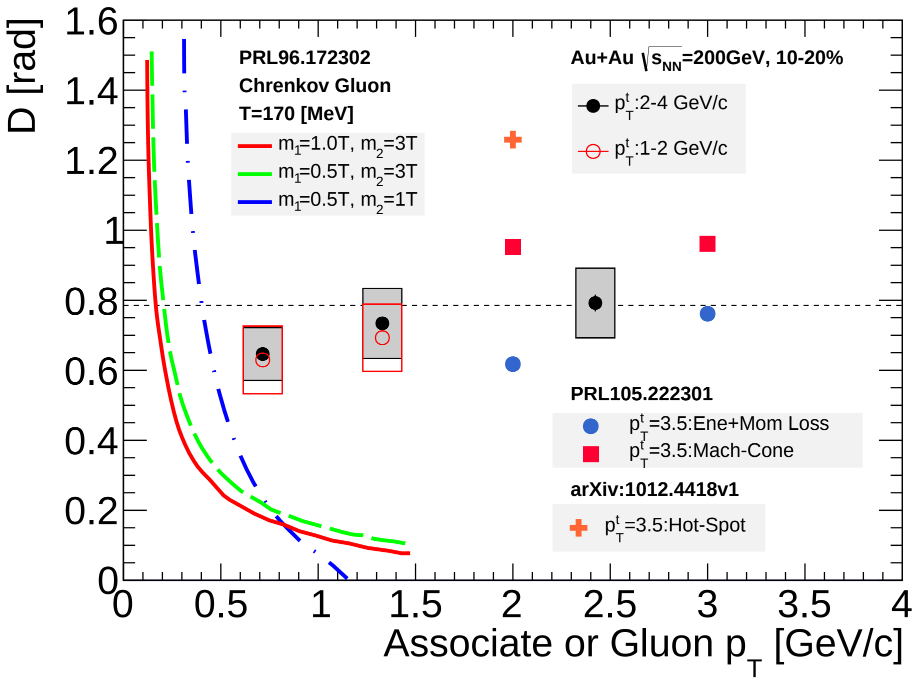

Figure 5.4: Opening angle of away-side double humps from $\Delta\phi = \pi$ compared with (Blue-Green-Red Lines) Gluon Cherenkov Radiation Model[27], (Blue Circle) Energy-Momentum Loss+Hydro Model[26], (Red Square) Mach-Cone Model[26], and (Orange Cross) HotSpot+Hydro Model[32].

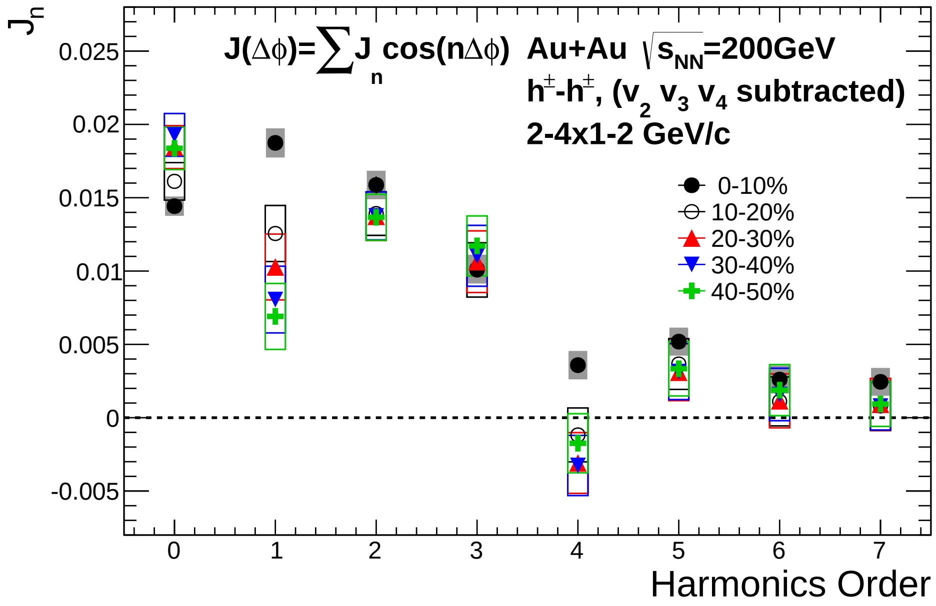

Figure 5.5: Harmonic decomposition of two-particle correlated yield per trigger in five different centralities and in p_T: 2-4x1-2 GeV/c, where contributions of $v_n(n = 2, 3, 4)$ is subtracted based on the ZYAM assumption.

correlations yield per $\Delta\phi$ bin. Comparing J_n in above centrality 10% with those in centrality 0-10%, J_1 and J_4 have a strong centrality dependence, while other harmonic amplitudes are almost independent of centrality. Since $J_1 \cos\Delta\phi$ is affecting to broaden the away-side distribution, this factor does not play a significant role on the existence of double-humps. The difference of J_4 corresponds to the away-side double-hump position D [rad] located around $\pi/4$. Therefore, possibility of creating any double-hump structure by v_4 subtraction should be considered further.

Fig.5.6 shows the central value with lower and upper boundaries of the correlations with $v_n(n = 2, 3, 4)$ subtracted for (Green-Band) $v_4{\pm}1\sigma$ and (Yellow-Band) $v_4{\pm}2\sigma$, where the values of v_2 and v_3 are fixed. The significance of the double-humps is at least 1σ level in terms of v_4 systematic uncertainties.

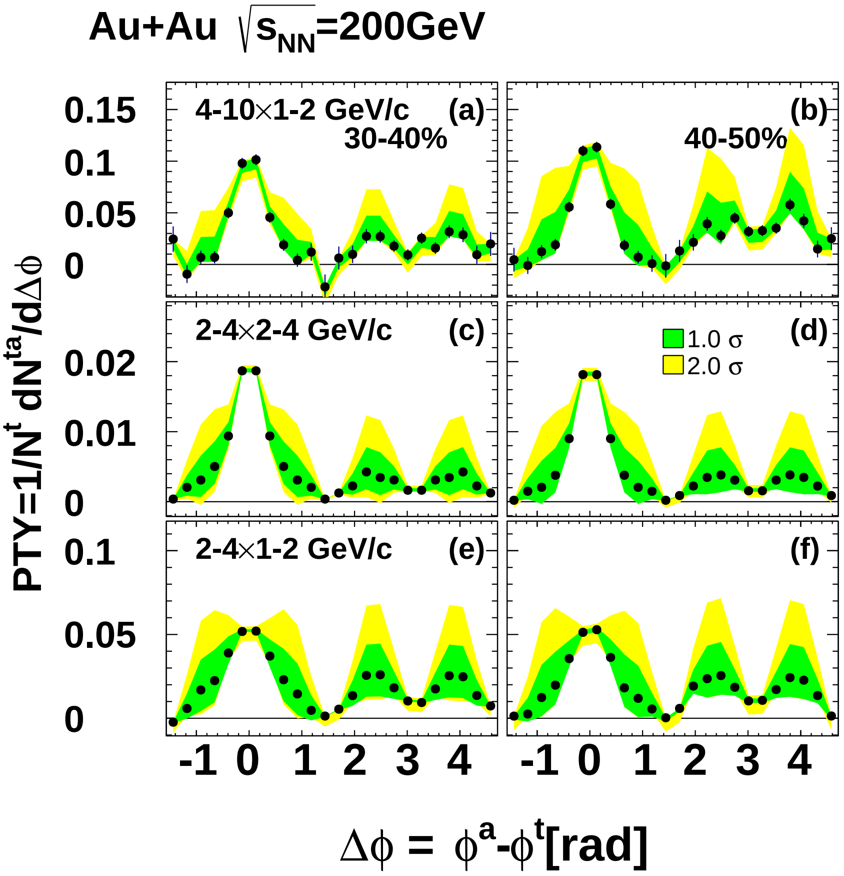

Figure 5.6: Per trigger yield with $v_n(n = 2, 3, 4)$ subtracted in (a)-(b) $p_T^t \otimes p_T^a$ = 4-10 ⊗ 1-2 GeV/c, (c)-(d) $p_T^t \otimes p_T^a$ = 2-4 ⊗ 2-4 GeV/c, and (e)-(f) $p_T^t \otimes p_T^a$ = 2-4 ⊗ 1-2 GeV/c, and in centrality 30-40%, and 40-50%, with different v_4 amplitude in the subtraction (Green Band) $\pm 1.0\sigma$ and (Yellow Band) 2.0σ from centroid in terms of systematics.

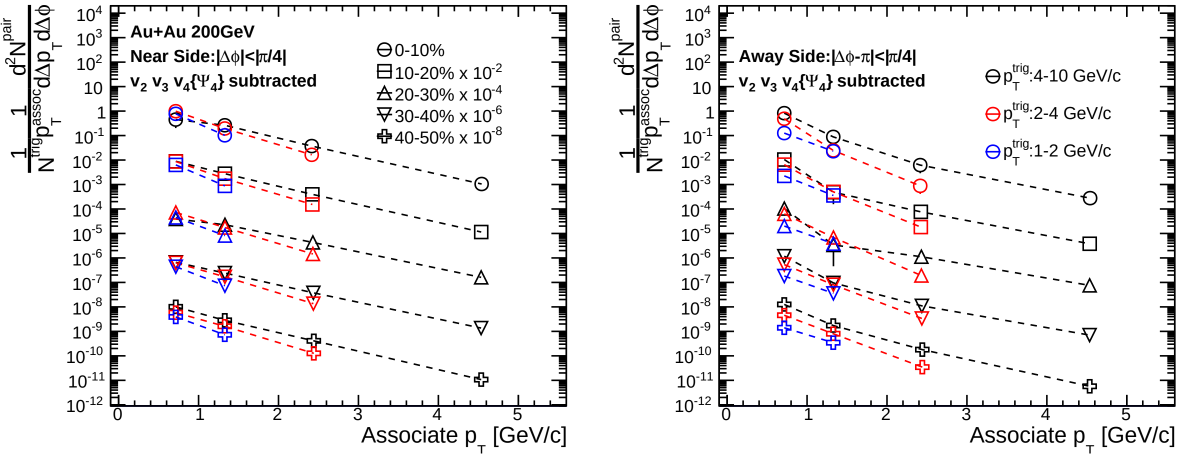

Figure 5.7: p_T spectra of per trigger yields as a function of associate p_T for trigger p_T (Black) 4−10, (Red) 2−4, and (Blue) 1−2 GeV/c and in 5 different centralities. Marker styles indicate the centrality selections.

5.1.2 p_T dependence of Correlation Yield

The two-particle correlations are converted into p_T spectra in order to discuss the p_T dependence of the integrated correlation yield at near-side($|\Delta\phi| < \pi/4$) and away-side($|\Delta\phi - \pi| < \pi/4$) with a definition of

$$\frac{1}{p_T^a}\frac{dY}{d\Delta p_T} = \frac{1}{p_T^a}\frac{1}{(p_T^{a,max} - p_T^{a,min})}\int d\Delta\phi \frac{1}{N_{trig}}\frac{dN}{d\Delta\phi}, \tag{5.3}$$

where Y denotes the integrated yield and $p_T^{a,max}$ is an upper boundary of associate p_T bin and $p_T^{a,min}$ is a lower boundary. Fig.5.7 shows the correlation yield spectra as a function of associate p_T for trigger p_T ranges:1-2, 2-4, and 4-10 GeV/c and in five centrality selections.

The spectra become harder with trigger p_T in both near and away-side at a same associate p_T range in both near and away side. The change is more significant in away-side than in near-side.

5.1.3 Latest Theoretical Effort in Two-Particle Correlations

After the subtractions of $v_n(n = 2, 3, 4)$ contributions, the experimental results of two-particle correlation functions are more appropriate to discuss the possible physics effects by comparing with theoretical models. While the models mentioned in the discussion of the double-hump position are based on simple assumptions, a new model calculation [58] has an attempt to run a more realistic Monte Carlo simulation to describe general features of two-particle correlations. The model takes into account the fluctuation of parton energy density at initial collisions, parton cascades after initial collisions to equilibrium, and the collective expansion driven by ideal event-by-event (3+1)D hydrodynamics calculations [59], including a jet-quenching effect(energy-momentum loss) as performed in the energy-momentum loss model.

Fig.5.8 presents the short-range per trigger yield across $|\Delta\eta| < 1$ with long-range per trigger yield across $2 < |\Delta\eta| < 4$ subtracted for charged hadrons of p_T: 2-4x1-2 GeV/c obtained from the simulations [58] of Au+Au collisions at $\sqrt{s_{NN}} = 200$ GeV in 4 different centrality selections

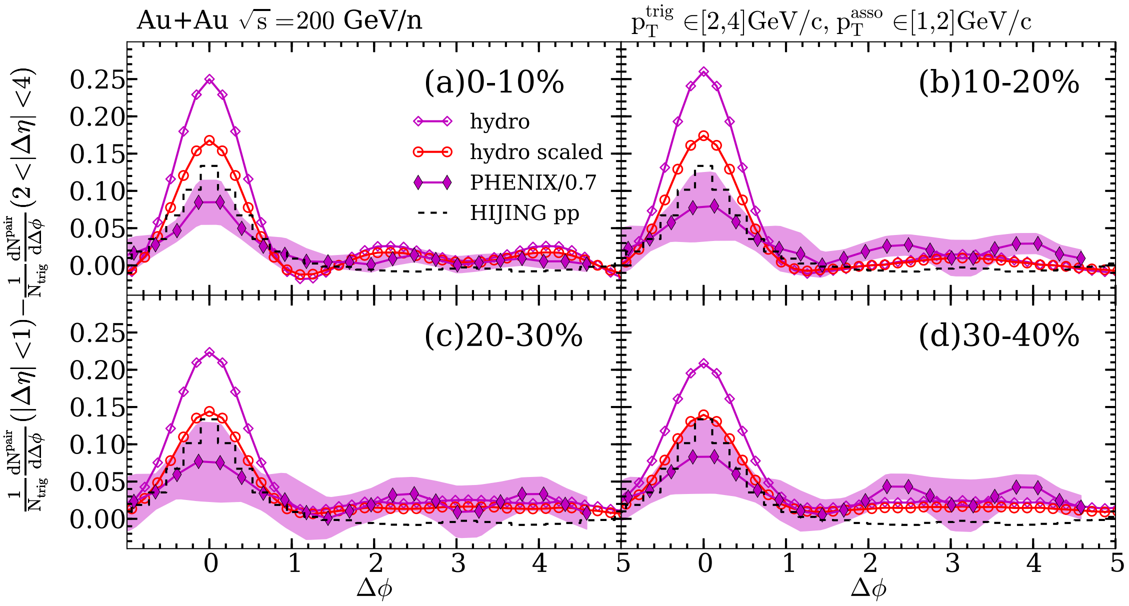

Figure 5.8: Short-range per trigger yield ($|\Delta\eta| < 1$) with long-range per trigger yield($2 < |\Delta\eta| < 4$) subtracted for charged hadrons at $p_T^a \otimes p_T^a$ = 2-4 ⊗ 1-2GeV/c from the simulations [58] of Au+Au collisions at $\sqrt{s_{NN}}$ = 200 GeV in 4 different centrality selection, compared with $v_n(n = 2, 3, 4)$ subtracted correlations by the PHENIX experiment[60].

(0-10%,10-20%,20-30%m and 40-50%). The results are compared with a scaled hydrodynamics calculation, pure HIJING simulations[51], and previous $v_n(n = 2, 3, 4)$ subtracted correlations by the PHENIX experiment[60]. The PHENIX results are scaled by 1/0.7 to employ a consistent definition of the correlation with the model calculations.

In the "hydro scaled" results in Fig.5.8, the per trigger yield is scaled by the ratio of invariant yields in associate p_T ranges of the experimental data over that of the calculation as

$$C = \frac{\left(\int^{\Delta p_T} dp_T d^2N/d\eta dp_T\right)_{Expt.}}{\left(\int^{\Delta p_T} dp_T d^2N/d\eta dp_T\right)_{Hydro}}, \tag{5.4}$$

in order to compare correlations with the same multiplicity between the experimental data and the simulation.

The away-side correlation yields are qualitatively reproduced by this model. The discrepancy in near-side is due to the different rapidity ranges between long-range correlations in the simulation ($2 < |\Delta\eta| < 4$) and the rapidity separation between central arm to the forward/backward RXN detectors at $1.0 < \eta_{EP} < 2.8$ of PHENIX flow harmonics measurements. The flow subtractions correspond to the subtraction of long-range correlations ($0.65 < |\Delta\eta| < 3.15$) due to the central arm acceptance $|\Delta\eta|$ <0.35. The weak double-hump is seen in most central 0-10% Au+Au collisions in the model calculation, however very wide and single peak is seen in other centrality ranges.

Developing this approach including physics effects in each phase of heavy ion collisions seems a right way of future theoretical calculations in order to understand the physics in heavy ion

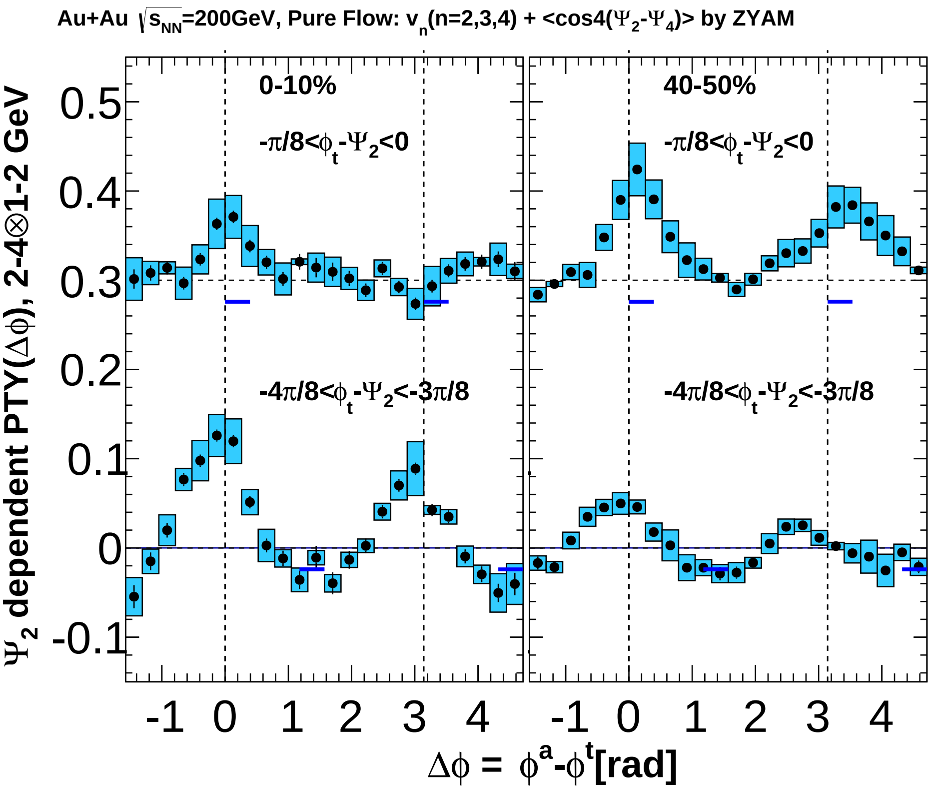

Figure 5.9: Ψ_2 dependent correlations of p_T: 2-4x1-2 GeV/c in most-central and mid-central collisions in the in-plane ($-\pi/8<\phi^t-\Psi_2<0$) and out-of-plane ($-4\pi/8<\phi^t-\Psi_2<-3\pi/8$) direction.

collisions.

5.2 Event-Plane Dependent Correlations

A selected portion of event-plane dependent correlations in Au+Au collisions at $\sqrt{s_{NN}} = 200$ GeV of trigger and associate p_T: 2-4x1-2 GeV/c are shown in Fig.5.9 for Ψ_2 dependence and in Fig.5.10 for Ψ_3 dependence.

For Ψ_2 dependent correlations, in mid-central collisions 40-50%, both near and away side correlation yields become larger in in-plane direction ($-\pi/8<\phi^t - \Psi_2<0$) compared to those in out-of-plane direction ($-4\pi/8<\phi^t - \Psi_2<-3\pi/8$), which indicates the correlation yield in mid-central collisions becomes larger with decrease of average medium thickness.

On the other hand, in most-central collisions 0-10%, both near and away side correlation yields become smaller in in-plane direction ($-\pi/8<\phi^t - \Psi_2<0$) compared to those in out-of-plane direction ($-4\pi/8<\phi^t - \Psi_2<-3\pi/8$), which indicates the correlation yield in most-central collisions becomes larger with increase of average medium thickness.

Usually, we expect the correlated yield per trigger increases from out-of-plane to in-plane direction, where the average thickness decreases, because the penetration probability of hadrons increases in the parton energy-loss framework. However, the measured yield also increases especially close to the out-of-plane direction, where the average thickness becomes the largest, which

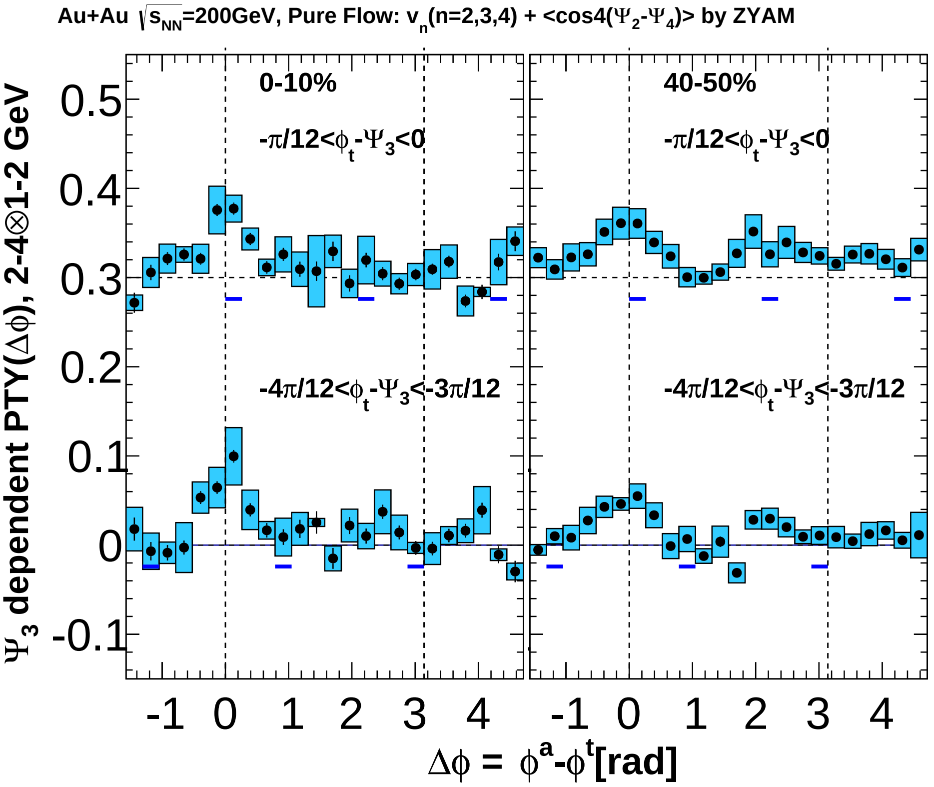

Figure 5.10: Ψ_3 dependent correlations of p_T: 2-4x1-2 GeV/c in most-central and mid-central collisions in the in-plane ($-\pi/12<\phi^t-\Psi_2<0$) and out-of-plane ($-4\pi/12<\phi^t-\Psi_2<-3\pi/12$) direction.

cannot be simply interpreted by the suppression of partons controlled by the parton energy-loss.

We need to consider the possible coexistence of re-distribution of the deposited parton energy in the longer path direction, in parallel with parton energy-loss. We also would like to mention that the near and away-side peaks of Ψ_2 dependent correlations change their positions depending on the direction of trigger particle with respect to event-planes. The gravity position of near and away-side peaks as a function of trigger angle from event-planes will be introduced in later section.

For the Ψ_3 dependent correlations, we can not see a clear trigger dependence which can be observed in Ψ_2 dependent correlations.

5.2.1 Path-length Dependence of Per Trigger Yield

For a quantitative discussion on the path-length dependence of correlation yield, integrated correlated yields at near-side($|\Delta\phi|<\pi/4$) and away-side($|\Delta\phi-\pi|<\pi/4$) as a function of absolute value of associate angle relative to event-planes are plotted in Fig.5.11 and 5.12 for Ψ_2 dependence, in Fig.5.13 and 5.14 for Ψ_3 dependence, for three different p_T combinations: 2-4x1-2, 2-4x2-4 and 4-10x2-4 GeV/c. The most out-of-plane $\phi^a-\Psi_n = -\pi/n$ corresponds to the direction of the largest path-length and the in-plane direction $\phi^a-\Psi_n = 0$ is the direction of the shortest path-length.

For the Ψ_2 dependence, the near-side correlations in p_T: 2-4x1-2 GeV/c show enhancements in out-of-plane in centrality 0-10% more than 1 σ level of the systematics. The yields in both out-of-plane and in-plane are consistent within systematic uncertainties at 20-40%, and the yield shows enhancement in in-plane direction above centrality 40% more than 1 σ level of the systematics. The centrality dependence is similar between the near and away-side. The away-side correlations show enhancements in out-of-plane in centrality 0-10% more than 1 σ level of the systematics. The yields in both out-of-plane and in-plane are consistent within systematic uncertainties at 20-30%, and the yield shows enhancement in in-plane direction above centrality 30% more than 1 σ level of the systematics. The mid-central case can be interpreted by the suppression via parton energy-loss and most-central case can be done as the re-distribution of deposited energy. In the correlations of p_T: 2-4x2-4 and 4-10x2-4 GeV/c, the yields in in-plane and in out-of-plane are consistent within systematics.

For Ψ_3 dependence, we can not see the enhancement of out-of-plane yield of both near and away-side in most-central collisions 0-10% for p_T : 2-4x1-2 GeV/c, where Ψ_2 dependent correlations show the enhancement in out-of-plane direction. The Ψ_3 dependence is not seen in mid-central collisions. For all p_T and centrality selections, Ψ_3 dependent correlations do not show Ψ_3 dependencies.

The Ψ_2 dependence seems to switch between the suppression via parton energy-loss and the energy re-distribution effects depending on centrality, while the Ψ_3 dependence is not seen.

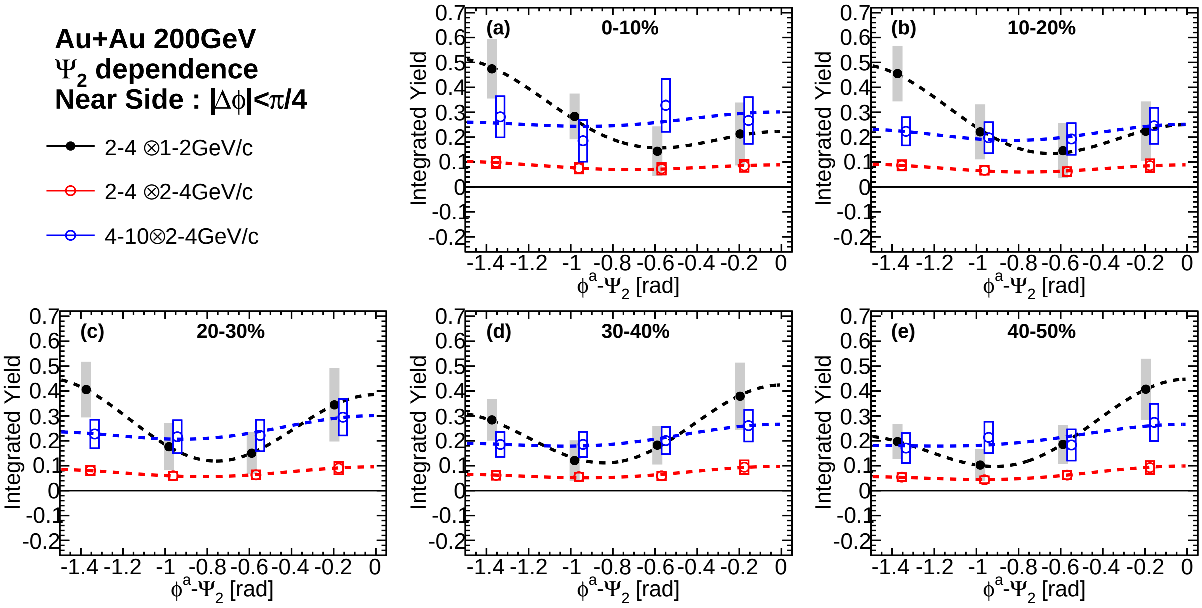

Figure 5.11: Integrated yield of near-side ($|\Delta\phi| < \pi/4$) as a functions of associate azimuth with respect to Ψ_2 for different p_T selections. The dashed curves indicate the results of Fourier fitting to each data.

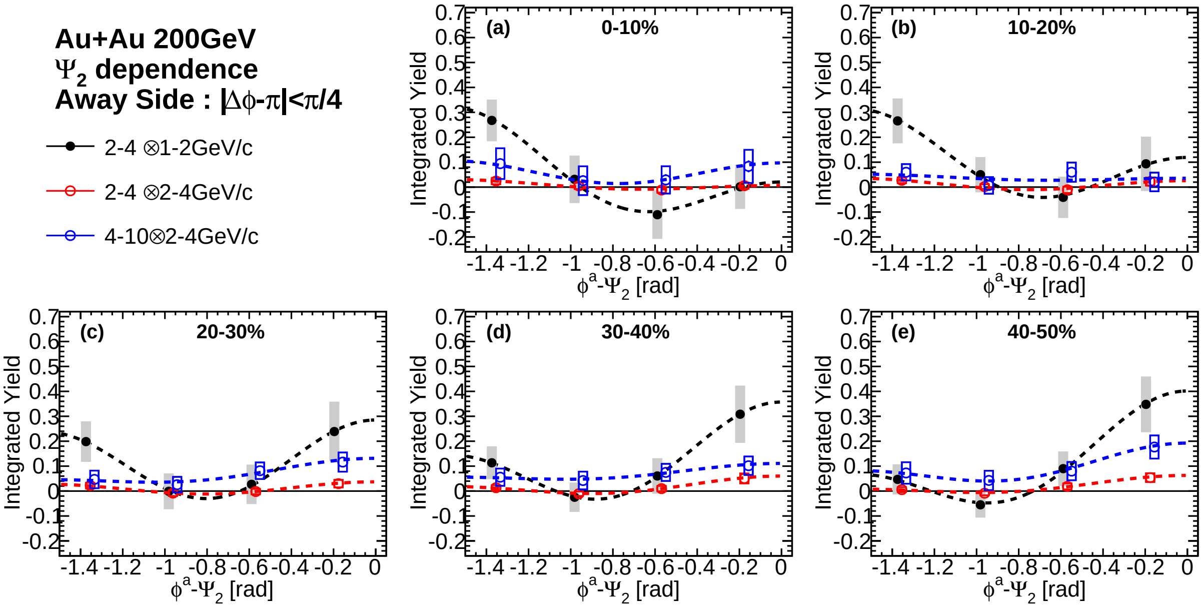

Figure 5.12: Integrated yield of away-side ($|\Delta\phi - \pi| < \pi/4$) as functions of associate azimuth with respect to Ψ_2 for different p_T selections. The dashed curves indicate the results of Fourier fitting to each data.

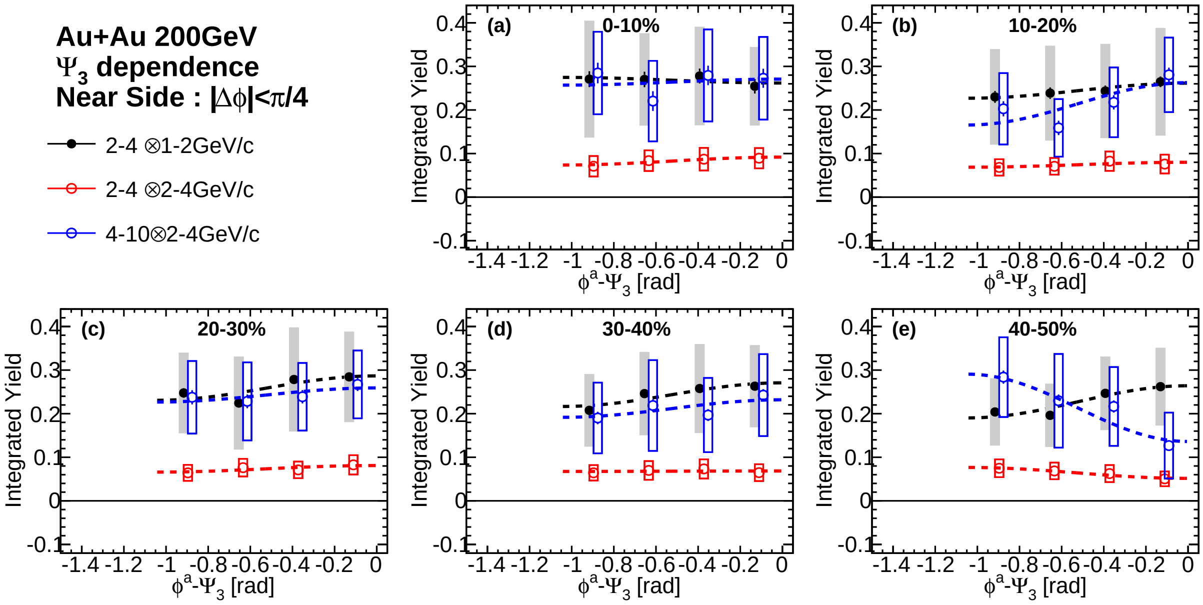

Figure 5.13: Integrated yield of near-side ($|\Delta\phi| < \pi/4$) as a functions of associate azimuth with respect to Ψ_3 for different p_T selections. The dashed curves indicate the results of Fourier fitting to each data.

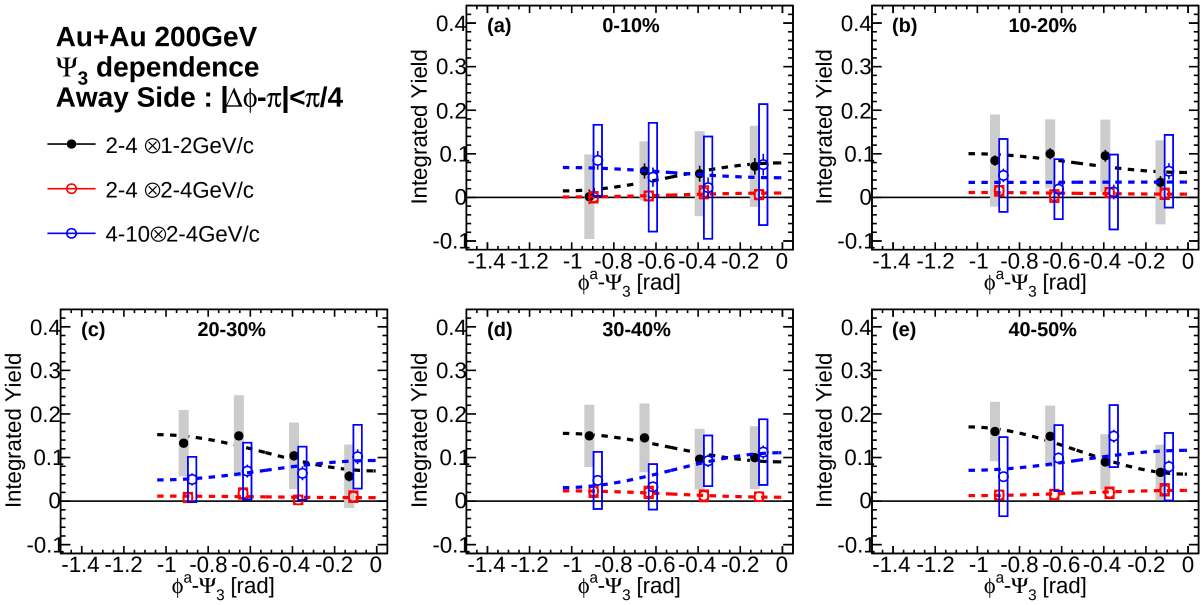

Figure 5.14: Integrated yield of away-side ($|\Delta\phi - \pi| < \pi/4$) as functions of associate azimuth with respect to Ψ_3 for different p_T selections. The dashed curves indicate the results of Fourier fitting to each data.

5.2.2 Azimuthal Anisotropy of Per Trigger Yield

In the definition of per trigger yield $\frac{1}{N^t}\frac{dN^{ta}}{d\Delta\phi}$, the number of pairs is normalized by the number of triggers, so that the dimension of par trigger yield is a number of particles. Thus, the azimuthal anisotropy of per trigger yield can be compared with that of single particles.

The azimuthal anisotropy of correlated associate yield v_n^{PTY} is obtained by Fourier fitting to the yield as a function of associate angle with respect to event-plane:$Y^{intg.}(\phi^a - \Psi_n)$. We extract v_n^{PTY} of both near and away-side using the following functions: for Ψ_2 dependent correlations

$$F(\phi^a - \Psi_2) = a\{1 + 2v_2^{PTY}\cos 2(\phi^a - \Psi_2) + 2v_4^{PTY}\cos 4(\phi^a - \Psi_2)\}, \tag{5.5}$$

and for Ψ_3 dependent correlations

$$F(\phi^a - \Psi_3) = a\{1 + 2v_3^{PTY}\cos 3(\phi^a - \Psi_3)\}, \tag{5.6}$$

where a is the average of the yields. The fitting curves are presented in Fig.5.11-5.14.

Since per trigger yield is normalized by number of triggers, v_n^{PTY} is defined by the azimuthal distribution of associate particle relative to the number of trigger particles, which also have the azimuthal distribution. Therefore, we need to add the trigger particle $v_n^t \cos n(\phi^t - \phi^a)$ to the extracted v_n^{PTY} to obtain correct anisotropy of correlated yield.

Fig.5.15 and 5.16 show the corrected v_n^{PTY} compared with charged hadron v_n via event-plane method of this analysis, v_n of hydrodynamics calculations with Glauber initial condition and $4\pi\eta/s = 0.08$, and high p_T π^0 v_2 of a previous PHENIX measurement[61].

The azimuthal anisotropy of low p_T hadron v_n is well described by the relativistic hydrodynamics and the high p_T π^0 v_2 data is consistent with a calculation based on a parton energy-loss assumption [63, 64, 65]. Therefore a comparison of azimuthal anisotropy of per trigger yield v_n^{PTY} with other experimental results and theoretical calculations is useful to discuss the behavior of a parton inside a medium.

First, we would like to point out v_2 of hydrodynamics calculation, high p_T π^0 v_2 described by parton energy-loss and hadron v_2 as superposition of those effects show always positive value. Hence negative v_2 cannot be assembled by the hydrodynamic expansion and the parton energy-loss.

The both near and away-side v_2^{PTY} of p_T 2-4x2-4, and 4-10x2-4 GeV/c are consistent with zero within systematics or positive depending on centrality selections. The near-side v_2^{PTY} of p_T: 2-4x1-2 GeV/c shows positive value than above 20% and negative value at 0-10%. This negative v_2 cannot be explained by hydrodynamics and parton energy-loss as mentioned above. This sign flipping of v_2^{PTY} indicates the mechanism of jet-medium coupling varies depending on centrality. We suggest a re-distribution effect of deposited parton energy inside a medium as a possible explanation of negative v_2^{PTY}, because the suppression via parton energy-loss can explain only the positive v_2^{PTY} and the deposited energy increases with the path length especially in central collisions and in the direction of out-of-plane. The away-side v_2 shows a similar trend in mid-central collisions, except most-central value which is consistent with 0 due to the large systematic uncertainties. The Ψ_2 dependent jet-medium coupling of near and away-side seems to be similar in mid-central collisions.

The both near and away-side v_3^{PTY} of p_T 2-4x2-4, and 4-10x2-4 GeV/c do not have enough sensitivity to be compared with measured hadron v_3 due to large systematics. The near-side

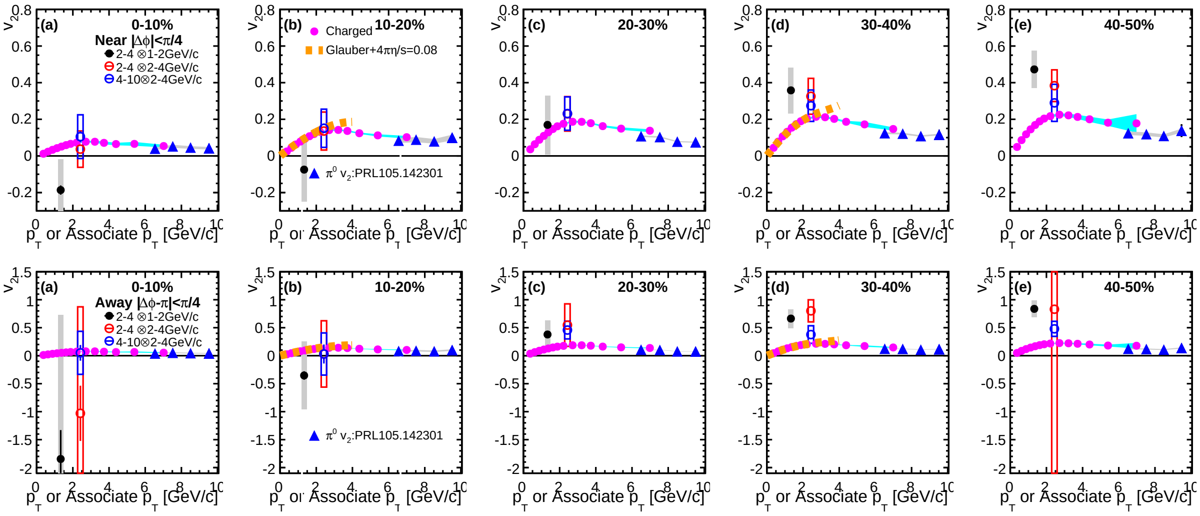

Figure 5.15: v_2^{PTY} of near and away-side correlation as a function of associate p_T for three p_T combinations, (Black) 2-4x1-2, (Red) 2-4x2-4, and (Blue) 4-10x2-4 GeV/c, compared with (Magenta) hadron v_2 via event-plane method of this analysis, (Orange-Line) hydrodynamics calculations[24], and (Blue-Triangle) high p_T π^0 v_2[61] .

v_3^{PTY} of p_T: 2-4x1-2 GeV/c shows positive value in 20-50% within measured accuracy, and the measured trend might imply that it becomes slightly larger than the single charged hadron v_3 at most 1 σ level in the most peripheral bin 40-50%. However, the away-side v_3^{PTY} shows negative value in 20-50%. The negative value is more significant than the systematic uncertainties.

We can also apply the discussion of parton energy re-distribution to explain the away-side negative v_3^{PTY}. The similarity between near and away-side of v_2^{PTY} is not observed in v_3^{PTY}, and the centrality range where negative v_n^{PTY} appears is also different between v_2^{PTY} and v_3^{PTY}. We might see a possible different jet-medium interplay in the second and third-order geometry of media.

5.2.3 Gravity Position of Event-Plane Dependent Correlations

The event-plane dependent correlations change their position of near and away-side peaks, at least, depending on the trigger azimuthal angle from Ψ_2 event-plane, as seen in Fig.5.9. The shift of near and away-side peak cannot be seen before the correlations are measured selecting trigger angle with respect to event-planes separating the sign of $\phi^t - \Psi_n$, since the information of left/right asymmetry of correlation is averaged in a measurements without differential trigger selections. This is another information the event-plane dependent correlations with sign separation can provide, in addition to the event-plane dependence of correlation yield. We expect this peak shift, together with correlation yield, also give constraints to future model calculations.

Here, we would like to mention the relation of the away-side peak shift and Mach-Cone Model. The peak shift of left/right asymmetry does not disfavor the existence of Mach-Cone effect. A mach-cone shock wave should propagate isotropically in azimuthal direction in a medium which has an ideal large enough volume, however heavy ion collision creates has a limited volume. If a super-sonic parton propagate near surface, shock-wave towards surface side cannot develop

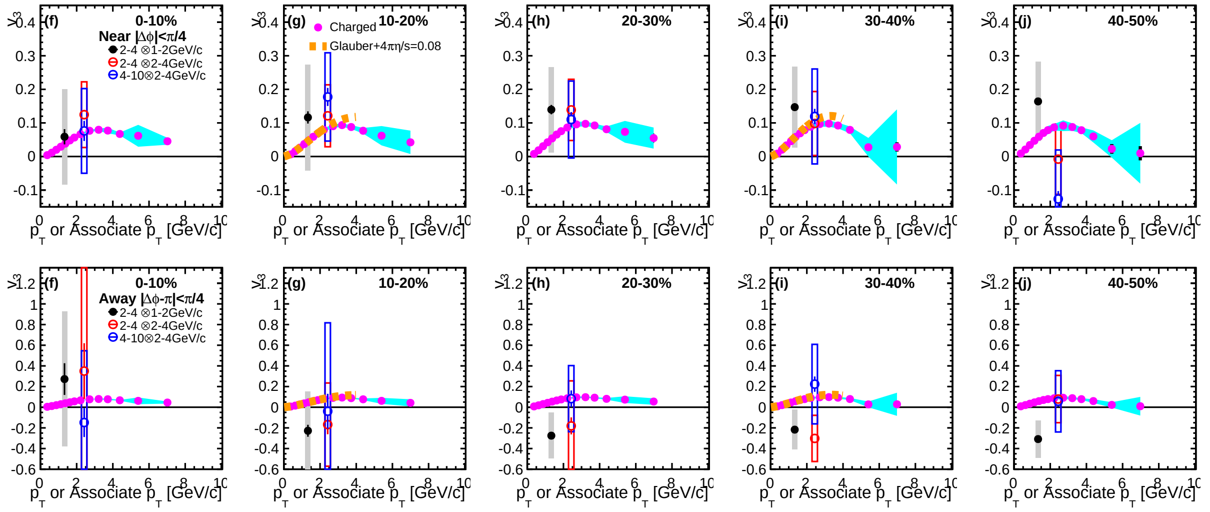

Figure 5.16: v_3^{PTY} of near and away-side correlation as a function of associate p_T for three p_T combinations, (Black) 2-4x1-2, (Red) 2-4x2-4, and (Blue) 4-10x2-4 GeV/c, compared with (Magenta) hadron v_3 via event-plane method of this analysis, (Orange-Line) hydrodynamics calculations[24].

compared to the shock-wave propagating towards the deep inside the medium. Therefore, Mach-Cone Model does not contradict the observation of left/right asymmetry.

The degree of the shift of near ($|\Delta\phi| < \pi/3$) and away-side ($|\Delta\phi - \pi| < \pi/3$) peak is quantified by the gravity position A_{LR} of correlation yield defined as

$$A_{LR} = \frac{\int d\Delta\phi \Delta\phi Y(\Delta\phi)}{\int d\Delta\phi Y(\Delta\phi)} - \begin{cases} 0 \text{ if near} - \text{side} \\ \pi \text{ if away} - \text{side} \end{cases}, \tag{5.7}$$

where $Y(\Delta\phi)$ is a correlation yield as a weight of $\Delta\phi = \phi^a - \phi^t$. The back to back position:$\Delta\phi = 0$ or $\Delta\phi = \pi$ is subtracted from the average to compare near and away-side peak shift width. The negative A_{LR} indicates that a peak has a gravity position in the negative direction of $\Delta\phi$ from the back-to-back direction *i.e.* the right side from the back-to-back direction, if we see the back-to-back direction from the center of a medium. The positive A_{LR} means the opposite direction of peak position shift. The Ψ_3 dependence of A_{LR} is also calculated in this section. The results of Ψ_2 dependence is shown in Fig.5.17 and Ψ_3 dependence is shown in Fig.5.18.

The Ψ_2 dependence of A_{LR} shows a p_T combination dependence, in which the absolute value of A_{LR} becomes smaller with increase of trigger and associate p_T combinations. The near-side A_{LR} for p_T: 2-4x1-2 GeV/c is negative or consistent with 0 independent of trigger angle in most-central collisions. While the A_{LR} in out-of-plane trigger selections remains always negative in all centrality, that in in-plane trigger selections gets larger with increase of centrality and becomes positive above centrality 30%. The A_{LR} of two out-of-plane trigger selections are negative and that of two in-plane trigger selections are positive in mid-central collisions. A similarity is seen in away-side peak, the sign flip of A_{LR} depending trigger angle is also seen for p_T: 2-4x1-2 GeV/c in mid-central collisions. Due to large statistical and systematic uncertainties, no conclusion on the peak shift for p_T: 2-4x2-4 and 4-10x2-4 GeV/c can be made. They are currently consistent with 0, which indicate no shift of peak.

The Ψ_3 dependence of A_{LR} also shows a p_T combination dependence, in which the absolute value of A_{LR} becomes smaller with increase of trigger and associate p_T combinations. The values of near and away-side A_{LR} for p_T: 2-4x1-2 GeV/c are always negative and there is no sign change with increase of centrality unlike Ψ_2 dependence. Again due to large statistical and systematic uncertainties, no conclusion on the away-side peak shift of p_T: 2-4x2-4 and 4-10x2-4 GeV/c can be made. They are currently consistent with 0, which indicate no peak shift.

Fig.5.19 and 5.20 show the per trigger yield in polar coordinate with an offset for p_T: 2-4x1-2 GeV/c, where the peak shift is clearly seen. From the Ψ_2 dependent correlations in mid-central collisions, we can find both the near and away-side of in-plane triggered correlations shift to in-plane direction and those of out-of-plane triggered correlations shift to out-of-plane direction. This observation corresponds to the positive A_{LR} of in-plane trigger selections in mid-central collisions, which is consistent with the increase of v_2^{PTY} because the yield in in-plane increases. On the other hand, in most-central collisions, the near-side peak does not seem to shift to the in-plane direction, which is consistent with possible negative or zero v_2^{PTY}.

However, the Ψ_3 dependent correlations show different trends of peak shifts. The near-side peak always shifts to out-of-plane direction and the away-side does to in-plane direction, independent of trigger angle and centrality. This observation can be interpreted that near-side always shifts to longer path length direction and the away-side does to shorter path length direction, where the interpretation of this A_{LR} is different from that of v_3^{PTY}. Note that here we discuss the gravity position of correlations A_{LR}, not the absolute value of yields, so that the different Ψ_3 dependence of near and away-side between correlation yield and A_{LR} does not mean a contradiction because the suppression via parton energy-loss and energy re-distribution should coexist. For example Ψ_3 dependence of near-side in centrality 40-50%, the correlation yield appears to be determined by suppression and the gravity position of correlation *i.e.* correlations shape seems to be determined by the energy re-distribution. The correlation yield and shape may show different sensitivity to those two effects in the Ψ_3 dependent case.

We can interpret these observations of A_{LR} as following; while the Ψ_2 dependence of A_{LR} in both near and away-side sense same effects: suppression via parton energy-loss or energy re-distribution effects depending on the trigger angle, Ψ_3 dependence of A_{LR} in near-side senses energy re-distribution effect and that in the away-side does the both suppression in parallel despite of the same trigger angle. This difference between Ψ_2 and Ψ_3 dependence of A_{LR}, also seen in correlation yield *i.e.* v_2^{PTY} and v_3^{PTY}, is the first remarkable observation. The flip of interpretations of near and away-side between v_3^{PTY} and the Ψ_3 dependent A_{LR} is the second remarkable observations.

We have seen the different behavior of v_2^{PTY} and v_3^{PTY} as well as the different peak shifts A_{LR} with respect to the Ψ_2 and Ψ_3, through the analysis performed in this thesis. The analysis results might indicate the different jet-medium interplay in the second and third-order geometry of media are reflected in the event-plane dependent correlations.

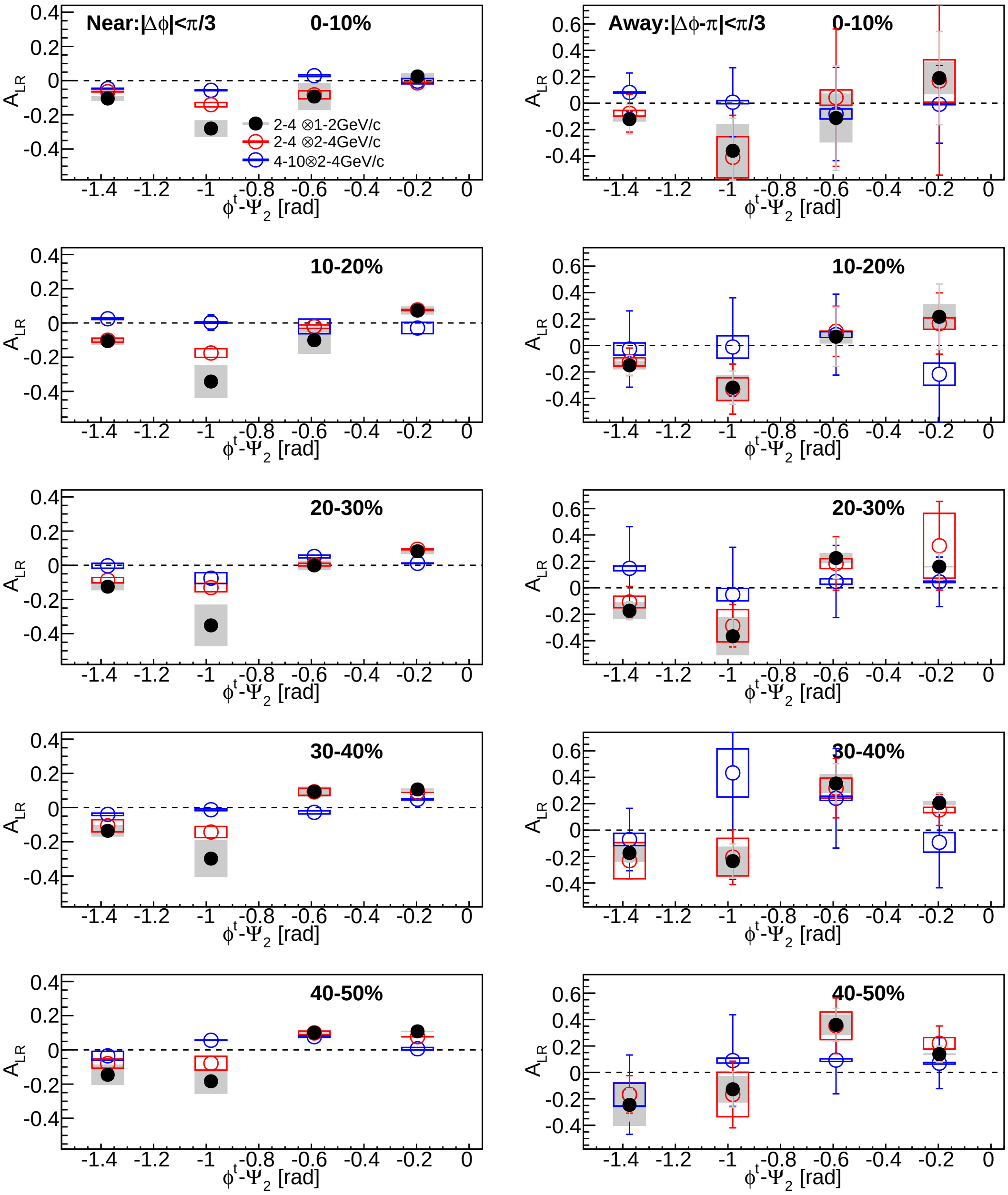

Figure 5.17: The gravity position of near and away-side per trigger yield, from back-to-back direction of near-side:$\Delta\phi$=0 and away-side:$\Delta\phi$=π, as a functions of trigger azimuthal angle with respect to Ψ_2.

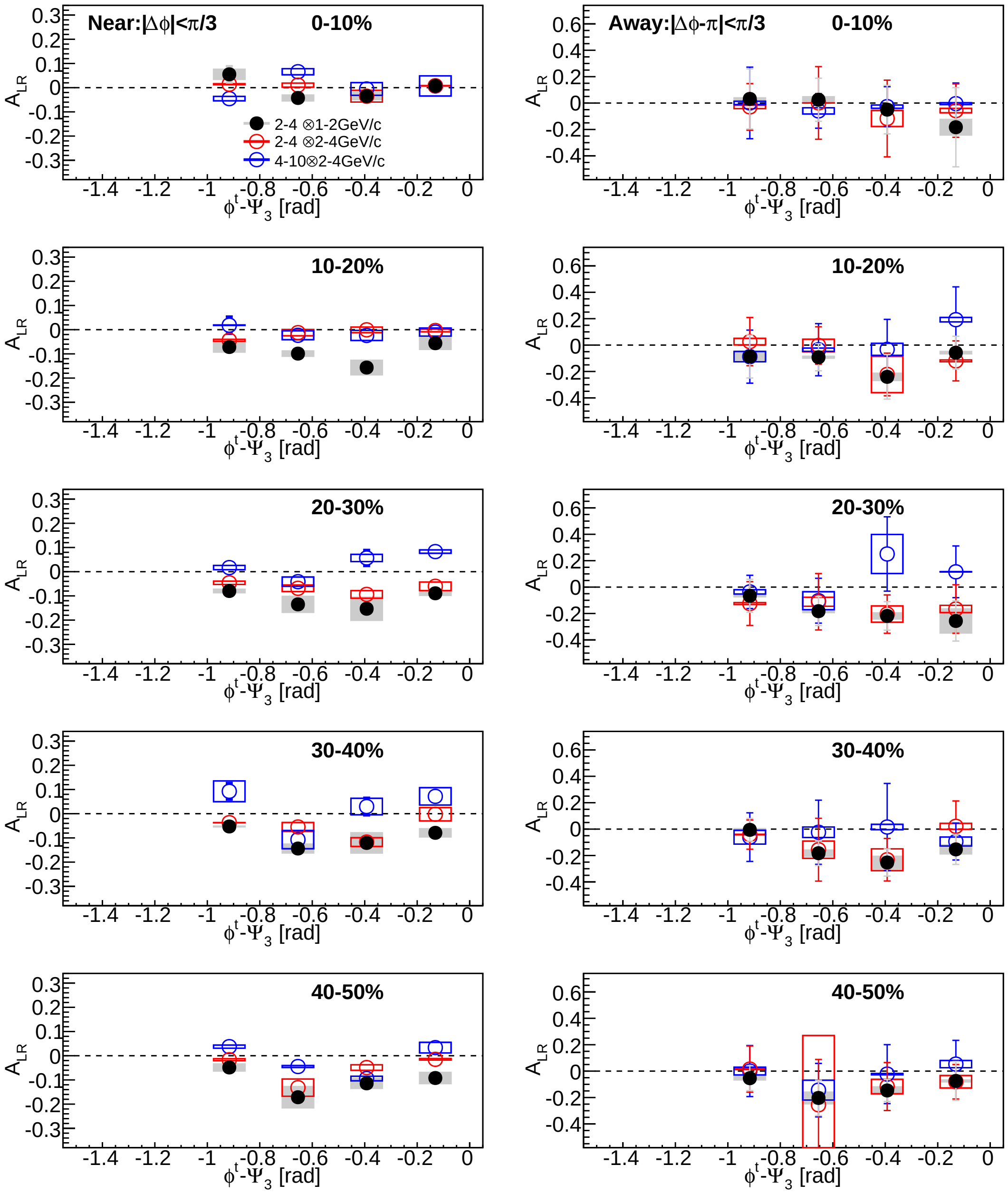

Figure 5.18: The gravity position of near and away-side per trigger yield, from back-to-back direction of near-side:$\Delta\phi$=0 and away-side:$\Delta\phi$=π, as a functions of trigger azimuthal angle with respect to Ψ_3.

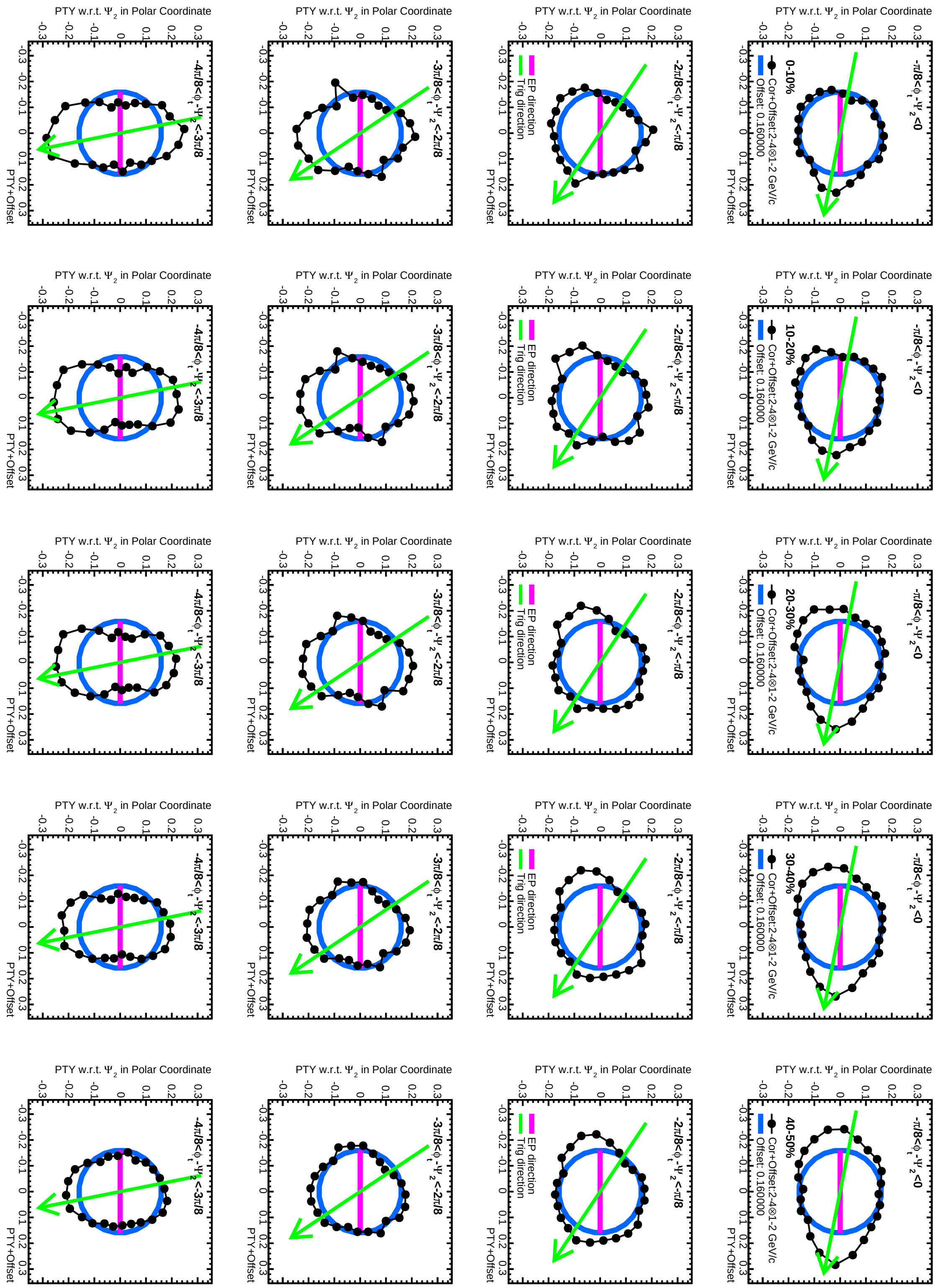

Figure 5.19: The Ψ_2 dependent per trigger yield with an offset (blue-circle) for p_T: 2-4x1-2 GeV/c in polar coordinate. The magenta lines indicate the direction of event-plane. The green arrows indicate the direction of the trigger angle and its back-to-back direction.

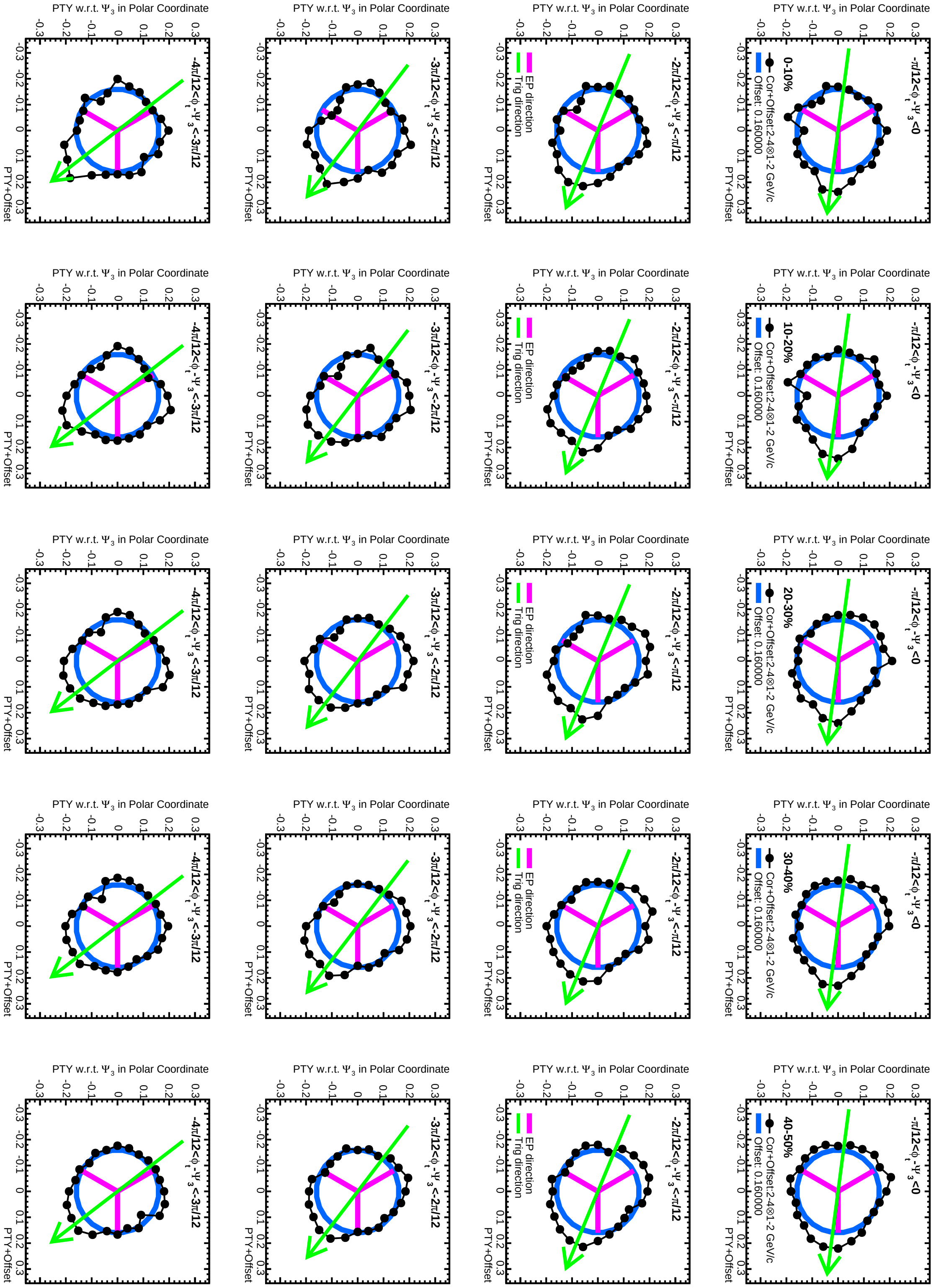

Figure 5.20: The Ψ_3 dependent per trigger yield with an offset (blue-circle) for p_T: 2-4x1-2 GeV/c in polar coordinate. The magenta lines indicate the direction of event-plane. The green arrows indicate the direction of the trigger angle and its back-to-back direction.

Chapter 6

Conclusion

Two-particle charged hadron correlations in Au+Au collisions at $\sqrt{s_{NN}} = 200$ GeV have been measured with the data obtained by the RHIC-PHENIX Experiment in 2007, with a subtraction of backgrounds from $v_n (n = 2, 3, 4)$. The rapidity gap between trigger and associate particles in this measurement is $|\Delta\eta| < 0.7$.

The representing results of the two-particle correlations at high-p_T trigger particles of p_T =4-10 GeV/c are as following:

- suppression of away-side in most-central collisions at 0-10%,
- single-peaked away-side similar to that in p+p collisions at centrality 10-50%.

On the other hand, correlations with intermediate-p_T trigger particles of $p_T < 4$ GeV/c show the following features:

- suppressed or broadened away-side in most-central collisions at 0-10%,
- double-hump structures of away-side at centrality 10-50%.

The significance of latter feature is observed at most 1σ level in terms of the systematics in v_4 measurements.

The position of the double-hump structure is estimated by the two Gaussian fitting to away-side correlations ($\pi/2 < |\Delta\phi - \pi| < 3\pi/2$) and compared with four theoretical calculations. The double-hump position of experimental data above associate at p_T=1 GeV/c is approximately more than 4 times larger than that of Cherenkov-Gluon-Radiation. The p_T independence seen in the experimental data is also seen in Mach-Cone and Energy-Momentum Loss model, and their opening angle is about 20% larger and smaller than the experimental data, respectively. The opening angle of Hot-Spot Model is almost 50% larger than the experimental results.

A recent model including initial fluctuation, parton cascade, event-by-event ideal (3+1)D hydrodynamic expansion, and parton energy-momentum loss in medium also succeeded to explain the qualitative shape of away-side of the experimental results in p_T: 2-4x1-2 GeV/c. The success of this model is an important progress because the superposition of the realistic effects in each phase of heavy ion collisions can reproduce the experimental data without a strong assumption of a parton behavior inside a medium.

The two-particle correlations with a trigger selection with respect to second and third-order event-planes are also measured for three p_T combinations of p_T: 2-4x1-2, 2-4x2-4, and 4-10x2-4 GeV/c. The representing results of Ψ_2 dependent correlations of p_T 2-4x1-2 GeV/c are as following;

- yield increases close to in-plane direction of Ψ_2 especially for mid-central to peripheral collisions,
- yield increases close to out-of-plane direction of Ψ_2 especially for most-central collisions.

The increase of in-plane yield from central to peripheral collisions, where the average path length decreases, can be taken as the increase of penetration probability due to less parton energy loss. While the increase of out-of-plane yield in central collisions, where the average path length becomes larger, can be regarded as a result of possible increase of re-distribution of the lost energy in the long path-length. Neither of this clear path-length dependence is seen in Ψ_3 dependent correlations.

The azimuthal anisotropy of correlated associate yield v_n^{PTY} with respect to Ψ_2 and Ψ_3 is calculated from the event-plane dependent correlations. We see following features in v_n^{PTY} via correlations in p_T: 2-4x1-2 GeV/c:

- positive near and away-side v_2^{PTY} above centrality 20% and negative near-side one in centrality 0-10%,
- positive near-side v_3^{PTY} but negative away-side v_3^{PTY} above centrality 20%.

The negative v_2^{PTY} cannot be explained by hydrodynamics or the suppression via parton-energy loss because the v_2 values calculated by both effects are positive: we need to consider an effect neither hydrodynamics nor the suppression. The centrality and near-away dependence of v_n^{PTY} is different between Ψ_2 and Ψ_3 dependent correlations, which may suggest parton-medium coupling is different in the second and third-order geometry of a media.

The peak shift of near and away-side correlations is also seen depending on trigger direction. A value A_{LR} to quantify the degree of peak shift is compared between Ψ_2 and Ψ_3 dependent correlations. A_{LR} of Ψ_2 dependent correlations shows the sign change depending on trigger direction on the other hand that of Ψ_3 dependent correlations is always negative. This value also shows different trend between Ψ_2 and Ψ_3 dependent correlations.

We suggest the importance of considering the re-distribution effect of lost parton energy and the different jet-medium interplay in the second and third-order geometry of media in future theoretical calculations.

As a possible future improvements of experimental measurement, we mention the following points. First, the systematics of higher-order flow measurements could be improved by the Forward Silicon Vertex detector operated since 2012 experiment of the PHENIX due to a fine granularity compared to the previous event-plane detectors. Second, the systematics in flow measurements could be ignored by using a subtraction technique of correlations with large rapidity gap from correlations with short rapidity gap, since the correlations with large rapidity gap automatically include the contributions from all higher-order flow harmonics thus helping in an exclusion of systematics in flow measurements. The both improvements will be achievable in the “sPHENIX Experiment”: a future upgrade of the PHENIX Experiment and the STAR Experiment at RHIC as well as the ATLAS and CMS at the LHC.

Appendix A

Systematic Uncertanities of Two-Particle Correlations

A.1 Systematic Uncertainties in Two Particle Correlations

A.1.1 Systematic from Matching Cut (Inclusive Trigger)

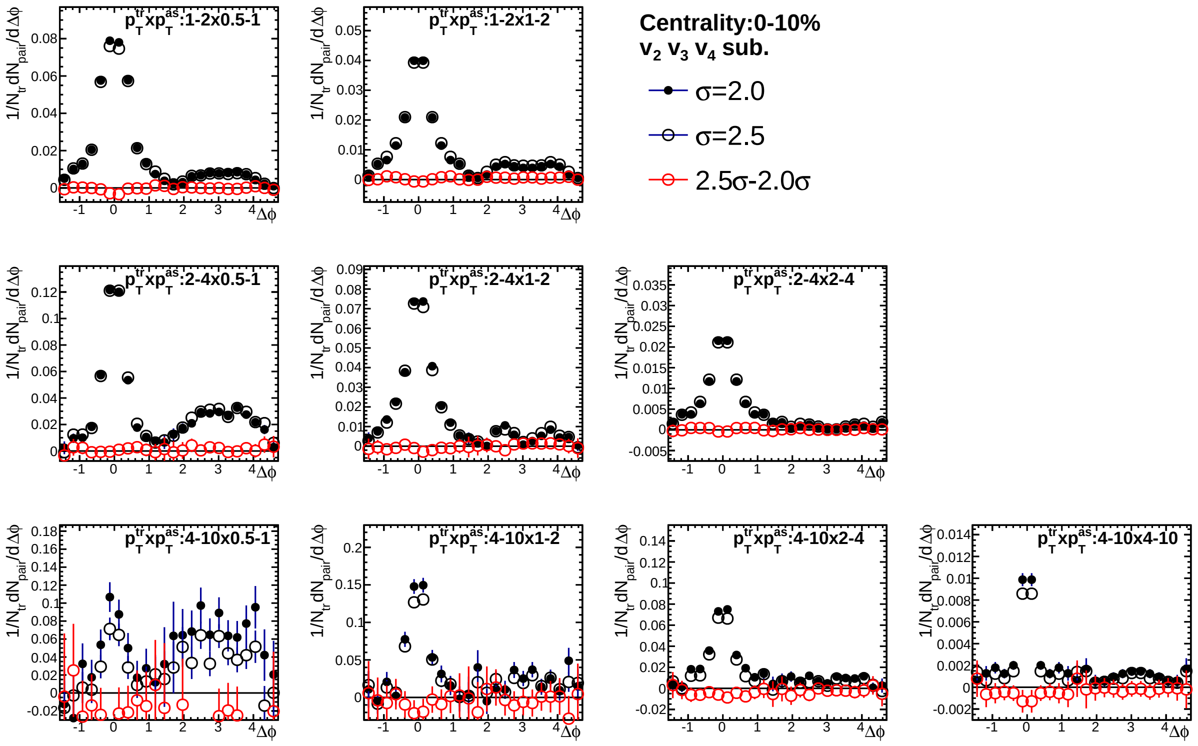

Figure A.1: Correlations where contributions of v_2, v_3 and v_4 is subtracted in centrality 0-10% with (Solid-Black) 2σ matching cut, (Opened-Black) 2.5σ matching, and (Red) difference of those.

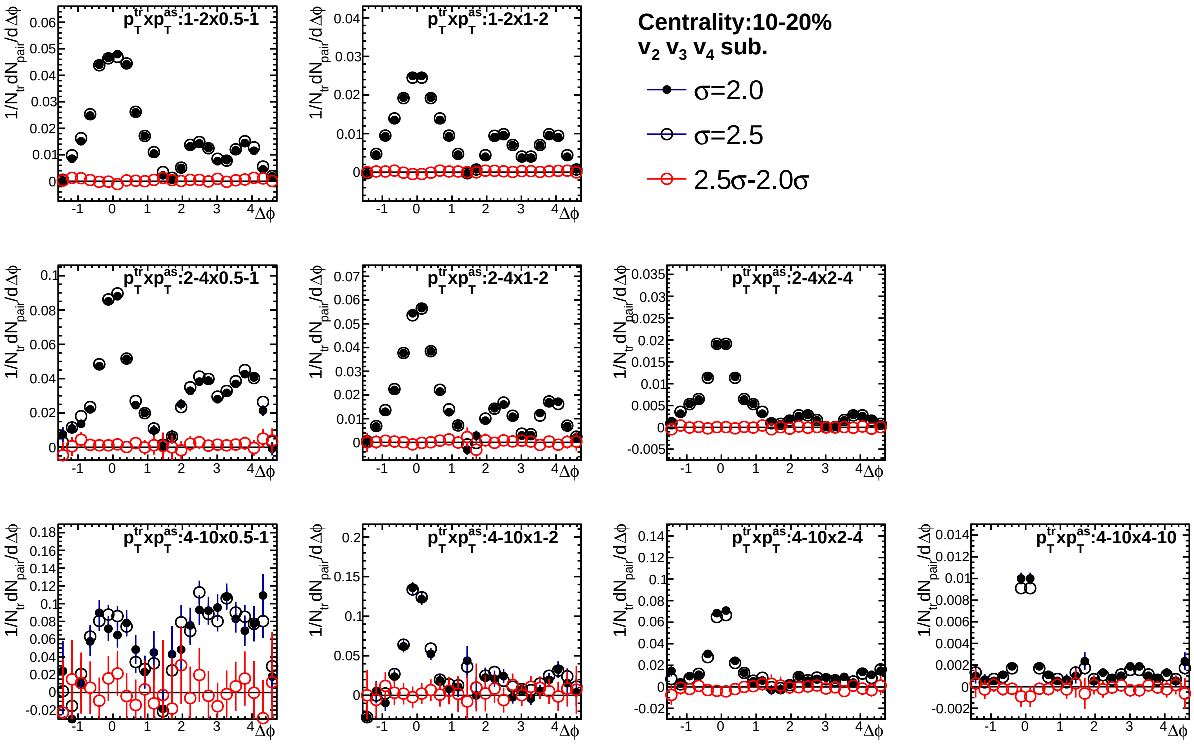

Figure A.2: Correlations where contributions of v_2, v_3 and v_4 is subtracted in centrality 10-20% with (Solid-Black) 2σ matching cut, (Opened-Black) 2.5σ matching, and (Red) difference of those.

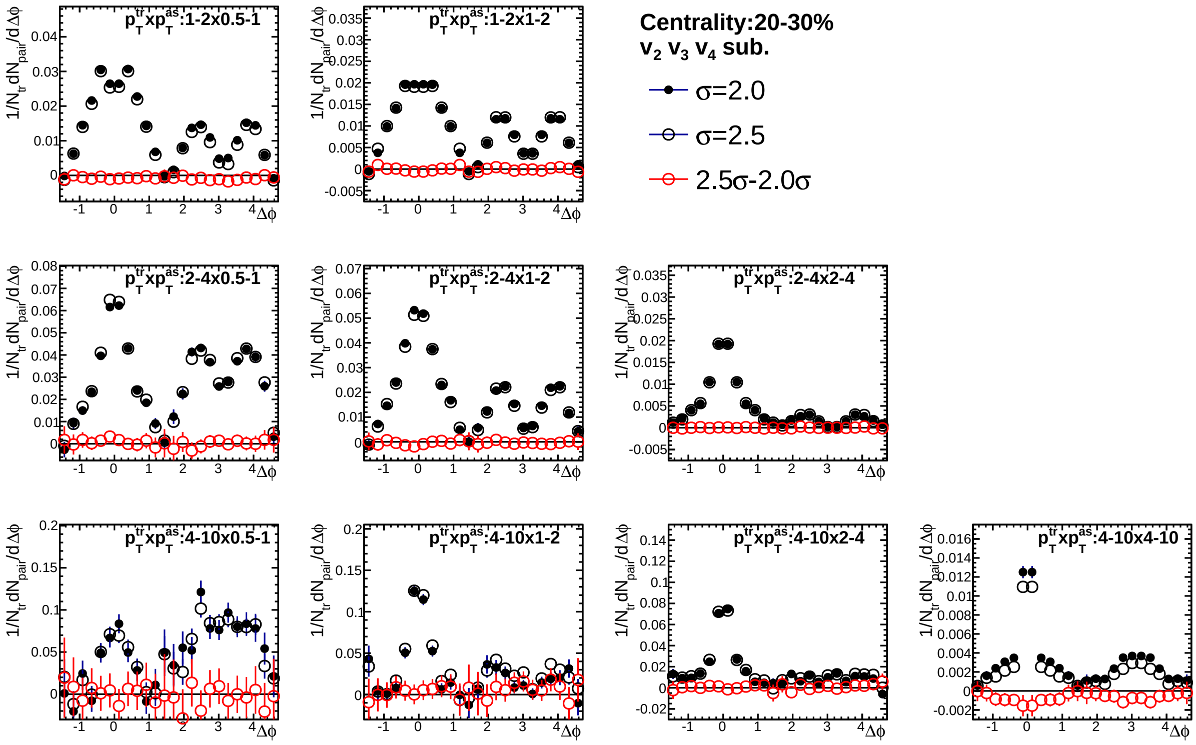

Figure A.3: Correlations where contributions of v_2, v_3 and v_4 is subtracted in centrality 20-30% with (Solid-Black) 2σ matching cut, (Opened-Black) 2.5σ matching, and (Red) difference of those.

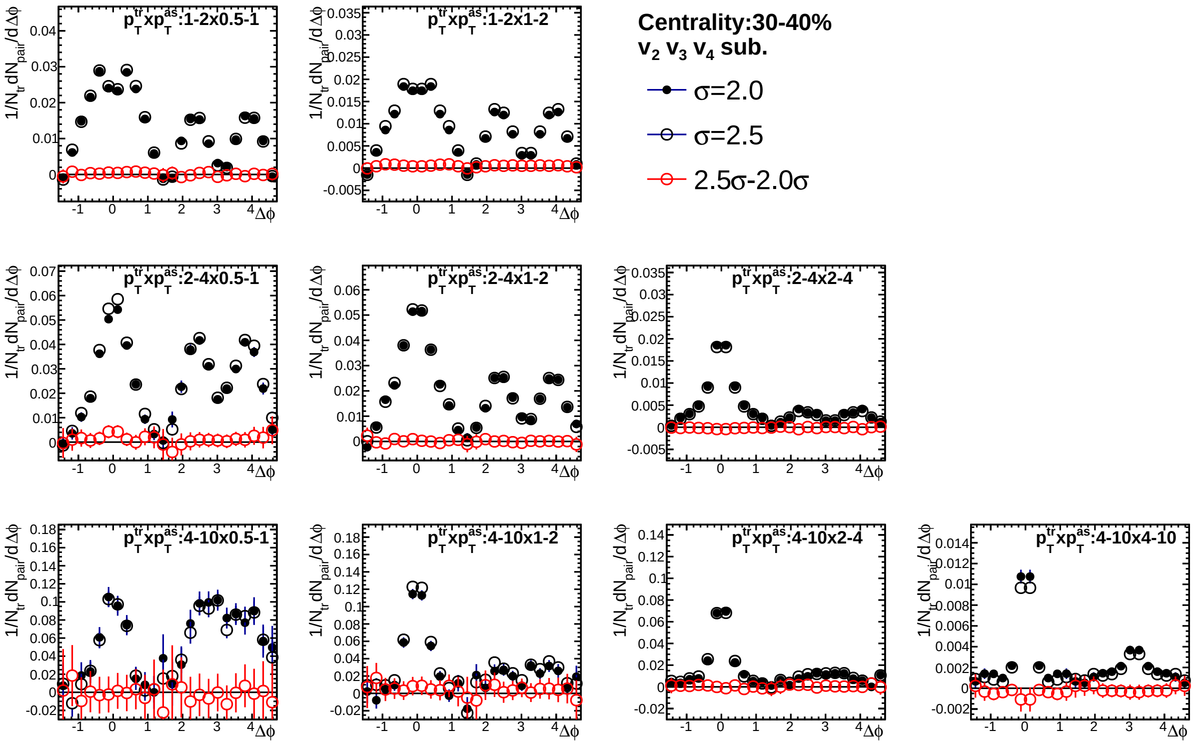

Figure A.4: Correlations where contributions of v_2, v_3, and v_4 is subtracted in centrality 30-40% with (Solid-Black) 2σ matching cut, (Opened-Black) 2.5σ matching, and (Red) difference of those.

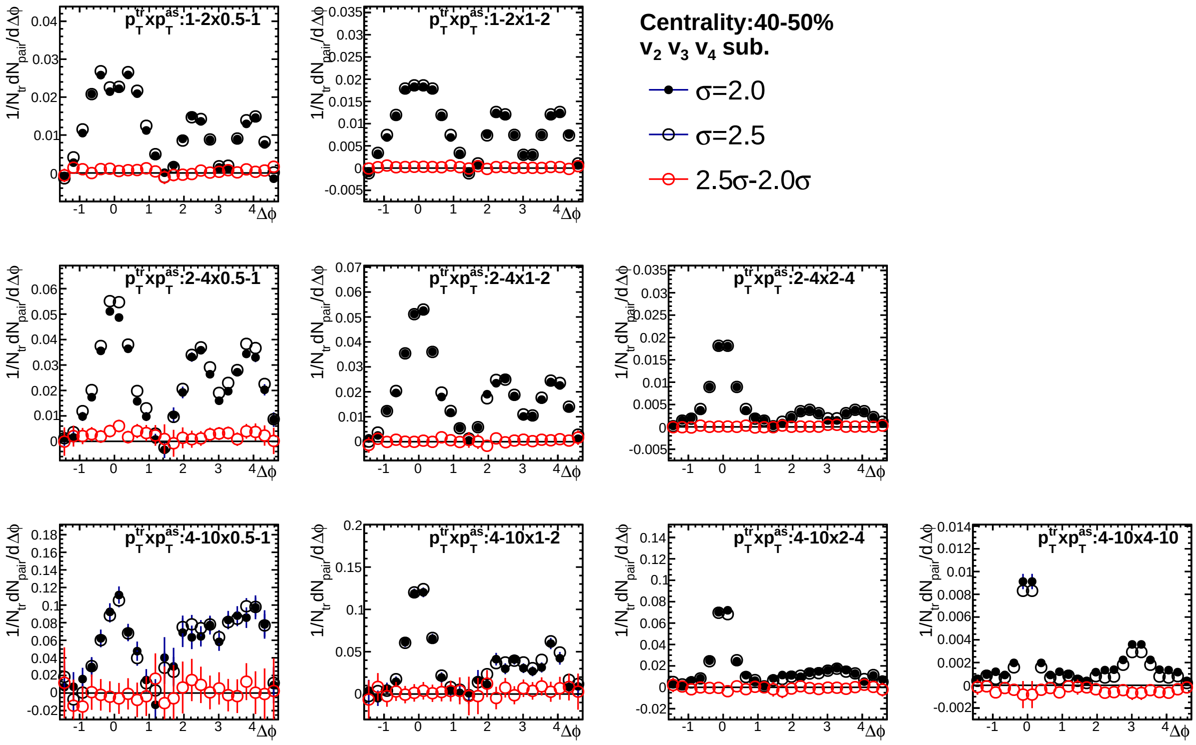

Figure A.5: Correlations where contributions of v_2, v_3, and v_4 is subtracted in centrality 40-50% with (Solid-Black) 2σ matching cut, (Opened-Black) 2.5σ matching, and (Red) difference of those.

A.1.2 Systematic from Flow Harmonics (Inclusive Trigger)

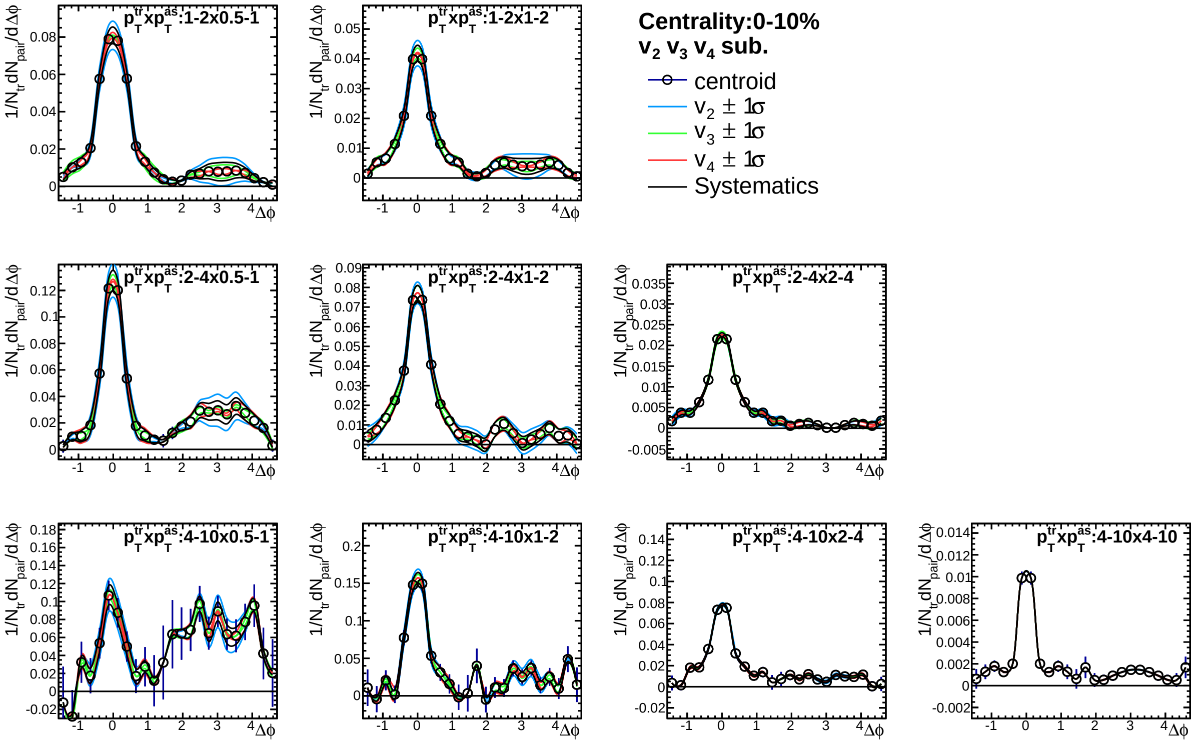

Figure A.6: Per trigger pair yield where contributions of v_2, v_3, and v_4 is subtracted in centrality 0-10%. v_n value is varied (blue-line) $v_2 \pm 1\sigma$ (green-line) $v_3 \pm 1\sigma$, and (red-line) $v_4 \pm 1\sigma$, other harmonics being fixed. Systematics are expressed by black lines.

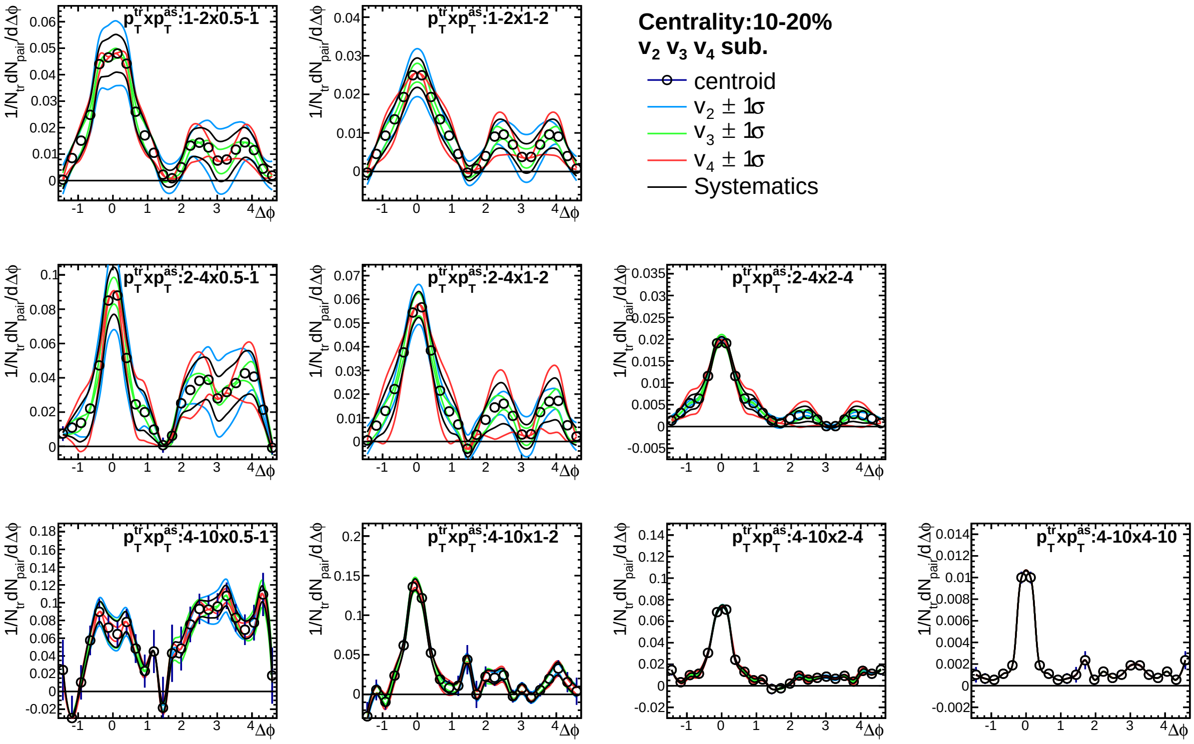

Figure A.7: Per trigger pair yield where contributions of v_2, v_3, and v_4 is subtracted in centrality 10-20%. v_n value is varied (blue-line) $v_2 \pm 1\sigma$ (green-line) $v_3 \pm 1\sigma$, and (red-line) $v_4 \pm 1\sigma$, other harmonics being fixed. Systematics are expressed by black lines.

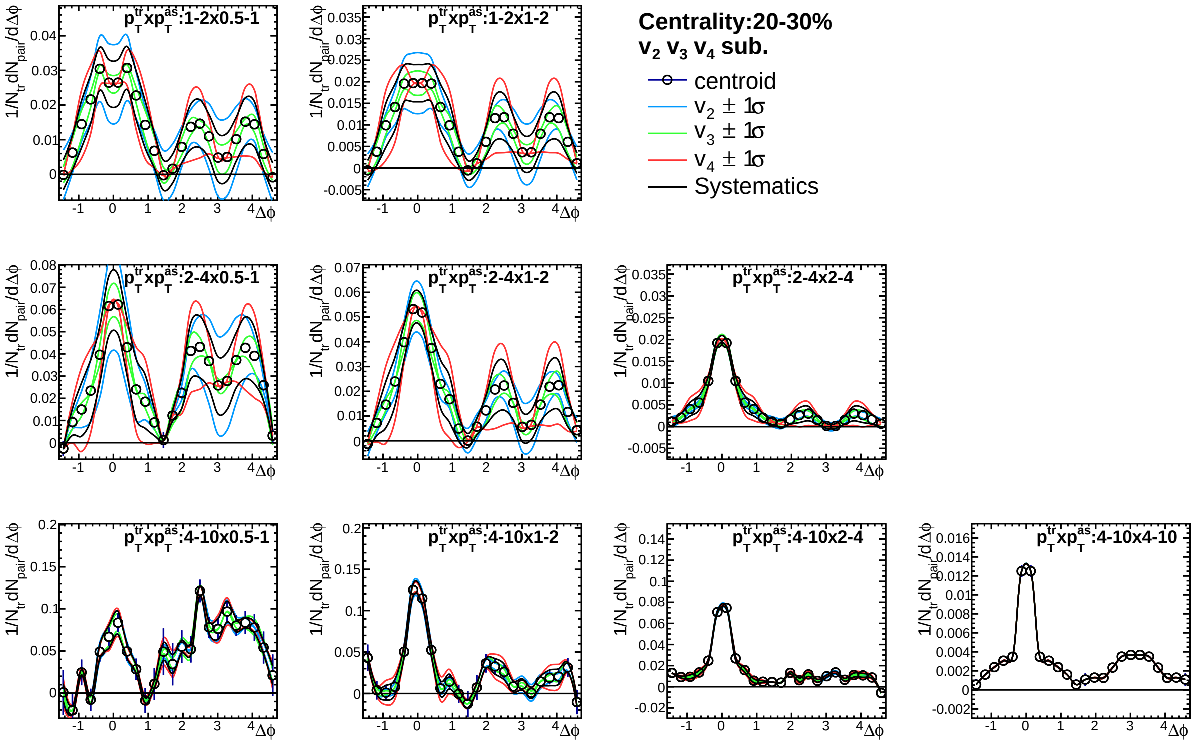

Figure A.8: Per trigger pair yield where contributions of v_2, v_3, and v_4 is subtracted in centrality 20-30%. v_n value is varied (blue-line) $v_2 \pm 1\sigma$ (green-line) $v_3 \pm 1\sigma$, and (red-line) $v_4 \pm 1\sigma$, other harmonics being fixed. Systematics are expressed by black lines.

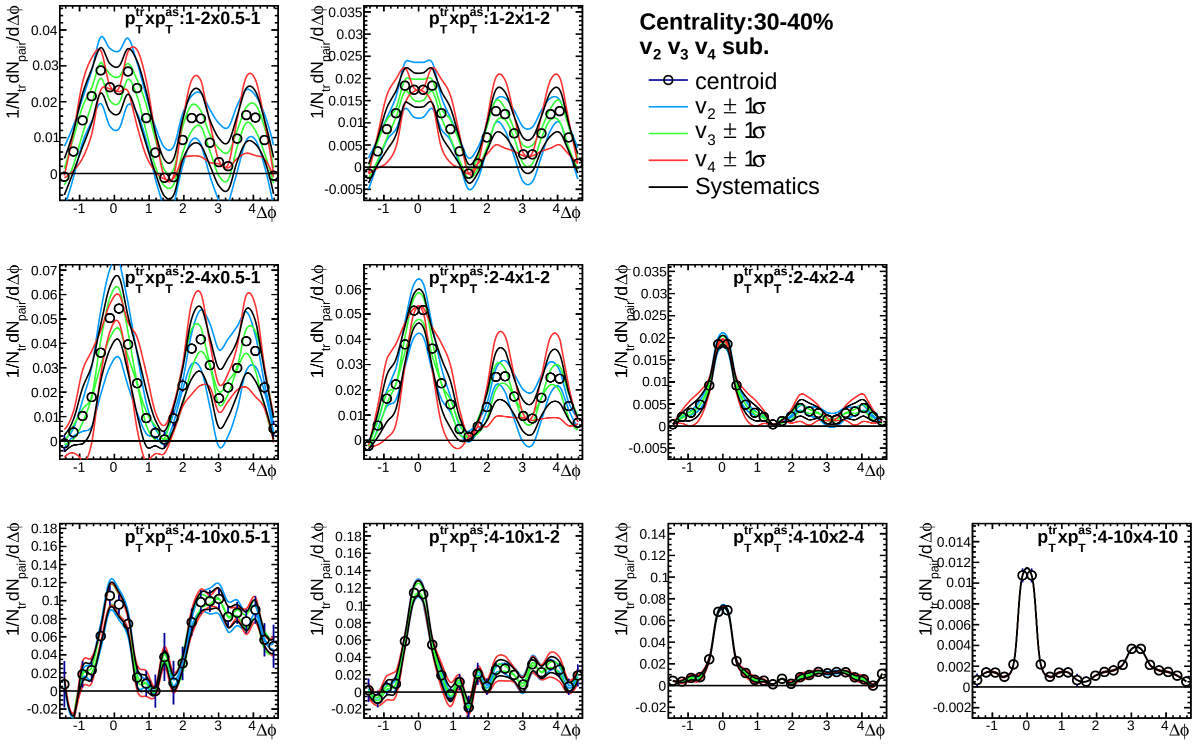

Figure A.9: Per trigger pair yield where contributions of v_2, v_3, and v_4 is subtracted in centrality 30-40%. v_n value is varied (blue-line) $v_2 \pm 1\sigma$ (green-line) $v_3 \pm 1\sigma$, and (red-line) $v_4 \pm 1\sigma$, other harmonics being fixed. Systematics are expressed by black lines.

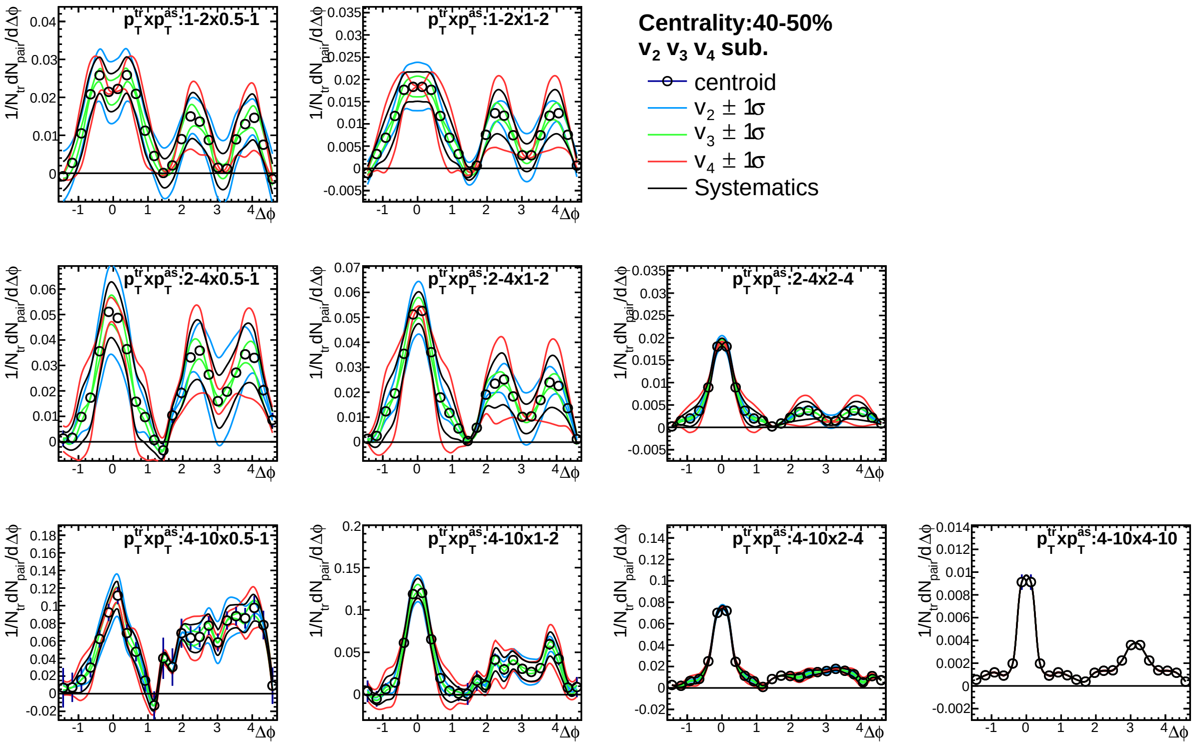

Figure A.10: Per trigger pair yield where contributions of v_2, v_3, and v_4 is subtracted in centrality 40-50%. v_n value is varied (blue-line) $v_2 \pm 1\sigma$ (green-line) $v_3 \pm 1\sigma$, and (red-line) $v_4 \pm 1\sigma$, other harmonics being fixed. Systematics are expressed by black lines.

A.2 Systematic Uncertainties in Event Plane Dependent Correlations

A.2.1 Systematics from Matching Cut (Event-Plane Dependent)

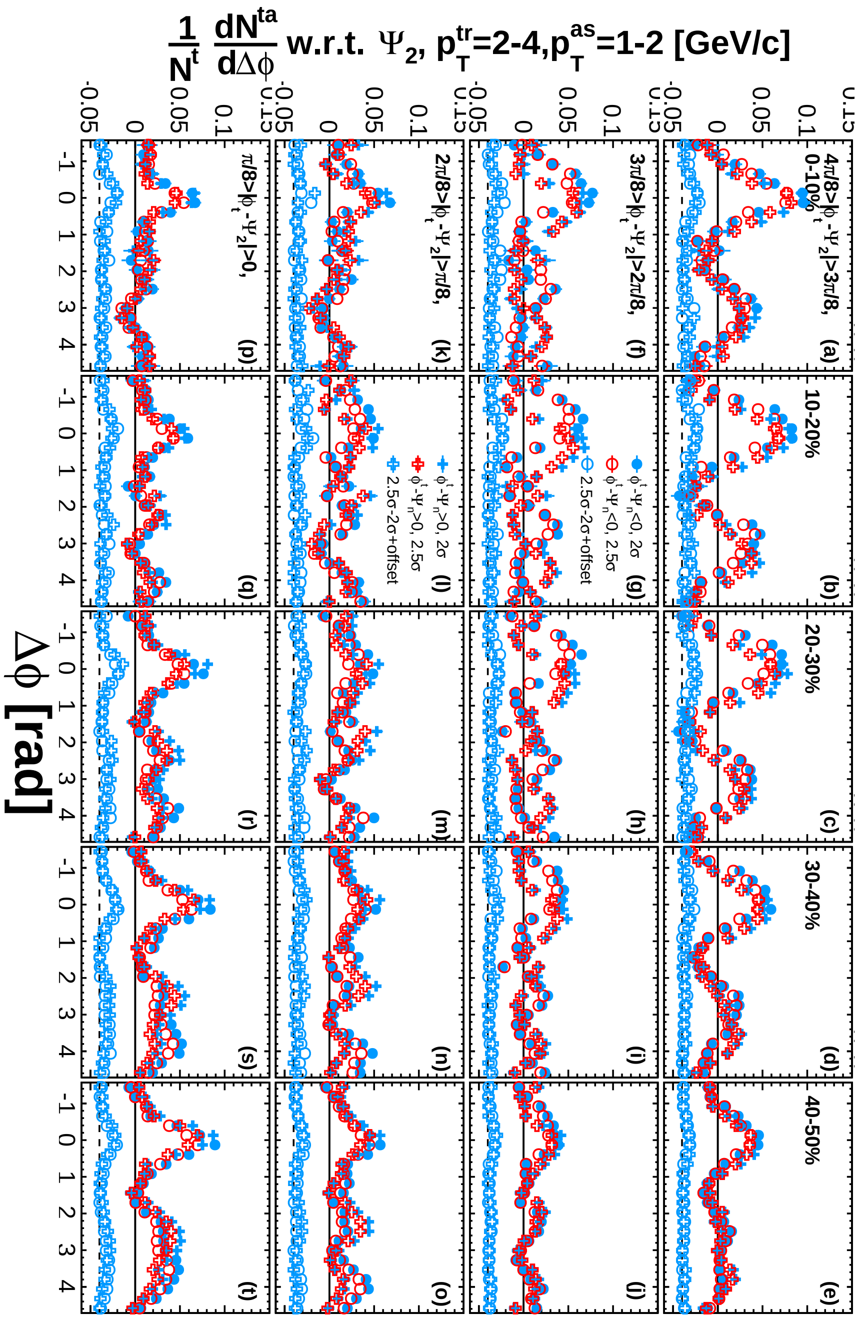

Figure A.11: Ψ_2 dependent correlations at 2-4⊗1-2 GeV/c before resolution correction where contributions of v_2, v_3, and v_4 is subtracted using (Black) 2σ matching cut, (Red) 2.5σ matching, and (Blue) difference of those.

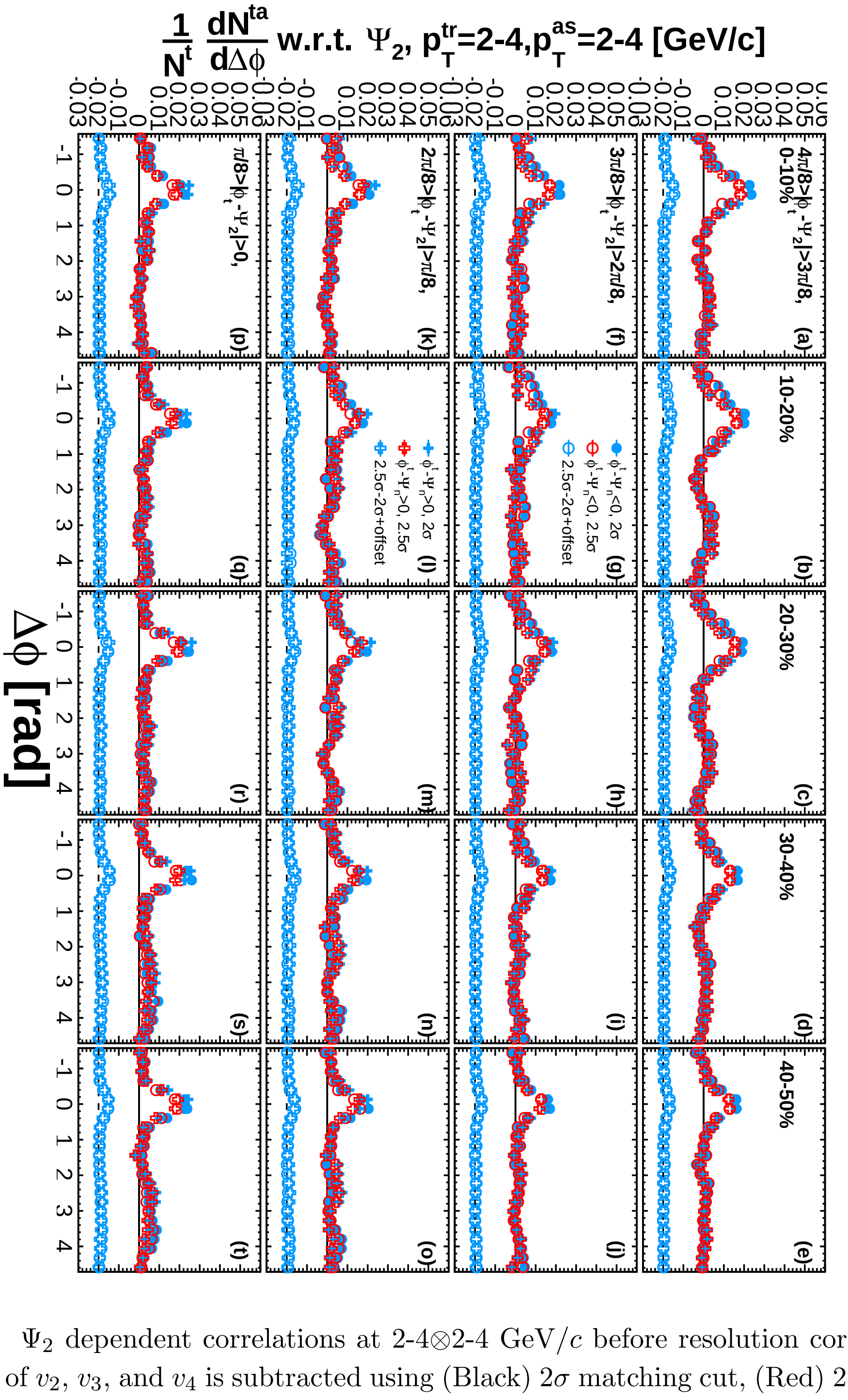

Figure A.12: Ψ_2 dependent correlations at 2-4$\otimes$2-4 GeV/c before resolution correction where contributions of v_2, v_3, and v_4 is subtracted using (Black) 2σ matching cut, (Red) 2.5σ matching, and (Blue) difference of those.

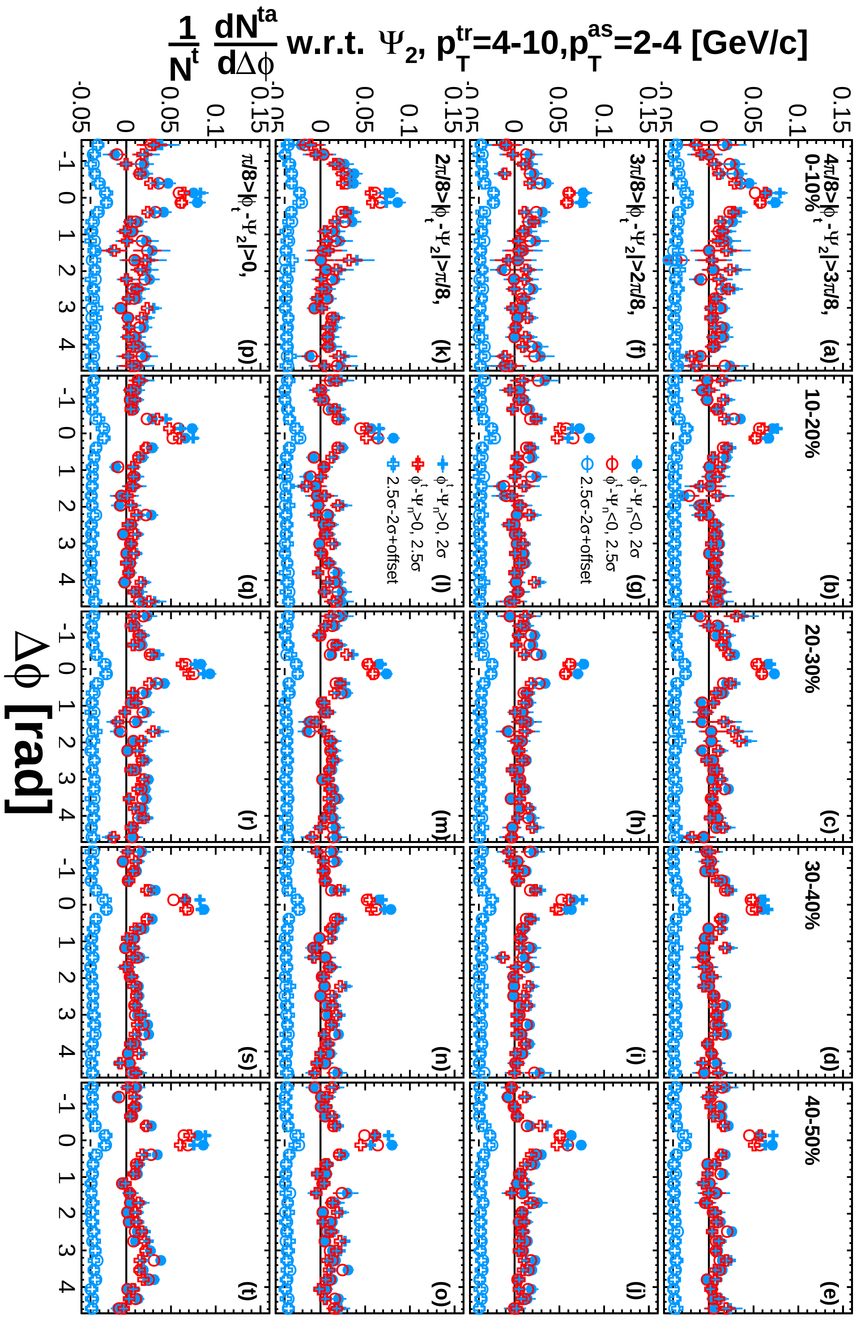

Figure A.13: Ψ_2 dependent correlations at 4-10⊗2-4 GeV/c before resolution correction where contributions of v_2, v_3, and v_4 is subtracted using (Black) 2σ matching cut, (Red) 2.5σ matching, and (Blue) difference of those.

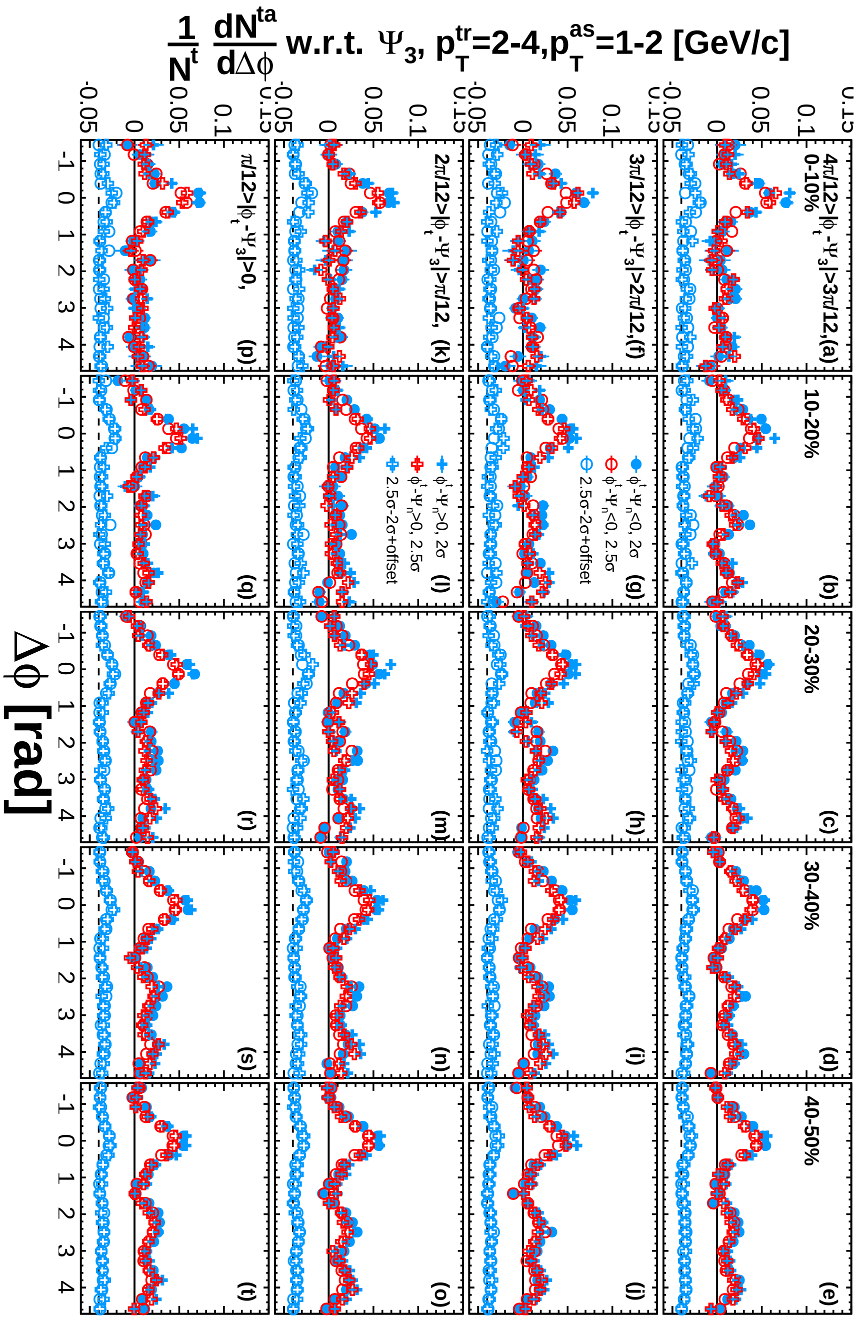

Figure A.14: Ψ_3 dependent correlations at 2-4⊗1-2 GeV/c before resolution correction where contributions of v_2, v_3, and v_4 is subtracted using (Black) 2σ matching cut, (Red) 2.5σ matching, and (Blue) difference of those.

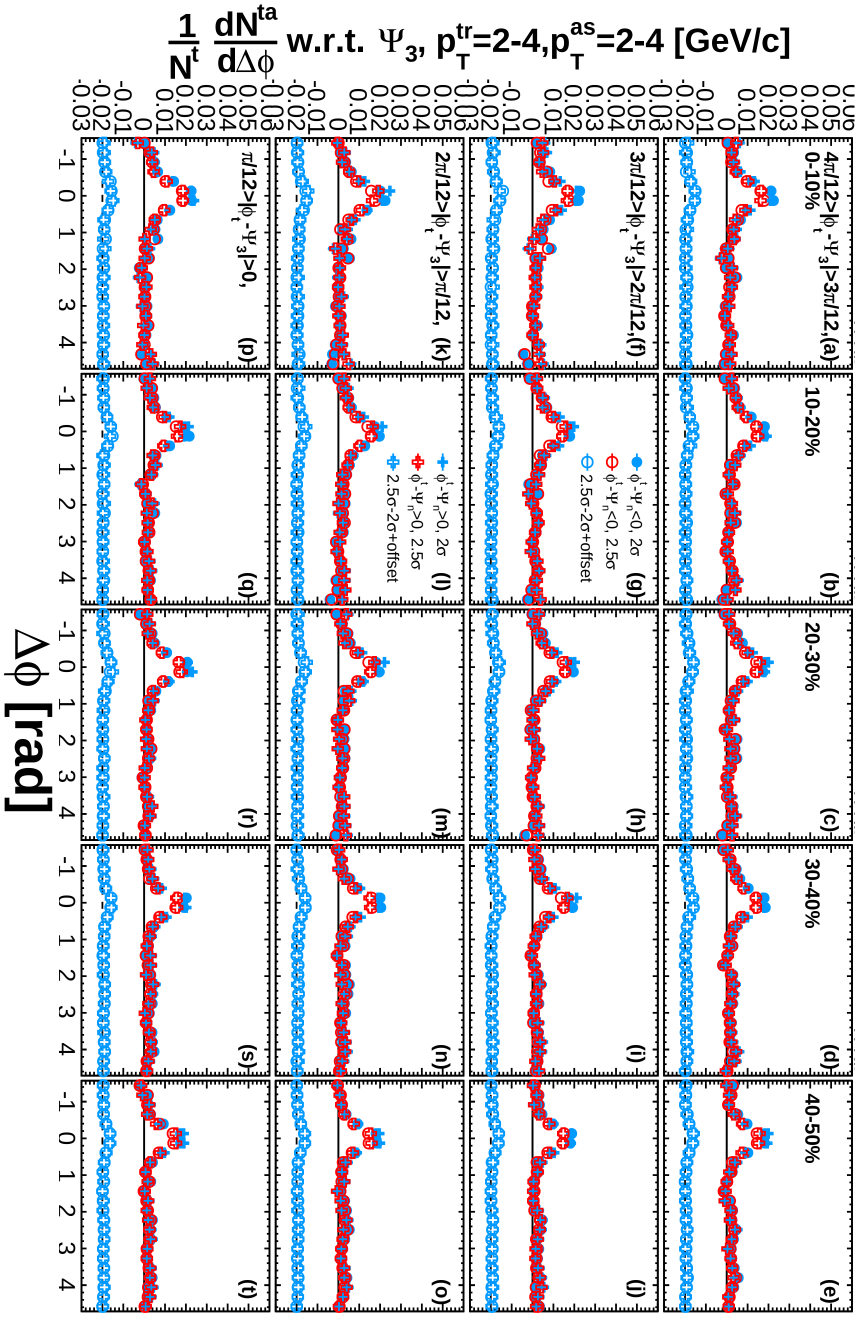

Figure A.15: Ψ_3 dependent correlations at 2-4⊗2-4 GeV/c before resolution correction where contributions of v_2, v_3, and v_4 is subtracted using (Black) 2σ matching cut, (Red) 2.5σ matching, and (Blue) difference of those.

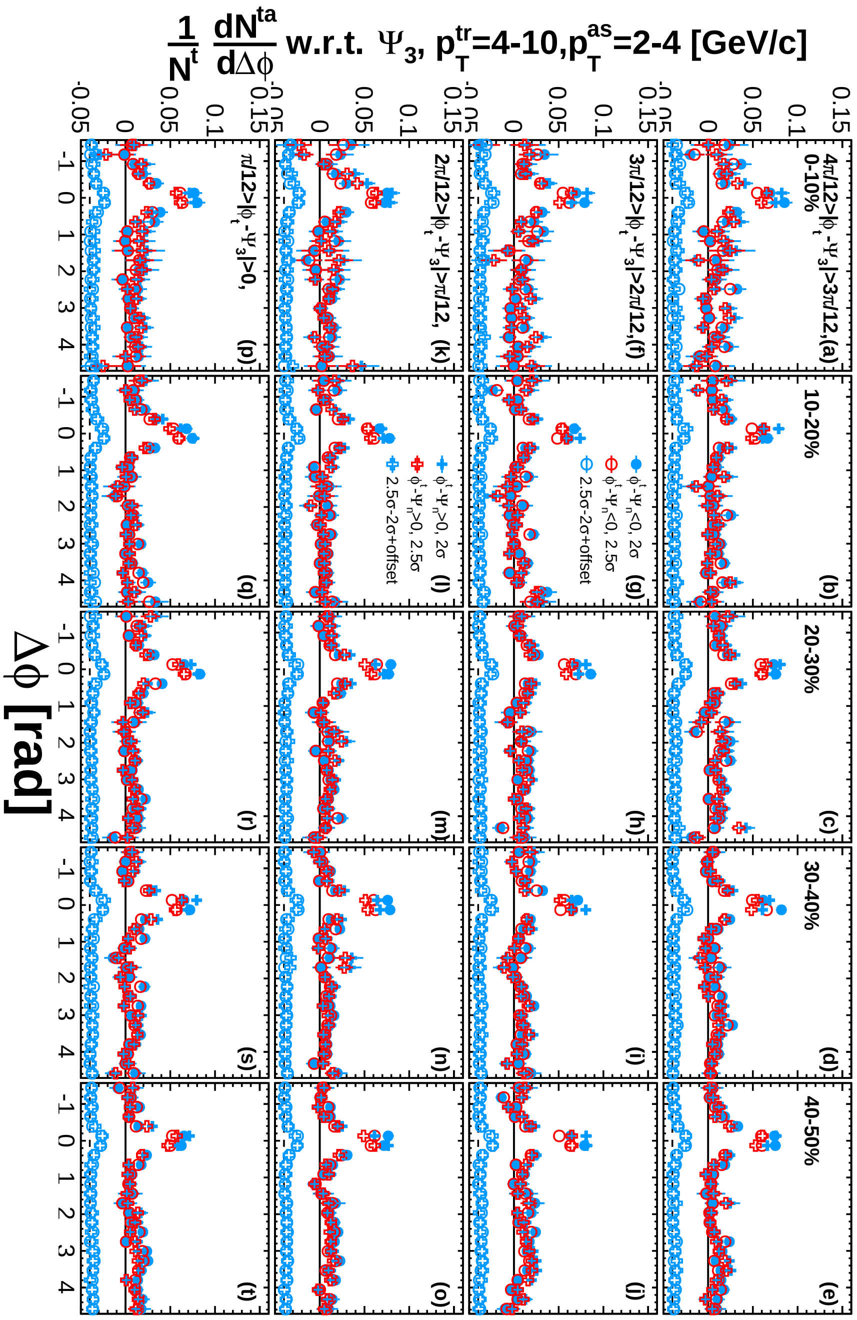

Figure A.16: Ψ_3 dependent correlations at 4-10⊗2-4 GeV/c before resolution correction where contributions of v_2, v_3, and v_4 is subtracted using (Black) 2σ matching cut, (Red) 2.5σ matching, and (Blue) difference of those.

A.2.2 Systematics from Flow Harmonics (Event-Plane Dependent)

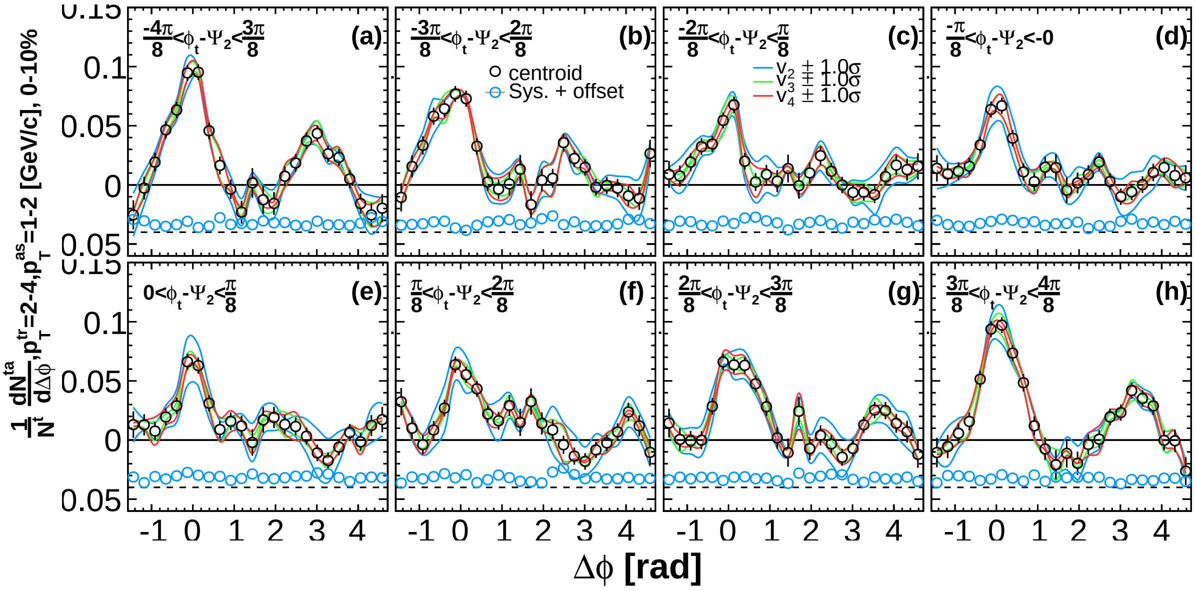

Figure A.17: Ψ_2 dependent correlations at 2-4⊗1-2 GeV/c before resolution correction where contributions of v_2, v_3, and v_4 is subtracted. v_n value is varied (blue-line) $v_2 \pm 1\sigma$, (green-line) $v_3 \pm 1\sigma$, and (red-line) $v_4 \pm 1\sigma$, other harmonics being fixed. Systematics are expressed by blue open circle with an offset.

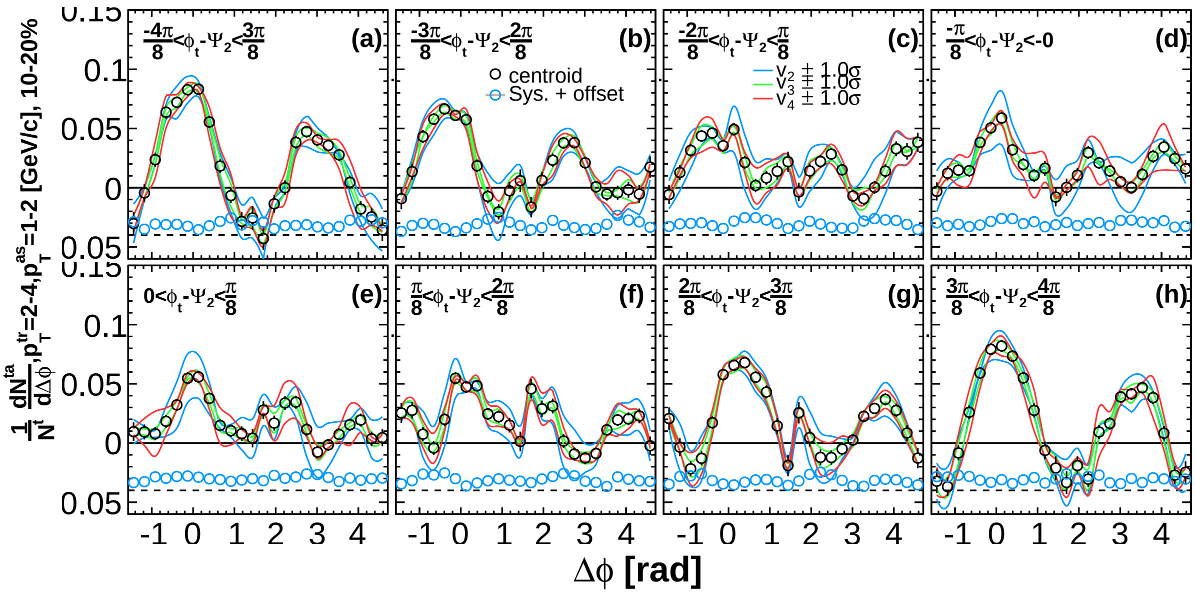

Figure A.18: Ψ_2 dependent correlations at 2-4$\otimes$1-2 GeV/c before resolution correction where contributions of v_2, v_3, and v_4 is subtracted. v_n value is varied (blue-line) $v_2 \pm 1\sigma$, (green-line) $v_3 \pm 1\sigma$, and (red-line) $v_4 \pm 1\sigma$, other harmonics being fixed. Systematics are expressed by blue open circle with an offset.

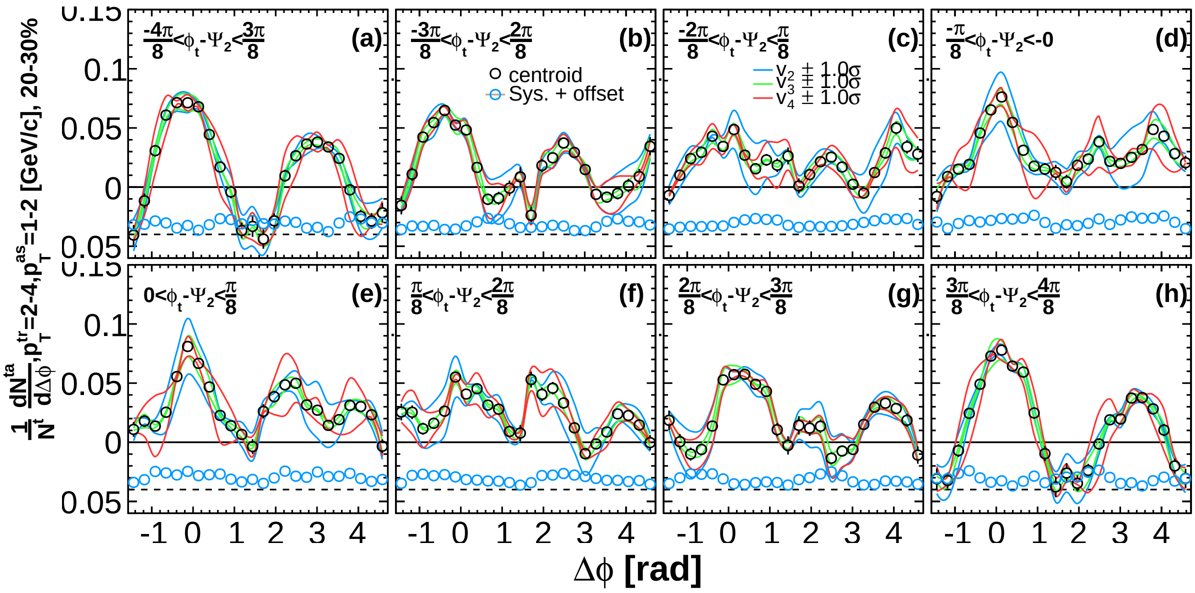

Figure A.19: Ψ_2 dependent correlations at 2-4$\otimes$1-2 GeV/c before resolution correction where contributions of v_2, v_3, and v_4 is subtracted. v_n value is varied (blue-line) $v_2 \pm 1\sigma$, (green-line) $v_3 \pm 1\sigma$, and (red-line) $v_4 \pm 1\sigma$, other harmonics being fixed. Systematics are expressed by blue open circle with an offset.

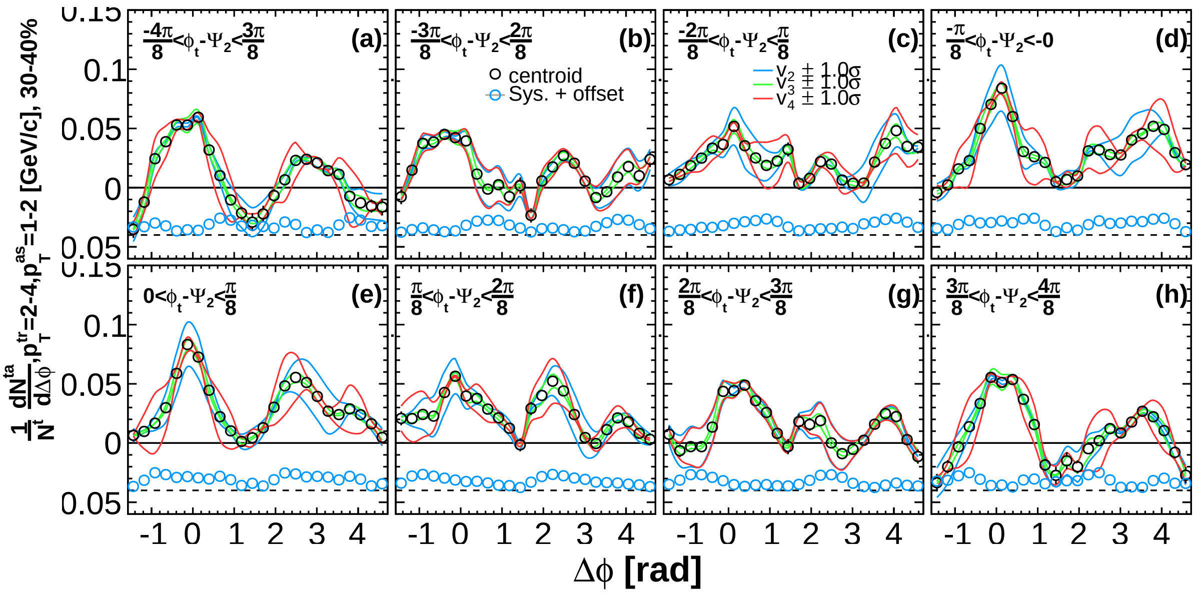

Figure A.20: Ψ_2 dependent correlations at 2-4⊗1-2 GeV/c before resolution correction where contributions of v_2, v_3, and v_4 is subtracted. v_n value is varied (blue-line) $v_2 \pm 1\sigma$, (green-line) $v_3 \pm 1\sigma$, and (red-line) $v_4 \pm 1\sigma$, other harmonics being fixed. Systematics are expressed by blue open circle with an offset.

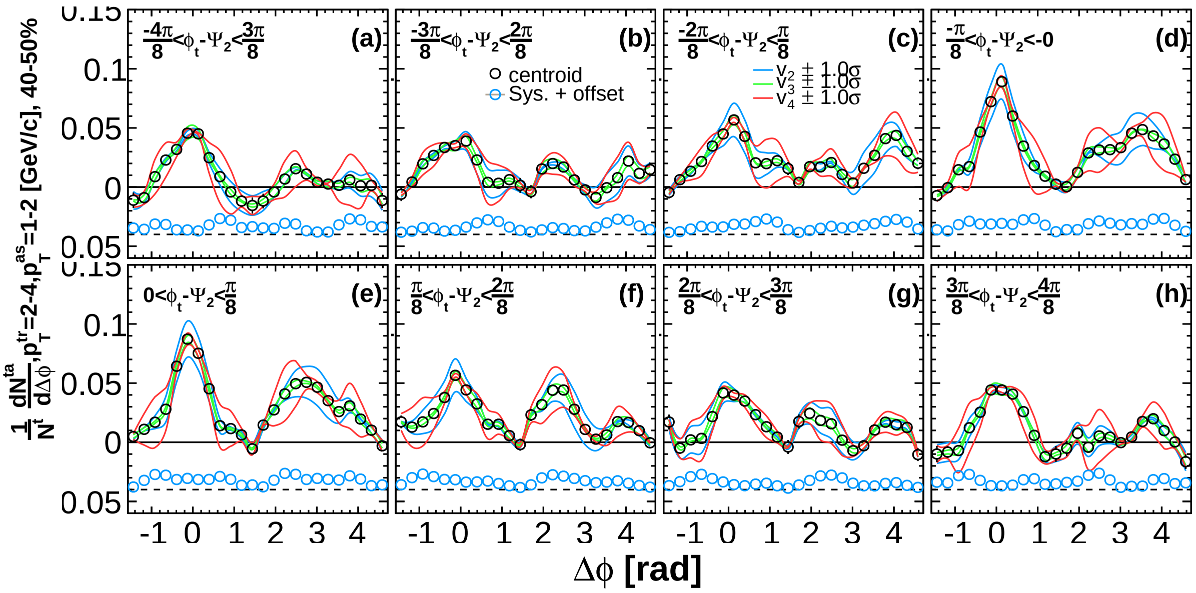

Figure A.21: Ψ_2 dependent correlations at 2-4⊗1-2 GeV/c before resolution correction where contributions of v_2, v_3, and v_4 is subtracted. v_n value is varied (blue-line) $v_2 \pm 1\sigma$, (green-line) $v_3 \pm 1\sigma$, and (red-line) $v_4 \pm 1\sigma$, other harmonics being fixed. Systematics are expressed by blue open circle with an offset.

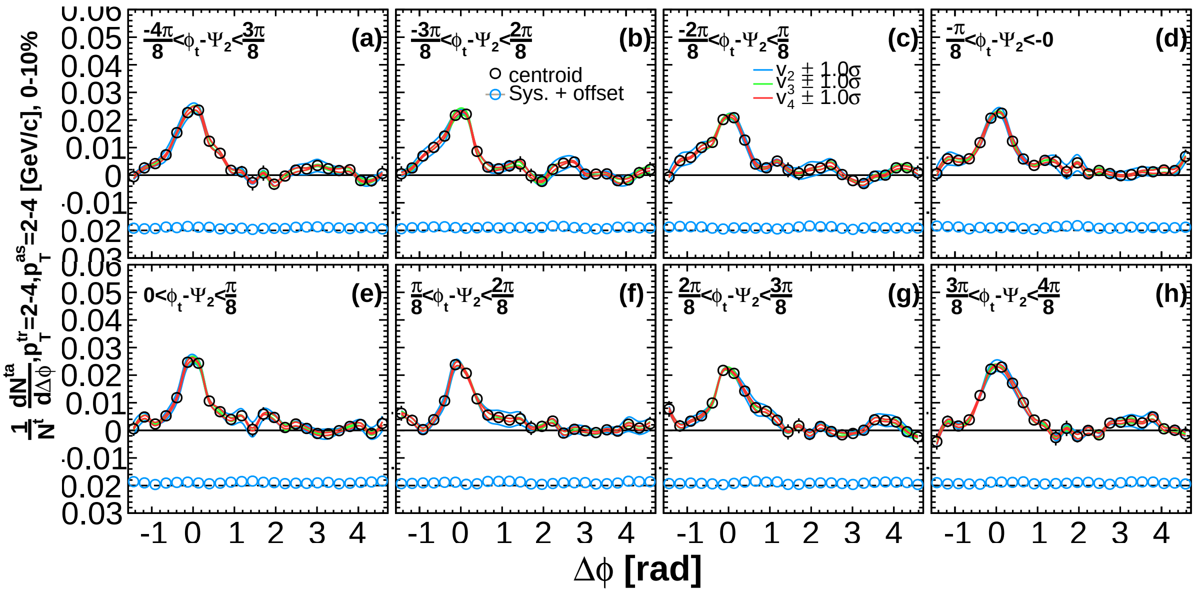

Figure A.22: Ψ_2 dependent correlations at 2-4$\otimes$2-4 GeV/c before resolution correction where contributions of v_2, v_3, and v_4 is subtracted. v_n value is varied (blue-line) $v_2 \pm 1\sigma$, (green-line) $v_3 \pm 1\sigma$, and (red-line) $v_4 \pm 1\sigma$, other harmonics being fixed. Systematics are expressed by blue open circle with an offset.

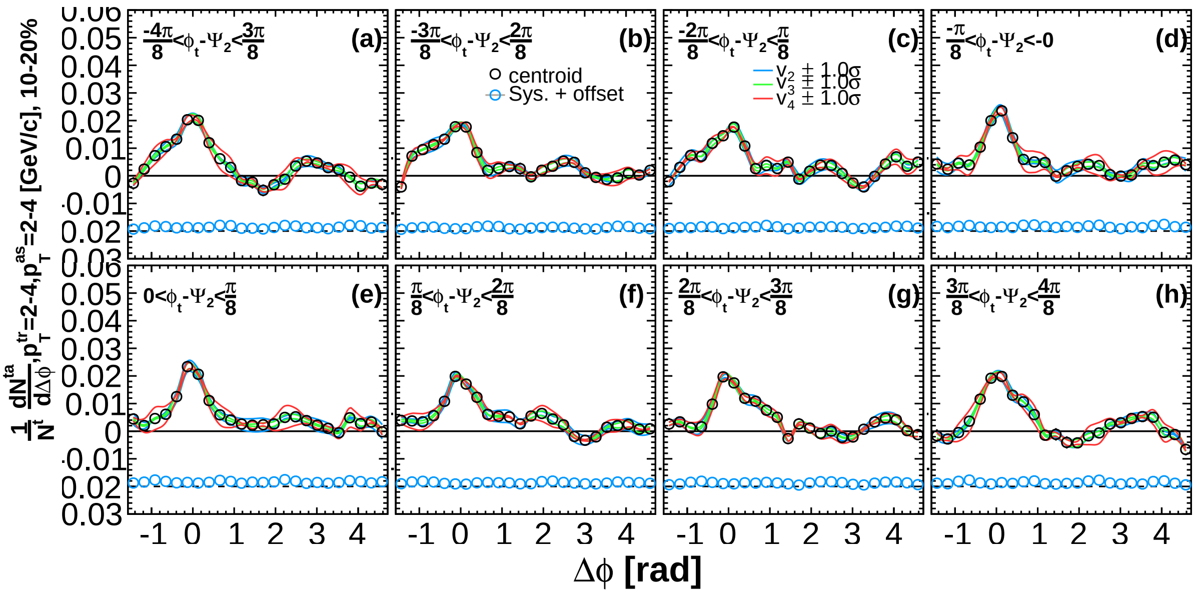

Figure A.23: Ψ_2 dependent correlations at 2-4⊗2-4 GeV/c before resolution correction where contributions of v_2, v_3, and v_4 is subtracted. v_n value is varied (blue-line) $v_2 \pm 1\sigma$, (green-line) $v_3 \pm 1\sigma$, and (red-line) $v_4 \pm 1\sigma$, other harmonics being fixed. Systematics are expressed by blue open circle with an offset.

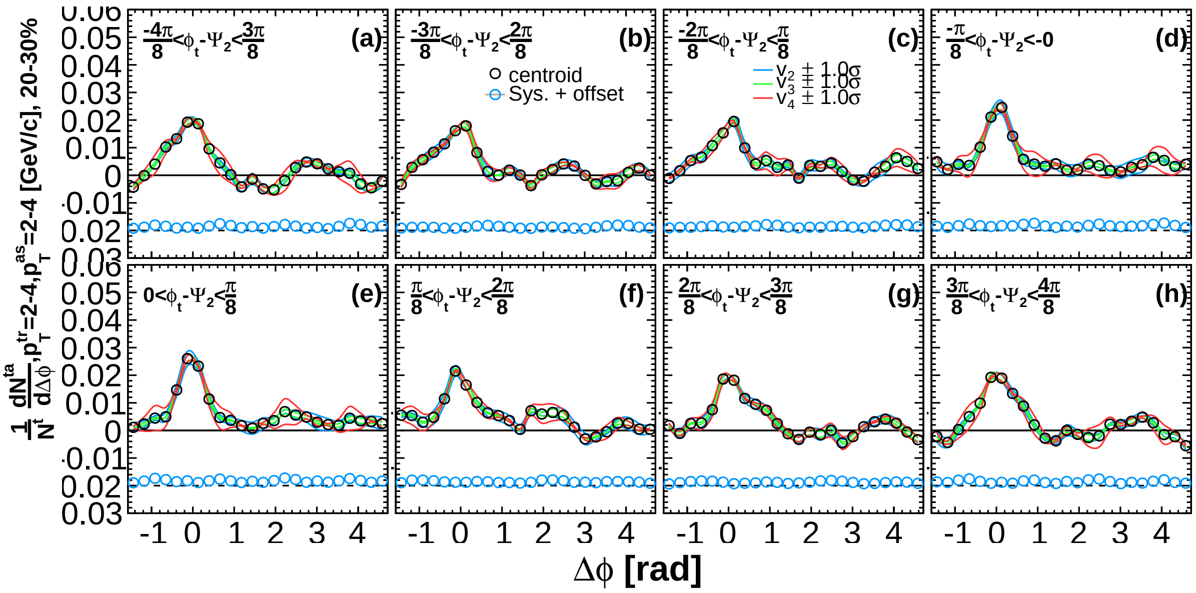

Figure A.24: Ψ_2 dependent correlations at 2-4⊗2-4 GeV/c before resolution correction where contributions of v_2, v_3, and v_4 is subtracted. v_n value is varied (blue-line) $v_2 \pm 1\sigma$, (green-line) $v_3 \pm 1\sigma$, and (red-line) $v_4 \pm 1\sigma$, other harmonics being fixed. Systematics are expressed by blue open circle with an offset.

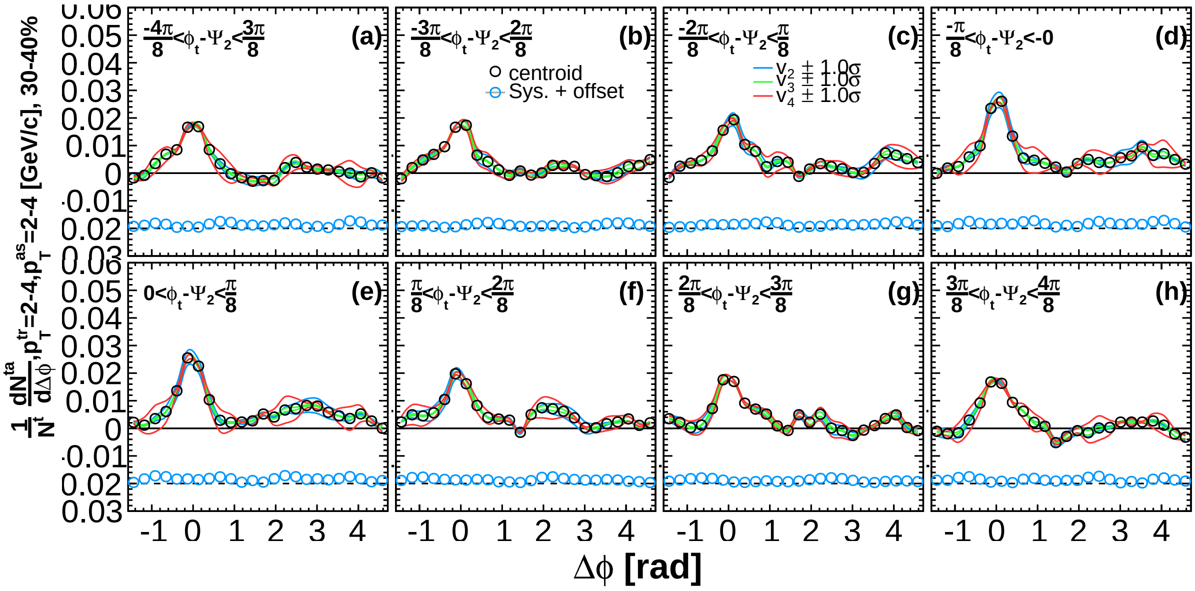

Figure A.25: Ψ_2 dependent correlations at 2-4$\otimes$2-4 GeV/c before resolution correction where contributions of v_2, v_3, and v_4 is subtracted. v_n value is varied (blue-line) $v_2 \pm 1\sigma$, (green-line) $v_3 \pm 1\sigma$, and (red-line) $v_4 \pm 1\sigma$, other harmonics being fixed. Systematics are expressed by blue open circle with an offset.

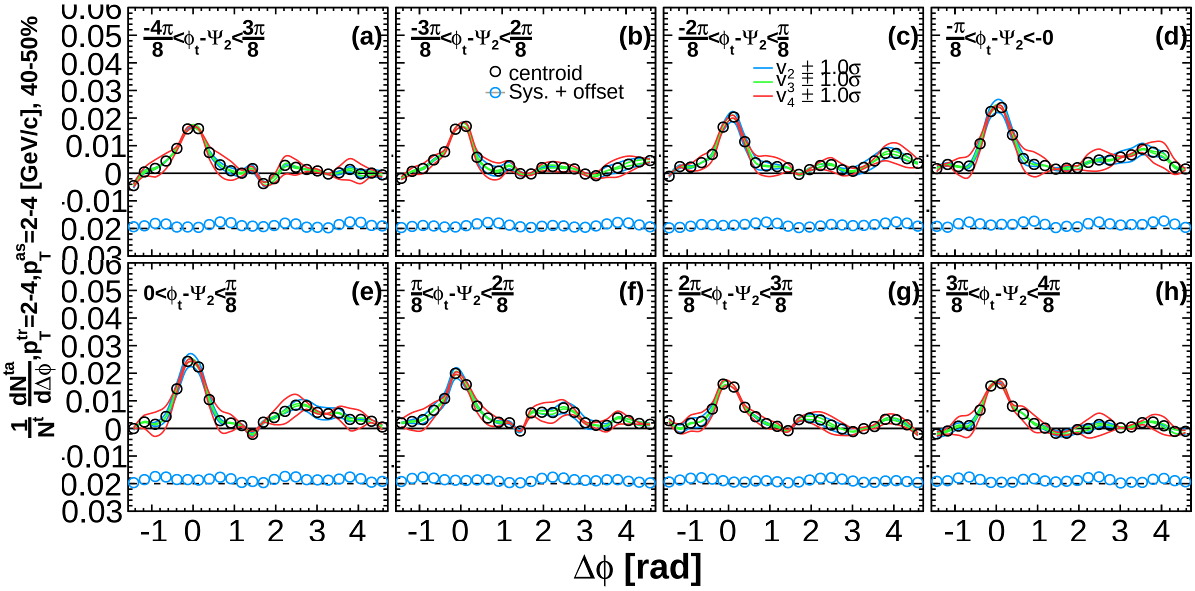

Figure A.26: Ψ_2 dependent correlations at 2-4$\otimes$2-4 GeV/c before resolution correction where contributions of v_2, v_3, and v_4 is subtracted. v_n value is varied (blue-line) $v_2 \pm 1\sigma$, (green-line) $v_3 \pm 1\sigma$, and (red-line) $v_4 \pm 1\sigma$, other harmonics being fixed. Systematics are expressed by blue open circle with an offset.

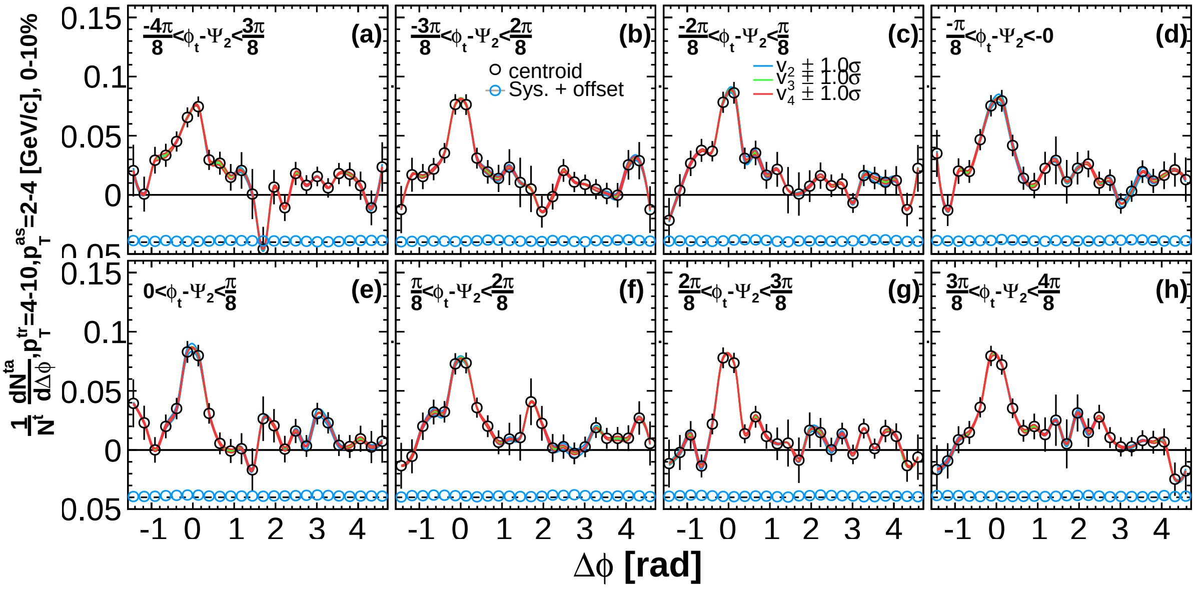

Figure A.27: Ψ_2 dependent correlations at 4-10⊗2-4 GeV/c before resolution correction where contributions of v_2, v_3, and v_4 is subtracted. v_n value is varied (blue-line) $v_2 \pm 1\sigma$, (green-line) $v_3 \pm 1\sigma$, and (red-line) $v_4 \pm 1\sigma$, other harmonics being fixed. Systematics are expressed by blue open circle with an offset.

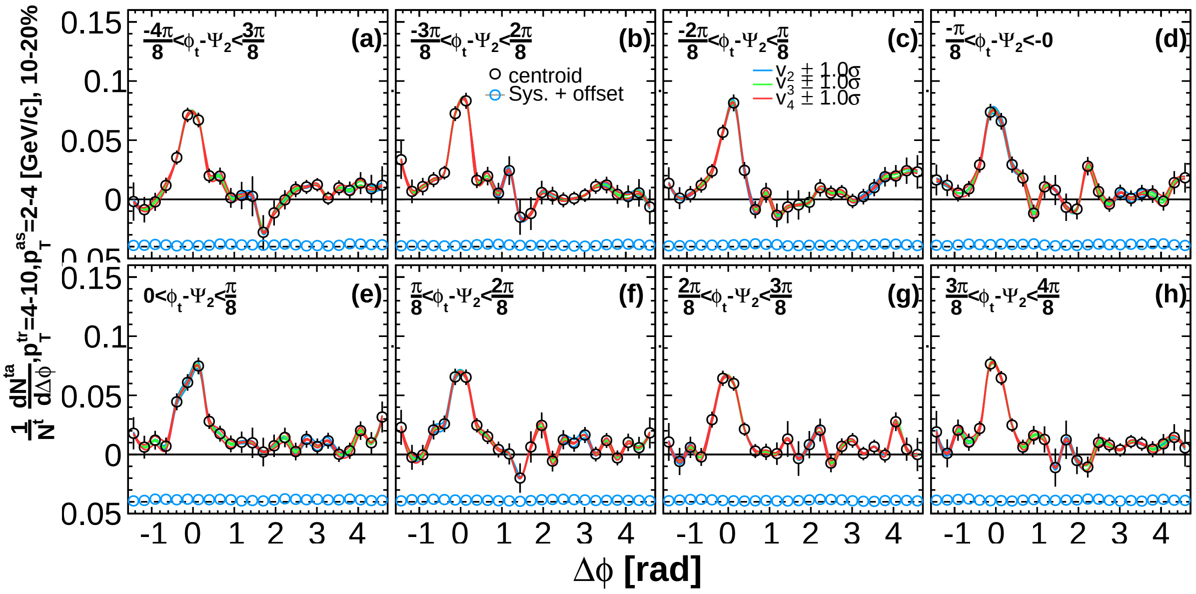

Figure A.28: Ψ_2 dependent correlations at 4-10$\otimes$2-4 GeV/c before resolution correction where contributions of v_2, v_3, and v_4 is subtracted. v_n value is varied (blue-line) $v_2 \pm 1\sigma$, (green-line) $v_3 \pm 1\sigma$, and (red-line) $v_4 \pm 1\sigma$, other harmonics being fixed. Systematics are expressed by blue open circle with an offset.

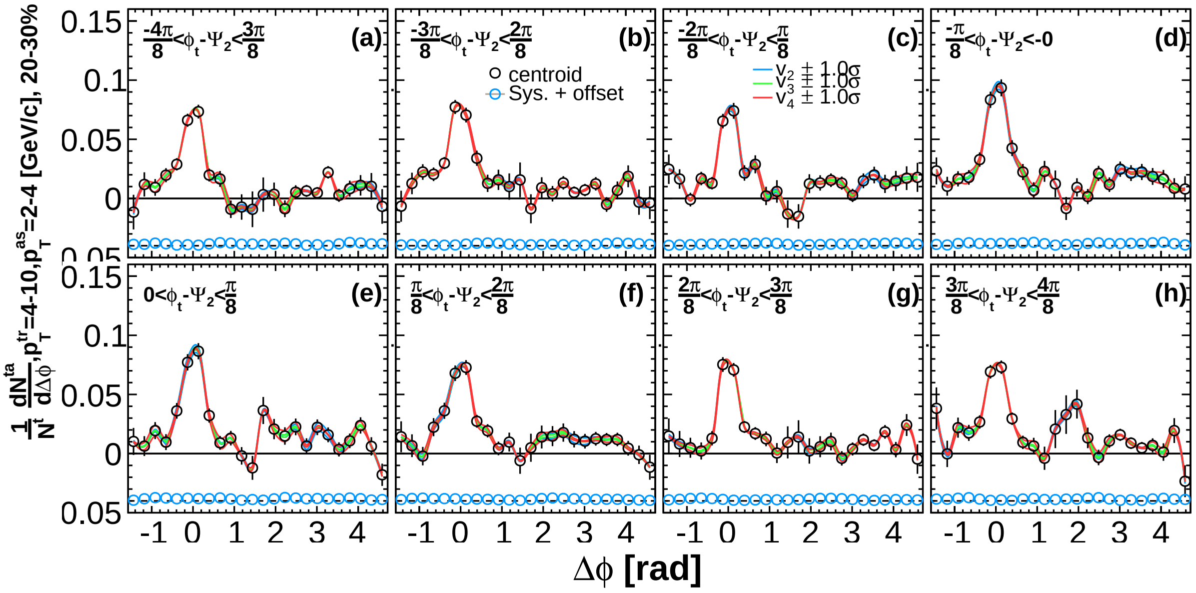

Figure A.29: Ψ_2 dependent correlations at 4-10$\otimes$2-4 GeV/c before resolution correction where contributions of v_2, v_3, and v_4 is subtracted. v_n value is varied (blue-line) $v_2 \pm 1\sigma$, (green-line) $v_3 \pm 1\sigma$, and (red-line) $v_4 \pm 1\sigma$, other harmonics being fixed. Systematics are expressed by blue open circle with an offset.

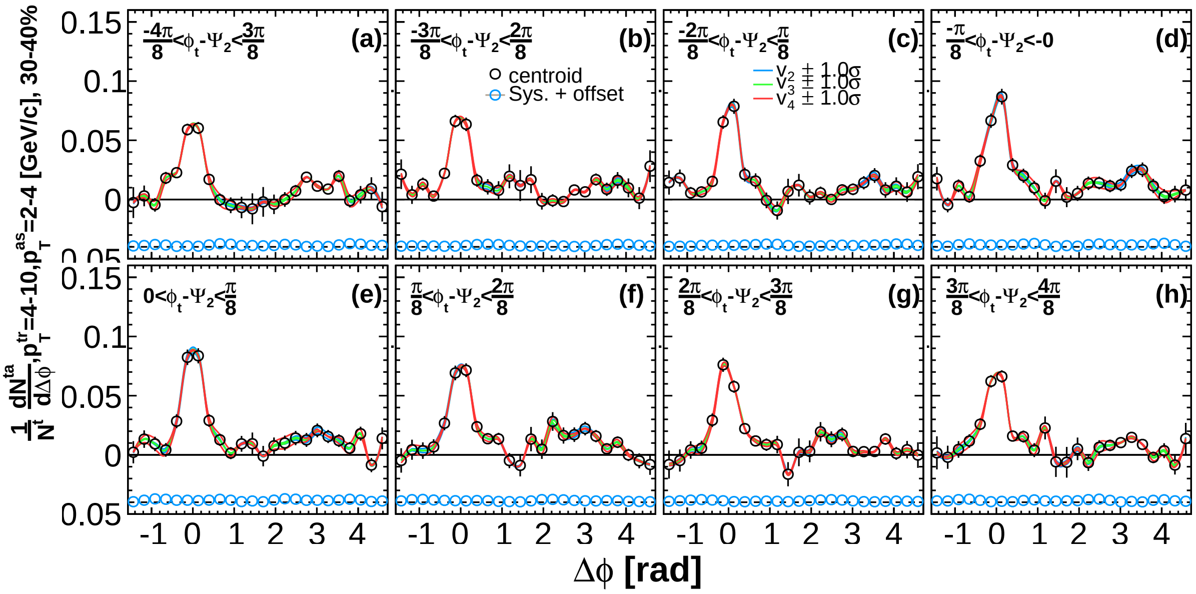

Figure A.30: Ψ_2 dependent correlations at 4-10$\otimes$2-4 GeV/c before resolution correction where contributions of v_2, v_3, and v_4 is subtracted. v_n value is varied (blue-line) $v_2 \pm 1\sigma$, (green-line) $v_3 \pm 1\sigma$, and (red-line) $v_4 \pm 1\sigma$, other harmonics being fixed. Systematics are expressed by blue open circle with an offset.

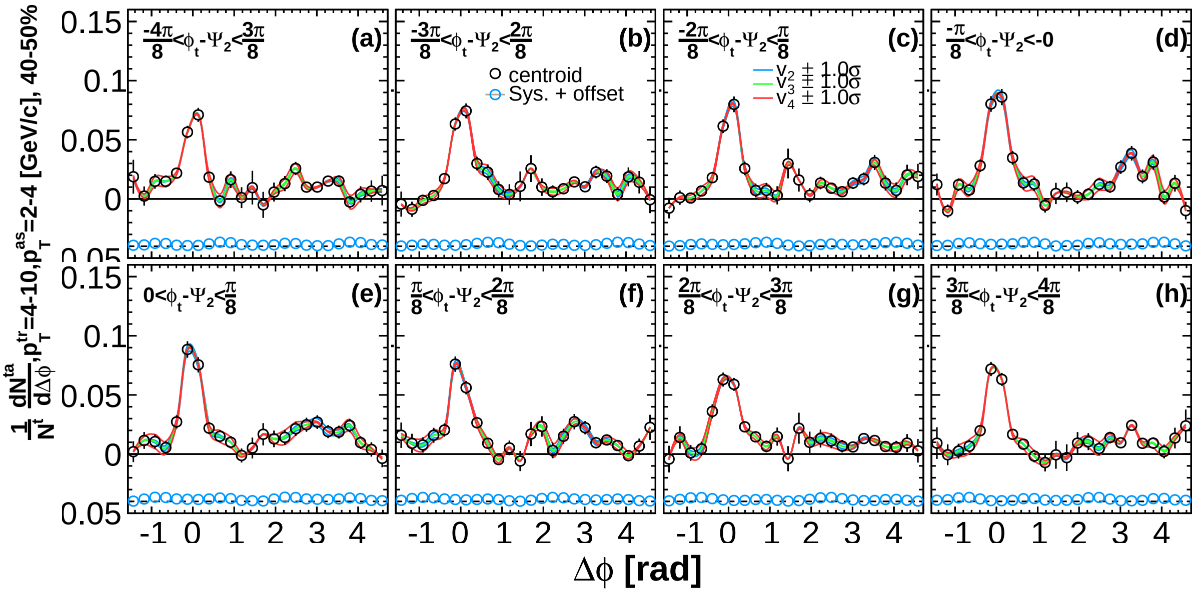

Figure A.31: Ψ_2 dependent correlations at 4-10$\otimes$2-4 GeV/c before resolution correction where contributions of v_2, v_3, and v_4 is subtracted. v_n value is varied (blue-line) $v_2 \pm 1\sigma$, (green-line) $v_3 \pm 1\sigma$, and (red-line) $v_4 \pm 1\sigma$, other harmonics being fixed. Systematics are expressed by blue open circle with an offset.

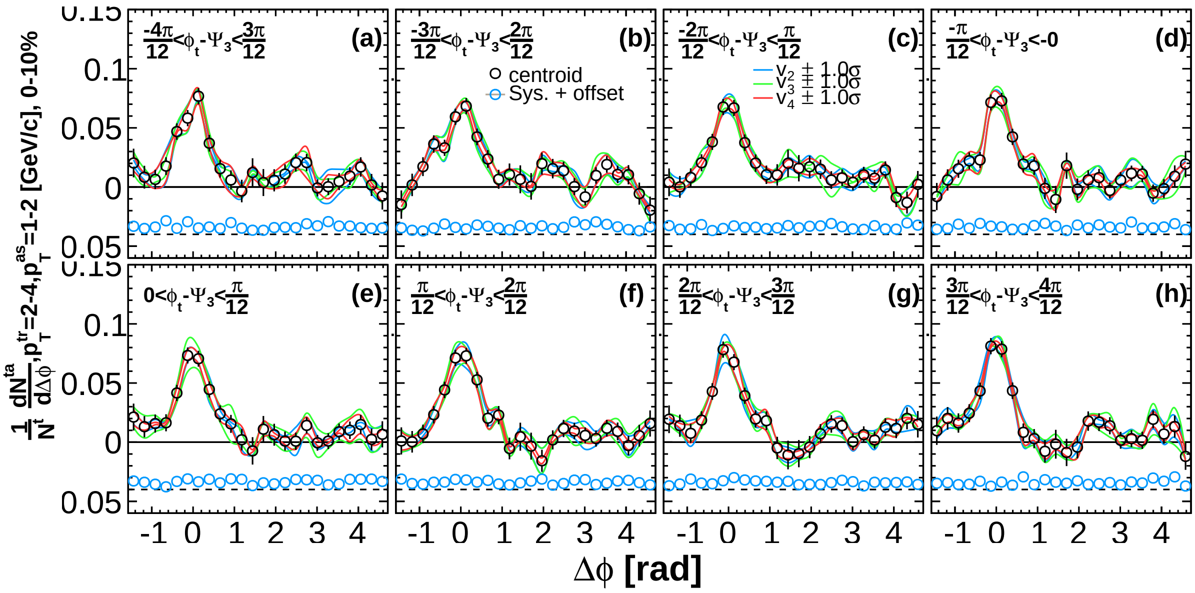

Figure A.32: Ψ_3 dependent correlations at 2-4⊗1-2 GeV/c before resolution correction where contributions of v_2, v_3, and v_4 is subtracted. v_n value is varied (blue-line) $v_2 \pm 1\sigma$, (green-line) $v_3 \pm 1\sigma$, and (red-line) $v_4 \pm 1\sigma$, other harmonics being fixed. Systematics are expressed by blue open circle with an offset.

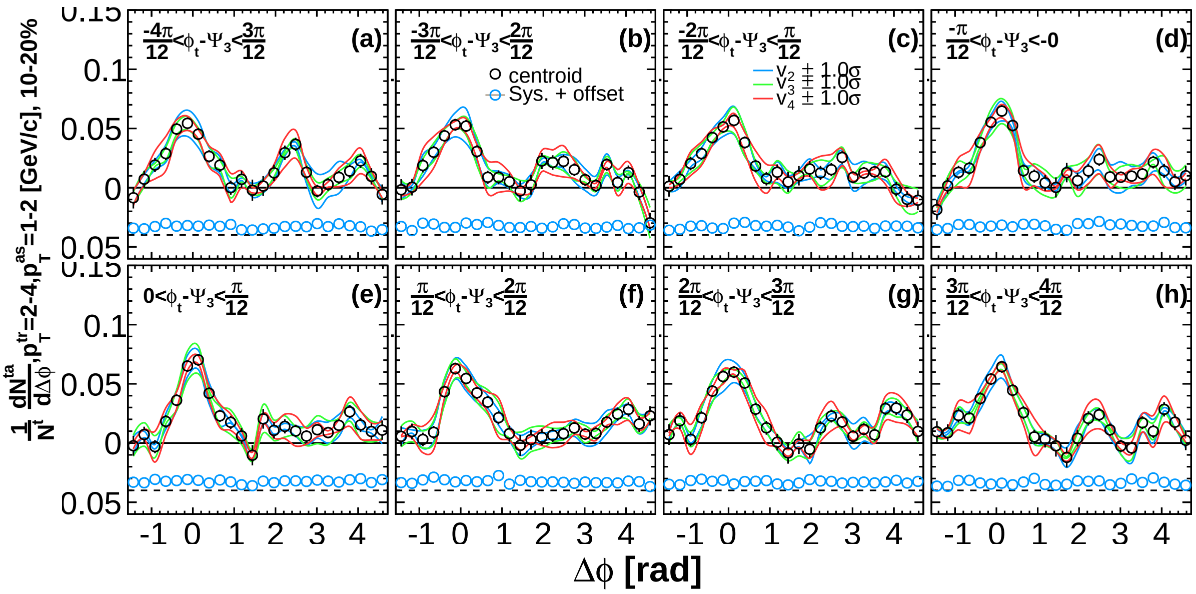

Figure A.33: Ψ_3 dependent correlations at 2-4⊗1-2 GeV/c before resolution correction where contributions of v_2, v_3, and v_4 is subtracted. v_n value is varied (blue-line) $v_2 \pm 1\sigma$, (green-line) $v_3 \pm 1\sigma$, and (red-line) $v_4 \pm 1\sigma$, other harmonics being fixed. Systematics are expressed by blue open circle with an offset.

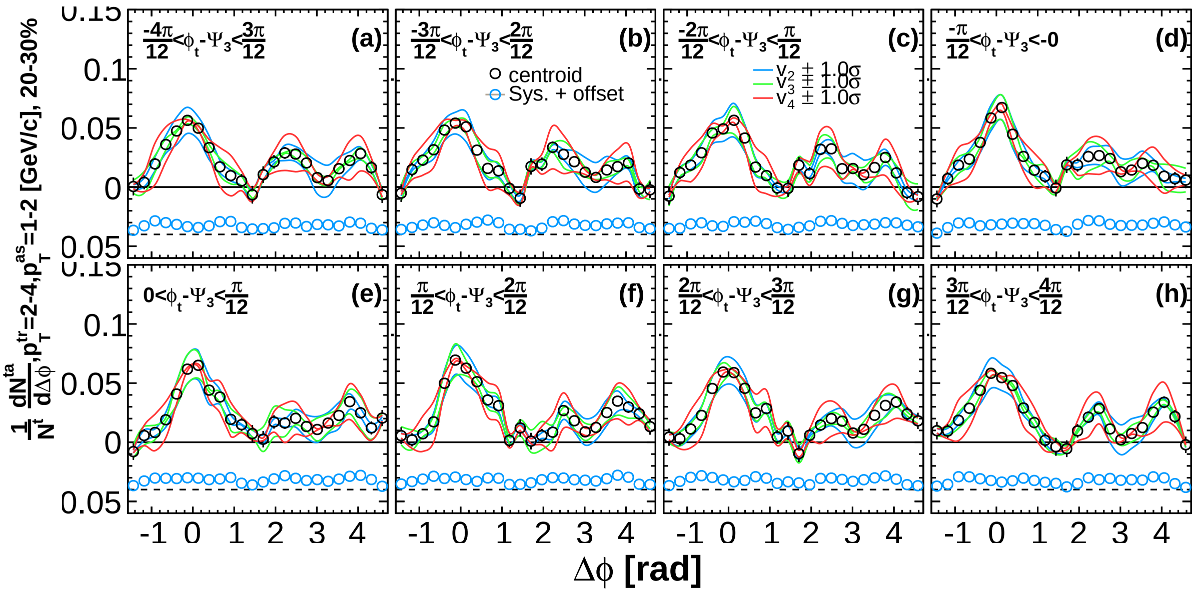

Figure A.34: Ψ_3 dependent correlations at 2-4⊗1-2 GeV/c before resolution correction where contributions of v_2, v_3, and v_4 is subtracted. v_n value is varied (blue-line) $v_2 \pm 1\sigma$, (green-line) $v_3 \pm 1\sigma$, and (red-line) $v_4 \pm 1\sigma$, other harmonics being fixed. Systematics are expressed by blue open circle with an offset.

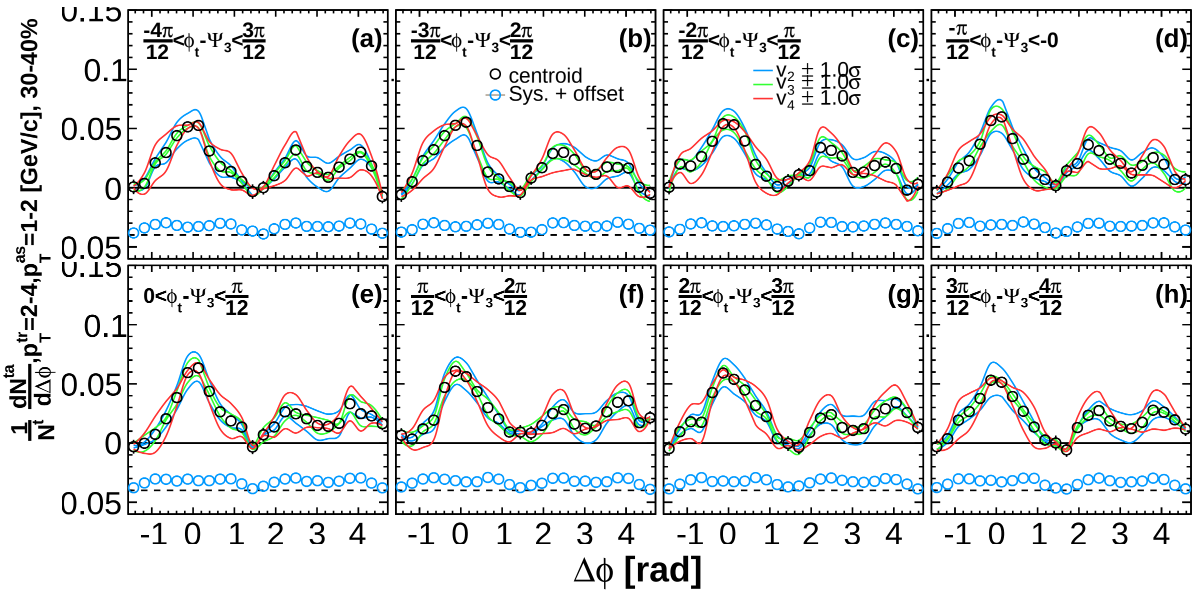

Figure A.35: Ψ_3 dependent correlations at 2-4⊗1-2 GeV/c before resolution correction where contributions of v_2, v_3, and v_4 is subtracted. v_n value is varied (blue-line) $v_2 \pm 1\sigma$, (green-line) $v_3 \pm 1\sigma$, and (red-line) $v_4 \pm 1\sigma$, other harmonics being fixed. Systematics are expressed by blue open circle with an offset.

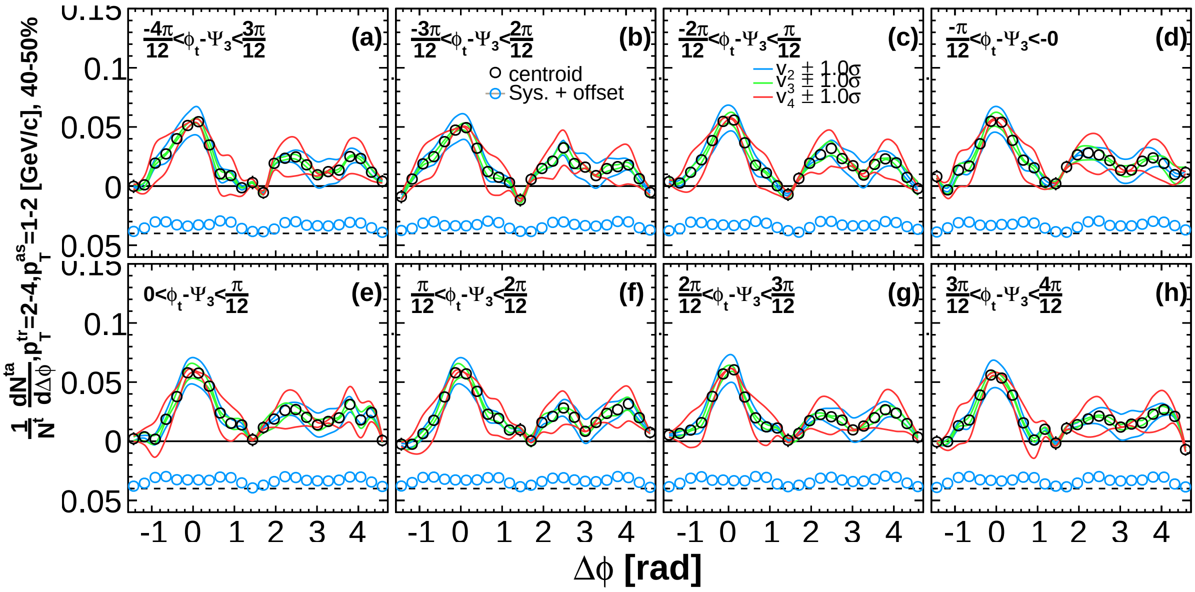

Figure A.36: Ψ_3 dependent correlations at 2-4⊗1-2 GeV/c before resolution correction where contributions of v_2, v_3, and v_4 is subtracted. v_n value is varied (blue-line) $v_2 \pm 1\sigma$, (green-line) $v_3 \pm 1\sigma$, and (red-line) $v_4 \pm 1\sigma$, other harmonics being fixed. Systematics are expressed by blue open circle with an offset.

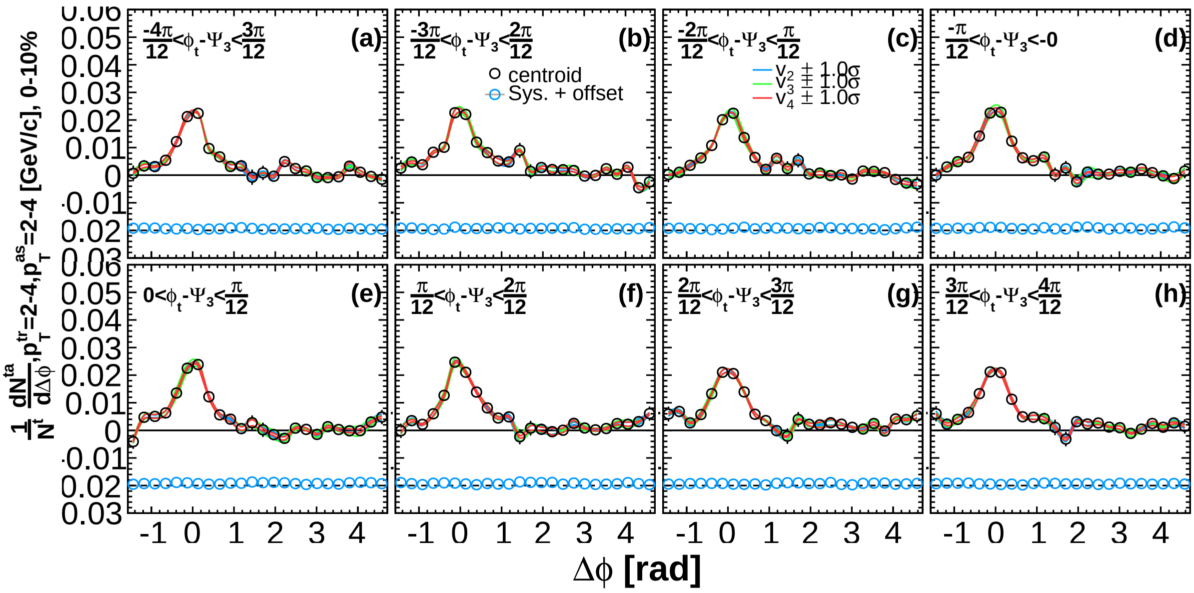

Figure A.37: Ψ_3 dependent correlations at 2-4$\otimes$2-4 GeV/c before resolution correction where contributions of v_2, v_3, and v_4 is subtracted. v_n value is varied (blue-line) $v_2 \pm 1\sigma$, (green-line) $v_3 \pm 1\sigma$, and (red-line) $v_4 \pm 1\sigma$, other harmonics being fixed. Systematics are expressed by blue open circle with an offset.

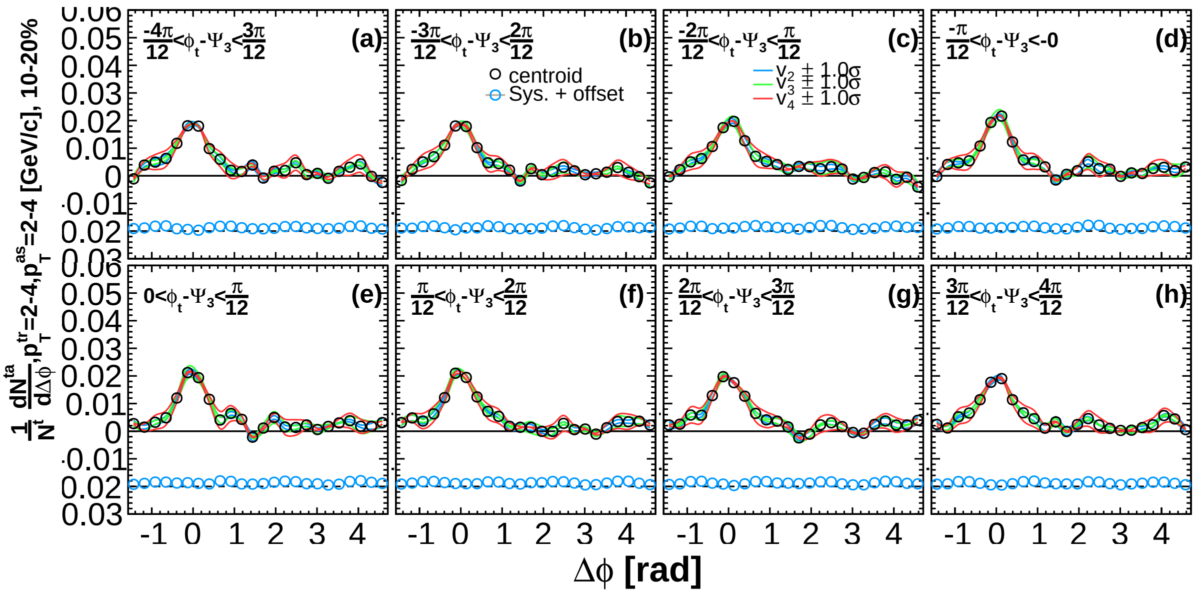

Figure A.38: Ψ_3 dependent correlations at 2-4⊗2-4 GeV/c before resolution correction where contributions of v_2, v_3, and v_4 is subtracted. v_n value is varied (blue-line) $v_2 \pm 1\sigma$, (green-line) $v_3 \pm 1\sigma$, and (red-line) $v_4 \pm 1\sigma$, other harmonics being fixed. Systematics are expressed by blue open circle with an offset.

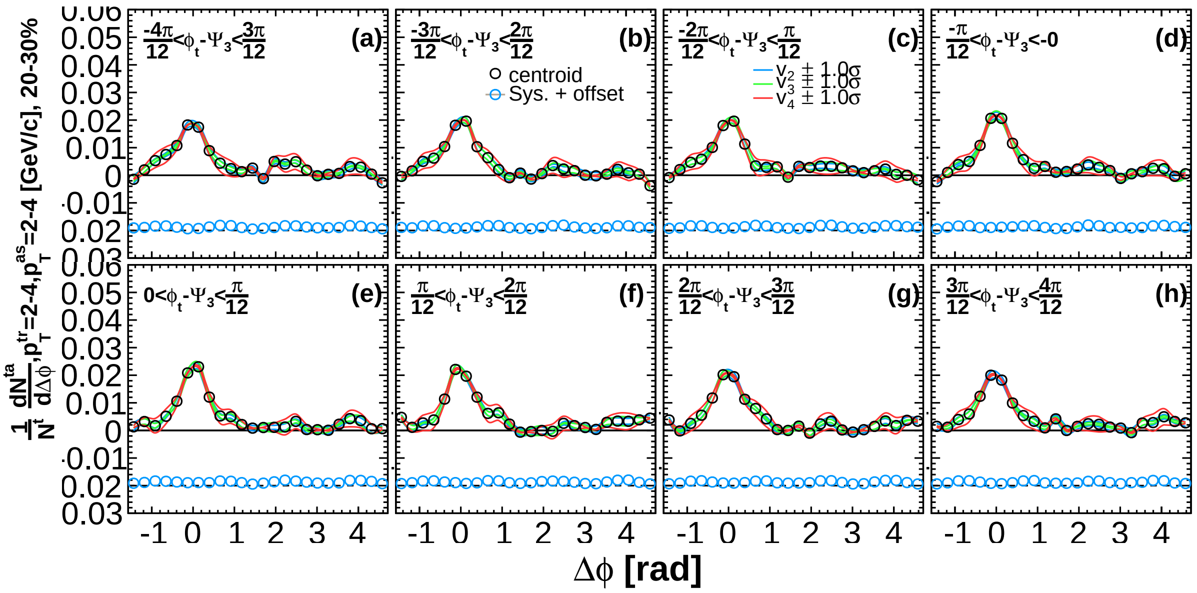

Figure A.39: Ψ_3 dependent correlations at 2-4⊗2-4 GeV/c before resolution correction where contributions of v_2, v_3, and v_4 is subtracted. v_n value is varied (blue-line) $v_2 \pm 1\sigma$, (green-line) $v_3 \pm 1\sigma$, and (red-line) $v_4 \pm 1\sigma$, other harmonics being fixed. Systematics are expressed by blue open circle with an offset.

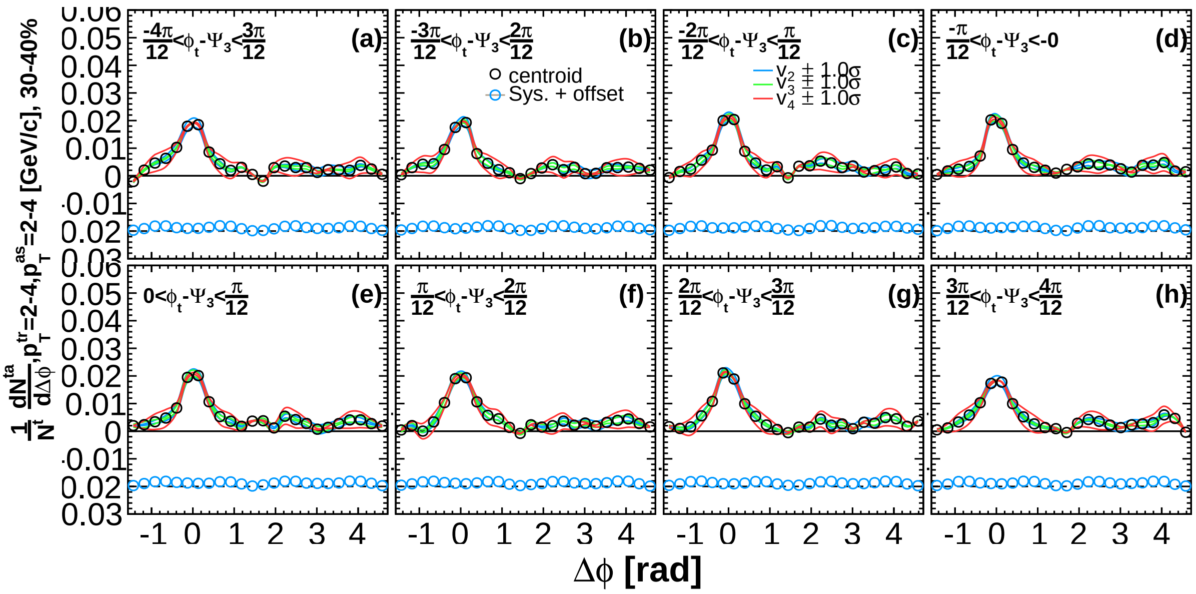

Figure A.40: Ψ_3 dependent correlations at 2-4$\otimes$2-4 GeV/c before resolution correction where contributions of v_2, v_3, and v_4 is subtracted. v_n value is varied (blue-line) $v_2 \pm 1\sigma$, (green-line) $v_3 \pm 1\sigma$, and (red-line) $v_4 \pm 1\sigma$, other harmonics being fixed. Systematics are expressed by blue open circle with an offset.

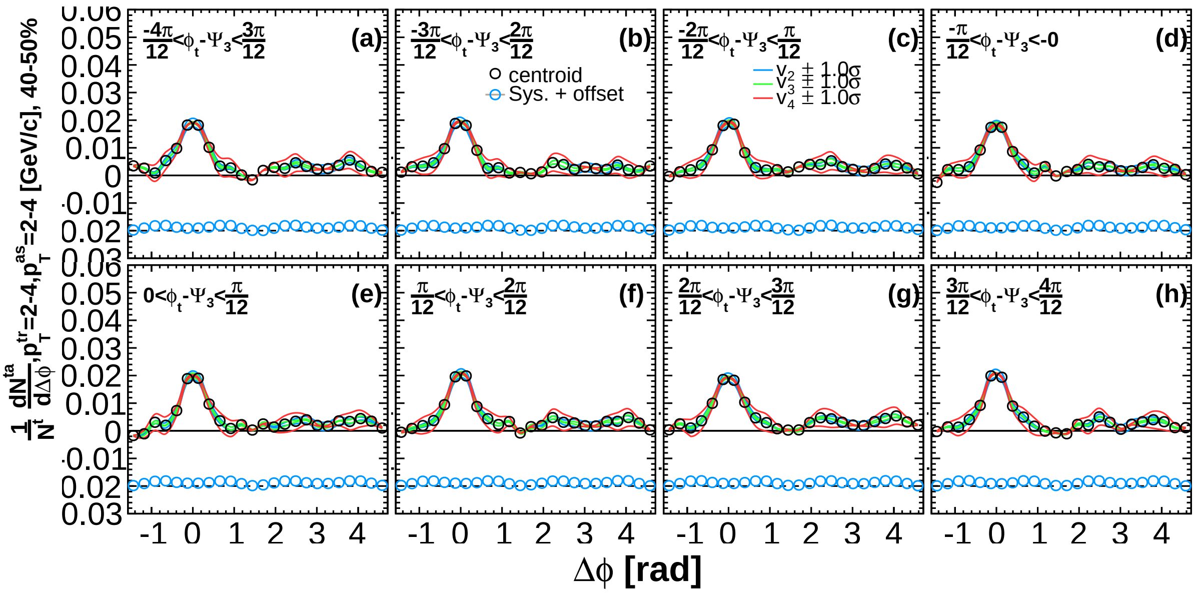

Figure A.41: Ψ_3 dependent correlations at 2-4$\otimes$2-4 GeV/c before resolution correction where contributions of v_2, v_3, and v_4 is subtracted. v_n value is varied (blue-line) $v_2 \pm 1\sigma$, (green-line) $v_3 \pm 1\sigma$, and (red-line) $v_4 \pm 1\sigma$, other harmonics being fixed. Systematics are expressed by blue open circle with an offset.

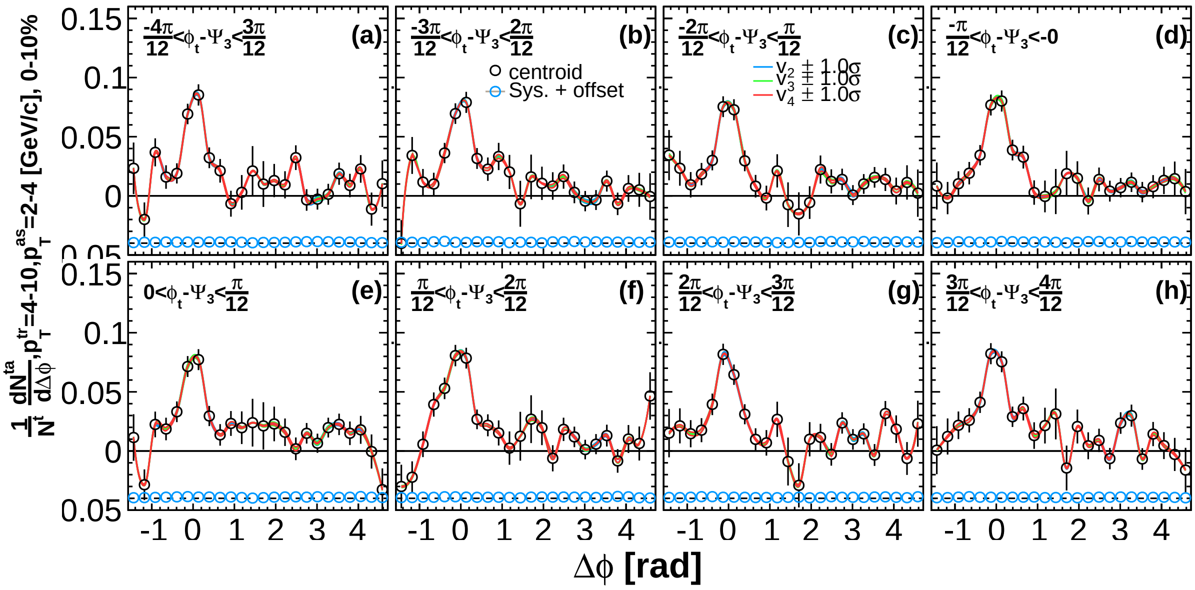

Figure A.42: Ψ_3 dependent correlations at 4-10⊗2-4 GeV/c before resolution correction where contributions of v_2, v_3, and v_4 is subtracted. v_n value is varied (blue-line) $v_2 \pm 1\sigma$, (green-line) $v_3 \pm 1\sigma$, and (red-line) $v_4 \pm 1\sigma$, other harmonics being fixed. Systematics are expressed by blue open circle with an offset.

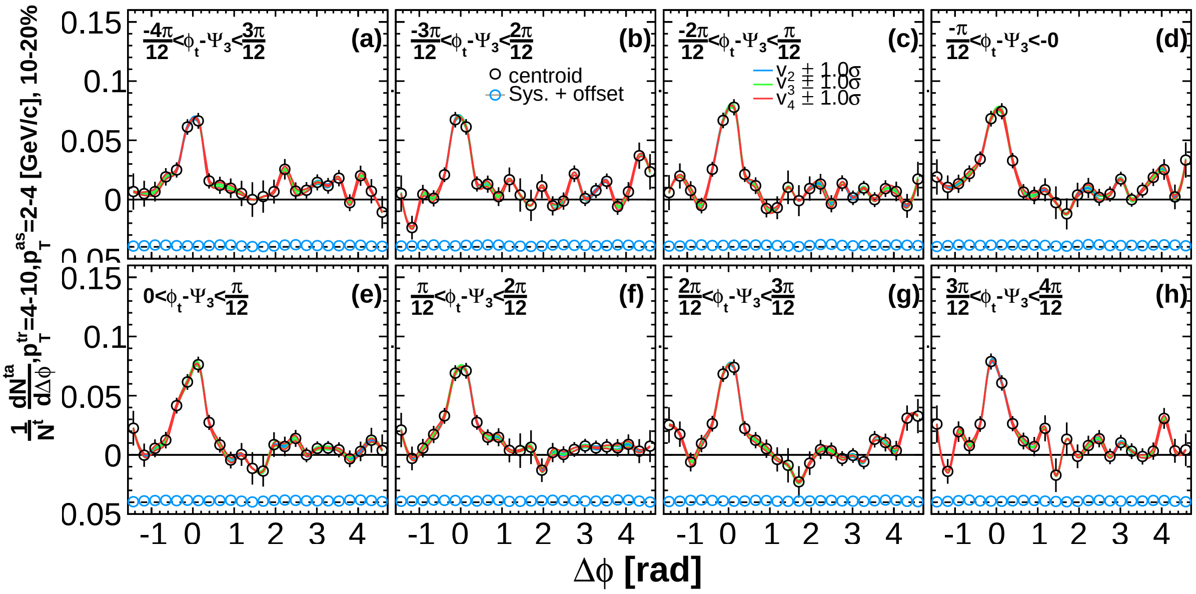

Figure A.43: Ψ_3 dependent correlations at 4-10⊗2-4 GeV/c before resolution correction where contributions of v_2, v_3, and v_4 is subtracted. v_n value is varied (blue-line) $v_2 \pm 1\sigma$, (green-line) $v_3 \pm 1\sigma$, and (red-line) $v_4 \pm 1\sigma$, other harmonics being fixed. Systematics are expressed by blue open circle with an offset.

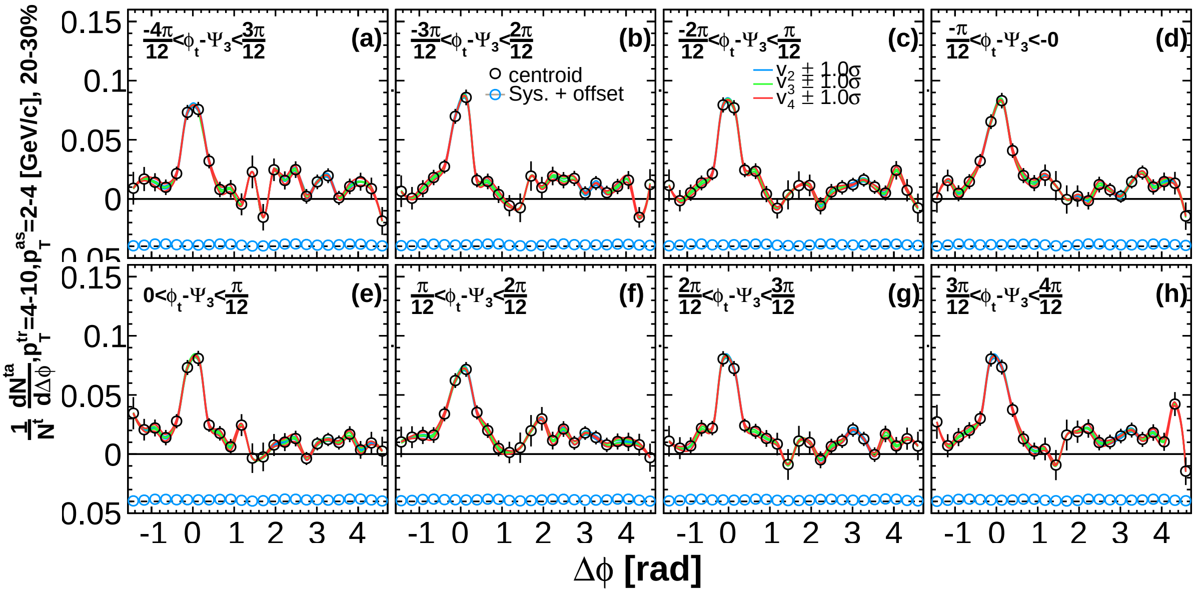

Figure A.44: Ψ_3 dependent correlations at 4-10⊗2-4 GeV/c before resolution correction where contributions of v_2, v_3, and v_4 is subtracted. v_n value is varied (blue-line) $v_2 \pm 1\sigma$, (green-line) $v_3 \pm 1\sigma$, and (red-line) $v_4 \pm 1\sigma$, other harmonics being fixed. Systematics are expressed by blue open circle with an offset.

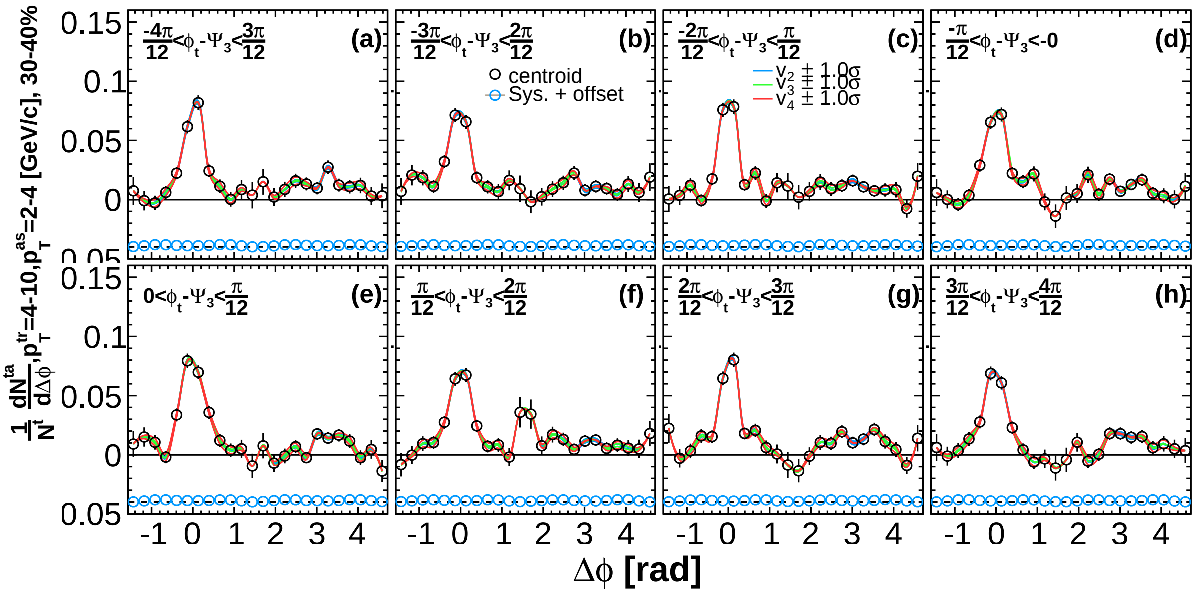

Figure A.45: Ψ_3 dependent correlations at 4-10$\otimes$2-4 GeV/c before resolution correction where contributions of v_2, v_3, and v_4 is subtracted. v_n value is varied (blue-line) $v_2 \pm 1\sigma$, (green-line) $v_3 \pm 1\sigma$, and (red-line) $v_4 \pm 1\sigma$, other harmonics being fixed. Systematics are expressed by blue open circle with an offset.

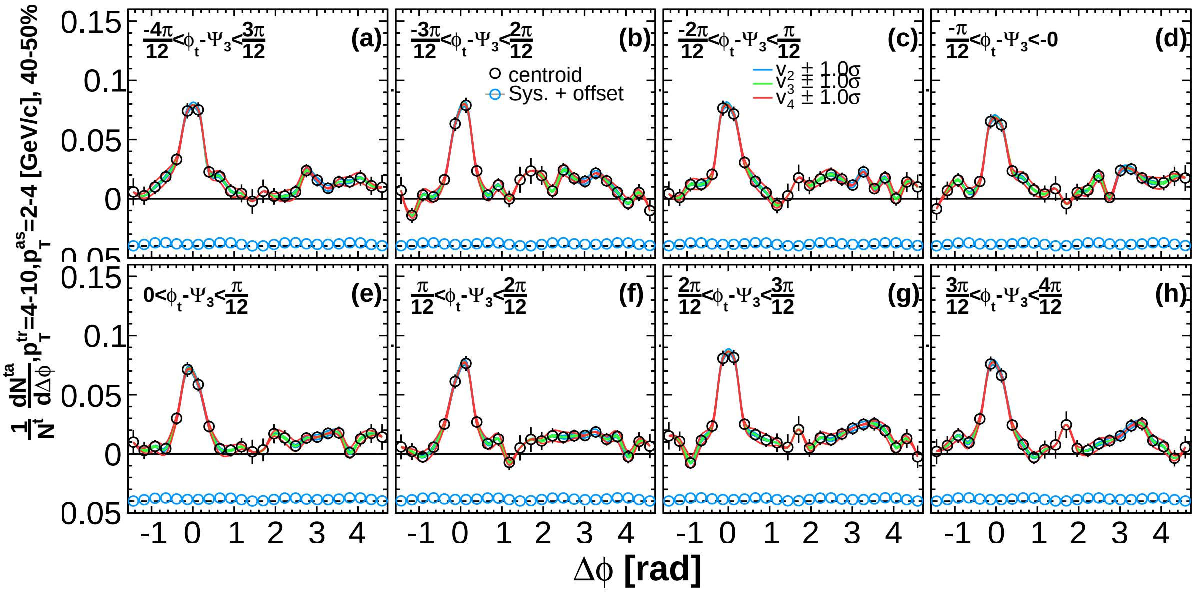

Figure A.46: Ψ_3 dependent correlations at 4-10$\otimes$2-4 GeV/c before resolution correction where contributions of v_2, v_3, and v_4 is subtracted. v_n value is varied (blue-line) $v_2 \pm 1\sigma$, (green-line) $v_3 \pm 1\sigma$, and (red-line) $v_4 \pm 1\sigma$, other harmonics being fixed. Systematics are expressed by blue open circle with an offset.

A.2.3 Systematics from $\Psi_2 - \Psi_4$ correlation (Event-Plane Dependent)

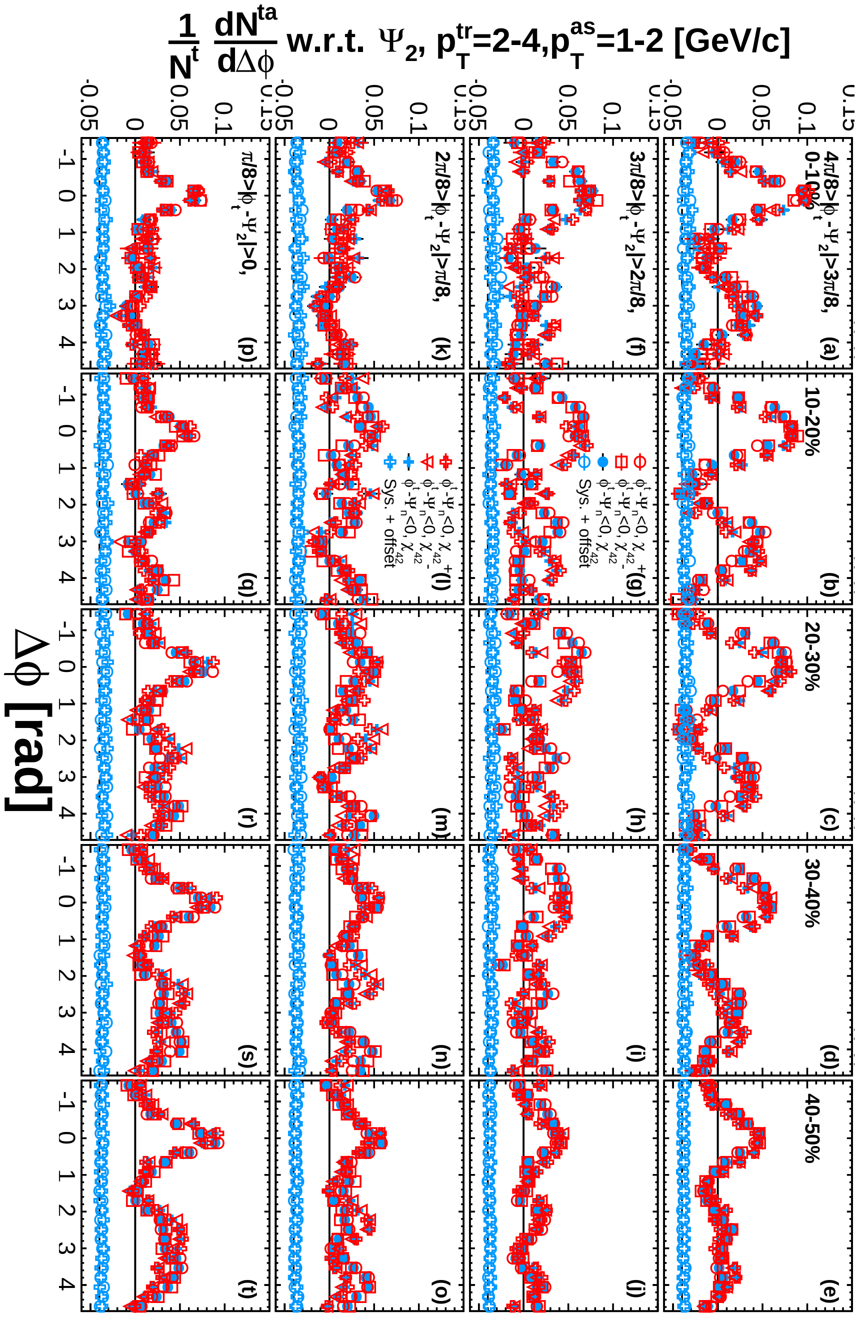

Figure A.47: Ψ_2 dependent correlations at 2-4$\otimes$1-2 GeV/c before resolution correction where contributions of v_2, v_3, and v_4 is subtracted using (Blue) centroid χ_{42} and (Red) $\pm$ 1σ χ_{42}. The systematics are plotted with an offset.

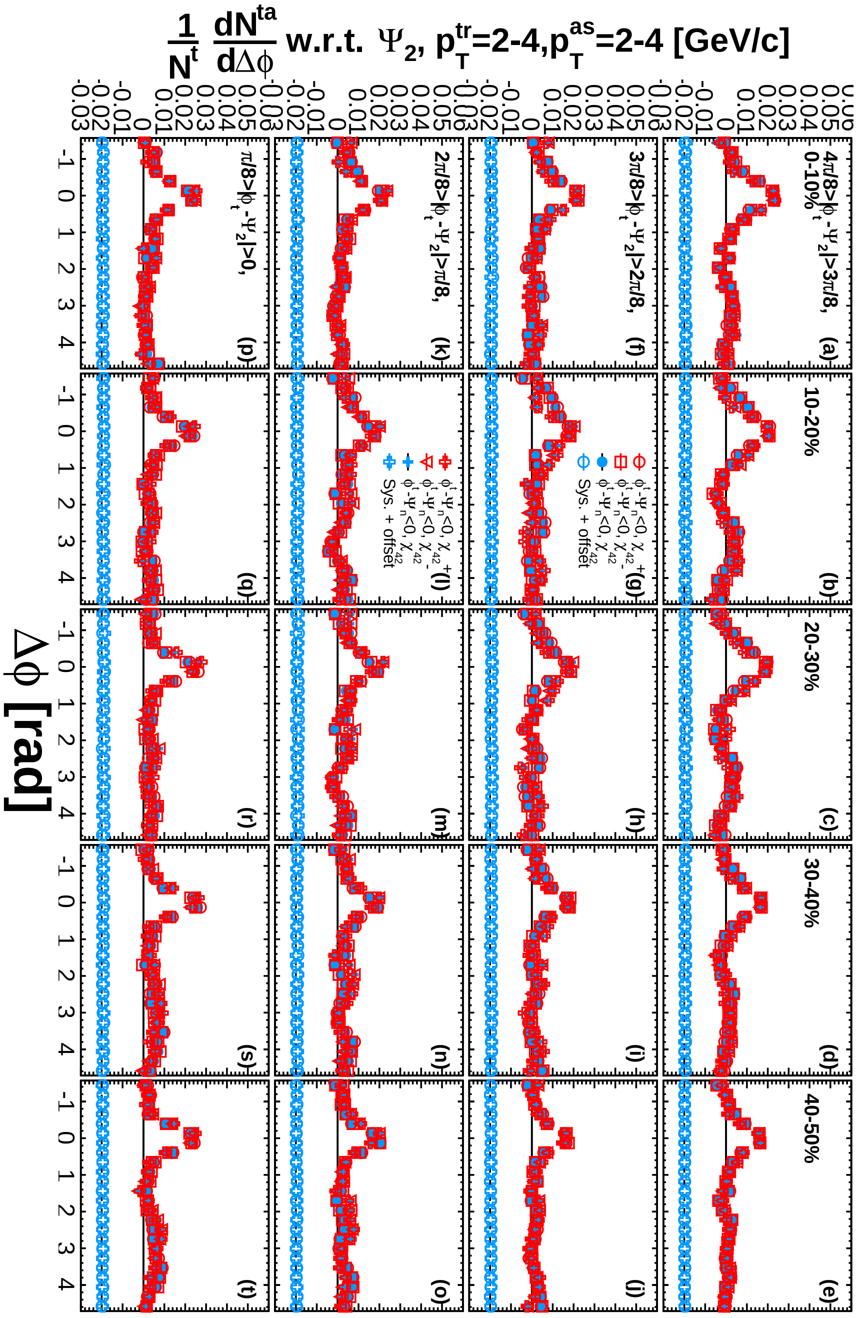

Figure A.48: Ψ_2 dependent correlations at 2-4⊗2-4 GeV/c before resolution correction where contributions of v_2, v_3, and v_4 is subtracted using (Blue) centroid χ_{42} and (Red) $\pm$ 1σ χ_{42}. The systematics are plotted with an offset.

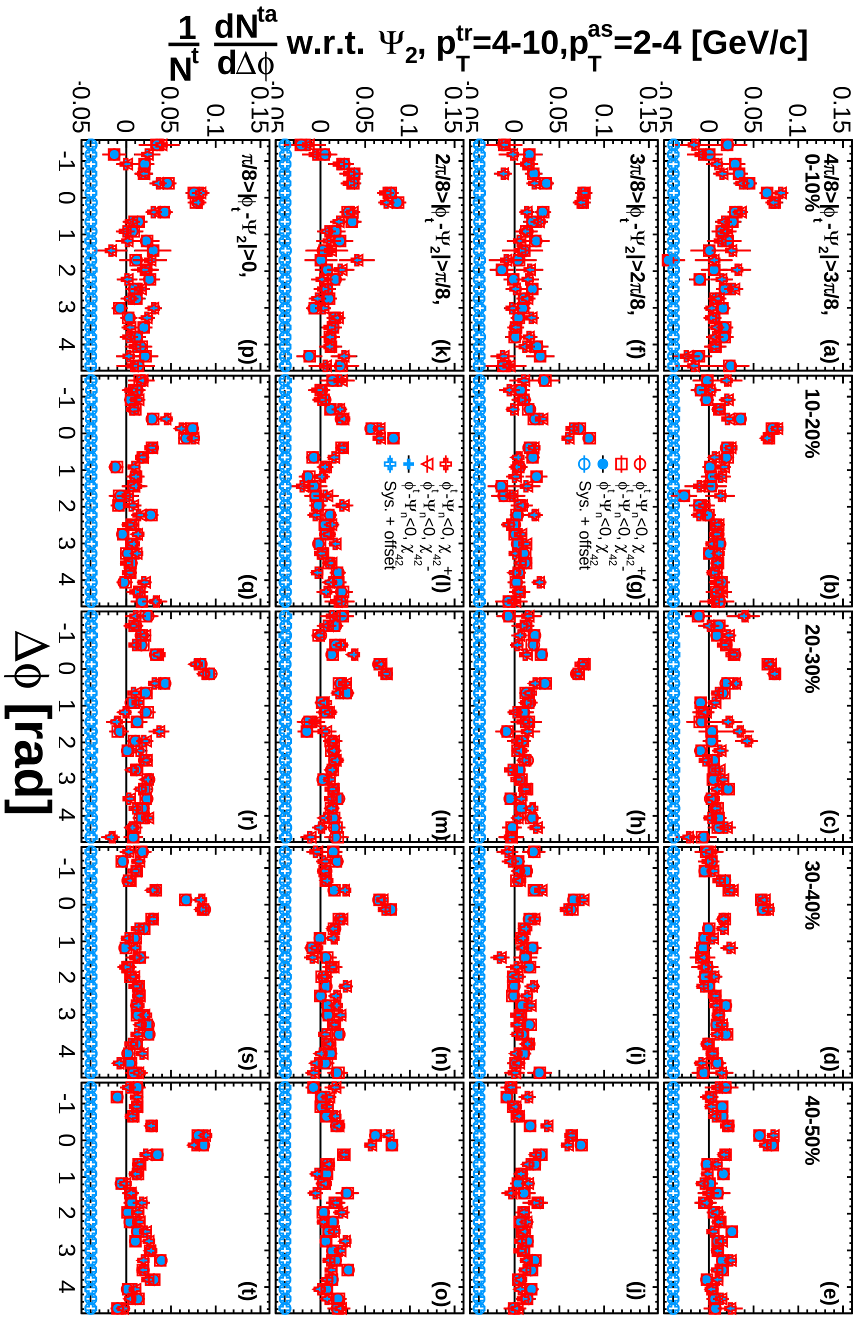

Figure A.49: Ψ_2 dependent correlations at 4-10⊗2-4 GeV/c before resolution correction where contributions of v_2, v_3, and v_4 is subtracted using (Blue) centroid χ_{42} and (Red) ± 1σ χ_{42}. The systematics are plotted with an offset.

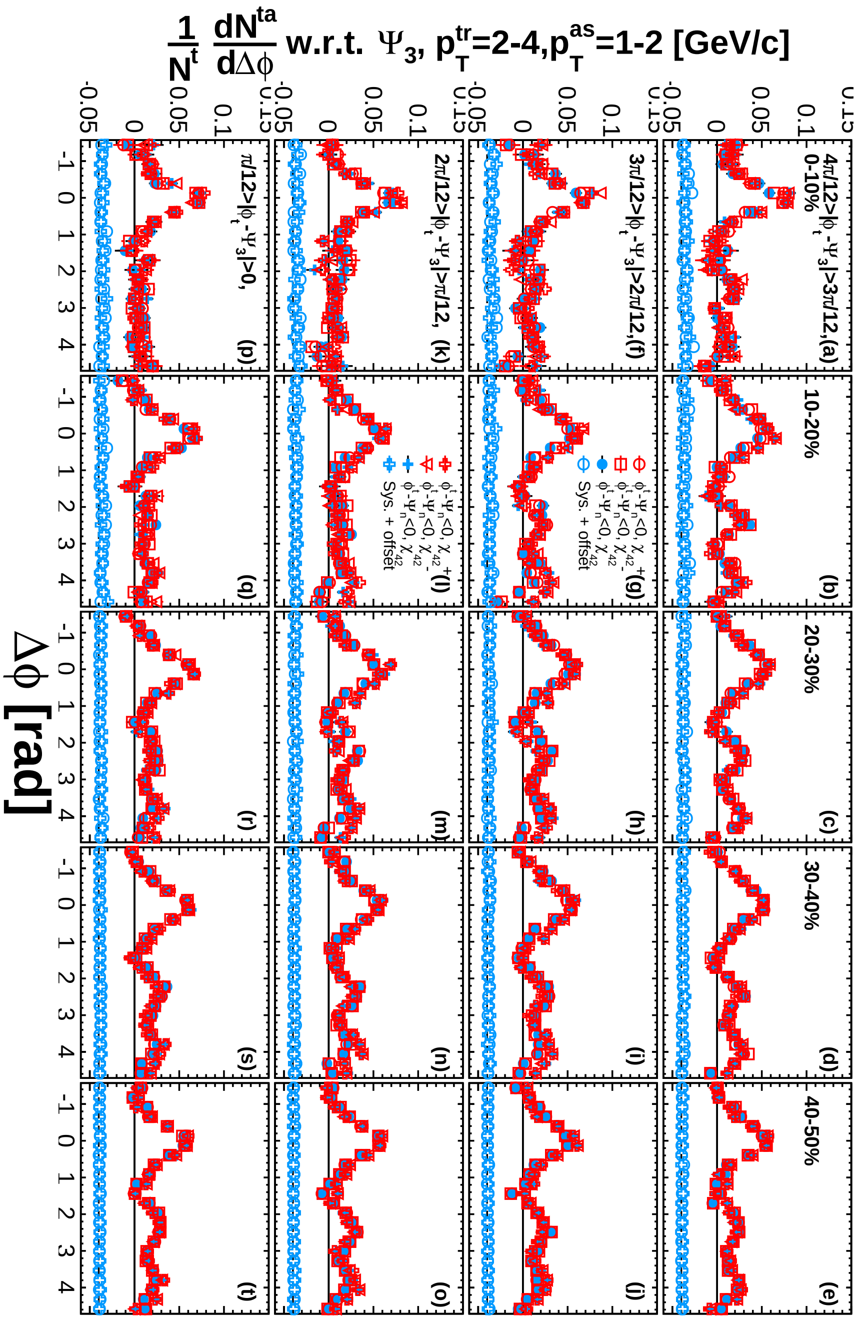

Figure A.50: Ψ_3 dependent correlations at 2-4⊗1-2 GeV/c before resolution correction where contributions of v_2, v_3, and v_4 is subtracted using (Blue) centroid χ_{42} and (Red) $\pm$ 1σ χ_{42}. The systematics are plotted with an offset.

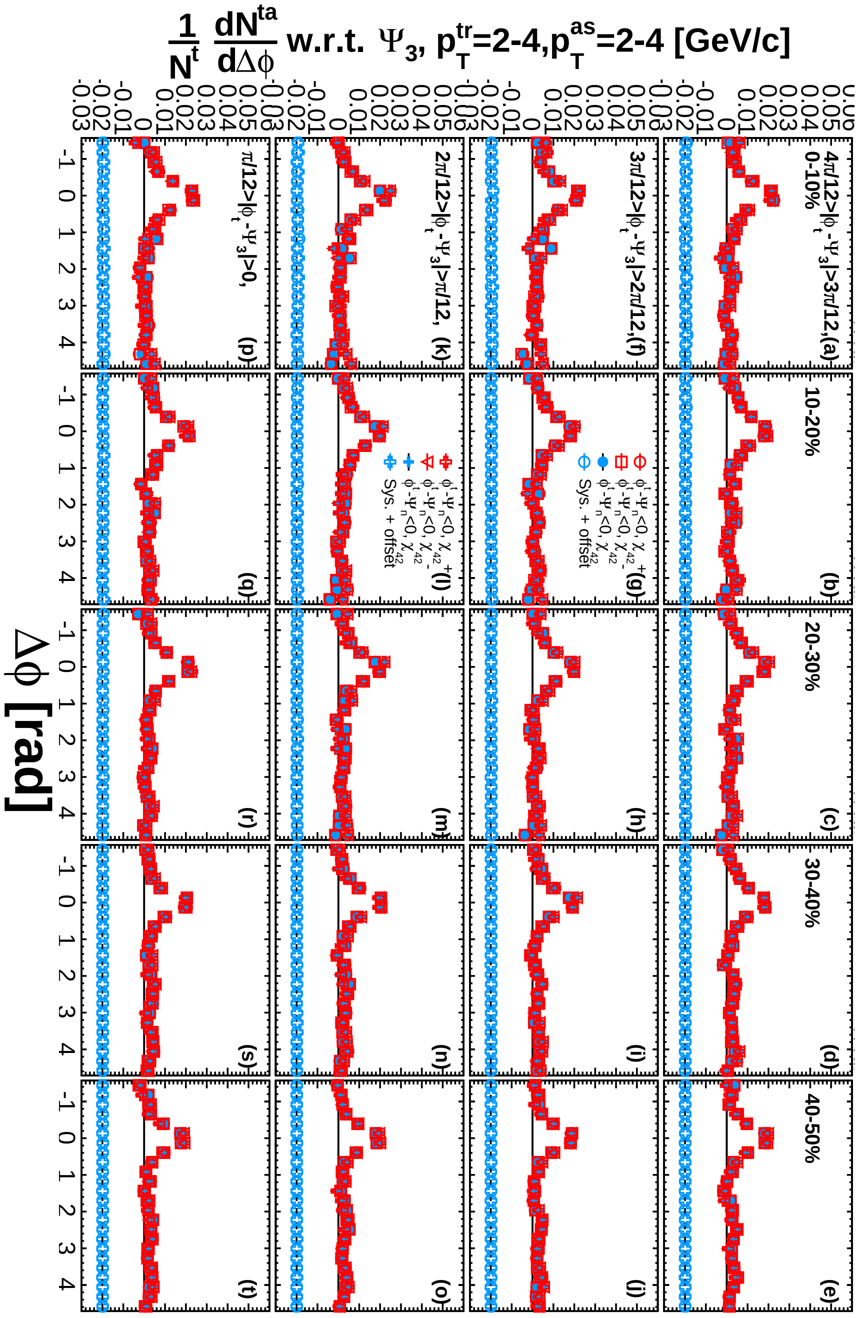

Figure A.51: Ψ_3 dependent correlations at 2-4⊗2-4 GeV/c before resolution correction where contributions of v_2, v_3, and v_4 is subtracted using (Blue) centroid χ_{42} and (Red) ± 1σ χ_{42}. The systematics are plotted with an offset.

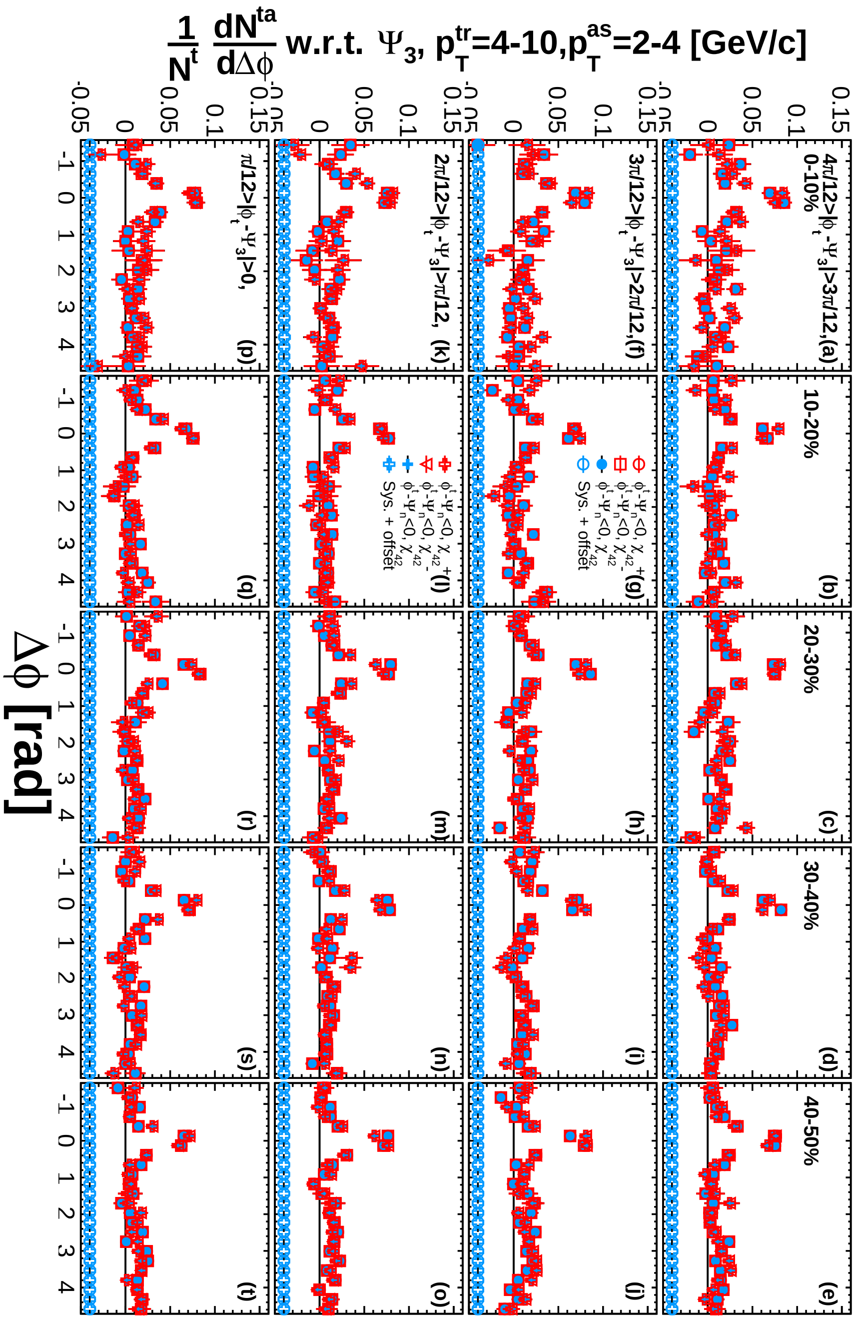

Figure A.52: Ψ_3 dependent correlations at 4-10⊗2-4 GeV/c before resolution correction where contributions of v_2, v_3, and v_4 is subtracted using (Blue) centroid χ_{42} and (Red) $\pm$ 1σ χ_{42}. The systematics are plotted with an offset.

A.2.4 Systematics from Unfolding Parameter

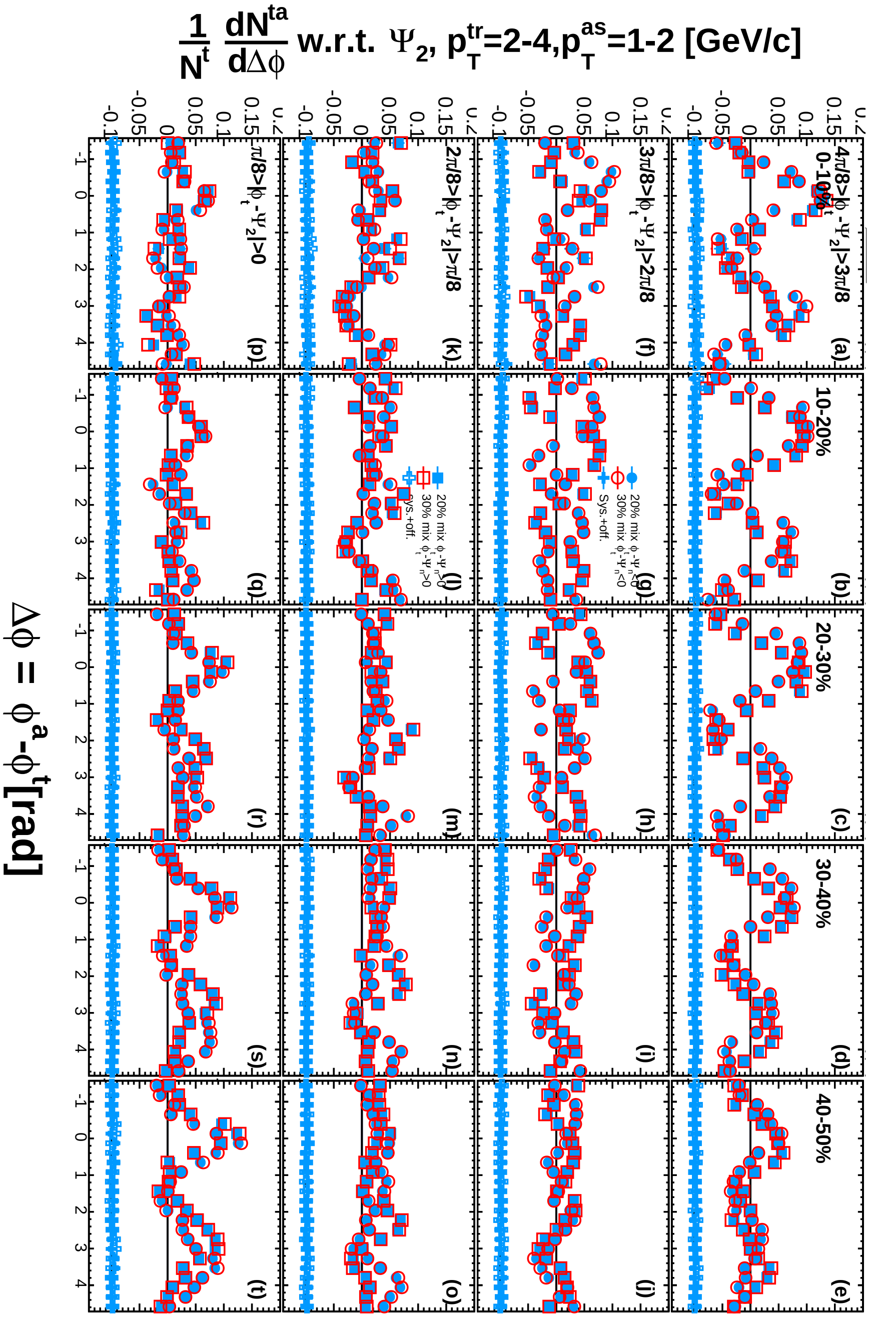

Figure A.53: Ψ_2 dependent correlations at 2-4⊗1-2 GeV/c where contributions of v_2, v_3, and v_4 is subtracted. Data points show the results of (Blue) 20% and (Red) 30% smoothing factors and their difference with an offset.

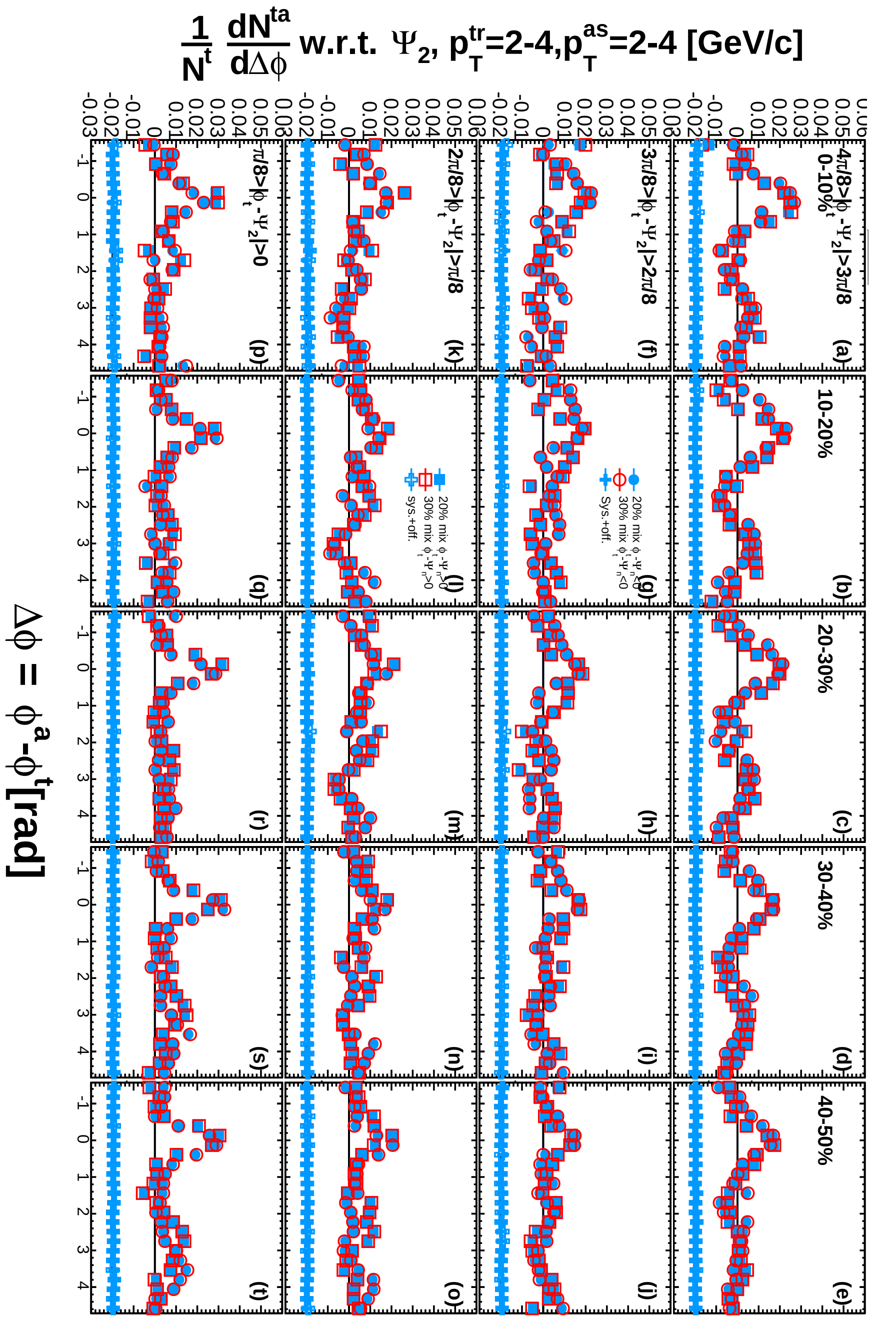

Figure A.54: Ψ_2 dependent correlations at 2-4⊗2-4 GeV/c where contributions of v_2, v_3, and v_4 is subtracted. Data points show the results of (Blue) 20% and (Red) 30% smoothing factors and their difference with an offset.

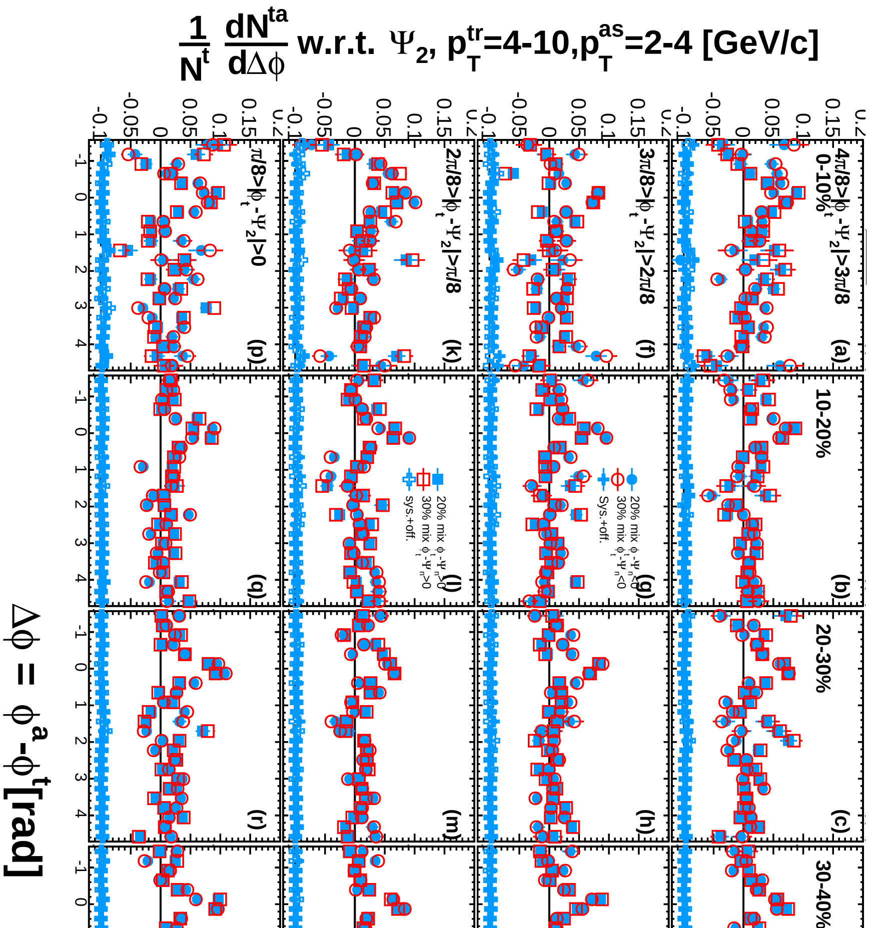

Figure A.55: Ψ_2 dependent correlations at 4-10⊗2-4 GeV/c where contributions of v_2, v_3, and v_4 is subtracted. Data points show the results of (Blue) 20% and (Red) 30% smoothing factors and their difference with an offset.

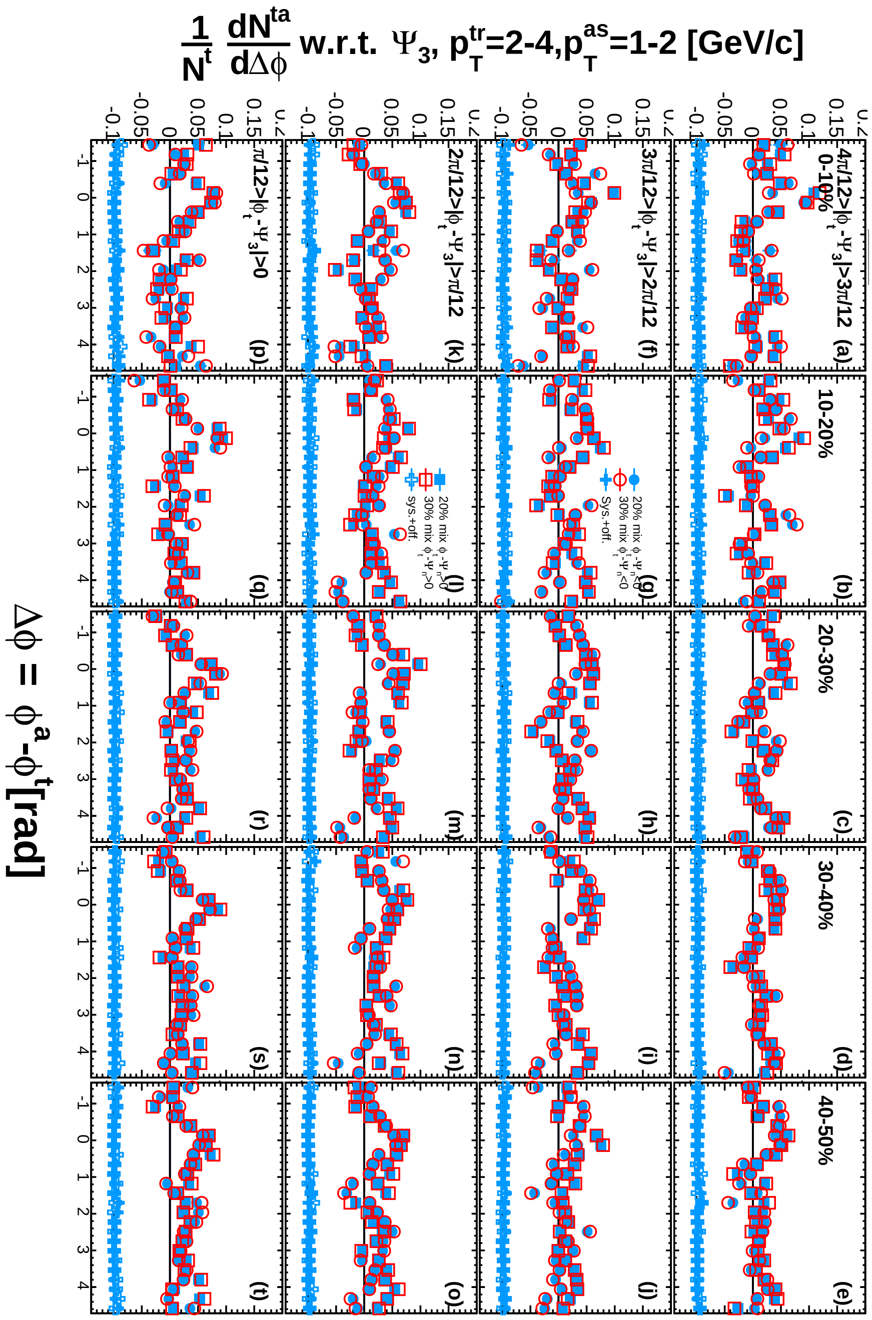

Figure A.56: Ψ_3 dependent correlations at 2-4⊗1-2 GeV/c where contributions of v_2, v_3, and v_4 is subtracted. Data points show the results of (Blue) 20% and (Red) 30% smoothing factors and their difference with an offset.

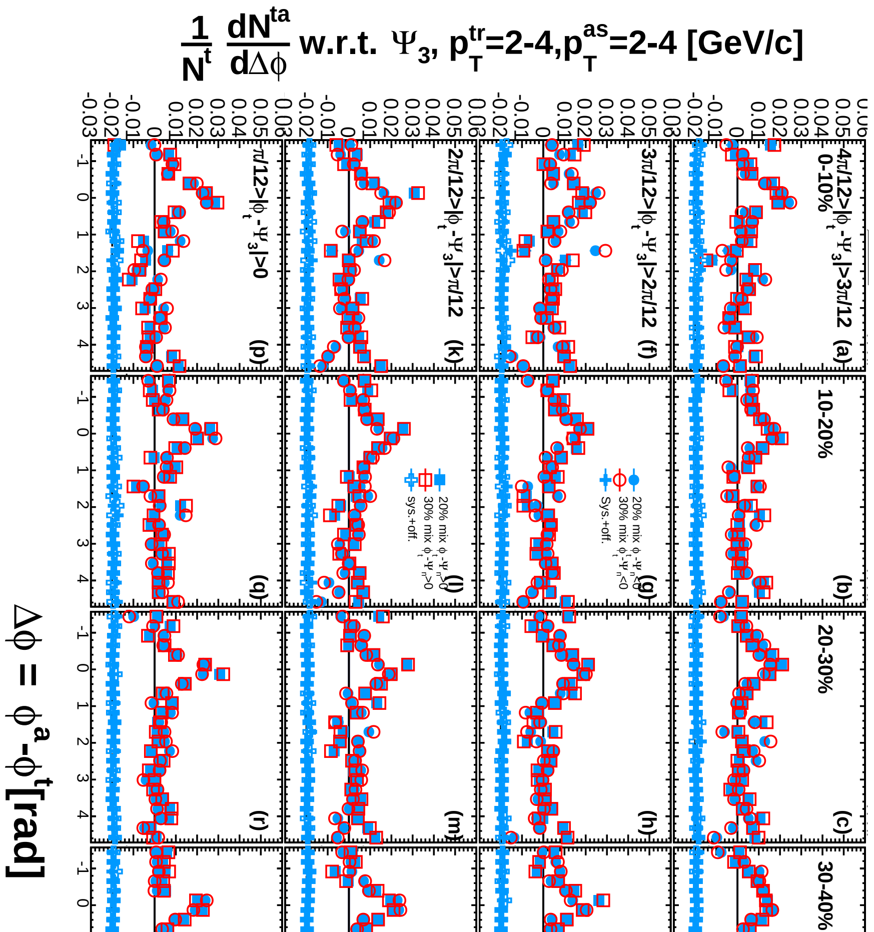

Figure A.57: Ψ_3 dependent correlations at 2-4⊗2-4 GeV/c where contributions of v_2, v_3, and v_4 is subtracted. Data points show the results of (Blue) 20% and (Red) 30% smoothing factors and their difference with an offset.

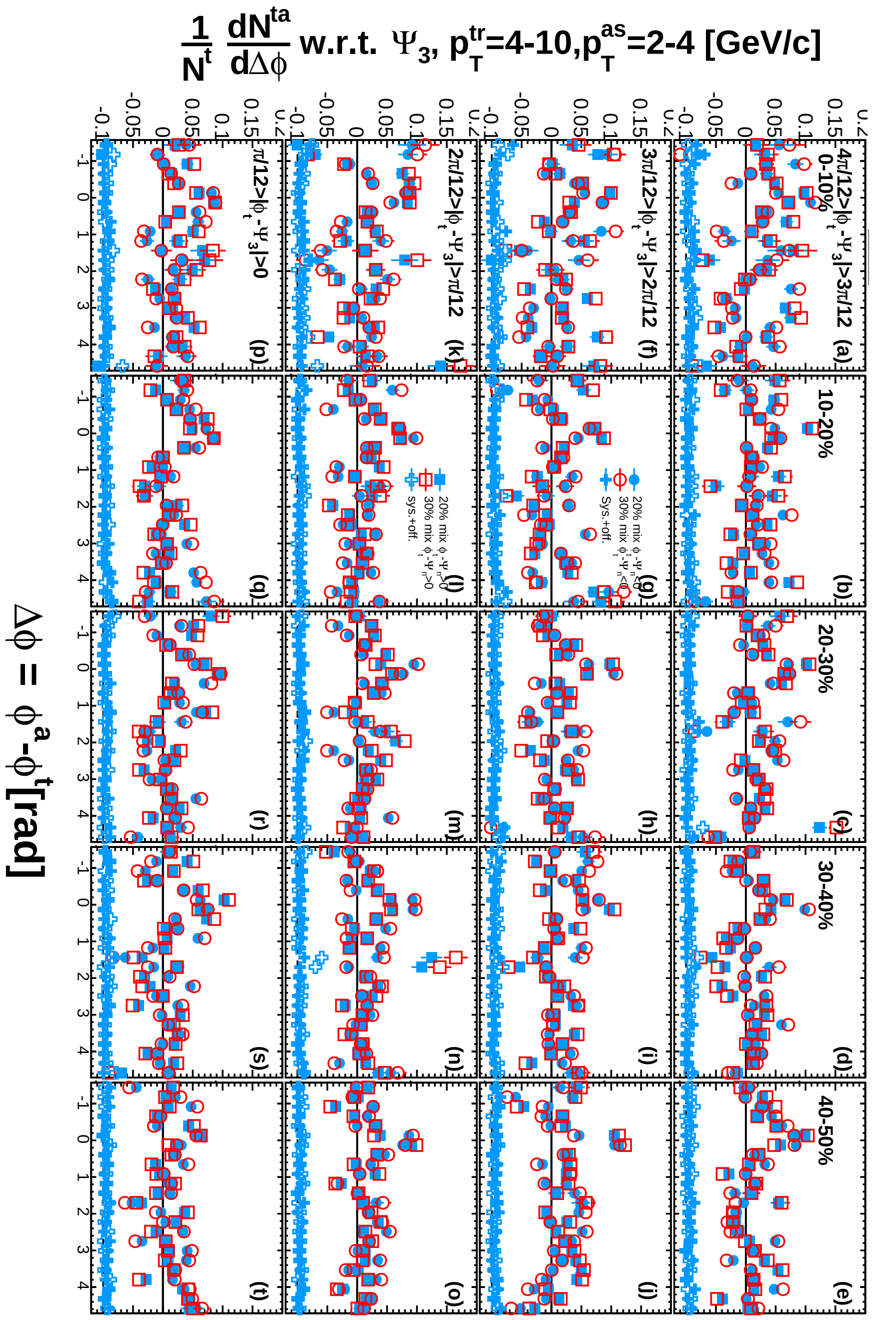

Figure A.58: Ψ_3 dependent correlations at 4-10⊗2-4 GeV/c where contributions of v_2, v_3, and v_4 is subtracted. Data points show the results of (Blue) 20% and (Red) 30% smoothing factors and their difference with an offset.

A.2.5 Systematics from Unfolding Method

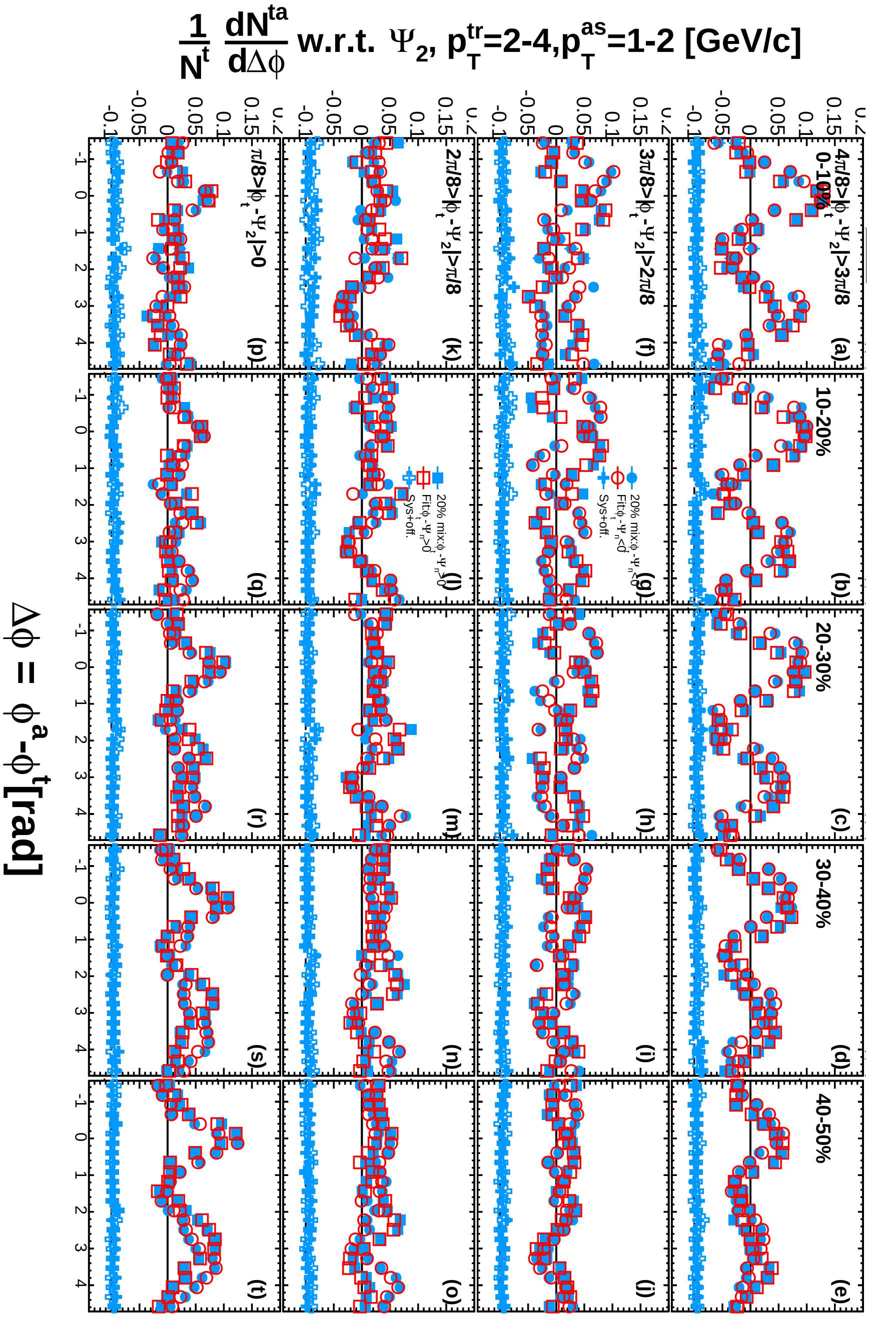

Figure A.59: Ψ_2 dependent correlations at 2-4⊗1-2 GeV/c where contributions of v_2, v_3, and v_4 is subtracted. Data points show the results of (Blue) iteration and (Red) fitting method and their difference with an offset.

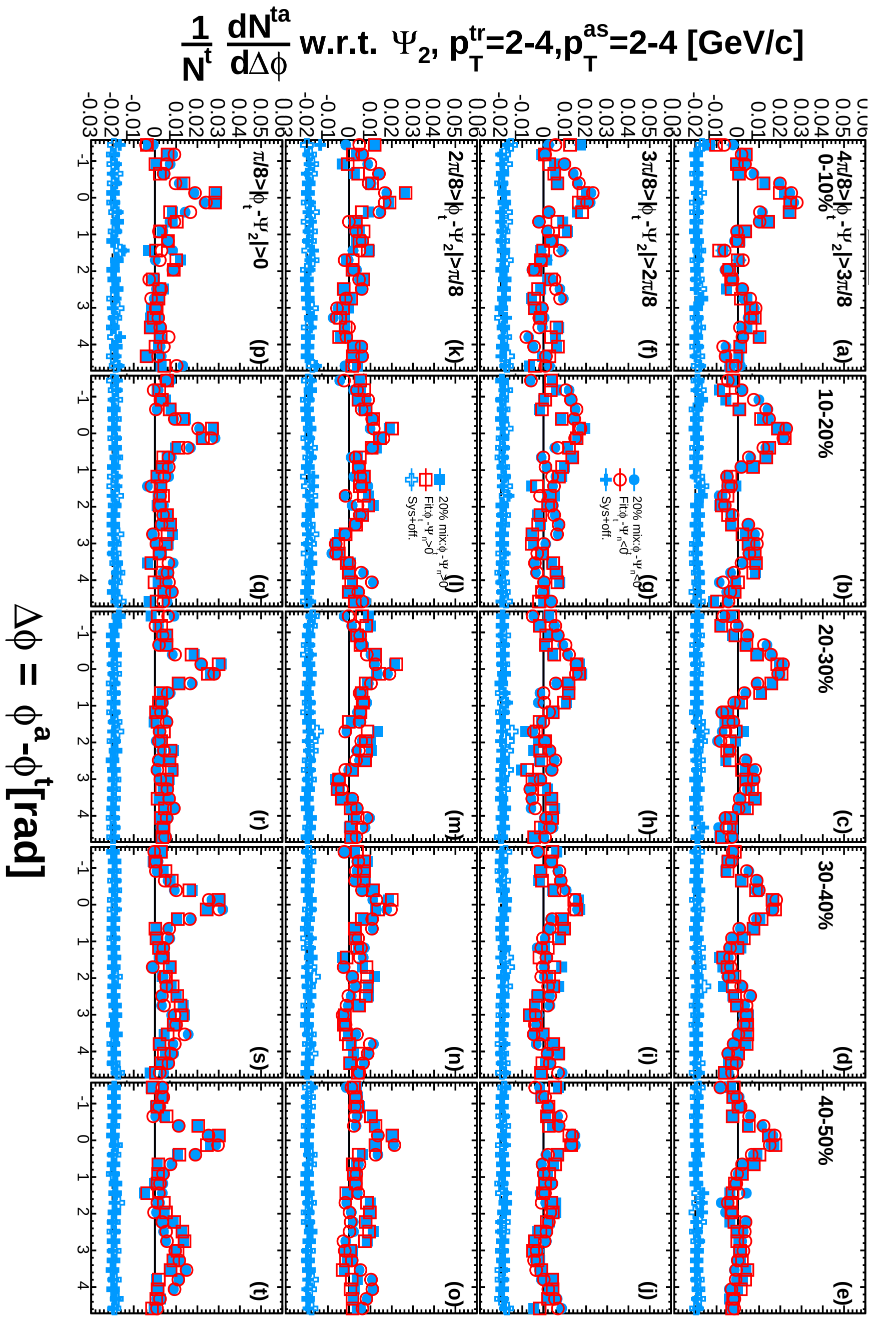

Figure A.60: Ψ_2 dependent correlations at 2-4⊗2-4 GeV/c where contributions of v_2, v_3, and v_4 is subtracted. Data points show the results of (Blue) iteration and (Red) fitting method and their difference with an offset.

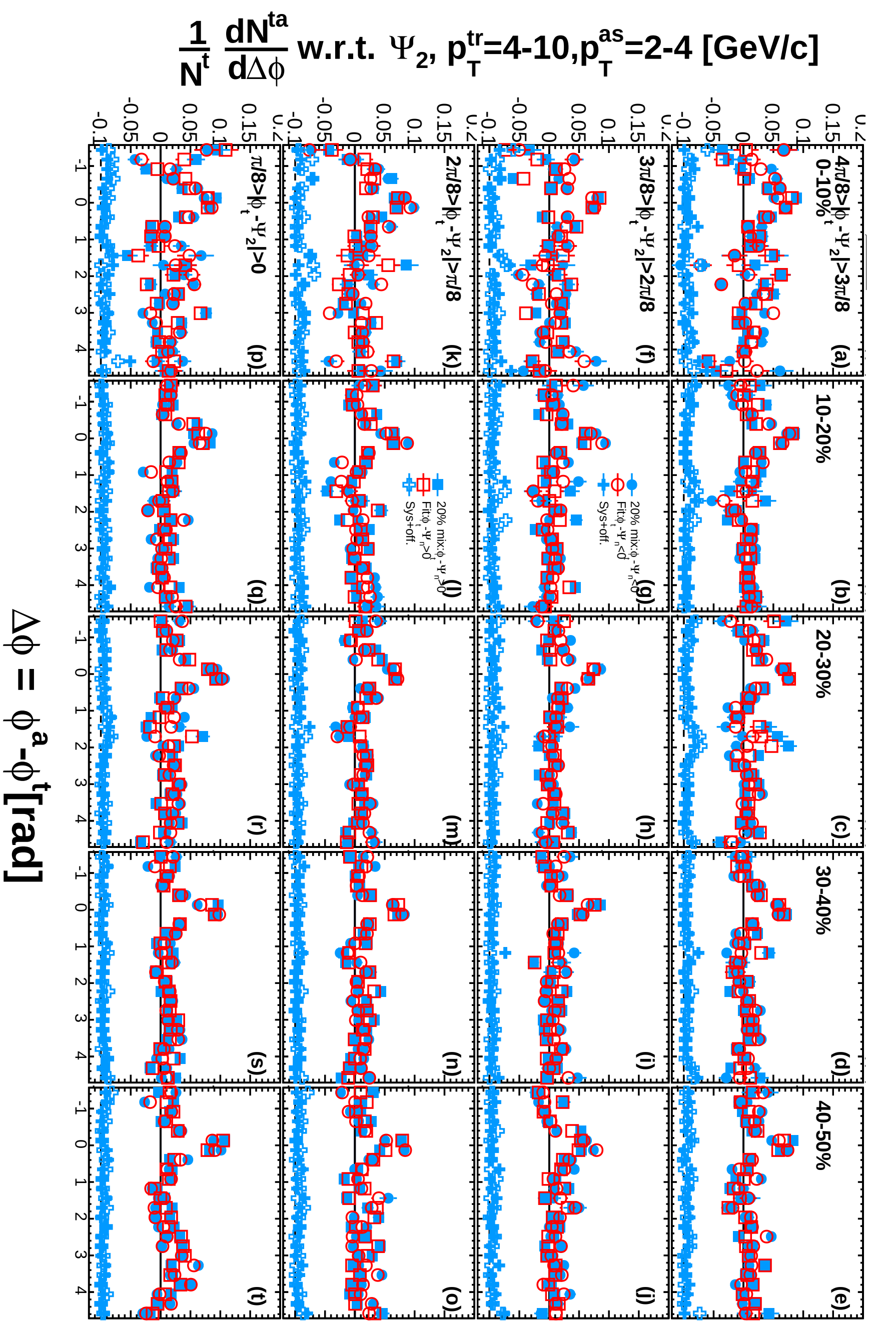

Figure A.61: Ψ_2 dependent correlations at 4-10⊗2-4 GeV/c where contributions of v_2, v_3, and v_4 is subtracted. Data points show the results of (Blue) iteration and (Red) fitting method and their difference with an offset.

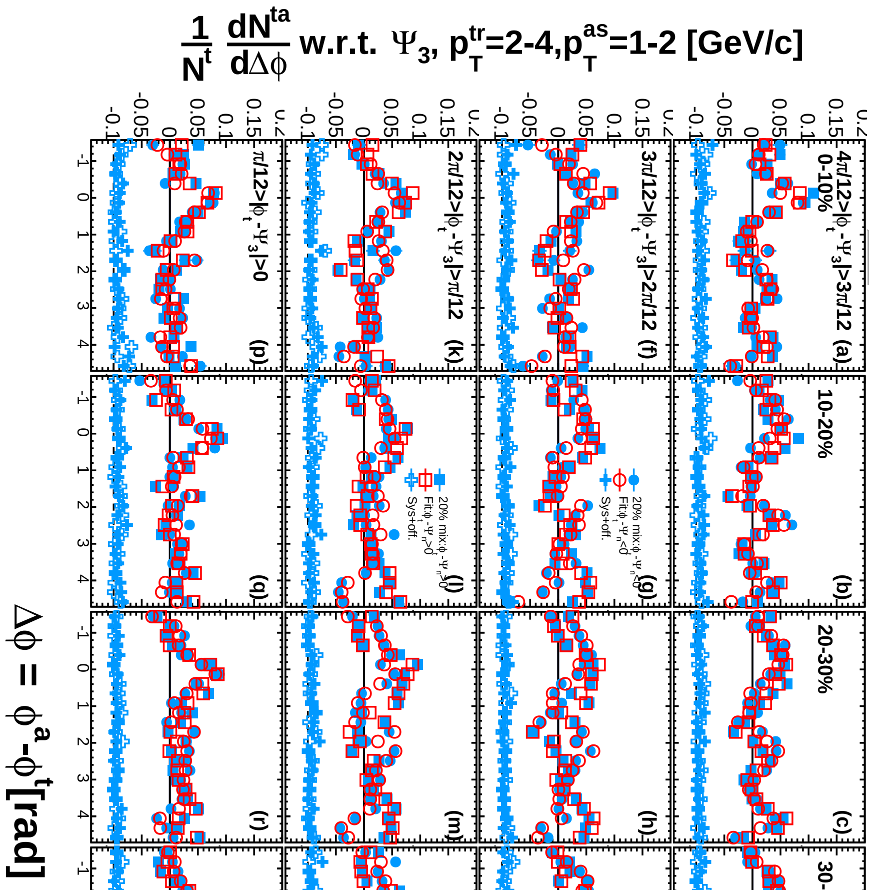

Figure A.62: Ψ_3 dependent correlations at 2-4⊗1-2 GeV/c where contributions of v_2, v_3, and v_4 is subtracted. Data points show the results of (Blue) iteration and (Red) fitting method and their difference with an offset.

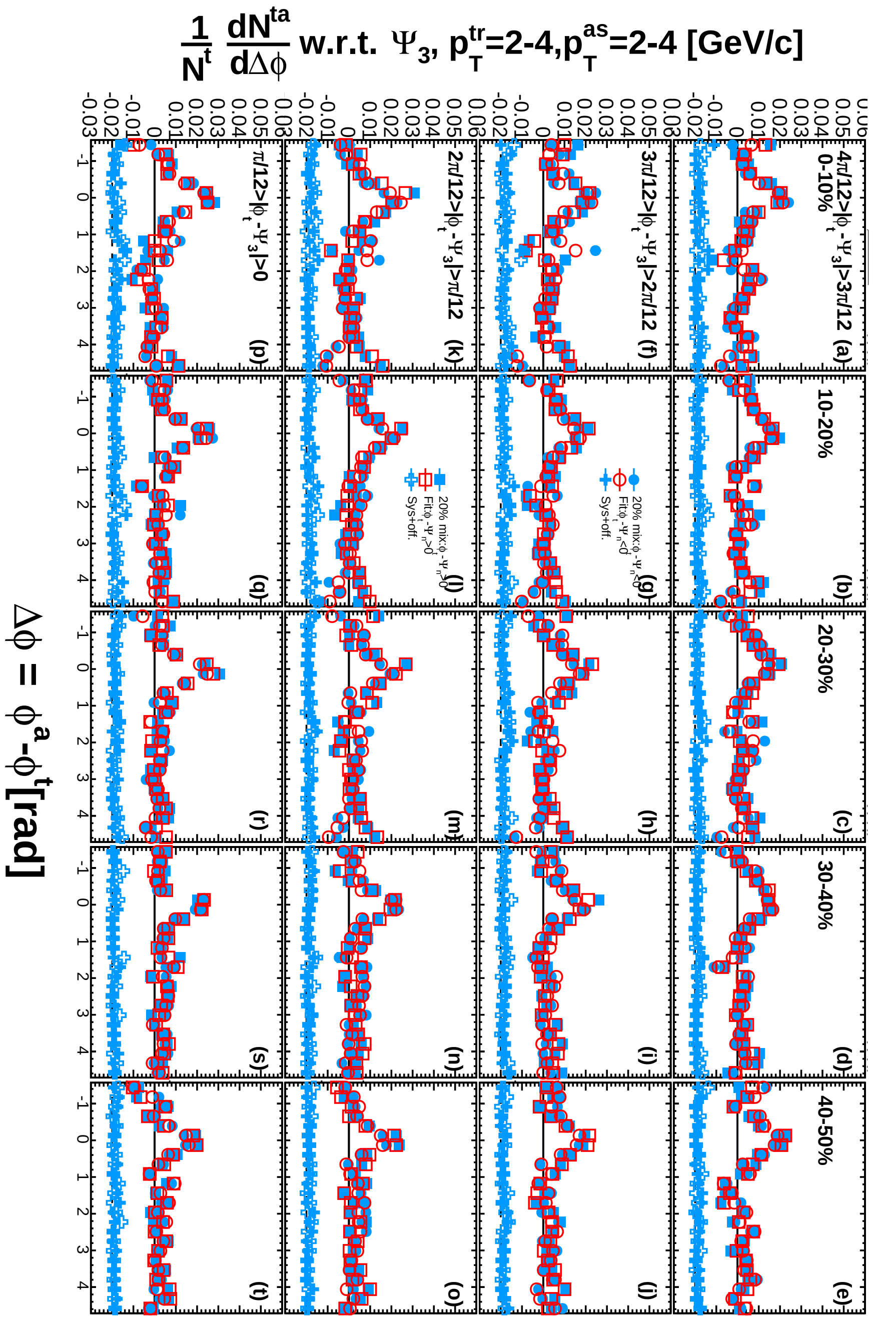

Figure A.63: Ψ_3 dependent correlations at 2-4$\otimes$2-4 GeV/c where contributions of v_2, v_3, and v_4 is subtracted. Data points show the results of (Blue) iteration and (Red) fitting method and their difference with an offset.

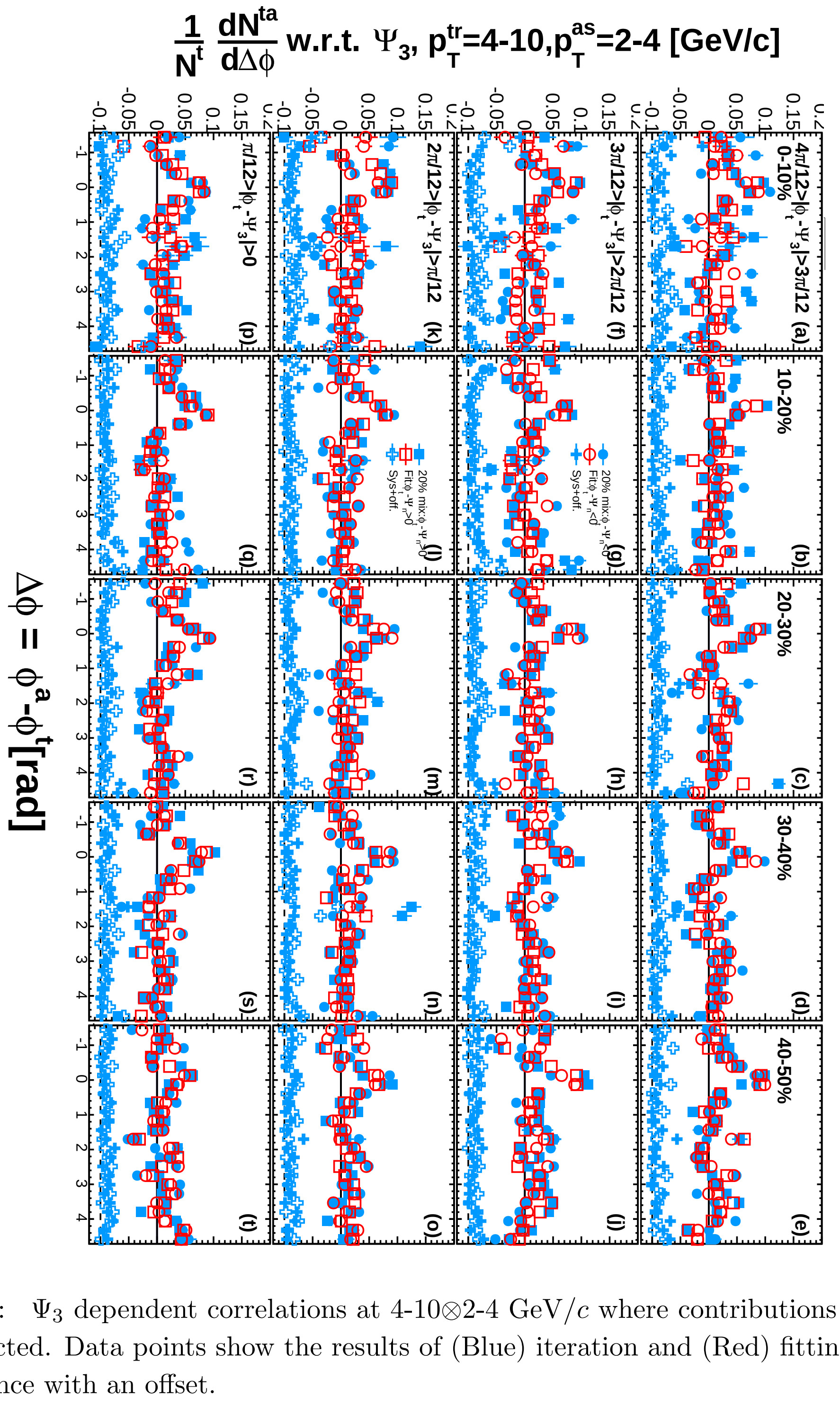

Figure A.64: Ψ_3 dependent correlations at 4-10$\otimes$2-4 GeV/c where contributions of v_2, v_3, and v_4 is subtracted. Data points show the results of (Blue) iteration and (Red) fitting method and their difference with an offset.

Bibliography

[1] Michael Schmelling, Status of the Strong Coupling Constant, hep-ex/9701002 (1997)

[2] F. Karsch, E. Laermann, and A. Peikert, “The pressure in 2, 2+1, and 3 flavour QCD”, Phys. Lett. **B478**, 447, (2000)

[3] M. A. Stephanov, “QCD phase diagram: an overview”, arXiv:hep-lat/0701002 (2006)

[4] H. Masui, “Measurement of Centrality Dependence of Elliptic Flow for Identified Hadrons in Au + Au Collisions at $\sqrt{s_{NN}}$=200GeV”, Ph.D Thesis at the University of Tsukuba (2007)

[5] Michael L. Miller*et. al.*, “Glauber Modeling in High Energy Nuclear Collisions”, nucl-ex/0701025 (2007)

[6] W-M Yao, *et al.*, “Review of Particle Physics”, J. Phys. G: Nucl. Part. Phys. **33**, 1 (2006)

[7] T. Matsui, “Dynamical evolution of the quark-gluon plasma and phenomenology”, Nucl. Phys.**A461**, 27 (1987)

[8] Larry. McLerran, “The Color Glass Condensate and Small x Physics: 4 Lectures.”, arXiv:hep-ph/0104285 (2001)

[9] Xinn-Nian Wang. “A pQCD-based approach to parton production and equilibration in high-energy nuclear collision”, Phys. Rep. 280, 287 (1997)

[10] P. F. Kolb and R. Rapp,“Transverse flow and hadrochemistry in Au+Au collisions at $\sqrt{s_{NN}}$=200GeV”, Phys. Rev. **C67** 044903 (2003)

[11] B. Alver and G. Roland, “Collision-geometry fluctuations and triangular flow in heavy-ion collisions”, Phys. Rev.**C81**, 054905 (2010)

[12] J. L. Nagle and M. P. McCumber, ”Heavy ion initial conditions and correlations between higher moments in the spatial anisotropy”, Phys. Rev.**C83**, 044908 (2011)

[13] A.Adare *et. al.*, (PHENIX Collaboration),“Neutral pion production with respect to centrality and reaction plane in Au+Au collisions at $\sqrt{s_{NN}}$=200 GeV”, arXiv:1208.2254 (2013)

[14] S.Afansiev *et. al.*, (PHENIX Collaboration),“Measurement of Direct Photons in Au+Au Collisions at $\sqrt{s_{NN}}$= 200 GeV”, arXiv:1205.5759 (2012)

[15] C. Adler *et. al.*, (STAR Collaboration), "Disappearance of Back-To-Back High-p_T Hadron Correlations in Central Au+Au Collisions at $\sqrt{s_{NN}}$=200GeV", Phys. Rev. Lett. **90**, 082302, (2003)

[16] J. Adamas *et. al.*, (STAR Collaboration), "Evidence from d+Au Measurements for Final-State Suppression of High-pT Hadrons in Au+Au Collisions at RHIC", Phys. Rev. Lett. **91**, 0720304, (2003)

[17] S.S. Adler *et. al.*, (PHENIX Collaboration), "Dense-Medium Modifications to Jet-Induced Hadron Pair Distributions in Au+Au Collisions at $\sqrt{s_{NN}}$=200GeV", Phys. Rev. Lett. **97**, 052301, (2006)

[18] A. Adare *et. al.*, (PHENIX Collaboration), "Dihadron azimuthal correlations in Au+Au Collisions at $\sqrt{s_{NN}} = 200$ GeV", Phys. Rev. **C 78**, 014901, (2008)

[19] A. Adare *et. al.*, (PHENIX Collaboration), "Suppression of away-side jet fragments with respect to reaction plane in Au+Au collisions at $\sqrt{s_{NN}} = 200$ GeV", Phys. Rev. **C 84**, 024904, (2003)

[20] A. Adare *et. al.*, (PHENIX Collaboration), "System Size and Energy Dependence of Jet-Induced Hadron Pair Correlation Shapes in Cu+Cu and Au+Au Collisions at $\sqrt{s_{NN}}$= 200 and 62.4 GeV", Phys. Rev. Lett. **97**, 052301, (2007)

[21] B.I. Abelev *et. al.*, (STAR Collaboration), "Long range rapidity correlations and jet production in high energy nuclear collisions", Phys. Rev. **C 80**, 046912, (2009)

[22] A. Adare *et. al.*, (PHENIX Collaboration), "Measurements of Higher Order Flow Harmonics in Au+Au Collisions at $\sqrt{s_{NN}}$=200 GeV", Phys. Rev. Lett. **107**, 252301, (2011)

[23] Burak Han Alver *et. al.*, "Triangular flow in hydrodynamics and transport theory", Phys. Rev. **C 82**, 034913, (2010)

[24] Björn Schenke, *et. al.*, "Elliptic and Triangular Flow in Event-by-Event D=3+1 Viscous Hydrodynamics", Phys. Rev. Lett.**106**, 042301, (2011)

[25] Hannah Petersen *et. al.*, "Triangular flow in event-by-event ideal hydrodynamics in Au+Au collisions at $\sqrt{s_{NN}}$=200A GeV", Phys. Rev. **C 82**, 041901(R), (2010)

[26] B. Abelev *et. al.*, (STAR Collaboration), "Indications of Conical Emission of Charged Hadrons at the BNL Relativistic Heavy Ion Collider", Phys. Rev. Lett.**102**, 052302, (2009)

[27] V. Koch, A. Majumder, and Xin-Nian Wang, "Cherenkov Radiation from Jets in Heavy-Ion Collisions", Phys. Rev. Lett.**96**, 172302, (2006)

[28] T. Renck, and J. Ruppert, "Mach cones in an evolving medium", Phys. Rev. **C 73**, 011901(R), (2006)

[29] M. G. Mustafa and R. Ray, "Thermodynamics of the Polyakov-Nambu-Jona-Lasinio model with nonzero baryon and isospin chemical potentials", Phys. Rev. **D 75**, 094015, (2007)

[30] B. Betz *et. al.*, "Universal Flow-Driven Conical Emission in Ultrarelativistic Heavy-Ion Collisions", Phys. Rev. Lett.**105**, 222301, (2010)

[31] R.P.G. Andrade *et. al.*, "Temporal evolution of tubular initial conditions and their influence on two-particle correlations in relativistic nuclear collisions", Phys. Lett.**B 712**, 226, (2012)

[32] J. Takahashi *et. al.*, "Topology Studies of Hydrodynamics Using Two-Particle Correlation Analysis", Phys. Rev. Lett.**103**, 242301, (2009)

[33] H.J. Drescher *et. al.*, "Initial condition for quark-gluon plasma evolution", Phys. Rev. **C 65**, 054902, (2002)

[34] C. E. Aguiar *et. al.*, "Event-by-event fluctuations in hydrodynamical description of heavy-ion collisions", Nucl. Phys. **A 698**, 639, (2002)

[35] G. Aad *et. al.*, (ATLAS Collaboration), "Measurement of the azimuthal anisotropy for charged particle production in $\sqrt{s_{NN}}$=2.76 TeV lead-lead collisions with the ATLAS detector", Phys. Rev. **C 86**, 041907, (2012)

[36] M. Hahn *et. al.*, "RHIC project overview", Nucl. Instl. Method **A 499**, 235, (2003)

[37] M. Hahn *et. al.*, "The RHIC design overview", Nucl. Instl. Method **A 499**, 245, (2003)

[38] PHENIX Conceptual Design Report, BNL, 1993, unpublished

[39] M. Allebib *et. al.*, "PHENIX inner detector", Nucl. Instl. Method **A 499**, 549, (2003)

[40] E. Richardson *et. al.*, "A reaction plane detector for PHENIX at RHIC", Nucl. Instl. Method **A 636**, 99, (2011)

[41] P. B. Nilsson *et. al.*, "The pixel readout system for the PHENIX pad chambers", Nucl. Phys. **A 661**, (1999)

[42] K. Adcox *et. al.*, "Construction and performance of the PHENIX pad chambers", Nucl. Instl. Method **A 497**, 263, (2003)

[43] J. Haggerty *et. al.*, "Letter of intent for PHENIX reaction plane detector", Internal Letter of Intent, (2006)

[44] C. Adler *et. al.*, "The RHIC zero-degree calorimeters", Nucl. Instl. Method **A 461**, 337, (2001)

[45] K. Adcox *et. al.*, "PHENIX Central Arm Tracking Detectors", Nucl. Instl. Method **A 499**, 489, (2003)

[46] M. Aizawa *et. al.*, "PHENIX Central Arm Particle I.D. Detectors", Nucl. Instl. Method **A 499**, 508, (2003)

[47] L. Aphecetche *et. al.*, "The PHENIX calorimeter", Nucl. Instl. Method **A 499**, 521, (2003)

[48] G. David *et al.*, "The PHENIX lead-scintillator electromagnetic calorimeter: Test beam andconstruction experience, IEEE Trans. Nucl. Sci. **45**, 692, (1998)

[49] WA98 Collaboration,"Large acceptance measurement of photons and charged particles in heavy ion reactions. CERN SPSLC/91-17, (1991)

[50] PHENIX Collaboration S. Adler et al., High-p_T charged hadron suppression in Au+Au collisions at $\sqrt{s_{NN}}$=200 GeV, Phys. Rev.**C 69**, 034910 (2004)

[51] X. N. Wang and M. Gyulassy, HIJING: A Monte Carlo model for multiple jet production in pp, pA, and AA collisions, Phys. Rev. **D 44**, 3501 (1991)

[52] T. Hachiya et al., Study of the BBC trigger efficiency based on simulations for run-2 analysis, PHENIX Internal Analysis Note 107 (2002)

[53] J.Y. Ollitrault, Determination of the reaction plane in ultrarelativistic nucler collisions, Phys. Rev.**D 48**, 1132 (1993)

[54] A. M. Poskanzer and S. A. Voloshin, Methods for analyzing anisotropic flow in relativistic nuclear collisions, Phys. Rev.**C58**, 1671 (1998)

[55] Suppression of away-side jet fragments with respect to the reaction plane in Au + Au collisions at $\sqrt{s_{NN}}$=200 GeV, Phys. Rev.**C 84**, 024904 (2011)

[56] Elliptic flow contribution to two-particle correlations at different orientations to the reaction plane, Phys. Rev.**C 69**, 021901 (2003)

[57] B. Betz, "Deflected Jets or Hot Spots? Conical Correlations of Hard Trigger Particles", arXiv:nucl-th/1012.4418v1 (2010)

[58] L. Pang and X. N. Wan "Relics of Minijets amid Anisotropic Flows in High-energy Heavy-ion Collisions", arXiv:nucl-th/1309.6735v2 (2013)

[59] L. Pang and X. N. Wan, "Effects of initial flow velocity fluctuation in event-by-event (3 + 1)D hydrodynamics", Phys. Rev. **C 86**, 024911 (2012)

[60] T. Todoroki *et. al.*, (PHENIX Collaboration), "Two particle correlation measurements with respect to higher harmonic event planes at PHENIX", Nucl. Phys. **A 904-905**, 493c (2013)

[61] A. Adare *et. al.*, (PHENIX Collaboration), "Azimuthal Anisotropy of π^0 Production in Au+Au Collisions at $\sqrt{s_{NN}}$ = 200 GeV: Path-Length Dependence of Jet Quenching and the Role of Initial Geometry", Phys. Rev. Lett. **105**, 142301, (2010)

[62] S. Wicks *et. al.*, "Elastic, inelastic, and path length fluctuations in jet tomography", Nucl. Phys. **A 784**, 426 (2007)

[63] A. Drees *et. al.*, "Medium-induced jet absorption in relativistic heavy-ion collisions", Phys. Rev. **C 71**, 034909 (2005)

[64] J. Jia and R. Wei, "Dissecting the role of initial collision geometry for jet quenching observables in relativistic heavy ion collisions", Phys. Rev. **C 82**, 024902 (2010)

[65] C. Marquet and T.Renk, "Jet quenching in the strongly-interacting quarkgluon plasma", Phys. Lett. **B 685**, 270 (2010)